UNIVERSITY OF SOUTHAMPTON

Surveying the Gamma-ray sky with the BATSE and INTEGRAL satellites

Adam Ben Hill

Submitted for the degree of Doctor of Philosophy

SCHOOL OF PHYSICS AND ASTRONOMY
FACULTY OF SCIENCE

May 19, 2006

UNIVERSITY OF SOUTHAMPTON

ABSTRACT

FACULTY OF SCIENCE

SCHOOL OF PHYSICS AND ASTRONOMY

Doctor of Philosophy

Surveying the Gamma-ray sky with the BATSE and INTEGRAL satellites

by Adam Ben Hill

This thesis describes the developments and contributions made by Adam Hill to survey the Gamma-ray sky with the BATSE and INTEGRAL satellites. The soft γ-ray sky has been relatively unexplored on large scales. The last survey of the entire sky in this energy band was made by the HEAO-1 A4 mission in the late 1970's. This thesis takes advantage of new techniques and instruments to probe the source populations of the γ-ray sky in the energy band 20–160 keV.

The BATSE instrument served as the all-sky monitor on-board the Compton Gamma-Ray Observatory for 9 years. By applying the newly developed LIMBO software and CLEAN algorithms an all-sky map of the sky is constructed using all 9 years of BATSE data. The map is constructed using data which spans the 30–160 keV energy band and produces a source catalogue of 36 sources down to a flux of ~20 mCrab. The performance and limitations of this new technique are assessed and presented.

IBIS is the imager on-board the INTEGRAL γ-ray observatory. Data from IBIS is used in the construction of mosaics of the γ-ray sky which span the 20–100 keV energy band. The techniques and methods of the 1^{st} and 2^{nd} IBIS/ISGRI Survey Catalogues are presented which identify 123 and 209 discrete γ-ray sources respectively.

The global properties of the sources of the 1^{st} IBIS/ISGRI Survey Catalogue are analysed on a statistical basis. The properties of the X-ray binary populations and the unclassified INTEGRAL sources are presented. The unclassified source population are seen to share many of the characteristics of the high mass systems. A detailed study of IGR J18027-2016 indicates that it is a proto-typical example of the new INTEGRAL sources and is identified to be an obscured, supergiant high mass X-ray binary with a neutron star companion.

Publications

Material found in this thesis has been published or accepted for publication in the following places:

"Gamma-Ray All-Sky Imaging with the Burst and Transient Source Experiment", Shaw, S. E., Westmore, M. J., Hill, A. B., Bird, A. J., Dean, A. J., Ferguson, C., Knödlseder, J., Lockley, J. J., Willis, D. R., 2004, A&A, 418, 1187

"Gamma Ray All-Sky Imaging with BATSE", Hill, A. B., Barlow, E. J.,Bird, A. J., Dean, A. J., Ferguson, C., Shaw, S. E., Westmore, M. J., Willis, D. R., 2004, in The INTEGRAL Universe: Proceedings of the 5th INTEGRAL Workshop, Munich, 2004, ed. A. Gimenez, V. Reglero, & C. Winkler, Vol. ESA SP-552, 169–172

"The First IBIS/ISGRI Soft Gamma-Ray Galactic Plane Survey Catalogue", Bird, A. J., Barlow, E. J., Bassani, L., Bazzano, A., Bodaghee, A., Capitanio, F., Cocchi, M., Del Santo, M., Dean, A. J., Hill, A. B., Lebrun, F., Malaguti, G., Malizia, A., Much, R., Shaw, S. E., Stephen, J. B., Terrier, R., Ubertini, P., Walter, R., 2004, ApJ 607, L33

"The 1-50 keV spectral and timing analysis of IGR J18027-2016", Hill, A. B., Walter, R., Knigge, C., Bazzano, A., Belanger, G., Bird, A. J., Dean, A. J., Galache, J. L., Malizia, A., Renaud, M., Stephen, J. B., Ubertini, P., 2005, A&A, 439, 255

"Global characteristics of the 1st IBIS/ISGRI catalogue sources", Dean, A. J., Bazzano, A., Hill, A. B., Stephen, J. B., Bassani, L., Barlow, E. J., Bird, A. J., Lebrun, F., Sguera, V., Shaw, S. E., Ubertini, P., Walter, R., Willis, D. R., A&A, 443, 485

"The second IBIS/ISGRI Soft Gamma-Ray Galactic Plane Survey Catalogue", Bird, A. J., Barlow, E. J., Bassani, L., Bazzano, A., Belanger, G., Bodaghee, A., Capitanio, F., Dean, A. J., Fiocchi, M., Hill, A. B., Lebrun, F., Malizia, A., Mas-Hesse, J. M., Molina, M., Moran, L., Renaud, M., Sguera, V., Shaw, S. E., Stephen, J. B., Terrier, R., Ubertini, P., Walter, R., Willis, D. R. & Winkler, C., 2006, ApJ, 366, 765

Acknowledgements

This thesis would not have been possible without the support, guidance and assistance of many individuals. The BATSE All-Sky Survey and the IBIS/ISGRI survey are international collaborations involving people from many different institutions and countries.

Thanks must go to Drs' Matt Westmore, Simon Shaw, Dave Willis and Colleen Wilson-Hodge who introduced me to the mysterious world of BATSE. Specific thanks must go to Matt and Simon for originally developing the BATSE LIMBO imaging code and CLEAN algorithms which I had the pleasure of applying to the entire 9 year BATSE data set.

I have had the privilege of working with many people at the ISDC, IASF Rome and IASF Bologna. A very big thankyou goes to Dr. Tony Bird as the leader of the IBIS/ISGRI survey team and as the man who maintains the computer systems network. Without his intervention whenever the BATSE code crashed half the network the results presented here would never have materialised. His support and advice have proved invaluable

Thanks to Jose Galache, Liz Barlow and Andy Barnes, my fellow finalist PhD students, for the many varied discussions and conversations regarding astronomy and less related matters. Thankyou to my office mates Vito, Manuela, Dave for providing a stimulating working environment. I would like to thank all the members of the Southampton astronomy group past and present, especially Christian Knigge for patiently explaining the intricacies of timing analysis.

Thanks to all my friends in the Wessex Lane Wardenal Team who have given me support and encouragement through some trying times over the last few years. Special thanks must go to Jo Honey, Rich Dudley, Chris Yorke, Becky Maile, Chris Harper, Katherine Brown and Hannah Foreman. Thankyou to all my friends outside of astronomy.

I deeply appreciate the unwavering support and motivation of my Mum, Dad and sister, Sarah. Thankyou for putting up with me all this time. Finally a big thankyou has to go to my supervisor Prof. Tony Dean, without whose vision and belief in my capabilities this thesis would never have been written. The opportunity to work on INTEGRAL has been a wonderful, unforgetable experience.

Adam Hill, 2006

Contents

List of Figures

List of Tables

Chapter 1

Hard X-ray / γ-ray Astronomy

1.1 Introduction

The study of astronomical objects in the γ-ray regime in recent years has entered into the main stream of astrophysics, no longer the area of expertise of a minority community. Traditional X-ray missions have been most sensitive in the soft X-ray regime, < 10 keV and are exemplified by the current XMM-Newton and Chandra X-ray observatories. Although the distinction between high energy bands is arbitrary we shall consider photons of energy <10 keV to be the soft X-ray band and those >10 keV up to a few hundred keV as hard X-rays or soft γ-rays. The energy regime above 10 keV is relatively unexploited, in part, due to the technological challenges of observing emission in this band. However, it is in this band that non-thermal emission processes dominate and in which we can observe the behaviour of some the most extreme objects in our universe.

This chapter outlines the basic principles of the production and interaction of high energy photons in the hard X-ray and soft γ-ray regimes. Additionally, the properties of sources known to emit at these high energies is discussed specifically with regard to X-ray binaries.

1.2 Gamma-ray interactions with matter

The way in which γ-rays are produced and interact is directly related to the ways in which they can be detected and what the implications are for the physical systems which generate them. There are three key processes in which γ-rays interact with matter: the photoelectric effect; Compton scattering; pair production. Which process is dominant is dependent upon the energy of the incoming photon and the atomic number, Z, of the

material in which it is interacting.

1.2.1 The photoelectric effect

The photoelectric effect is dominant at low γ-ray energies and in high Z materials. Absorption occurs when an incident γ-ray interacts with a tightly bound atomic electron. The energy of the γ-ray is transferred to the electron ejecting it from the atom. If the original γ-ray energy, hν, is greater than the binding energy of the electron, E_{bind} then the residual energy is transferred to the electron in the form of kinetic energy, E_U.

$$E_U = h\nu - E_{bind} \tag{1.1}$$

The vacancy left by the ejected electron may be filled by another electron falling down from a higher energy level. This results in fluorescence and the emission of an X-ray photon with an energy dependent upon the energy level from which it drops.

The photoelectric absorption cross-section is dependent upon Z^n where n is dependent upon the material but is typically in the range 4 – 5.

1.2.2 Compton Scattering

Compton scattering occurs when a high energy photon scatters off a free electron. As the photon scatters off the electron it imparts energy and momentum to the electron, this is indicated in Fig. 1.1. From the principles of conservation of energy and momentum we find that the energy of the scattered photon, E'_γ, is given by:

$$E'_\gamma = \frac{E_\gamma}{1 + \frac{E_\gamma}{mc^2}(1 - \cos\theta)} \tag{1.2}$$

where E_γ is the energy of the incident photon, m is the rest-mass of the electron and θ is the scattering angle of the photon. The Compton scattering cross-section is given by the Klein-Nishina formula. For low photon energies this is equivalent to the Thomson cross-section and traditional electron scattering is observed.

It is also possible for high energy electrons to impart energy to photons through the process of inverse Compton scattering. Here an energetic electron scatters off a photon. In the case of an ensemble of particles where there are multiple scatterings then the energy of the up-scattered photon is $\sim\gamma_e^2$E. Where γ_e^2 is the Lorentz factor of electron and E is the initial photon energy.

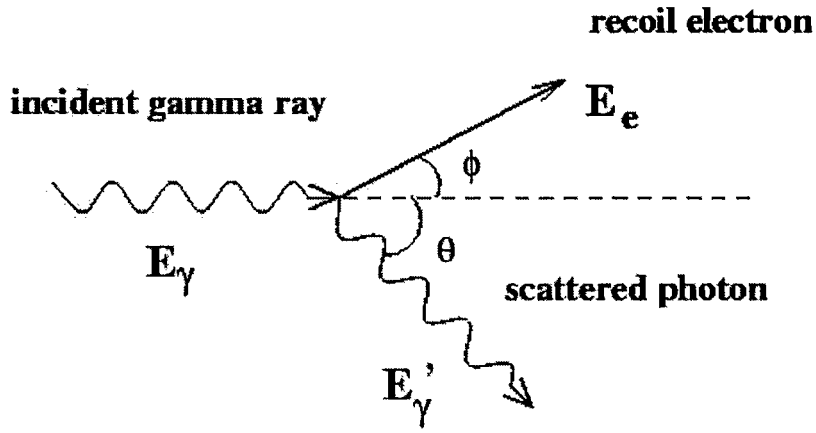

Figure 1.1: Schematic diagram of Compton scattering.

1.2.3 Pair production

At the highest energies a γ-ray can be completely annihilated when its energy is converted into a particle-antiparticle pair. Typically the interaction takes place in the Coulomb field of a nucleus in order to conserve momentum. The most common particle-antiparticle produced is an electron and positron requiring a γ-ray photon of energy > 1.022 MeV. Any excess energy is transferred in the form of kinetic energy of the particles. Pair production dominates over the photoelectric and Compton effects at energies > 10 MeV.

The positron will eventually encounter an electron and annihilate with it producing γ-rays. The best known γ-ray line is the annihilation line at 511 keV which results from the annihilation of electron positron pairs at rest.

1.3 Gamma-ray generation mechanisms

Besides the interaction of γ-rays with matter there are a number of important mechanisms for the production of γ-rays in astrophysical sources.

1.3.1 Blackbody emission

Hard X-rays and soft γ-rays can be produced by thermal processes and have their origin in blackbody emission of an object. From Wien's displacement law we can see at what frequency the Planck law has the maximum specific intensity. This is given by:

$$\nu = 5.879 \times 10^{10} T K^{-1} Hz \tag{1.3}$$

Hence, for the maximum intensity of a blackbody to be at > 20 keV requires tem-

peratures in excess of $\sim 5 \times 10^7$ K. Temperatures of this magnitude can be found in the accretion disks of stellar mass black holes.

1.3.2 Synchrotron radiation

Synchrotron radiation is generated by the acceleration of relativistic electrons by magnetic fields. As an electron moves through a magnetic field it experiences a force perpendicular to its line of motion and so changes direction. As the electron is accelerating it consequently emits electromagnetic radiation. The frequency of the radiation is purely dependent upon the energy of the electron, E, the magnetic field strength, B, and the direction of motion relative to the magnetic field. In an ensemble of particles moving in an isotropic fashion only field strength and the energy spectrum of the electrons is important.

The average photon energy is proportional to BE^2. The synchrotron spectrum is dependent upon the energy spectrum of the electrons, which is generally assumed to be a power-law. If the magnetic field is aligned then the resultant synchrotron radiation will be polarised.

1.3.3 Bremsstrahlung

Bremsstrahlung, or "braking radiation", occurs when a charged particle moves through an electric field, such as the Coulomb field of an ion. The rate of energy loss is proportional to m^{-2}, hence electrons are the dominant source of emission. As the electron passes through the ion's electric field it is accelerated and so emits radiation.

Thermal Bremsstrahlung is the radiation spectrum emitted by a body of electrons in thermal equilibrium in the presence of an electric field. The higher the temperature, the faster the motion of the electrons and the higher the energy of emitted photons. Temperatures of the order of $\sim 10^8$ K are required to produce γ-rays. The spectrum is characteristically flat with a cut-off at an energy E~kT. Hence, the temperature of the plasma can be measured by identifying the cut-off.

1.3.4 De-excitation of nuclei

The de-excitation of nuclei will result in characteristic γ-rays being emitted. The classic example of this is through the radioactive decay of unstable isotopes, However, nuclei may also be placed in an excited state through collisions with energetic particles, for example cosmic rays. As the γ-rays emitted are dependent upon the type of nucleus and

the level of excitation this leads to line emission which can be used to identify isotopic abundances.

1.4 Powering by accretion

The predominant method of powering high energy emission in galactic and extragalactic systems is the action of accreting matter onto a compact object. Accretion is the gradual addition of material onto an object. The origin of transfer of material is dependent upon the system in question, for example in some X-ray binaries the companion star fills its Roche-lobe and material is transferred from it through the inner Lagrangian point onto the compact object. However, regardless of the origin of the accreting material the energy release in all of these systems obeys the same physical laws.

The energy available through accretion is the release of gravitational potential energy as material falls onto the compact object. For a compact object of mass, M_x, radius, R_x, the energy released through accretion of a mass, m, is given by:

$$E_{acc} = \frac{GM_x m}{R_x} \tag{1.4}$$

where G is the gravitational constant. If matter is continually supplied over time then the luminosity attributable to accretion is given by:

$$L_{acc} = \frac{GM_x}{R_x}\frac{dm}{dt} \tag{1.5}$$

As the matter is accreted the gravitational potential energy is released by heating the material within the accretion disk. The efficiency of the accretion process can be ascertained by comparing the total energy the matter posseses. The efficiency can be expressed as:

$$\eta = \frac{GM_x}{R_x c^2} \tag{1.6}$$

Table 1.1 indicates typical values of the accretion efficiency for different objects as well as for nuclear fusion reactions. The efficiency of the accretion process is directly related to the compactness of the object. In the case of black holes the situation is complicated by the fact that there is no hard surface, hence R is estimated as the Schwarzchild radius. However, simultaneously it must be anticipated that a lot of the accretion energy may be lost in the black hole. This effect can be modelled by the efficiency factor, η. For a black hole η~0.1 is considered a good estimate (Frank et al., 1992).

Table 1.1: The estimated efficiency of the accretion process onto different compact objects and nuclear reactions

Process	η
Accretion onto a neutron star	0.1
Accretion onto a black hole	0.06 – 0.42
Accretion onto a white dwarf	0.001
Nuclear fusion	0.01 – 0.001

A further limit on the energy emitted through accretion is that of the Eddington limit. Although, typically very small, the scattering of photons off matter exerts a force on the matter. This radiation pressure is proportional to the flux of the incident radiation field. Large fluxes therefore have a noticeable impact on the matter through which they travel. The force exerted at a distance, r, from a source of luminosity, L is:

$$F = \frac{\sigma_0 L}{4\pi R^2 c} \tag{1.7}$$

where σ_0 is the Thomson scattering cross-section. If the force of radiation pressure exceeds that of the gravitational attraction then accretion will cease. The luminosity at which this occurs is the Eddington luminosity and is given by:

$$L_{Edd} = \frac{4\pi G M_x m_p c}{\sigma_0} \tag{1.8}$$

$$= 1.3 \times 10^{38} (M/\,\mathrm{M}_\odot)\,\mathrm{erg\,s^{-1}} \tag{1.9}$$

where M_x is the mass of the compact object, m_p is the mass of a proton. It is also possible to estimate the spectrum resulting from the accretion process. In the optically thick regime we would expect the radiation to reach thermal equilibrium with the material of the disk and the source would radiate as a black body with a temperature T_{bb}. In the case of the optically thin regime, radiation would escape without any further interaction and the characteristic temperature, T_{th} would be reached if the gravitational potential of each proton-electron pair were converted directly into thermal radiation.

We expect the actual case to be somewhere in between these two states and hence the radiation temperature, T_{rad} lies in the range $T_{bb} \leq T_{rad} \leq T_{th}$. Thus for a neutron star or back hole system we would expect photons in the range 1 keV $\leq h\nu \leq$ 50 MeV. For a white dwarf system we would expect 6 eV $\leq h\nu \leq$ 100 keV.

1.5 Galactic Sources

The brightest, persistent sources of γ-rays are those which exist within our own galaxy. The sources are predominantly X-ray binaries which host a either a neutron star or black hole and in which accretion is the source of the high-energy emission. X-ray binaries are separated into two distinct classes, high mass X-ray binaries and low mass X-ray binaries. However, there are a variety of other source classifications which are observed to emit in the hard X-ray / γ-ray band including cataclysmic variables (CVs) and supernova remnants (SNRs). In all cases, the γ-ray emission is a clear signature of the non-thermal processes in action in these systems and provides an exploratory channel to understand the processes of accretion and the dynamics of the individual systems.

1.5.1 Low Mass X-ray binaries

The first point X-ray source discovered was Sco X-1 by Giacconi et al. (1962), and was later identified as a low mass X-ray binary. Low mass X-ray binaries (LMXBs) are classified as systems in which the donor star has a mass < 1 $M_{\odot}$ (Liu et al., 2000). The donor star can be anything later than spectral type A and can, in very evolved systems, be a white dwarf (White et al., 1995). These stars do not have a sufficient wind to generate the X-ray luminosity observed in these systems. The origin of the high energy emission is the accretion of matter from the donor star through the inner Lagrangian point due to Roche-lobe overflow. Matter passes through the inner Lagrangian point and spirals down onto the compact object forming an accretion disk. The accretion of matter onto the compact object makes these objects bright X-ray sources with luminosities $> 10^{34}$ erg s^{-1}. As of August 2000, 150 sources have been identified as LMXBs (Liu et al., 2000). A graphical representation of a typical neutron star LMXB system is shown in Fig. 1.2.

The galactic LMXB population is concentrated around the Galactic Centre although a number, ~17, are observed in Globular clusters. The distribution of these sources is seen to lie outside of areas associated with star formation and leads to the implication that these are old stellar systems (White et al., 1995). This is supported by the nature of the sub-solar mass companions which have very long lifespans. A consequence of the age of these systems is that the neutron star is expected to have a weak magnetic field, hence X-ray pulsations are not typically observed. Exceptions to this are Her X-1 and 1626-673, both of which are identified as LMXBs but also exhibit X-ray pulsations.

The orbital period of LMXB systems is typically identified using optical observations of the source. Identifying the orbital period through X-ray observations requires the system to be at a high inclination such that it is close to edge-on and hence X-ray eclipses

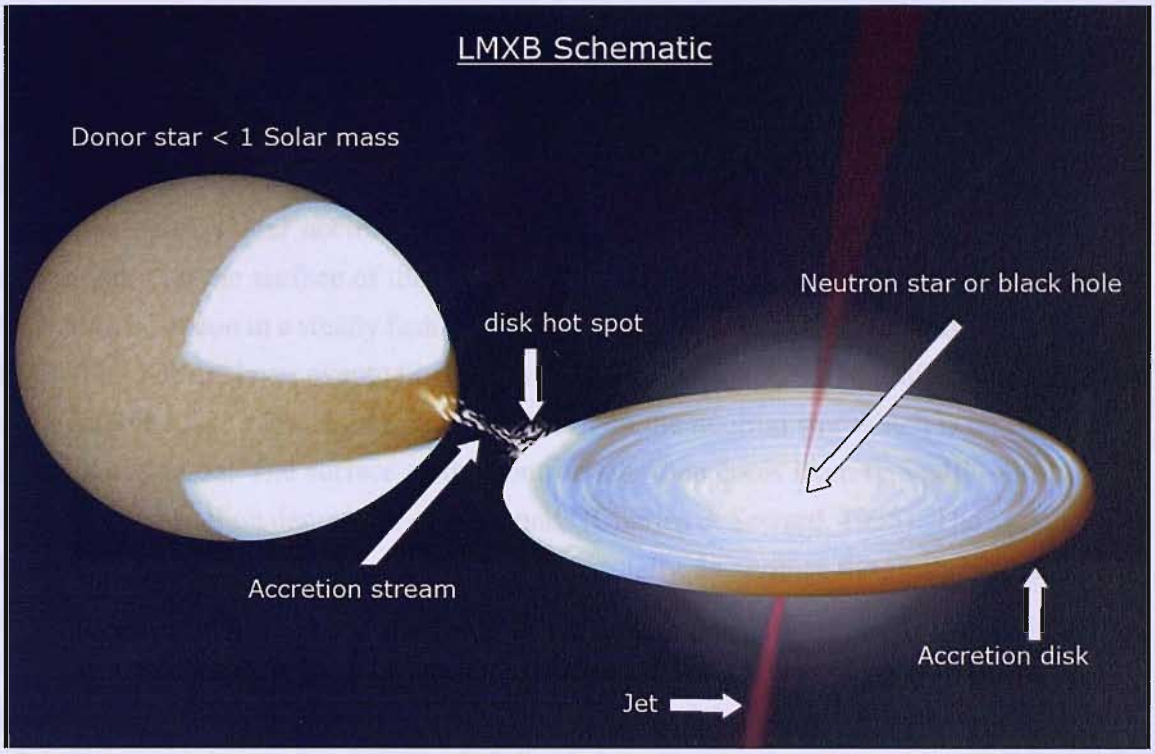

Figure 1.2: A graphical rendering of the typical components in a low mass X-ray binary system comprising a neutron star; visualisation code produced by Rob Hynes.

can be observed in its light curve. This is made more complicated as LMXBs have been observed to have thick accretion disks which can hide the X-ray source when the system is seen edge-on (White et al., 1981). Modulation of the optical emission is attributable to effects which are observable at a larger range of inclination angles. It is of interest to note that the optical emission in these systems is dominated by X-ray heating of the accretion disk and the donor star face, not the donor stars intrinsic optical emission. LMXBs are observed to have orbital periods in the range 0.19 – 398 hours.

1.5.1.1 Type I X-ray bursts

Type I X-ray bursts were first identified in 1975 by Grindlay et al. (1976) and Belian et al. (1976). These bursts were later associated with LMXB systems and explained as thermonuclear flashes on the surface of the neutron star. In excess of 40 LMXBs have exhibited Type I X-ray bursts.

The bursts are seen to reach their maximum intensity from fractions of a second to ten seconds after the burst begins and decay in ~10 seconds to minutes. In this time 10^{39} ergs of energy in the X-ray band is typically released (Charles & Seward, 1995). the profile of

the burst appears different depending upon the energy band in which it is observed. The initial rise is simultaneous across all bands, however the decay is sharper in the higher energy regimes. This is a signature of thermal X-ray emission, i.e. the temperature of the burst starts out high and cools as time progresses.

As the neutron star accretes hydrogen from the accretion disk a layer of hydrogen accumulates on the surface of the neutron star. This hydrogen layer begins to burn under the action of fusion in a steady fashion, building up a layer of helium beneath the hydrogen layer. This helium layer eventually begins to burn to carbon, however, this process is rapid and unstable resulting in a thermonuclear flash on the neutron star which is observed as a type I X-ray burst. The surface of the neutron star then cools from typically ~30 million degrees to 15 million degrees in ~ 10 seconds (Charles & Seward, 1995). The system then begins to accrete material again resulting, eventually, in another thermonuclear flash. A schematic of this process is shown in Fig. 1.3.

During the burst decay the X-ray spectrum represents that of a cooling blackbody (Swank et al., 1977). From the flux and temperature of the blackbody emission the radius of the neutron star can be estimated if the distance to the system is known. Taking the X-ray flux as, F_x, from a type I burst at a distance, d, due to blackbody emission of a sphere of radius, R, and temperature, T, then Stefan's law gives:

$$4\pi d^2 F_x = 4\pi R^2 \sigma T^4 \tag{1.10}$$

Hence, the radius of the neutron star is given by:

$$R = \frac{d}{T^2}\sqrt{\frac{F_x}{\sigma}} \tag{1.11}$$

For sources with reasonable distance estimates this yields a radius of ~ 10 km, the typical value associated with neutron stars. Careful examination of the X-ray spectrum during a burst indicates that the blackbody temperature changes and hence the radius is changing. This is explained as an initial expansion of the neutron star photosphere followed by a contraction. The X-ray luminosity reaches the Eddington limit and the radiation pressure forces the hydrogen layer to expand. The luminosity can then continue to increase as the Eddington limit for helium is higher by ~1.75 (Charles & Seward, 1995).

The Eddington Limit for a 1.4 $M_\odot$ neutron star is ~1.8×10^{38} erg $s^{-1}$and hence the luminosity of a type I X-ray burst should not exceed this value. Therefore, type I X-ray bursts can provide estimates of source distances. However, this is always an upper limit as the peak flux of a burst does not have to have reached the Eddington limit.

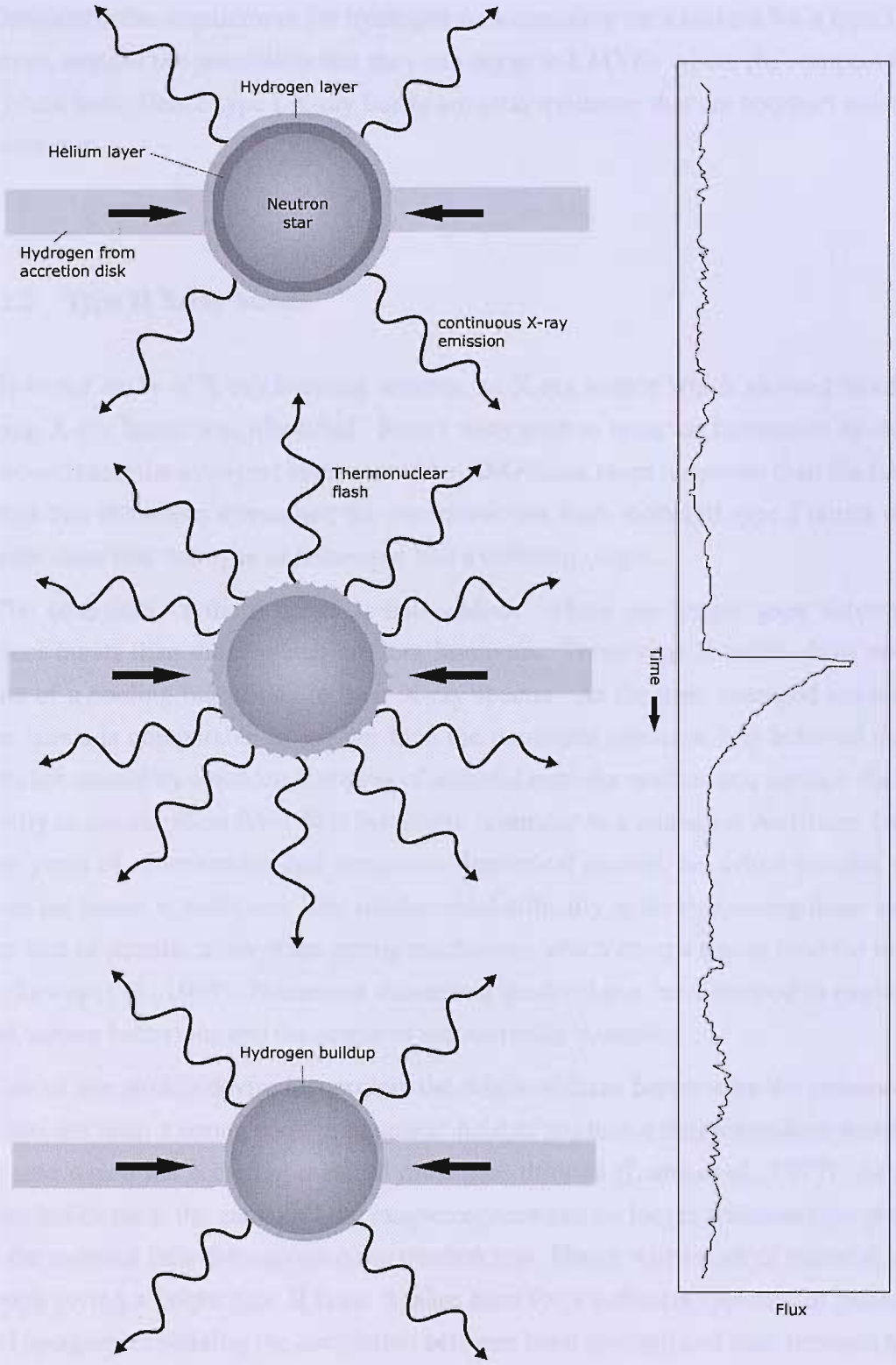

Figure 1.3: A schematic of a type I X-ray burst. The neutron star accretes hydrogen onto its surface. This hydrogen burns forming a layer of helium beneath it (top panel). Eventually the helium layer ignites and a thermonuclear flash occurs (middle panel). The neutron star then begins to build up hydrogen again (bottom panel).

Obviously, the requirement for hydrogen to accumulate on a surface for a type I burst to occur, negates the possibility that they can occur in LMXBs where the compact object is a black hole. Hence type I X-ray bursts are clear evidence that the compact object is a neutron star.

1.5.1.2 Type II X-ray bursts

Early in the study of X-ray bursting sources, an X-ray source which showed rapidly recurring X-ray bursts was identified. Bursts were seen to recur on timescales as short as 10 seconds and the strongest bursts could be 1000 times more luminous than the faintest. At first this behaviour threatened the thermonuclear flash model of type I bursts until it became clear that this type of behaviour had a different origin.

The behaviour of these bursts is not random. There are longer gaps between the brighter bursts than those which are less luminous. These type II bursts show no indication of a cooling blackbody in their X-ray spectra. As the time averaged emission of these bursts is comparable or greater than the persistent emission it is believed that the bursts are caused by a sudden dumping of material onto the neutron star surface via an instability in the accretion flow. This behaviour is similar to a relaxation oscillator. Despite many years of observations and numerous theoretical models the actual process which causes the bursts is unknown. The fundamental difficulty in understanding these sources is the lack of identification of the gating mechanism which dumps matter onto the neutron star (Lewin et al., 1995). Numerous theoretical models have been devised to explain the rapid burster behaviour and the origin of the accretion instability.

One of the models devised to explain the origin of these bursts is by the presence of a neutron star with a strong enough magnetic field to produce a magnetosphere which acts as a gate which the accreting material must pass through (Lamb et al., 1977). Accreted matter builds up at the gate until the magnetosphere can no longer withstand the pressure and the material falls through onto the neutron star. Hence when a lot of material passes through giving a bright type II burst it takes time for a sufficient quantity of material to build up again, explaining the correlation between burst strength and time between bursts.

However, the accretion of matter via a gating mechanism does not prevent a layer of hydrogen from accumulating on the neutron star surface eventually causing a thermonuclear flash. Therefore these rapid burster sources can exhibit both type I and type II X-ray bursts

1.5.1.3 Identification characteristics

The classification of a system as a LMXB is typically based upon the identification of the donor star spectral type or of the mass function of the system. However, in those cases where there are limited observations which are in the X-ray or γ-ray energy regimes then the characteristic X-ray properties of traditionally identified systems can be used to classify newly detected sources. A source may be classified as an LMXB if it exhibits any of the following properties (White et al., 1995):

- Type I X-ray burst are observed.
- The orbital period if less than $\sim$ 12 hours.
- The 1-10 keV spectrum is soft with a typical temperature of 5–10 keV.

1.5.2 High Mass X-ray binaries

High mass X-ray binaries (HMXBs) are X-ray binary systems in which the donor star has a mass $\geq$ 10 $M_{\odot}$. The donor star is typically an O or B spectral type. As of June 2000 130 HMXBs had been identified (Liu et al., 2000). The donor star in the system is much more luminous in the optical than the X-ray source, X-ray heating is minimal and so the optical properties of the system are dominated by the donor star (White et al., 1995). The neutron stars in these systems are typically observed to be X-ray pulsars. This follows from the idea that HMXBs must be young systems due to the short life span of the OB stars. Hence, the neutron stars in these systems are expected to be young and so have large magnetic fields. That these are young stellar systems means that they are found in star forming regions, such as the spiral arms of the galaxy.

The donor stars are of sufficient size to have a strong stellar wind. This wind can supply the accreting compact object with typically 10^{-6} – 10^{-10} $M_{\odot}$ per year. This is sufficient to sustain an X-ray luminosity of 10^{35} – 10^{36} erg s^{-1} if the compact object is close enough to the donor star. However, the donor star may fill its Roche-lobe and hence matter will be accreted onto the compact object through the inner Lagrangian point, as in the case of LMXBs. This results in a much larger accretion rate than in the wind-fed systems and gives rise to a much higher X-ray luminosity, 10^{38} erg s^{-1} (Kaper et al., 2004). As the X-ray emission must propagate through the wind to the observer the signature of photoelectric absorption is clear in the X-ray spectrum of the source. A graphical representation of an HMXB comprising of a supergiant filling its Roche-lobe and a neutron star is shown in Fig. 1.4.

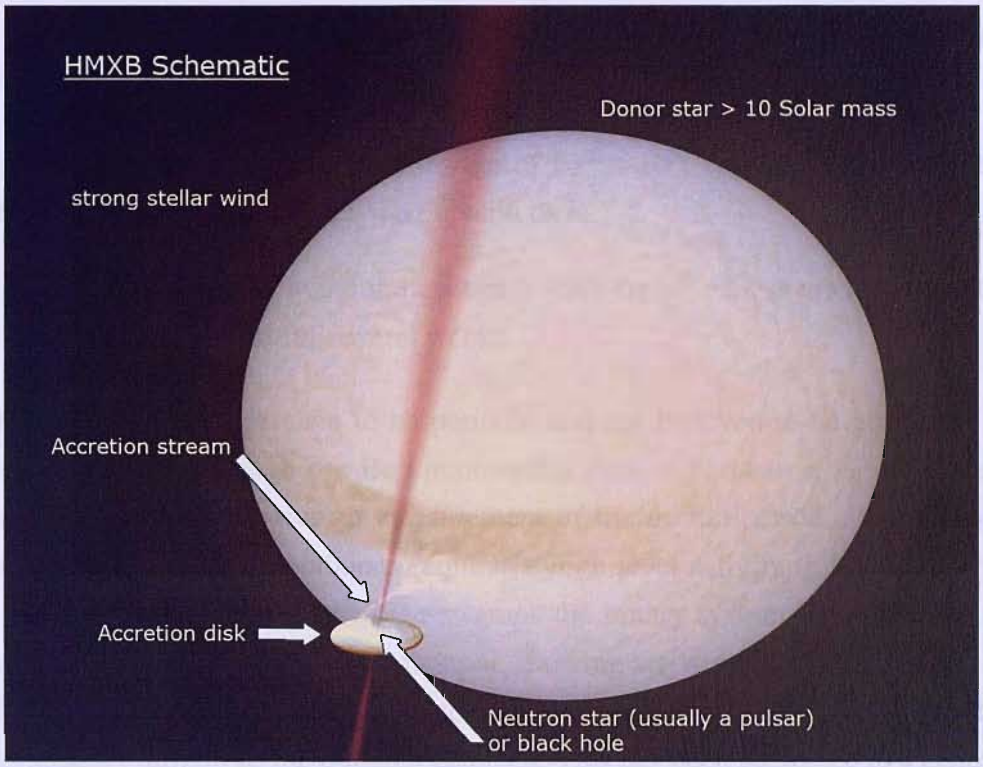

Figure 1.4: A graphical rendering of the typical components in a high mass X-ray binary system comprising a neutron star and supergiant which has filled its Roche-lobe; visualisation code produced by Rob Hynes.

HMXBs can be split into two individual classes: (*i*) Be/X-ray binaries; (*ii*) Supergiant X-ray binaries (Corbet, 1986). The majority of HMXBs belong to the first class (~80%) (Kaper et al., 2004). Be systems are often seen as transient X-ray sources whilst the supergiant systems are persistent although variable.

1.5.2.1 Be X-ray Binaries

By far the most dominant class of HMXB are the Be X-ray binaries. In these systems the compact object is a neutron star and the donor is a Be star. Be stars are fast rotators, moving at close to the break-up speed, and consequently have a ring of material around their equator. It is this material which is responsible for the emission lines which are the characteristic signature of Be stars. Be X-ray systems are typically bright transient sources. These systems are observed to have moderately eccentric orbits with periods of 12.7 – 262 days (Negueruela & Coe, 2002). The orbital period is typically identified through pulse arrival time analysis.

Be X-ray binaries can be seen to show a number of different X-ray states. They may be observed at a persistent low-luminosity of $\leq 10^{36}$ erg s^{-1} or they may be undetectable.

These systems are observed to have two principal types of transient behaviour (Negueruela, 1998);

- Short X-ray outbursts with luminosities of $10^{36} - 10^{37}$ erg s^{-1}. These are known as type I outbursts and typically last several days.
- Giant X-ray outbursts with luminosities > 10^{37} erg s^{-1}. These are known as type II outbursts and can last for several weeks.

The type I outbursts are seen to be periodic and are believed to be attributed to the neutron star passing through the Be circumstellar disk at periastron. Hence, the time separation between bursts gives a measurement of the orbital period. The mechanism proposed to explain type II outbursts requires a high level activity in the Be star which ejects a large quantity of matter which swamps the binary system. The neutron star is then fuelled by this large quantity of material, showing activity for several weeks.

In those Be X-ray binaries with the fastest spinning pulsars it has been observed that the X-rays suddenly turn off as the outburst declines. This has been attributed to a centrifugal barrier preventing accretion from occurring below a critical mass accretion rate (Charles & Seward, 1995). As the mass transfer rate declines so to does the pressure exerted on the magnetosphere of the neutron star. Consequently the magnetosphere expands. This results in material entering the magnetosphere at speeds greater than the orbital speed at that radius and so the matter is ejected.

1.5.2.2 Supergiant X-ray binaries

The supergiant systems represent ~20% of the known population of HMXBs and are principally found in the Milky Way. These systems comprise an OB supergiant star and either a black hole or neutron star. The source of accreting material is typically the strong stellar wind of the donor star, however for systems with orbital periods of, typically, < 2 days Roche-lobe overflow can also occur resulting in a stable accretion disk forming around the compact object. The orbital periods of these systems are generally shorter than in the case of Be X-ray binaries, lying in the range 1.4 – 41.5 days. These orbital periods are detected by the observations of X-ray eclipses and/or by pulse arrival time analysis.

If the compact object is accreting material from the stellar wind, then there are limits on the quantity of material available for accretion based upon the velocity of the stellar wind and the velocity of the compact object through the material. This calculation was first performed by Hermann Bondi and Fred Hoyle. If we assume that the stellar wind

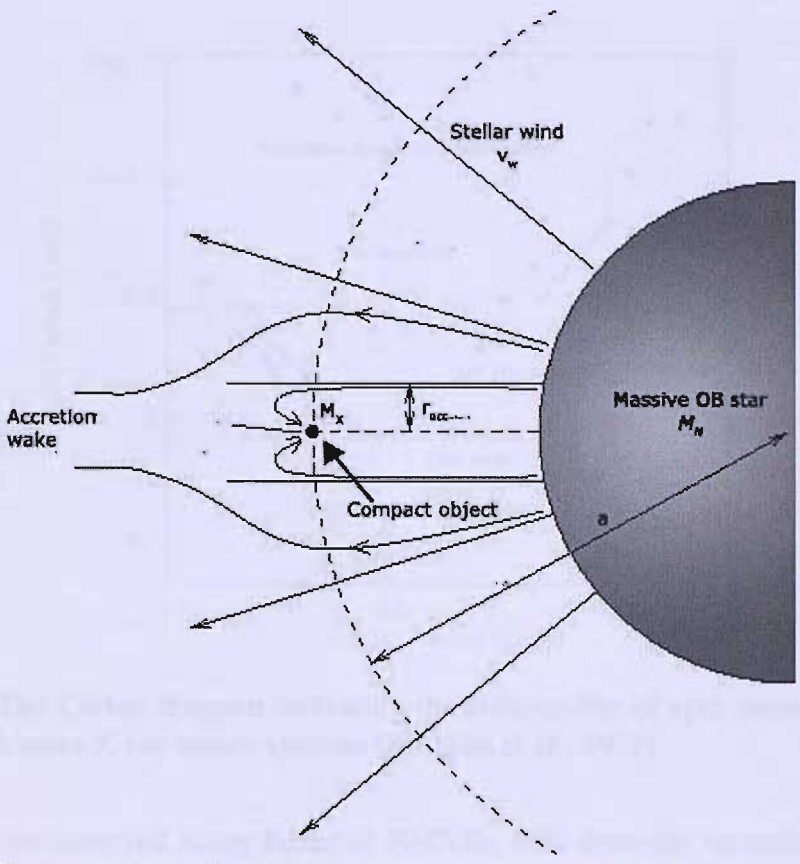

Figure 1.5: The geometry of accretion onto a compact object in a supergiant system. The wind is assumed to be spherically symmetric and smooth. The wind will only be successfully accreted by the compact object if it is within a distance, r_{crit},(Charles & Seward, 1995).

is a uniform density material we can apply Bondi-Hoyle accretion to supergiant X-ray binaries.

The assumed geometry of the system is shown in Fig. 1.5. Material within a radius r_{crit} will be accreted by the compact object. For a compact object of mass, M_x this radius is:

$$r_{crit} = \frac{2GM_x}{v_{rel}^2} \tag{1.12}$$

where v_{rel} is the relative velocity of the accreting object and the stellar wind and is given by:

$$v_{rel}^2 = v^2 + v_w^2 \tag{1.13}$$

where the object velocity is $v = \sqrt{GM_{don}/a}$, M_{don} is the mass of the donor star, a is the separation of the compact object and the donor star and v_w is the stellar wind velocity.

However, stellar winds are not homogeneous and uniform and this leads to the large

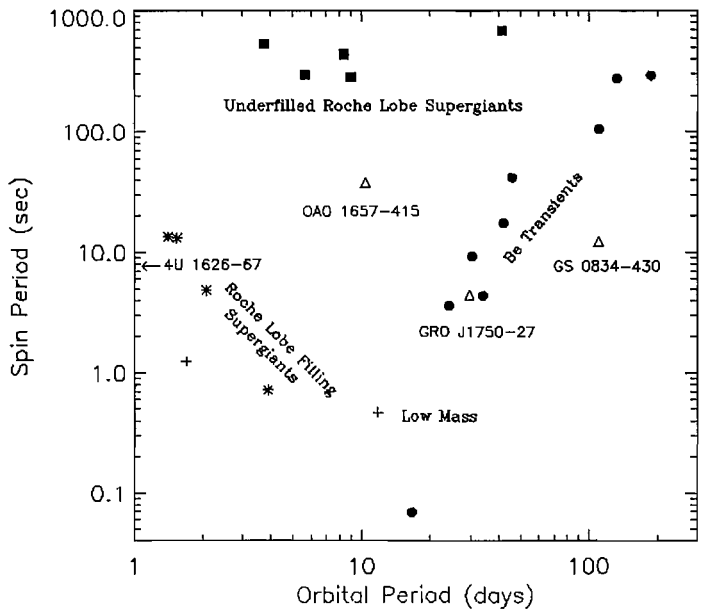

Figure 1.6: The Corbet diagram indicating the relationship of spin period and orbital period in high mass X-ray binary systems (Bildsten et al., 1997).

variations in the observed X-ray fluxes of HMXBs, both from the variation in available accreting material and the variation in the absorbing material density. This makes HMXBs a powerful probe of stellar wind properties. In the case of the eclipsing systems the X-ray source can also be used as a probe of the atmosphere of the supergiant donor star (Clark et al., 1994).

1.5.2.3 X-ray pulsations

In the case of the compact object being a neutron star X-ray pulsations are typically observed from the HMXB. The young age of these binary systems inevitably means that the neutron stars have powerful magnetic fields. Hence, as material is accreted onto the neutron star there will come a point when the magnetic field is dominant; this is at the magneto-spheric radius. At this point, an accretion disk will be disrupted and material will move along the magnetic field lines. The material will arrive at the magnetic poles of the neutron star where a hot shock will form when the material hits the surface. This shock is what produces the X-ray emission in a beam. If the magnetic axis of the neutron star is displaced from the spin axis, then this beam may pass in and out of our line of sight, consequently we observe pulsations.

Corbet (1986) found that the spin period, P_{pulse}, and the orbital period, P_{orb}, of the different types of HMXB system were correlated in different fashions. This is summarised

in the Corbet diagram shown in Fig. 1.6. It is possible for the accretion disks which may form in these systems to apply a torque to the neutron star and change its spin frequency. Be X-ray binaries are seen to show positive correlation between the spin and orbital periods. Supergiant systems where the donor is filling its Roche-lobe show an anti-correlation between the spin and orbital periods. Finally the supergiants under-filling their Roche-lobe are all seen to have long spin periods but there appears to be no correlation with the orbital period. This is not surprising, as there is a lot less angular momentum available to transfer in systems accreting via stellar winds.

During accretion it is expected that the angular momentum flow from the accretion material increases as the accretion rate increases. Consequently the pulsar is spun up. However, at very low mass accretion rates it is believed that the neutron stars spin down as the magnetic field lines which couple to the outer, slower accretion flow disk remove angular momentum from the neutron star (Psaltis, 2004).

1.5.2.4 Identification characteristics

The classification of a system as a HMXB is typically based upon the identification of the donor star spectral type or of the mass function of the system. However, in those cases where there are limited observations which are in the X-ray or γ-ray energy regimes then the characteristic X-ray properties of traditionally identified systems can be used to classify newly detected sources. A source may be classified as an HMXB if it exhibits any of the following properties (White et al., 1995):

- Strong flaring and absorption variability on timescales of minutes.
- Transient outbursts.
- X-ray pulsations.
- A hard 1–10 keV spectrum with a power-law energy index of ~0–1.

1.5.3 Cataclysmic Variables

Cataclysmic variables (CVs) are very similar to X-ray binaries in their make-up. The chief difference is that the compact object in these systems is a white dwarf (WD). In these systems the donor star is typically a late-type star on or near the main sequence which is filling its Roche-lobe. These systems typically have very small separations such that the orbital periods range from ~80 minutes to several hours (Córdova , 1995).

CVs show a wide variety of behaviours principally governed by the rate of mass transfer from the donor and by the magnetic moment of the WD. CVs are split into many different sub-classes including:

- Non-magnetic systems
  - Dwarf nova
  - Classical nova
- Magnetic systems
  - Polars
  - Intermediate Polars

All classes of CVs have been observed to emit X-rays although the properties of the emission are different between classes. For WDs with a magnetic field of less than 10^4 Gauss, the system is considered non-magnetic. In these systems the donor star fills its Roche-lobe and matter builds up an accretion disk around the WD, just as in the case of LMXBs. The magnetic field has negligible effects on the accretion flow. For low accretion rates through the disk the disk is at a lower temperature and the disk viscosity is too low to transfer mass through the disk at the same rate at which it arrives. Consequently the disk acts as reservoir of gas (Kuulkers et al., 2004). When the critical density is reached the disk becomes optically thick, heats up and rapidly transfers mass onto the surface of the WD. This results in Dwarf Nova outbursts which can last for weeks.

In the magnetic systems, the magnetic field is sufficient to disrupt the accretion flow from the donor. Polars have magnetic fields of $\sim 10^6$ Gauss and the rotation of the WD is phase-locked with the binary (Córdova , 1995). Consequently, material flows down the field lines from the donor star to the WD. In the case of Intermediate Polars the WD is spinning more rapidly than the binary orbital period and a partial accretion disk may form. Both classes of magnetic CVs show variations in their mass accretion rates which are reflected in their luminosities.

Almost all CVs are believed to build up a layer of hydrogen on their surface which will eventually undergo a thermonuclear runaway and result in a Classical Nova outburst. This is a similar process to the type I X-ray bursts seen in LMXBs and results in the production of radioactive isotopes which have key γ-ray line signatures.

1.5.4 Supernova remnants

Supernova explosions are the most energetic stellar events known; the energy output is typically 10^{51} ergs. The majority of this energy is released as kinetic energy of the debris, with initial velocities of 10 000 – 15 000 km s^{-1} (Charles & Seward, 1995). The propagation of this material heats the ejected material and the surrounding medium to very high temperatures resulting in X-ray emission.

Supernovae are traditionally subdivided into two classes:

1.5.4.1 Type I Supernovae

Type I supernovae all display similar light curves indicating a similar mechanism and progenitor star. They occur in binary systems where one of the objects is a white dwarf. The WD accretes matter until its mass can no longer be supported by electron degeneracy pressure. The collapse raises the temperature to the point where carbon and oxygen in the core begin to undergo fusion. This results in an explosive wave which propagates through the WD blowing it apart. Large quantities of radioactive material including Ni^{56} are expected to be produced.

1.5.4.2 Type II Supernovae

Type II supernovae rise more slowly to their maximum luminosity and are generally less luminous than Type I supernovae. There appear to be more differences in the light curves of these systems indicating a more individualistic progenitor. The optical spectra are dominated by broad hydrogen emission lines suggesting that these supernovae occur in young massive stars with hydrogen rich envelopes (Charles & Seward, 1995). The star is typically a red giant or supergiant and has undergone many different levels of fusion such that at the core is Fe, surrounded by a layer of Si which is surrounded by layers of lighter and lighter elements. Eventually the core reaches a pressure where the Fe begins to decay into lighter nuclei, reducing the pressure and causing the core to shrink. This reduction in pressure eventually allows the core to collapse under its own gravity in a runaway effect. The energy release causes a shock wave which propagates outward blowing the star apart.

1.6 Extragalactic sources

Besides all of the galactic X-ray sources there are numerous sources of high energy emission which are external to the Milky Way.

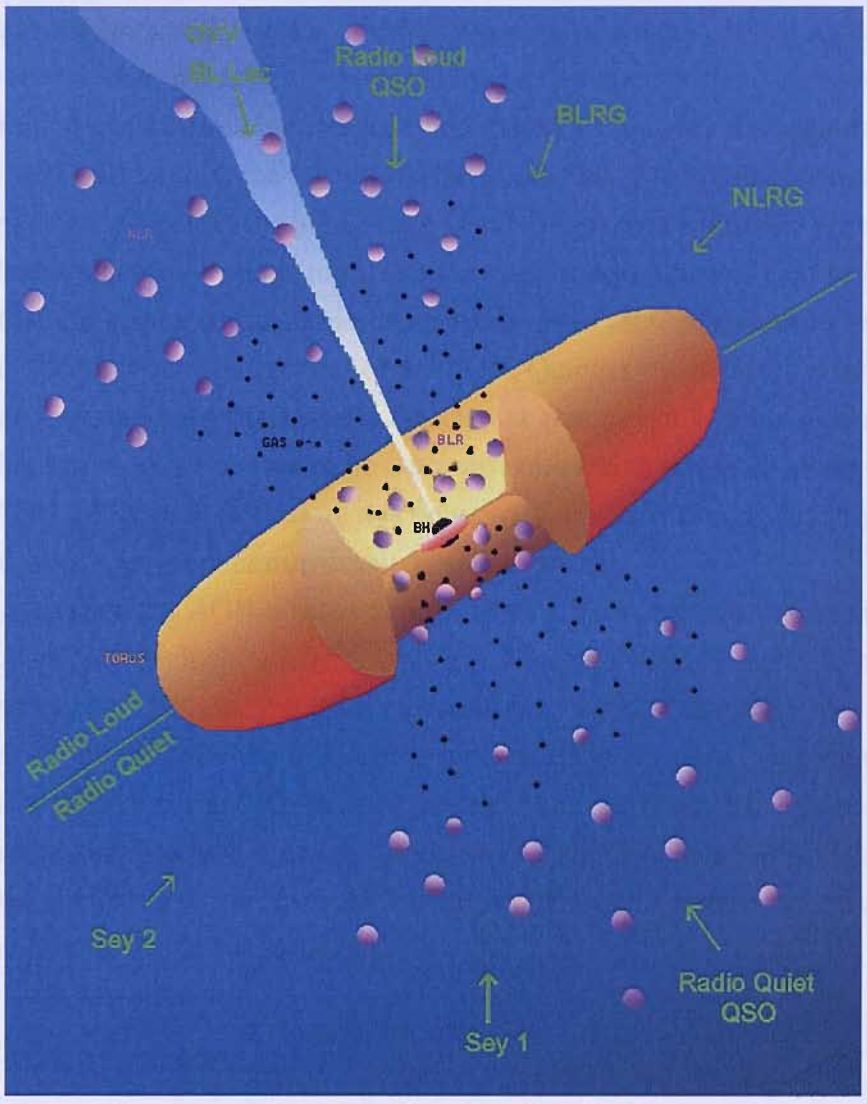

Figure 1.7: The unification scheme of Active Galactic Nuclei; depending upon the observation angle different characteristics are observed resulting in the 'zoo' of AGN classifications, from ESA/ISDC.

1.6.1 Active Galactic Nuclei

Active Galactic Nuclei (AGN) are very luminous and variable galaxies where a large quantity of energy is liberated in the galactic nucleus. The source of this emission is believed to be the accretion of material onto a super-massive ($\sim 10^8$ $M_\odot$) black hole at the centre of the galaxy. Based upon their optical and radio properties a large number of different AGN sub-classes were derived including: Seyfert galaxies; Quasars; Blazars; radio galaxies.

Seyfert galaxies can be split into two classifications type 1 and type 2. Seyfert galaxies exhibit narrow optical emission lines with widths $\leq$ 1000 km s^{-1}. Seyfert 1 galaxies

also exhibit broad lines with widths ~ 10,000 km s^{-1} (Antonucci , 1993). Quasar optical spectra are very similar to that of Seyferts implying a common mechanism responsible for their emission, in fact a distant luminous Seyfert galaxy would look like a quasar (Charles & Seward, 1995). Blazars on the other hand have completely featureless optical spectra.

Looking at these objects in the high energy band we discover a different set of features. Seyfert galaxies are seen to emit most of their high energy emission up to ~100 keV, indicating that the source of this emission is likely from thermal processes and give an indication of the physical environment of the AGN. Quasars can be much more luminous at higher energies and are preferentially detected at energies of 100 MeV or more. The source of this emission is believed to be a powerful jet which is visible along our line of site to the AGN. In the case of Blazars it is believed that we are looking directly down the AGN jet and hence the jet emission dominates what we see.

Although each of the AGN classes appears distinctly different it has been proposed that the properties of each class is attributable to viewing the same object from different angles (Antonucci , 1993). A graphical representation of this idea is shown in Fig. 1.7. Hence all AGN are believed to consist of a super-massive black hole surrounded by an accretion disk and hot corona. Outside of this exists a cold molecular torus of material. Viewing through the molecular torus the object would appear to be a Seyfert 2 but looking directly down the jet then object would appear as a Blazar. If a jet is not present in the system then the source appears radio quiet.

1.6.2 Galaxy Clusters

Galaxy clusters range in size from a few galaxies to several thousand. These galaxies are bound together gravitationally and the space between them is filled with hot gas. This gas has temperatures in excess of 10^7 K and produces diffuse high energy emission.

The gas emits a thermal Bremsstrahlung spectrum with typically kT ~ 1-10 keV (Westmore, 2002). A number of clusters have exhibited an excess of emission at energies above 20 keV. There are two likely causes for this excess, the inverse Compton scattering of cosmic microwave background photons or the hard X-ray excess may be explained by the presence of AGN within the cluster

1.6.3 Gamma-ray Bursts

Gamma-ray bursts (GRBs) are extremely bright and extremely brief transient events. When a GRB goes off it is more luminous than the entire γ-ray sky. The duration of a GRB ranges from milliseconds to minutes and each one has a unique light curve and

spectrum. They were originally discovered by the Vela-B military satellites in the 1960's and until recently were not very well understood.

The first major breakthrough in understanding the origins of these sources was by the BATSE experiment on-board the Compton Gamma-ray Observatory (CGRO). BATSE was an all-sky monitor, with the principal science goal of detecting and locating GRBs. Fig. 1.8 shows the locations of 2704 bursts detected by BATSE. The distribution of the bursts was found to be isotropic across the sky regardless of selection criteria. This indicated that GRBs were extragalactic in origin.

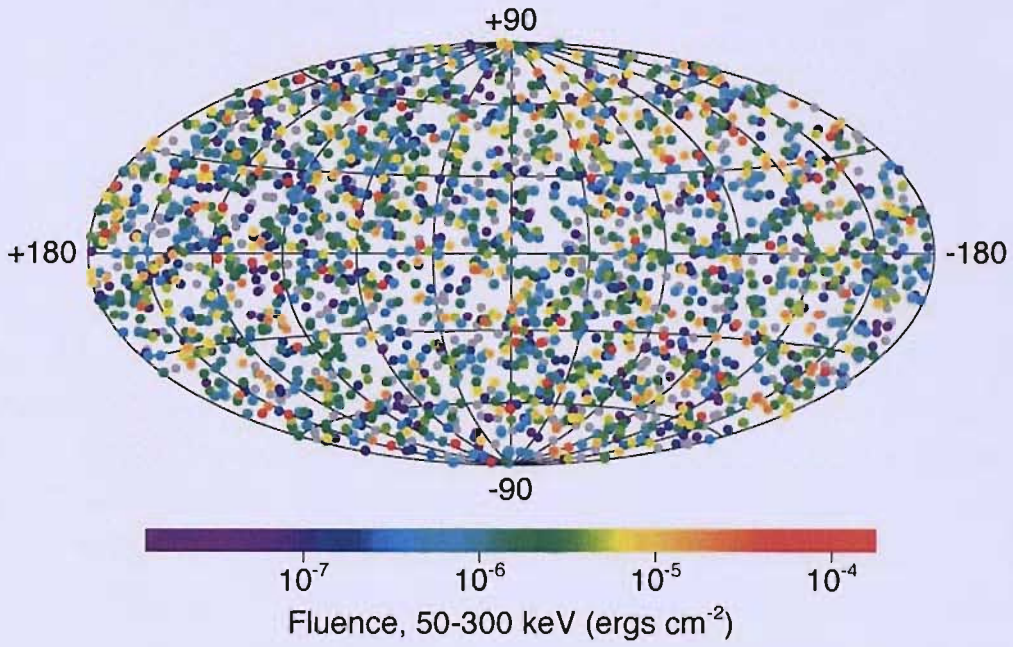

Figure 1.8: A galactic projection of the 2704 Gamma-ray bursts that were detected by BATSE. The colour of each burst is related to the fluence of the burst.

Another important breakthrough was the detection of X-ray afterglows, which lasted for weeks after the initial burst, by the BeppoSAX mission in 1997 (Piro et al., 1995). Observations of X-ray afterglows have allowed the identification of better source positions and allowed follow-ups in the optical band. The host galaxies of GRBs have since been detected. The origins of GRBs are still not fully understood. However, there are two core theoretical models to explain these objects. The first is the merger of two compact objects, for example a neutron star and a black hole. Such an event is believed to release a sufficient quantity of energy to account for what is observed in GRBs.

The second model is that of a hyper-nova. This is the collapse of a very massive star resulting in the formation of a black hole. This is a good candidate for GRBs as recent studies have identified the characteristics of supernovae in the optical afterglows of GRBs.

1.7 Conclusions

It is clear that there is a veritable zoo of astrophysical objects which emit γ-rays through a multitude of processes. Through careful study of their high energy emission we can hope to gain a better understanding of the processes which occur in these extreme and highly exotic environments.

Chapter 2

Surveys of the Hard X-Ray / γ-Ray Sky

2.1 Introduction

The hard X-ray / soft γ-ray band extends from tens of keV though to hundreds of keV. The unifying property of photons at these energies is the inability to focus them using the traditional techniques of reflection employed at lower energies. The penetrating power of these photons is such that grazing incidence optics are nominally of no use and hence, different approaches must be undertaken to explore this regime. It is necessary to make images by transforming the spatial information of the source through some form of coding or modulation onto a detector (Shaw et al., 2004). This can then be reconstructed to regain an image of the source through deconvolution algorithms. This energy band provides a wealth of information regarding the astrophysical processes in operation in some of the most extreme physical environments in the Universe.

Additionally, the capability of constructing an image of a region of the sky has many inherent advantages over simply detecting source fluxes. It allows crowded fields to be resolved, minimising source confusion. If the instrument has a large filed of view then multiple objects can be observed simultaneously allowing for the construction of surveys of the sky. Also, specific structure in extended or diffuse emission can be resolved allowing a more detailed analysis of the intrinsic geometry of sources, for example in the case of supernova remnants. An instrument with a large field of view which regularly scans across the sky is also sensitive to transient events.

The difficulty in detection and imaging of the γ-ray band has resulted in sparse information regarding the properties of objects in this regime. Similarly there have been few surveys of the sky in this energy band. Prior to the launch of the INTEGRAL mission the principal source of survey information for the 13 – 180 keV energy band came from the HEAO1-A4 experiment of 1978-79 (Levine et al., 1984). The catalogue of Macomb &

Gehrels (1999) is the most recent pre-INTEGRAL catalogue of sources known to emit at energies above 50 keV. They list 309 sources in the energy range 50 keV – 1 TeV which have been detected by at least one instrument; they do not include any γ-ray bursts or emission from the Sun. Of these sources 183 have only been detected at energies above 1 MeV. Out of the 309 sources 126 are classified objects which have been detected at 50 keV – 1 MeV. These include 83 accreting objects, 22 Seyfert galaxies, 1 galaxy cluster and 3 supernova remnants.

This chapter outlines previous hard X-ray and soft γ-ray missions which performed large scale surveys of the sky and their results. The properties and sensitivities of current missions and instruments are discussed as are proposed future missions.

2.2 HEAO-1

The HEAO-1 was the first of the High Energy Astronomical Observatories and was launched on 12 August 1977 on-board an Atlas Centaur rocket. The satellite was placed into a circular orbit with an apogee of ~445 km. HEAO was principally a scanning mission which rotated every 30 minutes about the Sun-Earth line. Consequently the on-board instruments scanned a great circle in the sky lying ~90° from the Sun. As the Earth orbited the Sun this scanning circle moved approximately 1° per day. Hence, over the course of the mission each part of the sky was scanned approximately 3 times. An artist impression of the HEAO-1 satellite is shown in Fig. 2.1.

On-board the HEAO satellite were four experiments:

- A1 experiment, the NRL Large Area Sky Survey (LASS)
- A2 experiment, the Cosmic X-ray Experiment (CXE)
- A3 experiment, the MIT/SAO scanning Modulation Collimator (MC)
- A4 experiment, the UCSD/MIT Hard X-ray/Low-Energy Gamma-Ray Experiment

The LASS was a 1.0 m^2 proportional counter array sensitive in the 1–20 keV energy band (Bradt et al., 1992). By the end of the mission analysis of the LASS data resulted in a catalogue of 842 X-ray sources seen down to approximately 1 mCrab in the 1–20 keV band. Other results to come from this experiment included the detection of rapid aperiodic variability in Cyg X-1 and the first observed eclipse of a LMXB, X1658-298.

The CXE was a smaller proportional counter, ~ 0.4 m^2, sensitive in the 0.2–60 keV band. The primary goal of this instrument was to study diffuse emission. A high latitude

Figure 2.1: An artist impression of the HEAO1 satellite. (Credit: NASA/HEASARC)

X-ray survey performed by this experiment was completed down to a flux sensitivity of 3.1×10^{-11} erg cm^{-2} s^{-1} in the 2–10 keV band (Piccinotti et al., 1982). Eighty five sources were observed and luminosity functions constructed for AGN and galaxy clusters were measured.

The MC was a modulation collimator designed to give accurate source positions to within 1'. The accurate positions obtained by the MC resulted in several hundred optical identifications and source classifications including many previously unknown active coronal type stars, CVs, AGN and galaxy clusters (Bradt et al., 1992).

The A4 high-energy experiment was constructed from seven inorganic phoswich detectors surrounded by large scintillators which operated as active anti-coincidence against ambient radiation. The two Low Energy Detectors (LEDs) were NaI/CsI phoswich scintillation detectors with an area of 100 cm^2 and were sensitive in the 13–180 keV range (Levine et al., 1984). The fields of view were 1.5° × 20° (FWHM). The four Medium Energy Detectors were sensitive in the range 80–2000 keV and had an area of 45 cm^2 with a field of view of 17° (FWHM). The High Energy Detector operated from 120 keV – 10 MeV with an area of 100 cm^2 and a circular beam of 37° (FWHM).

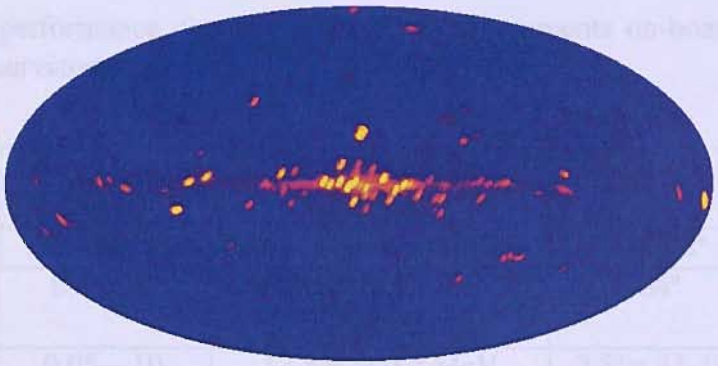

Figure 2.2: The 2–10 keV X-ray all-sky image generated from the observations of the HEAO1 mission. (Credit: NASA)

The primary goal of the A4 instrument was to produce a survey of the entire sky at energies > 10 keV. The HEAO1 A-4 catalogue of high-energy X-ray sources by Levine et al. (1984) makes use of the LED data to identify 72 sources in the 13–180 keV energy band. The flux sensitivity of the survey is ~14 mCrab. Of the 72 sources 44 were detected in the 40–80 keV band and only 14 were detected in the 80–180 keV band. The all-sky image of the 2–10 keV band produced by the HEAO1 mission is shown in Fig. 2.2.

2.3 Compton Gamma Ray Observatory

The Compton Gamma-Ray Observatory (CGRO) (Gehrels et al., 1994) was the second of NASA's Great Observatories. CGRO was launched aboard the space shuttle Atlantis on April 5 1991 and was safely de-orbited on June 4 2000. At 17 tons it was the heaviest astrophysical payload flown at the time. CGRO comprised of 4 different instruments which covered a total energy range of 30 keV – 30 GeV:

- The Oriented Scintillation Spectrometer Experiment (OSSE)
- The Imaging Compton Telescope (COMPTEL)
- The Energetic Gamma Ray Telescope (EGRET)
- The Burst and Transient Source Experiment (BATSE)

A rendering of the CGRO is shown in Fig. 2.3 indicating the locations of each of the individual instruments. An outline of the performance characteristics of each of the individual instruments is given in Table 2.1. CGRO was placed into a low Earth orbit at an average altitude of 450 km with an inclination of 28.5°. The orbital period of the

Table 2.1: The performance characteristics of the instruments on-board the Compton Gamma Ray Observatory.

Instrument	Energy Range (MeV)	Energy Resolution FWHM	FoV	Angular Resolution
EGRET	20 – 30,000	~20% 100 – 2000 MeV	20°× 20°	5 – 10 arc min
COMPTEL	0.8 – 30	6.5% at 2.75 MeV 6.3% at 4.43 MeV	~64°	0.5 – 1.0°
OSSE	0.05 – 10	12.5% at 0.2 MeV 4.0% at 5.0 MeV	3.8°× 11.4°	10 arc min
BATSE: LAD	0.02 – 1	32% at 0.06 MeV 20% at 0.66 MeV	4π steradians	> 3°
BATSE: SD	0.015 – 10	0.2% at 0.09 MeV 5.8% at 1.17 MeV	4π steradians	–

spacecraft was ~90 minutes and the plane of the orbit precessed with a period of ~53 days. During its orbit the satellite would pass through the South Atlantic Anomaly (SAA), an area with high proton fluxes. During and just after the passage of CGRO through the SAA all on-board instruments except for the charged particle detector on OSSE were switched off to prevent damage. This results in regular data gaps in the instrument data.

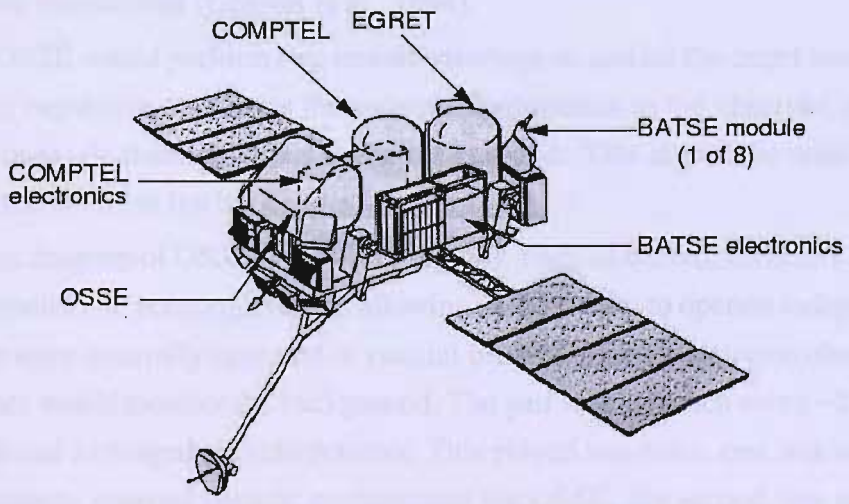

Figure 2.3: Schematic of the Compton Gamma-Ray Observatory. (Credit: NASA/NSSTC)

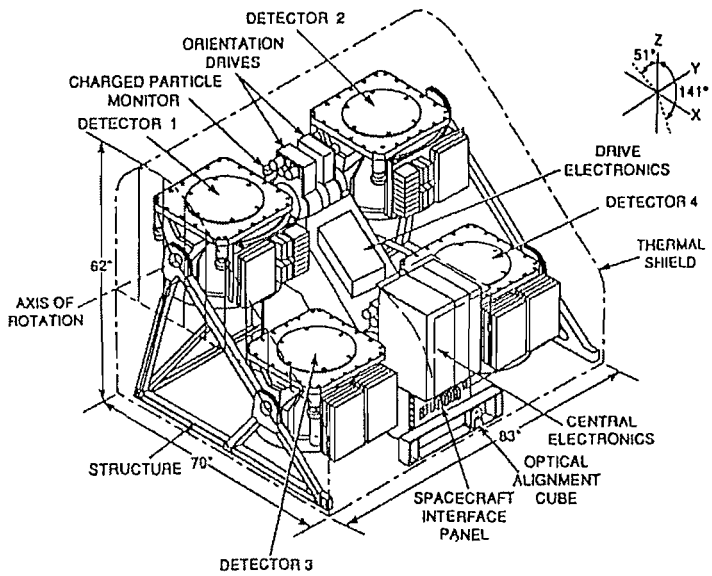

Figure 2.4: Schematic of the Oriented Scintillator Spectrometer Experiment. (Credit: NASA/HEASARC)

2.3.1 OSSE

OSSE was designed to make comprehensive observations of γ-ray sources in the energy range 0.05 – 10 MeV with some capability above 10 MeV for observations of solar γ-ray and neutron observations. The four OSSE detectors comprised of NaI(Tl)–CsI(Tl) phoswiches. The CsI crystals are located behind the NaI crystals to allow for the rejection of events penetrating from the rear of the detector by pulse-shape discrimination between the CsI and NaI interactions (Gehrels et al., 1994).

Normally OSSE would perform two minute viewings on and off the target source. This offset pointing capability modulates the source's contribution to the observed γ-ray flux on a shorter timescale than variations in the background. This allows the source flux to be reliably extracted from the background.

A schematic diagram of OSSE is shown in Fig. 2.4. Each of the four detectors had independent electronics and pointing systems allowing each of them to operate independently. The detectors were generally operated in coaxial pairs, whilst one detector observed the source the other would monitor the background. The pair would switch every ~2 minutes. OSSE also carried a charged particle detector. This played two roles: one was to monitor the the high energy charged particle environment for OSSE; the second was to provide detection of the entry of the CGRO spacecraft into the SAA.

OSSE made a number of discoveries during its 9 years in orbit. OSSE produced maps of the electron-positron annihilation which occurs at the centre of the galaxy. OSSE also

detected a number of γ-ray lines from supernova remnants including those from ^{44}Ti, ^{56}Co and ^{57}Co.

2.3.2 COMPTEL

COMPTEL was a Compton telescope capable of imaging 1 steradian of the sky in the 0.8 – 30 MeV energy range (Schönfelder et al., 1993).

COMPTEL comprised of two detector arrays separated by 1.5m. The upper detector consisted of a liquid scintillator which would scatter the incoming γ-rays. The lower detector was constructed from a NaI(Tl) crystal which would absorb the scattered photon. The location and energy losses of each interaction are recorded. The precision of these measurements determines the angular and energy resolution of the instrument. These precisions varied with the incident energy and angle but the angular resolution was typically $2-4\,^{\circ}$. The energy resolution was typically better than 10%. Each detector is surrounded by a thin anti-coincident shield of plastic scintillator allowing the rejection of charged particles.

The energy resolution of COMPTEL made it sensitive to a number of astrophysically important γ-ray lines. An example of this is the 1.8 MeV line from ^{26}Al β-decay. A map of the 1.8 MeV emission of the galaxy was made by COMPTEL and is shown in Fig. 2.5. The ^{26}Al isotope has a 720,000 year half-life which is short relative to the age of the solar system, hence the map of this emission shows the locations of active nucleosynthesis within our galaxy. Similarly COMPTEL made measurements of other isotopes, for example ^{57}Co was detected in SN 1987A (Gehrels et al., 1994). Other sources of nucleosynthesis such as novae were also observed.

2.3.3 EGRET

EGRET was the highest energy instrument operating on CGRO with a sensitivity in the range 20 MeV – 30 GeV (Kanbach et al., 1988). It had a field of view ~80° in diameter although the instrument's point-spread function and effective area degraded significantly beyond 30° off-axis. The effective area was more than 1000 cm^2 between 100 MeV and 3 GeV.

At the high energies at which EGRET operated photons interact primarily through the pair production process. Incoming γ-rays were detected using a spark chamber to obtain a direction measurement and a NaI(Tl) calorimeter to measure the energy. The spark chamber had interleaved tantalum foils and tracking layers. A fraction of the incident photons interact in the tantalum layers and produce electron-positron pairs. These particles are

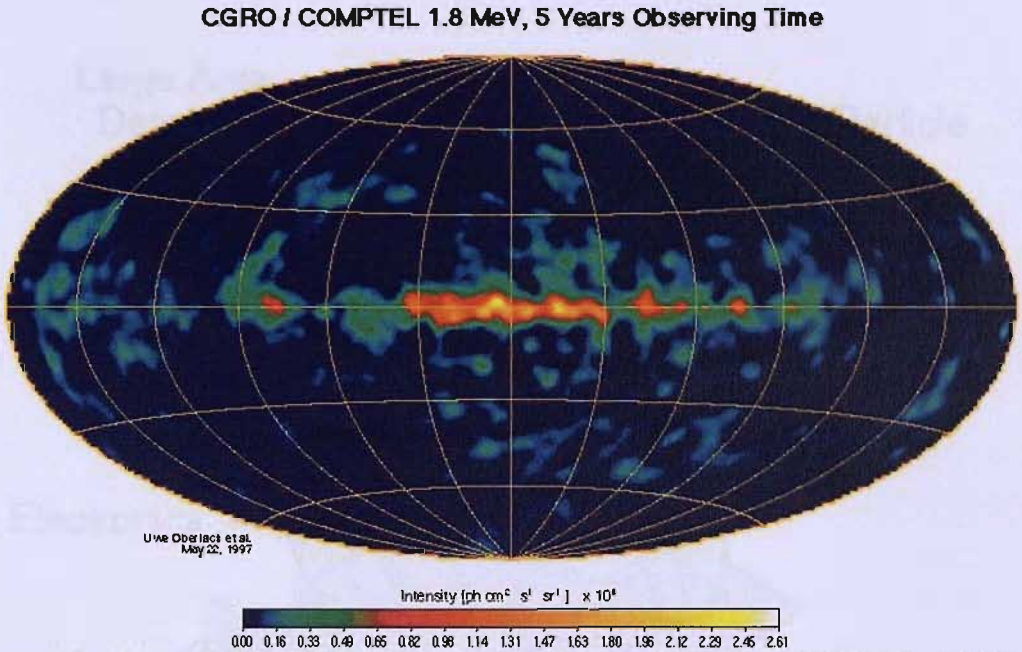

Figure 2.5: Map of the 1.8 MeV emission observed by the COMPTEL instrument. (Credit: NASA/HEASARC)

then tracked through the subsequent layers and absorbed by the calorimeter. From this information the direction and energy of the original photon can be reconstructed.

The principal objective of the EGRET instrument was to produce an all-sky survey of high energy emission. EGRET made a number of exciting discoveries over the course of its lifetime. This included the discovery of blazars as high energy γ-ray emitters. Dozens of blazars were detected and observed to be highly variable. EGRET also confirmed Geminga to be a radio-quiet pulsar and identified it as the first to be detected in γ-rays.

The third EGRET catalogue of Hartman et al. (1999) identifies 271 sources at energies above 100 MeV. Included in this are the Large Magellanic Cloud, five pulsars, 66 blazars and a possible detection of Cen A. However, one of the key discoveries by EGRET was the identification of 170 sources of an unclassified nature. To this day the nature of many of these sources is still unknown.

2.3.4 BATSE

The Burst and Transient Source Experiment (BATSE) is the primary source of data for the analysis performed in Chapter 3. BATSE operated as the all-sky monitor on-board CGRO. It had a 4π steradian field of view and was sensitive in the energy range 20 keV to over 1 MeV (Fishman et al., 1989a). BATSE comprised of eight uncollimated 2025 cm^2 NaI(Tl) Large Area Detectors (LADs). With each LAD there was also a spectroscopy

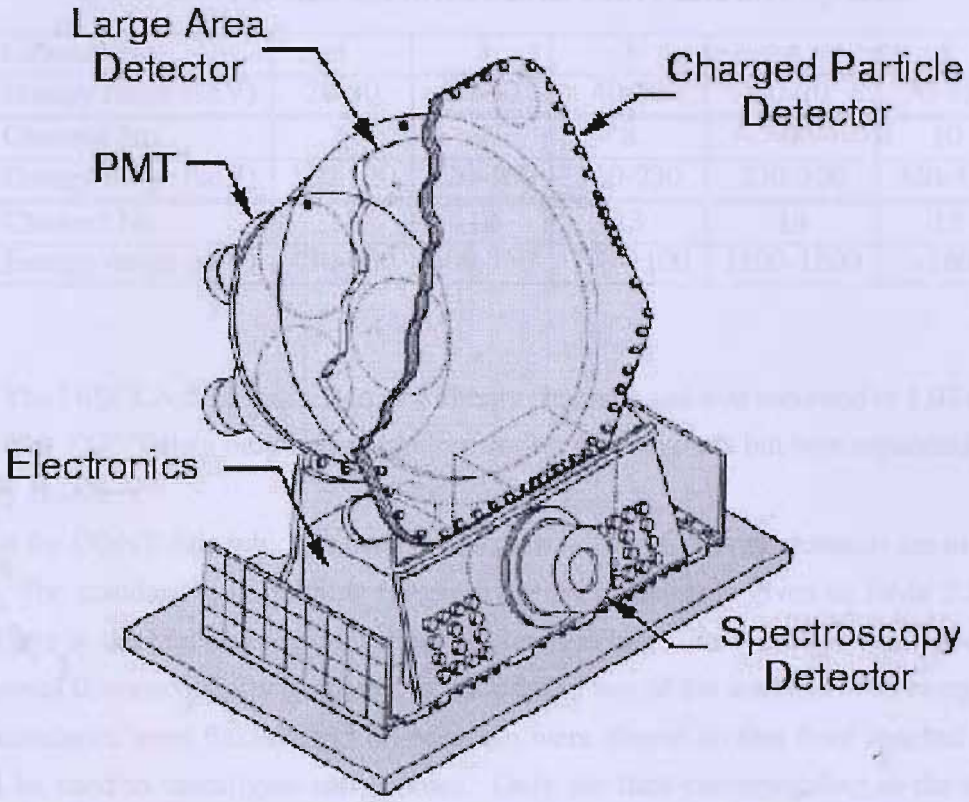

Figure 2.6: The BATSE detector module and LAD assembly. (Credit: NASA/HEASARC)

detector (SD) and charged particle detector (CPD). The SDs were constructed of a 127 cm^2 NaI(Tl) crystal and were optimised to operate over he 10 keV – 100 MeV energy range. A schematic of a detector module is shown in Fig. 2.6. The eight detector modules were located at the eight corners of the CGRO spacecraft.

BATSE was primarily designed to detect and locate Gamma Ray Bursts (Fishman et al., 1989b). Triangulation between LADs was used to crudely identify the direction of the GRBs to within a few degrees, depending upon the flux (Briggs et al., 1999; Pendleton et al., 1999). However, prior to launch it was realised that the angular resolution for non-transient γ-ray sources could be greatly improved by using the Earth occultation method (see Chapter 3 for more details).

The application of BATSE data in this thesis makes use of only the data from the Large Area Detectors. Though primarily designed for the detection of GRBs, BATSE had the flexibility in its data acquisition methods and telemetry to offer different energy and spectral resolutions. Twelve different data types were available, however, the predominant data type used by the LADs was the discriminator (DISCLA) and the continuous (CONT)

Table 2.2: The standard BATSE LAD CONT data look-up table.

Channel No.	1	2	3	4	5
Energy range (keV)	20-30	30-40	40-50	50-70	70-100
Channel No.	6	7	8	9	10
Energy range (keV)	100-120	120-160	160-230	230-320	320-430
Channel No.	11	12	13	14	15
Energy range (keV)	430-600	600-750	750-1100	1100-1800	>1800

data. The DISCLA data comprised of 4 energy channels and was recorded in 1.024 second bins. The CONT data only had a time resolution of 2 seconds but was separated into 16 energy channels.

It is the CONT data which is used in Chapter 3. The 16 energy channels are numbered 0–15. The standard look-up table for these energy channels is given in Table 2.2. If the count rate in the highest energy channel became too large the overflow would add counts to channel 0, consequently channel 0 is not used in any of the analysis. The energy channel boundaries were flexible and on occasion were altered so that finer spectral binning could be used to investigate soft-sources. Only the data corresponding to the standard look-up table is used in this thesis.

BATSE was a highly successful experiment that detected almost 3000 GRBs in a mission which far exceeded the nominal lifetime of the experiment. The map of the locations of the GRBs detected by BATSE is shown in Fig. 1.8. The identification of GRBs with cosmological rather than local events can be largely attributed to the wealth of data collected by BATSE (Meegan et al., 1992). Application of the Earth occultation method has resulted in the BATSE occultation catalogue of Harmon et al. (2004). They detect a total of 83 objects with an additional 36 possible detections.

2.4 GRANAT/SIGMA

GRANAT was a Russian X-ray satellite which operated for ten years from 1989–1999. It was launched into a highly eccentric 96 hour orbit with an apogee of 200,000 km. On board were four major instruments including the French SIGMA hard X-ray telescope. After an initial period of pointed observations GRANAT went into survey mode in September 1994 when the attitude gas was exhausted.

The SIGMA instrument was a coded-mask telescope functioning in the 30 – 1200 keV energy range. The field of view was $\sim 5° \times 5°$. It had a typical angular resolution of 15'

and a 20 hour, 2σ, sensitivity of ~26 mCrab (Vargas et al., 1996). An accumulation of 2600 hours of observations of the Galactic Centre region revealed a total of 15 highly variable sources.

2.5 INTEGRAL

The ESA observatory INTEGRAL (INTERnational Gamma-Ray Astrophysics Laboratory) was launched October 17 2002 on-board a Russian Proton rocket. The satellite is fully operational and currently has an extended mission lifetime to 2010. The mission is dedicated to fine imaging and spectrometry of γ-ray sources from 15 keV to 10 MeV with concurrent imaging in the X-ray and optical bands (Winkler et al., 2003). INTEGRAL carries 4 instruments on board:

- IBIS is the γ-ray imager operating at 15 keV – 10 MeV with an angular resolution of 12' FWHM
- SPI is the γ-ray spectrometer operating from 20 keV – 8 MeV with a spectral resolution of 2.5 keV FWHM at 1 MeV
- JEM-X is the on-board X-ray monitor observing in the 3 – 35 keV band
- OMC is the optical monitoring camera and images in the V band

A schematic of the INTEGRAL satellite is shown in Fig. 2.7, each of the individual instruments is labelled. The satellite was launched into a highly eccentric orbit with an orbital period of ~72 hours and an inclination of 52.2°. At perigee the satellite is at a height of 9,000 km, and at apogee it is at a height of 154,000 km. Background radiation effects in the high energy detectors mean that observations are only carried out when the satellite is at a nominal altitude of 60,000 km (upon entering the radiation belts) and 40,000 km (upon leaving the radiation belts), this excludes 10% of the time from observations (Winkler et al., 2003).

INTEGRAL was conceived as a high energy observatory for use by the general scientific community. As such the majority of observing time is dedicated to the General Programme of guest observations. The General Programme comprises of 65% of time in year 1, increasing to 70% in year 2 and up to 75% in year 3 and beyond. The remainder of the time is used for Core Programme observations as return to the scientific collaborations responsible for the development and operation of INTEGRAL. The three main elements of the Core Programme are a deep exposure of the Galactic central radian, regular scans of the Galactic Plane and pointed observations and TOO follow-up observations.

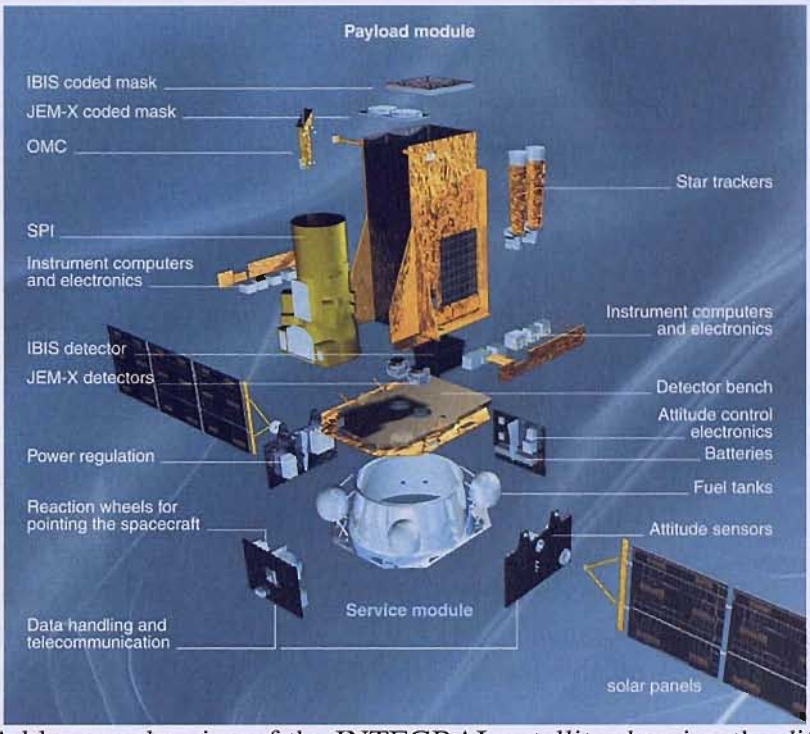

Figure 2.7: A blow-up drawing of the INTEGRAL satellite showing the different instruments and the satellite components. (Credit: ESA)

2.5.1 SPI

SPI is the spectrometer on-board the INTEGRAL satellite with an energy resolution of 2.5 keV at 1.3 MeV and an angular resolution of 2.5° within its field of view of 16° (Vedrenne et al., 2003). The details of the sensitivities and performance of SPI instrument are shown in Table 2.3.

SPI is a coded mask instrument. The spectrometer scans across the sky observing sources within the field of view. Incident γ-rays encounter the mask at the top of the spectrometer. The mask is constructed from an arrangement of hexagonal tungsten blocks 3 cm deep and 6 cm across. 63 of the hexagonal blocks are opaque and 64 are transparent. Consequently the incident γ-rays are coded by the mask and a shadow of the mask is cast onto the detector plane. A photograph of the SPI coded aperture mask is shown in Fig. 2.8.

The detector plane is composed of 19 high purity germanium crystal detectors with a total area of ~508 cm^2. These detectors require low-temperatures to operate and so are cooled to 85K by an an active cryogenic system. Under these conditions the energy resolution for γ-ray spectroscopy is close to that obtainable in a laboratory environment today (Vedrenne et al., 2003). The γ-rays incident on the detector plane generate a current proportional to the photon incident energy. The signal produced at the detector plane is amplified and converted into a digital signal by the Analogue Front End Electronics

Table 2.3: SPI instrument key parameters (Winkler et al., 2003).

Parameter	SPI
Energy range	18 keV–8 MeV
Detector	19 Ge detectors, each (6 × 7) cm cooled @ 85 K
Detector area (cm^2)	500
Spectral resolution (FWHM)	3 keV @ 1.7 MeV
Continuum sensitivity (photons cm^{-2} s^{-1} keV^{-1}) ($\Delta E = E/2, 3\sigma, 10^6$ s)	5.5×10^{-6} @ 100 keV 1.2×10^{-6} @ 1 MeV
Line sensitivity (photons cm^{-2} s^{-1}) (3σ, 10^6 s)	3.3×10^{-5} @ 100 keV 2.4×10^{-5} @ 1 MeV
Field of view (fully coded)	16° (corner to corner)
Angular resolution (FWHM)	2.5° (point source)
Source location (radius)	≤1.3° (depending on source strength)
Absolute timing accuracy (3σ)	≤200 μs
Mass (kg)	1309
Power [max/average] (W)	385/110

(AFEE). Simultaneously, the current pulse shape is digitised by the Pulse Shape Discriminator (PSD). In the 200 – 2000 keV energy range the dominant instrumental background is localised β-decay (Vedrenne et al., 2003). The pulse shape of a β-decay interaction is noticeably different from that of a γ-ray photon interaction and hence the PSD can reject a large fraction of these background events improving the signal-to-noise ratio of astrophysical sources.

The sensitivity of the detector is further enhanced by the use of an active anti-coincidence system (ACS) constructed of BGO crystals. The anti-coincident shield comprises of 91 BGO crystals each with a volume of ~790 cm^3. Each BGO crystal is viewed by 2 photomultipliers (with one exception). Cosmic rays and γ-rays from outside of the field of view interact in the ACS and are recorded as time-tagged events. This signal is sent with the signal from the detector plane to the Digital Front End Electronics (DFEE) unit which then rejects any detector signals which are associated with events from the ACS.

The power of the spectrometry which SPI is capable of allows for the detection, cartography and detailed study of sites of nucleosynthesis, specifically nearby supernova, supernova remnants and nova. Key γ-ray lines which it is capable of observing are ^{56}Co, ^{44}Ti, ^{22}Na, ^{26}Al, ^{60}Fe and the 511 keV annihilation lines. Already, SPI has produced measurements of the 1809 keV emission of ^{26}Al in Cygnus X as well as measurements of the

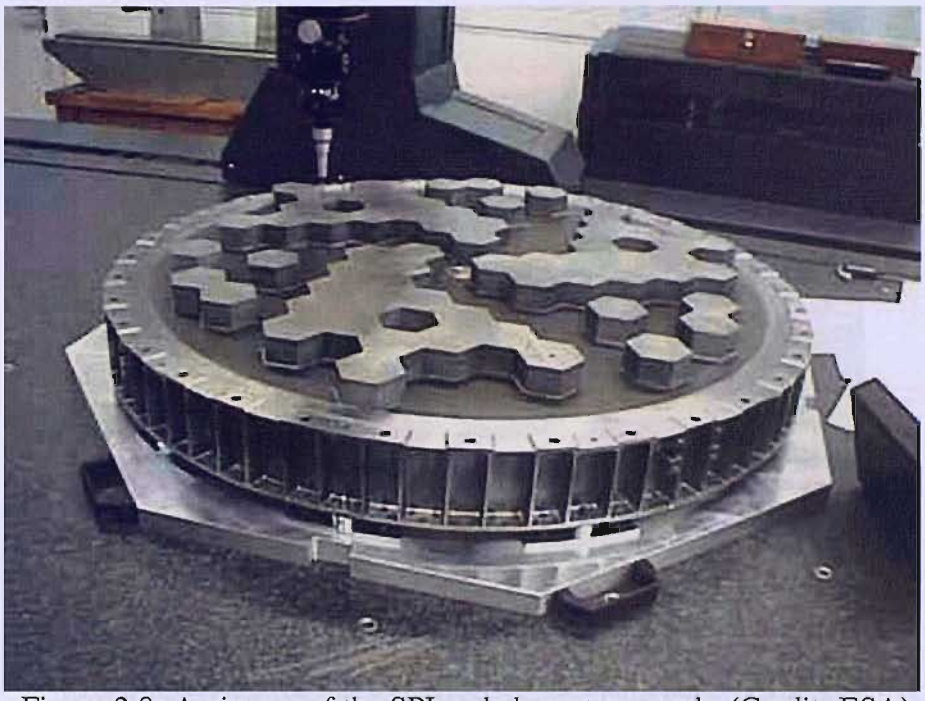

Figure 2.8: An image of the SPI coded aperture mask. (Credit: ESA)

annihilation radiation emitted by the Galactic Centre region.

2.5.2 IBIS

The IBIS telescope is the high angular resolution imager on-board the INTEGRAL satellite. The IBIS imager is based upon two independent solid state detectors optimised for low energy γ-rays, 15 – 1000 keV, and high energy γ-rays, 0.175 – 10.0 MeV. IBIS has a large field of view, 29°× 29° and an angular resolution of 12' FWHM (Ubertini et al., 2003). As in the case of SPI, IBIS is a tungsten coded aperture mask system. A γ-ray source projects a shadowgram onto the detector plane and images of the sky can be reconstructed by decoding the detector shadowgram with the mask pattern. A photograph of the IBIS coded aperture mask is shown in Fig. 2.9. An overview of the properties of the IBIS telescope is given in Table 2.4.

The primary source of data used in this thesis is from the ISGRI detector of IBIS. ISGRI is the low energy IBIS detector composed of an array of 128 × 128 multi-layer CdTe detectors covering a physical area of ~2600 cm^2 (Lebrun et al., 2003). The cadmium telluride detectors operate at the ambient temperature negating the requirement for a cryogenic cooling system. Each detector is 2mm thick, this small thickness restricts these detectors to the low energy domain. They have an efficiency of ~50% at 150 keV. Hence, ISGRI images in the soft γ-ray domain at energies above 15 keV. However, ISGRI

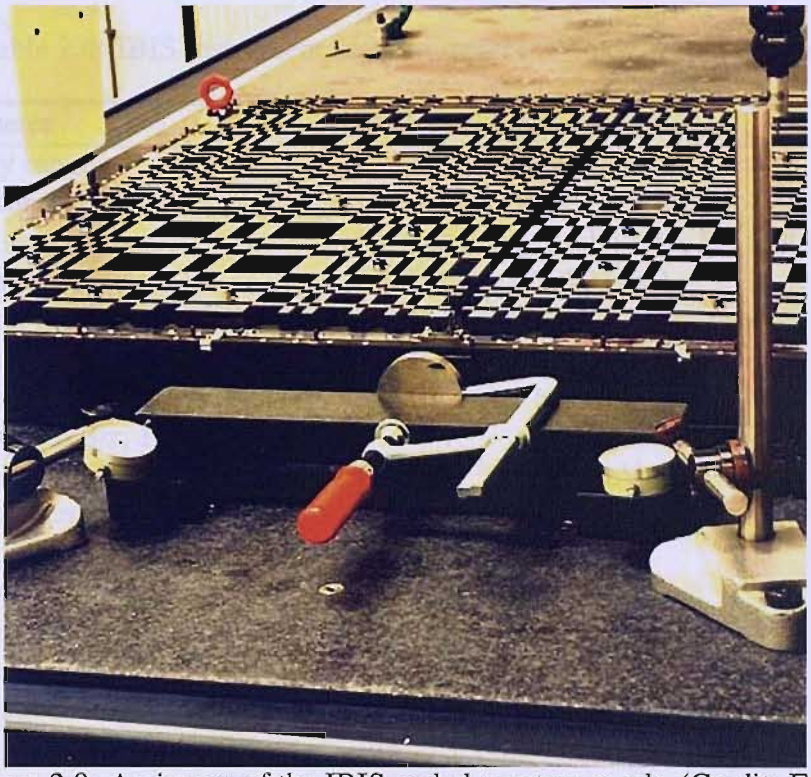

Figure 2.9: An image of the IBIS coded aperture mask. (Credit: ESA)

does have some sensitivity up to 1 MeV. The sensitivity of a coded mask telescope is dependent upon the ability of the detector plane to finely sample the projected mask pattern. The 4 mm ISGRI pixels are spaced every 4.6 mm ensuring, with 11.2 mm mask elements, an excellent imaging efficiency of 0.86. With a mask-ISGRI distance of 3.2 m the angular resolution is 12' and a 10σ source can be localised with an accuracy of 1' (Lebrun et al., 2003). The observed background in the detector implies a mCrab sensitivity for a 10^6 s observing time.

PICsIT is the Pixellated Imaging Caesium Iodide Telescope and provides the high energy detection of the IBIS instrument. PICsIT is located beneath the ISGRI detector and is composed of 4096 CsI(Tl) scintillator detectors which are sensitive in the energy range 175 keV – 20.4 MeV (Lasbanti et al., 2003). Each detector element is 8.4 × 8.4 × 300 mm in size. The overall sensitive geometric area is 2890 cm^2. The CsI(Tl) crystals are optically bonded to custom made low leakage silicon PIN photodiodes designed for optimal performance at 511 keV (Ubertini et al., 2003).

The separation of the ISGRI and PICsIT detector planes allows the paths of interacting photons to be tracked between the two surfaces. This allows the two detectors to be used together to function as a Compton telescope. This interaction is most probable for photons of a few hundred keV to a few MeV (Ubertini et al., 2003).

Table 2.4: IBIS instrument key parameters (Winkler et al., 2003).

Parameter	IBIS
Energy range	15 keV–10 MeV
Detector	16384 CdTe dets, each $(4 \times 4 \times 2)$ mm
	4096 CsI dets, each $(8.4 \times 8.4 \times 30)$ mm
Detector area (cm^2)	2600 (CdTe), 2890 (CsI)
Spectral resolution (FWHM)	8 keV @ 100 keV
Continuum sensitivity	6×10^{-7} @ 100 keV
(photons cm^{-2} s^{-1} keV^{-1})	5×10^{-7} @ 1 MeV
($\Delta E = E/2$, 3σ, 10^6 s)	
Line sensitivity	1.9×10^{-5} @ 100 keV
(photons cm^{-2} s^{-1})	3.8×10^{-4} @ 1 MeV
(3σ, 10^6 s)	
Field of view (fully coded)	$9° \times 9°$
Angular resolution (FWHM)	$12'$
Source location (radius)	$\leq 1'$ (for 10σ source)
Absolute timing accuracy (3σ)	≤ 200 μs
Mass (kg)	746
Power [max/average] (W)	240/208

As in the case of the SPI instrument an active anti-coincidence system (ACS) is required to discriminate between source events and high energy background from outside of the field of view. The ACS is comprised of 16 independent modules, the Veto Detector Modules (VDM). Each VDM is made of 2 BGO crystals $150 \times 75 \times 20$ mm and is optically connected to two photomultipliers. Two VDMs are located on each side of the detector plane, the remaining eight are located beneath the detectors. Interactions in the VDM are then used to reject co-incident events in the detector planes.

One of the primary science goals of the IBIS instrument was to regularly survey the Galactic Plane and monitor the activity of persistent sources and transients. The specifics of the IBIS survey are discussed in detail in Chapter 4. In the course of its surveying activities IBIS has already made some remarkable discoveries. These have included the detection of emission up to 100 keV of the symbiotic star RT Cru, the first time such high energy emission has been observed from this class of source. Additionally, IBIS has identified many new, previously unseen sources. In two cases these new sources have been found to have potential associations with two sources discovered by the H.E.S.S. telescope, indicating that they emit all the way up to the TeV energy range.

2.5.3 JEM-X

JEM-X is the X-ray monitor on-board INTEGRAL designed to give contemporaneous measurements in the traditional X-ray band. The JEM-X camera is sensitive in the 3 – 35 keV energy range and has a 3' angular resolution across a field of view ~10° in diameter (Lund et al., 2003). As in the case of the γ-ray instruments JEM-X makes use of a coded aperture mask which projects a pattern onto a micro-strip gas chamber. The properties of the JEM-X monitor are outlined in Table 2.5.

There are two JEM-X units on-board INTEGRAL, the code patterns are identical on both but are rotated 180° with respect to one another. The hexagonal pattern is cut in a 0.5 mm thick tungsten plate. The coded area is 535 mm across and the space between neighbouring hexagonal elements is 3.3 mm, centre to centre. Only ~25% of the mask pattern is transparent in an effort to aid source separation in crowded fields and to minimise background. The mask is separated from the detector plane by ~3,400 mm giving an angular resolution of the instrument of 3.35'.

The detector is a Microstrip Gas Chamber of an area of 500 cm^2. The chamber is filled with a mixture of 90% Xenon and 10% methane at a pressure of 1.5 bar (Lund et al., 2003). An on-board veto system rejects background events in real time to minimise telemetry requirements. JEM-X demonstrates the first successful use of a microstrip position sensitive X-ray detector in space.

2.5.4 OMC

The Optical Monitoring Camera (OMC) simultaneously observes the optical V-band emission of sources under investigation by SPI and IBIS. The OMC has a field of view of 5° $\times$ 5° and is able to monitor sources down to a magnitude of V=18. For bright sources fast optical monitoring is capable down to 3 s (Mas-Hesse et al., 2003). An overview of the capabilities of the OMC are given in Table 2.6.

The OMC is composed of an optical system which is focused onto a large format CCD detector which operates in frame transfer mode. An image of the OMC is shown in Fig. 2.10. The optics are based upon a refractive system with a entrance pupil of 50 mm and focal length of 154 mm. Six radiation hardened lenses are housed within a titanium barrel. The optical throughput is ~70% at the V filter passband central wavelength (550 nm). The CCD quantum efficiency is 88% in this passband. An LED is housed within the optical cavity to provide flat-field illumination of the CCD.

The CCD is composed of 1024 $\times$ 2048 pixels. One half of the CCD is used for imaging and the other half for frame transfer before readout. The frame transfer time of ~0.2 ms

Table 2.5: JEM-X instrument key parameters. (Winkler et al., 2003)

Parameter	JEM–X
Energy range	4 keV–35 keV
Detector	Microstrip Xe/CH_4–gas detector (1.5 bar)
Detector area (cm^2)	500 for each of the two JEM-X detectors[a]
Spectral resolution (FWHM)	2.0 keV @ 22 keV
Continuum sensitivity[b]	1.2×10^{-5} @ 6 keV
(photons cm^{-2} s^{-1} keV^{-1})	1.3×10^{-5} @ 30 keV
(3σ, 10^6 s)	
Line sensitivity[b]	1.9×10^{-5} @ 6 keV
(photons cm^{-2} s^{-1})	8.5×10^{-5} @ 30 keV
Field of view (fully coded)	4.8°
Angular resolution (FWHM)	3′
10σ source location (radius)	$\leq 30''$
Absolute Timing accuracy (3σ)	$\leq 200\ \mu s$
Mass (kg)	65
Power [max/average] (W)	50/37

[a] At the moment, only one of the two JEM-X detectors is being operated.
[b] Assumes operation of both detectors.

removes the need for a mechanical shutter(Mas-Hesse et al., 2003).

The main scientific objectives of the OMC as given by Mas-Hesse et al. (2003):

- The monitoring during extended periods of time the optical emission of all the high energy objects within its field of view in conjunction with the on-board γ-ray and X-ray instruments. The intention is to correlate the emission in the optical, X-ray and γ-ray bands.

- To provide simultaneous and calibrated V filter photometry of the high energy sources allowing comparisons of their behaviour with future ground-based optical observations.

- To monitor all of the serendipitous optically variable sources in the field of view.

The observation of γ-ray sources in the optical bands simultaneously with the X-/γ-ray instruments provides a powerful tool for understanding the underlying physical processes in operation in astrophysical sources. However, due to its limited field of view in comparison to the much larger fields observable by the IBIS and SPI instruments the use of the OMC and JEM-X in the γ-ray surveys will be extremely limited.

Table 2.6: OMC instrument key parameters (Winkler et al., 2003).

Parameter	OMC
Energy range	500 nm–600 nm
Detector	CCD + V-filter
Detector area (cm^2)	CCD: (2061 × 1056) pixels
	Imaging area (1024 × 1024) pixels
(3σ, 10^6 s)	
Limiting magnitude (mag)	17.8
Field of view (fully coded)	5° × 5°
Angular resolution (FWHM)	25″
10σ source location (radius)	6″
Absolute Timing accuracy (3σ)	≥1 s
Mass (kg)	17
Power [max/average] (W)	20/17

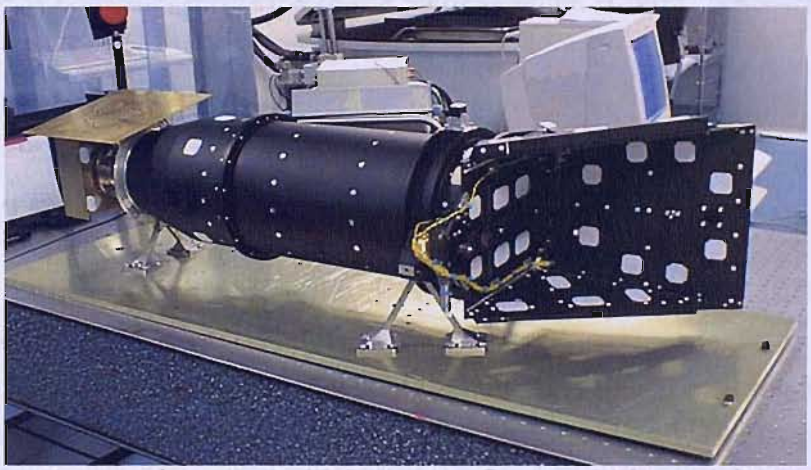

Figure 2.10: An image of the Optical Monitoring Camera flight model prior to the installation of the MLI thermal insulation. (Credit: ESA)

2.6 Swift

Swift is a NASA multi-wavelength transient observatory for GRB astronomy. Swift was launched on November 20 2004 and has a nominal mission lifetime of 2 years. Swift has three on-board instruments which work together to observe GRBs and their after-glows in the X-ray and optical energy regimes. The Burst Alert Telescope (BAT) monitors the entire sky to detect GRBs and calculate their initial position. Using this position the satellite then slews within 90 seconds to bring the GRB into the field of view of the X-Ray Telescope (XRT) and the Ultra-Violet/Optical Telescope (UVOT). Over the coming days Swift will return to look at the after-glow of each GRB. A computer rendering of the

Figure 2.11: A computer rendering of the Swift satellite. (Credit: NASA/HEASARC)

Swift satellite is shown in Fig. 2.11.

2.6.1 BAT

The BAT is sensitive over the 15 – 150 keV energy range. Like the IBIS and SPI instruments on-board INTEGRAL the BAT uses a coded aperture mask to modulate the incoming γ-rays. The mask is constructed of ~54,000 lead tiles measuring $5 \times 5 \times 1$ mm. The mask covers 1.4 steradians of the sky and is positioned ~1 metre from the detector plane. The detector plane is made of CdZnTe elements $4 \times 4 \times 2$ mm in size. The total geometric area covered by the detector is 5200 cm^2. The angular resolution of the BAT is 1–4' (Gehrels , 2004).

The BAT is expected to detect ~100 bursts per year and should be 2–5 times more sensitive than BATSE was. A secondary objective of the BAT is to build up a survey of the hard X-ray sky. Over the course of the mission lifetime it is anticipated that the final all-sky survey will be ~20 times more sensitive than that performed by the HEAO-1 A4 experiment.

2.6.2 XRT

The XRT is sensitive in the 0.2 – 10 keV band and will locate GRBs with a 5" accuracy (Gehrels , 2004). The XRT mirrors were originally designed and built for use on the JET-

X mission. The detector is a 600 square pixel CCD which was originally designed for the XMM-Newton EPIC telescope. The XRT has a field of view of ~24" and an effective area of 110 cm^3 at 1.5 keV.

The XRT measures the fluxes, spectra and light curves of the GRBs and afterglows. Additionally, the XRT can be used for observing targets of opportunity detected by other missions when it is not observing or following up burst observations.

2.6.3 UVOT

The UVOT is based upon the Optical Monitor on-board XMM-Newton. It is a 30 cm diameter modified Ritchey-Crétien telescope. The detector is an image intensified CCD sensitive in the 170 – 600 nm range (Gehrels , 2004). Optical and UV light enters the telescope and is directed to one of two redundant CCD detectors, each with an 11-position filter wheel. These filters consist of a blocked position for detector safety; a white light filter; a field magnifier; two grisms; U, B, and V filters; two broadband UV filters centred on 180 and 260 nm; and a narrow UV filter centred on 220 nm. The UVOT has a field of view of 17 ' × 17' and has an optical point spread function of ~0.9". By measuring the positions of local field stars the location accuracy of the UVOT can be reduced to <0.3" (Gehrels , 2004).

2.7 GLAST

The GLAST mission has a projected launch date for August 2007 with a nominal lifetime of 5 years. GLAST is the successor to the previous NASA γ-ray observatory the CGRO and principally a successor to the EGRET instrument. GLAST will employ two instruments; the main instrument on-board will be the Large Area Telescope (LAT) which will be sensitive in the 20 MeV – 300 GeV energy regime (Thompson , 2004). The GLAST Burst Monitor (GBM) will also be on-board and will provide a field of view several times larger than the LAT and will provide spectral coverage of GRBs from the lower limit of the LAT down to 10 keV.

At the energies to which the LAT will be sensitive the primary interaction mechanism of γ-rays is pair-production. An incident photon will first pass through an anti-coincidence shield which is only sensitive to charged particles. It then passes through thin layers of high-Z material where it will interact to form an electron-positron pair. After conversion, these particles are tracked through the telescope by Si-strip trackers. Finally the energy of the particles are measured by the calorimeter at the base of the tele-

scope. The calorimeter is constructed of 1536 CsI(Tl) crystals arranged in eight layers (Thompson , 2004). The field of view of the LAT is ~ 2 steradians and has an angular resolution of < 3.5° at 100 MeV and < 0.15° at >10 GeV.

The GBM incorporates two sets of detectors 12 NaI scintillators and 2 cylindrical BGO scintillators. The NaI scintillators are sensitive from a few keV to 1 MeV whilst the BGO operates from 150 keV – 30 GeV (Thompson , 2004). It has a field of few of ~8 steradians. GRBs will be detected by a significant change in the count rate in at least two of the NaI detectors. The GBM is expected to detect ~200 GRBs per year.

The first year of the GLAST mission will be an all-sky survey carried out in scanning mode. This means that the instruments will always be pointed away from the Earth, maximising the large fields of view of each instrument and allowing an all-sky survey to be produced on short (day) timescales. A simulation of the GLAST all-sky survey is shown in Fig. 2.12. After the first year, the scientific programme will be determined by peer-reviewed proposals. A key area of interest will be in identifying the unclassified sources originally discovered by EGRET. The enhanced capabilities of GLAST should allow for much tighter error circles enabling follow-ups in other wavebands. Additionally, GLAST should detect a much larger number of the source classifications observed by EGRET including blazars and other AGN, pulsars and supernova remnants.

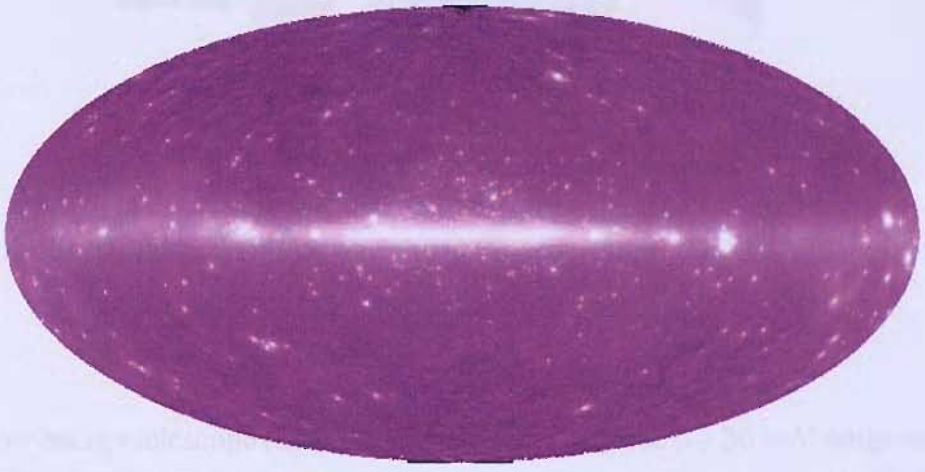

Figure 2.12: Simulated GLAST survey of the sky at E > 100 MeV. (Credit: NASA/HEASARC

2.8 EXIST

The Energetic X-ray imaging survey telescope (EXIST) is a proposed hard X-ray imaging all-sky deep survey mission. It is a strong candidate to be the Black Hole Finder Probe

(BHFP), one of the three "Einstein Probes" in the NASA Beyond Einstein programme (Grindlay , 2005). EXIST would be sensitive in the 5 – 600 keV energy range and would image the entire sky every ~95 minutes. The 1 year 5σ sensitivity would be 50 μCrab in the 10–200 keV band.

The instrument design is conceived to include two large field of view coded aperture telescope arrays. A computer rendering of the proposed EXIST spacecraft is shown in Fig. 2.13. A high energy telescope (HET) would be sensitive in the 10 – 600 keV band and be composed of an array of 6 × 3 coded aperture telescopes covering a 131° × 65° fully coded field of view. The overall detector area would be 5.6 m^2 composed of 1.25 mm CdZnTe pixels (Grindlay , 2005). The HET would have an angular resolution of 5'.

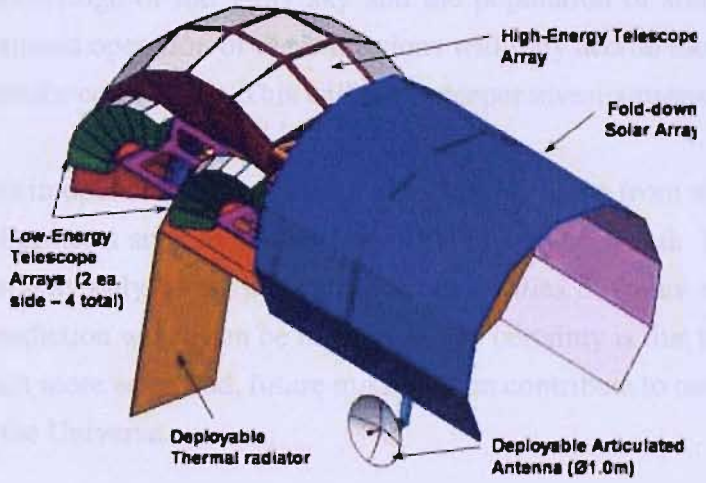

Figure 2.13: A computer rendering of the proposed design of EXIST. (Credit: Grindlay (2005))

The low energy telescope (LET) would be sensitive in the 5 – 30 keV range and would comprise four arrays of 7 × 1 coded aperture telescope covering a similar field of view and with a total detector area of 1.3 m^2 constructed from Si strips or pixels. The LET would have an angular resolution of 0.9'.

As a candidate to be the BHFP, EXIST would enable the most comprehensive survey for black holes, both stellar and super massive. The main science driving force would be based upon revealing obscured or dormant super massive black holes in AGN, conducting he highest sensitivity and bandwidth survey of GRBS out to a limit of z~15 and constraining the evolution and physics of black holes by measuring them on all scales.

2.9 Conclusions

The high energy sky reveals a rich range of astrophysical processes and emission mechanisms in both compact objects and diffuse sources. The difficulty in detection and imaging in this energy regime has restricted the level of scientific exploration. The last complete all-sky hard X-ray survey was completed by the HEAO-1 A4 experiment in the late 1970's. The Compton Gamma Ray observatory built upon the success of earlier missions and made many wonderful and interesting discoveries but was incapable of producing images of the sky in the tens to hundreds of keV energy range.

The current INTEGRAL and Swift missions are the most sensitive and capable instruments to observe in the energy range from a few keV up to 10 MeV to date. The results and surveys of these missions are still in progress but have already made a vast improvement upon our knowledge of the γ-ray sky and the population of sources of which it is made. The continued operation of these missions will only accrue more data to be exploited by the scientific community. This will allow deeper investiagtions in the properties of γ-ray sources.

The instruments in operation today provide the stepping stone from which future mission concepts and projects such as GLAST and EXIST can be based. The questions of todays exploration may only be answered by the capabilities of future missions such as these. The only prediction which can be made with any certainty is that there will always be something which more advanced, future missions can contribute to our knowledge and understanding of the Universe.

Chapter 3

The BATSE All Sky Survey

3.1 Introduction

The Burst and Transient Source Experiment (BATSE) was an instrument on-board the Compton Gamma-ray Observatory (CGRO). It was successfully launched in April 1991 and it operated in low Earth orbit (LEO) for over nine years until it was de-orbited in June 2000 (Harmon et al., 2004). BATSE had a 4π steradian field of view and so was able to view the entire sky. It's primary science goal was to detect and locate γ-ray bursts (Fishman et al., 1989b). However, prior to launch it was realised that the Earth could be used as an occulting disk to observe and detect persistent sources in the sky using traditional occultation techniques (Harmon et al., 2002).

These techniques have been applied to the BATSE data set since the launch of CGRO to observe known γ-ray sources and to search for new sources, culminating in a catalogue produced by Harmon et al. (2004) at the Marshall Space Flight Centre (MSFC). A different application of the occultation technique has also been developed at the Jet Propulsion Laboratory (JPL) (Ling et al., 2000).

A suite of software has been developed at the University of Southampton which takes a different approach to analysing the BATSE 9 year data set. This approach involves the generation of all-sky maps to perform a survey of the γ-ray sky through Maximum-Likelihood imaging. However there are a number of challenges in taking this approach to analysing the data.

This chapter will describe the standard Earth occultation technique and the Southampton imaging method. The results of the application of the Southampton Maximum-Likelihood imaging method to the full 9 year BATSE data set will then be discussed in the latter half of the chapter.

3.2 The Earth occultation technique

The Earth occultation technique is based upon the principal that as BATSE orbits the Earth the limb of the Earth passes across the sky blocking and then un-blocking the view of γ-ray sources in the sky. Consequently, the count rate in the BATSE detectors rise and fall as sources come into and disappear from view respectively. This imparts a step feature on the BATSE detector count rates. The amplitude of this step is a direct measure of the flux of the source which has just risen/set behind the Earth's limb. Two such steps are observed for every orbit which BATSE completes and for every source which is occulted.

As discussed in Section 2.3.4 BATSE comprises of 2 detector systems, the Large Area Detectors (LADs) and the Spectral Detectors (SDs). The LADs are significantly larger, and hence more sensitive than the SDs and so only the LAD data is used in the analysis of occulting sources. The data was recorded in two formats: DISCLA data consists of 4 energy channels recorded in 1.024 second bins; CONT data consists of 16 energy channels recorded in 2.048 second bins. Only the CONT data is used in all of the analysis discussed. The spacecraft orbits the Earth every ~90 minutes and the Earth's limb as seen by BATSE extends ~140° across the sky. A step in the count rate corresponds to a source rising or setting somewhere on that limb.

In the case of known sources the time and shape of the expected occultations, the response vector, can be calculated and correlated to the observed fluctuation in count rate to measure the amplitude of each step. The orbit of the CGRO was inclined at an angle of ~28° and had a precession period of 53 days. Over the course of an entire precession period BATSE is able to observe the entire sky, although high-declination sources, $|\delta| \geq 41°$, receive less coverage. Practically, a source is not observed twice an orbit due to gaps in the data for reasons such as passage through the radiation belts.

The response vector is the crucial element in measuring source fluxes with the Earth occultation technique. Given the exact location of the source and the position of the CGRO in its orbit about the Earth it is possible to construct the source response vector (Harmon et al., 2002). The occultation angle, β, is defined as the angle subtended between the orbital plane and the source, see Fig3.1. The duration of an occultation is highly dependent upon β. As the occultation angle increases the source appears to be moving more tangentially with respect to the Earth's limb. If the angle is in excess of ~65° then the source will not be occulted. As the orbit precesses β changes for each source after each orbit. The combination of the limits in occultation angle and data gaps results in 50% – 90 % of the sky being observed over a single precessional period.

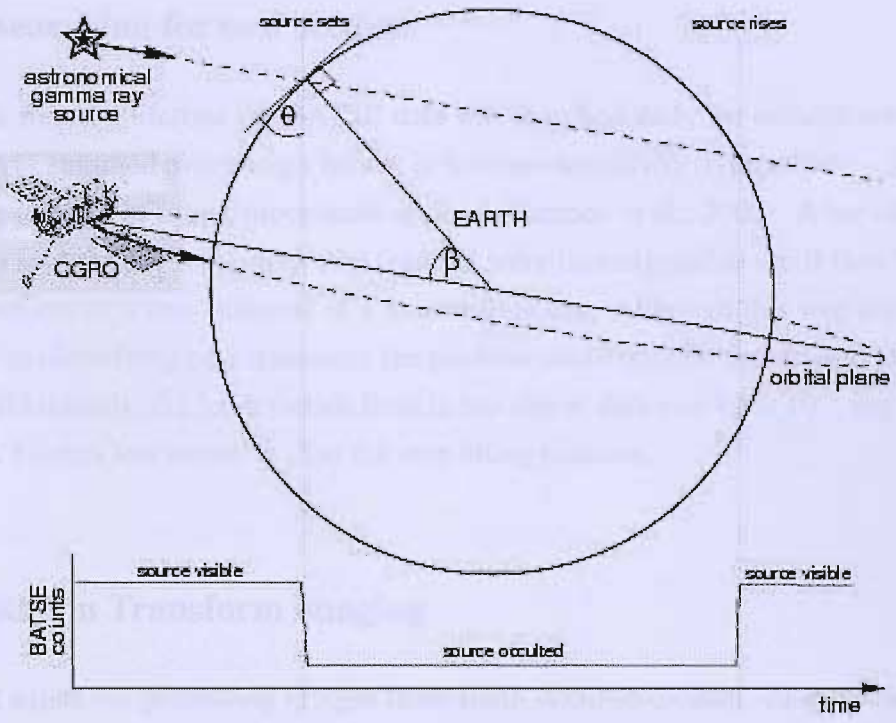

Figure 3.1: A schematic demonstrating the Earth occultation technique with BATSE. During the spacecraft's orbit, steps are observed in the detector count rates as a γ-ray emitting object sets below and rises above the Earth's horizon. The occultation angle, β, is defined as the angle between the orbital plane and the object measured at the geocentre (Shaw et al., 2004).

3.2.1 Step fitting

Fitting steps to known sources was achieved by examining a short section of data surrounding the expected occultation, the fit window. In this window the count rate in each LAD and energy channel is fitted by a quadratic curve to represent the detector background, a set of response vectors for any interfering sources and the response vector for the source of interest (Westmore, 2002). The larger the fit window the greater the sensitivity, however, the fit window size is limited by the time over which the background can be fit by a simple quadratic and by computing power. The techniques developed by MSFC employ a fit window of ~220 seconds reaching a sensitivity of $\sim 1.1 \times 10^{-9}$ erg cm^{-2} s^{-1}. The drawback to this technique is that it requires apriori knowledge of what sources are visible in the sky.

3.2.2 Searching for new sources

During the mission lifetime the BATSE data was searched daily for occultation features. The data was summed over energy bands, to increase sensitivity (typically 30 – 200 keV), and then a number of fitting procedures applied (Harmon et al., 2002). After identifying the known sources any remaining step features were investigated to see if they belonged to a new source or a new outburst of a known transient. Although this was a successful technique in identifying new transients the position could only be determined to $\sim 1°$ accuracy. Additionally, the 3σ detection limit in one day of data was 4.6×10^{-9} erg cm^{-2} s^{-1} more than 4 times less sensitive than the step fitting routines.

3.2.3 Radon Transform imaging

A method exists for generating images from Earth occultation data. Zhang et al. (1994) and Harmon et al. (2002) describe a method of imaging the sky using BATSE occultation data through a combination of radon transformations and maximum entropy methods. This method has proved successful in locating new transient objects to within 30' as well as allowing imaging known sources including AGN and supernova remnants. However, the imaging process requires the assumption that the Earth's limb is linear and hence can only produce images of $20° \times 20°$. Additionally, the process is highly computationally expensive making it difficult to examine large sections of data.

3.3 The Southampton imaging technique

Techniques were developed by Dr. M. J. Westmore and Dr. S. E. Shaw to produce all-sky maps using the BATSE 9 year data set. This allows the full exploitation of the 4π steradian field of view which BATSE had. The Likelihood Imaging Method for BATSE Occultation data (LIMBO) was developed based upon the work of Knödlseder (1999). The LIMBO code generates a pixellated image by using the Maximum-Likelihood method to test for source emission across a predefined sky grid (Shaw et al., 2001, 2004). This uses all of the data to produce a map of the whole sky, however, it a a map of statistical tests not a deconvolution of the occultation data itself. This technique works well, however the sensitivity limit is restricted due to the level of temporally changing detector background resulting from the LEO the spacecraft is in.

3.3.1 Flat-fielding the data set

The MSFC step fitting approach was limited by the temporal variations in the detector background and the timescales on which their models could fit this data. Ling et al. (2000) report similar problems and have attempted to fit the background with a more complicated empirical multi-parameter fit. Dean et al. (2003) discuss the application of Mass Modelling to the simulation of the expected detector backgrounds experienced by spacecraft. This process involves constructing a model of the spacecraft taking into account geometries and component chemical composition using the GEANT particle physics code. A Monte-Carlo simulation is then run placing the model in the anticipated radiation environment.

The Batse Mass Model (BAMM) was constructed for use with the Southampton LIMBO code (Shaw et al., 2003). The background is modelled as three separate components:

- Cosmic diffuse background γ-rays (CD)
- Cosmic rays (CR)
- Atmospheric Albedo γ-rays (ATM)

The spacecraft is initially assumed to be in deep space. Each energy deposit is recorded as well as the entire history of the particle which caused the deposit. However, BATSE is in LEO and hence exposed to a highly variable background. The database of energy deposits is now filtered using the location and orbit of the CGRO as discriminating parameters. This filtered data set can then be used to reconstruct the expected background for any point in the orbit. The three components are summed to estimate the overall background count rate. However, due to uncertainty in the input spectra of the background only the variations of the background are successfully modelled not the amplitude (Shaw et al., 2003). The components need to be normalised to the data set.

A section of data for each LAD and energy channel is selected which is free from contamination by additional sources of noise, e.g. the South Atlantic Anomaly (SAA). The bright sources above ~200 mCrab are subtracted from the data set. The model is then fit to the data as:

$$C(t) = \alpha \times CD(t) + \beta \times CR(t) + \gamma \times ATM(t) \tag{3.1}$$

The data set can then be flat-fielded by simply subtracting C(t). An example of the the individual components and the flat-fielded data set is shown in Fig. 3.2. The figure clearly shows how the dominant background component changes with energy and how significant

the process is in minimising background variations in the data. This process has to be applied to the entire section of data which is to be analysed. Once the background model has been fit the final model is stored in a database so that it can be reused. The model is capable of reducing the variations in the background flux by an order of magnitude.

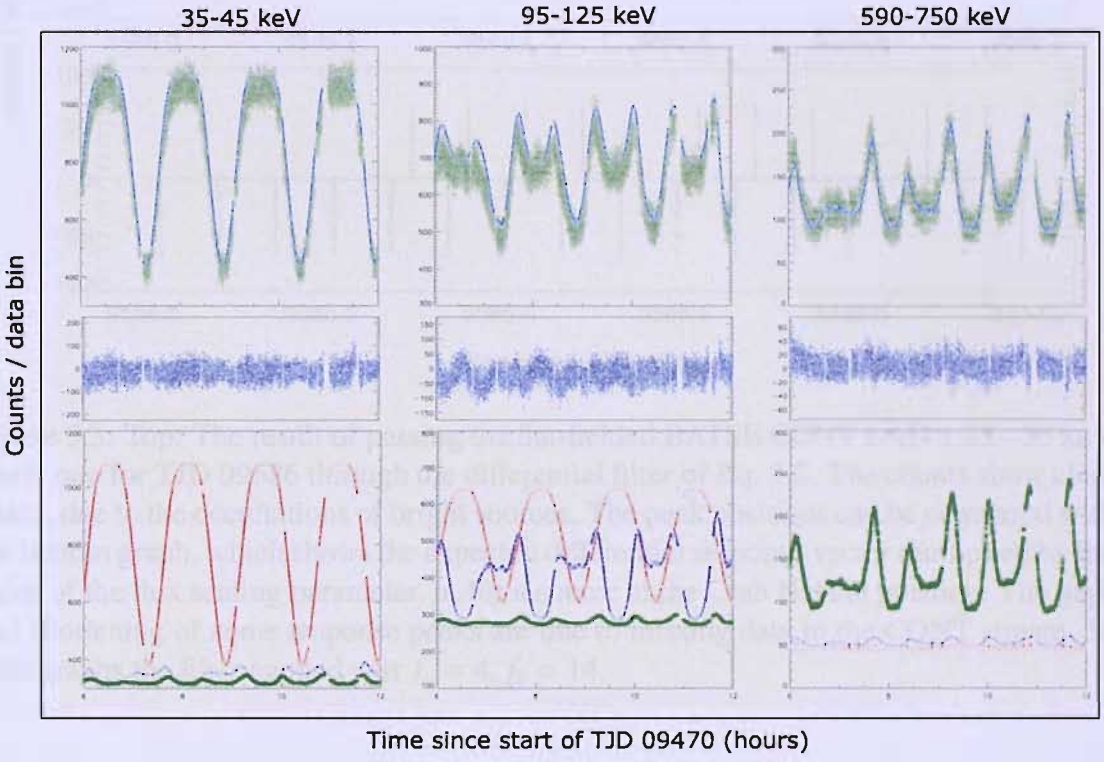

Figure 3.2: The Soton background model. The top three panels show the BATSE count rate from LAD 5 in three energy channels as the green data points. The solid blue line is the Soton background model. The middle panel shows the residuals (data-model) or *flat-fielded* data. The bottom three panels show the individual components. The red line shows the CD components, the blue line the ATM component, and the green line the CR component. (Westmore, 2002)

3.3.2 The differential filter

The limb of the Earth as seen by BATSE is a large entity, ~140°, hence it is highly likely that more than one source will undergo occultations at any one time. This leads to the superposition of steps in the count rate. The data set is passed through a differential filter to turn each step into a set of peaks and troughs, acting as a high-pass filter. The filter is given by:

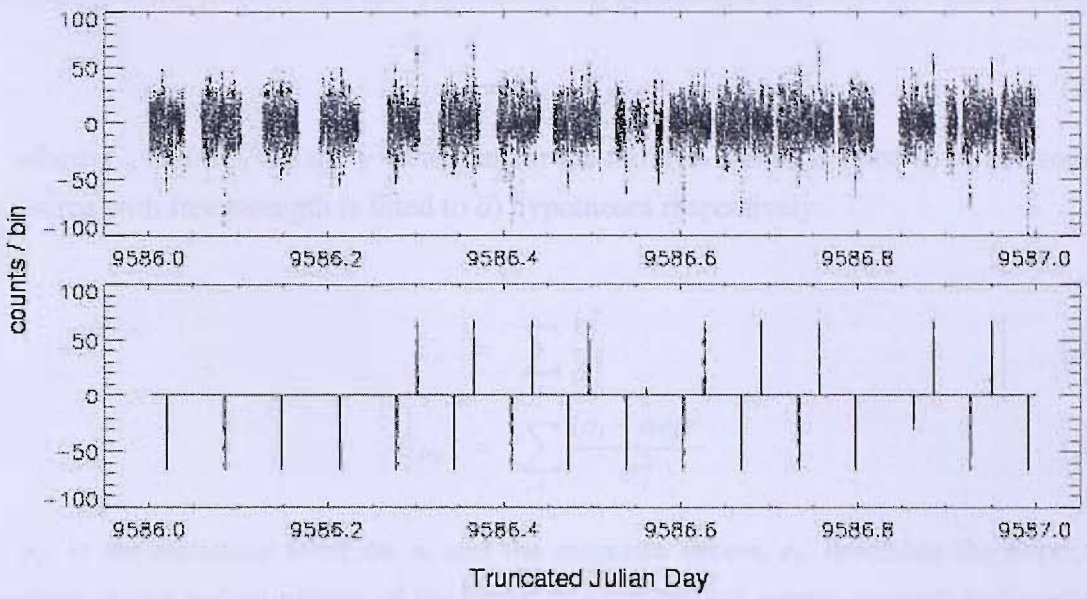

Figure 3.3: Top: The result of passing the flat-fielded BATSE CONT LAD 1 25 - 35 keV count rate for TJD 09586 through the differential filter of Eq. 3.2. The counts show clear peaks, due to the occultations of bright sources. The peak positions can be compared with the bottom graph, which shows the expected differential response vector multiplied by the value of the flux scaling parameter, α, for a source at the Crab Nebula position. The gaps and shortening of some response peaks are due to missing data in the CONT stream. In both graphs the filter applied was $f_a = 4, f_b = 14$.

$$o_i = \frac{\sum_{j=i+f_a}^{j=i+f_b} d_j - \sum_{j=i-f_b}^{j=i-f_a} d_j}{f_b - f_a + 1} \tag{3.2}$$

d_j is the flat-fielded data set and f=f_b-f_a corresponds to the width of the differential filter. f_b corresponds to the outer bound of the filter and f_a corresponds to the inner bound of the filter. This causes a step at bin i to be transformed into a peak with width $2f$. The amplitude of the spike/trough is proportional to the flux of the source. The selection of f effects the sensitivity and angular resolution of the imaging process. A large value for f improves sensitivity but reduces angular resolution (Shaw et al., 2001). The sensitivity and angular resolution are optimised with f=10. An example of the differentiated data set and the expected differentiated response vector for the Crab is shown in Fig. 3.3.

3.3.3 Maximum Likelihood Imaging

The next stage of the analysis process involves the generation of the Maximum Likelihood images. The significance of flux detection at any point on the sky grid is calculated from

the differentially filtered data set. The Maximum Likelihood test, λ, is calculated from:

$$\lambda = C_o - C_{src}, \tag{3.3}$$

where C_o and C_{src} are the χ^2 statistics for the null (no source is fitted to $\vec{o}$) and source (a source with free strength is fitted to $\vec{o}$) hypotheses respectively:

$$C_o = \sum_i \frac{o_i^2}{\sigma_i^2} \tag{3.4}$$

$$C_{src} = \sum_i \frac{(o_i - \alpha e_i)^2}{\sigma_i^2} \tag{3.5}$$

σ_i, is the statistical error on o_i and the response vector, e_i, describes the expected position, shape and amplitude of the peaks as a function of source strength and position on the sky (Shaw et al., 2004). Assuming that the error on the modelled background is small;

$$\sigma_i^2 = \frac{o_i}{2f+1} \tag{3.6}$$

The differentiated response vector scales between 0 (no change in transmission) to ±1 (maximum change in transmission) as a function of the angular response of each LAD. The scaling factor, α, is proportional to the flux received from each point in the sky for all eight LADs,

$$\alpha = \frac{\alpha_{top}}{\alpha_{bot}} \tag{3.7}$$

$$= \frac{\sum_i \frac{o_i e_i}{\sigma_i^2}}{\sum_i \frac{e_i^2}{\sigma_i^2}} \tag{3.8}$$

and has a statistical uncertainty given by,

$$\Delta\alpha = \left(\sum_i \frac{e_i^2}{\sigma_i^2} \right)^{-1/2} \tag{3.9}$$

The likelihood image is constructed by calculating λ across all of the sky grid positions. The size of the grid defines the angular resolution of the image. However, finer grids require more computation power and the grid size is limited to 0.5°×0.5° due to the finite time taken for an occultation to occur. The final likelihood image appears as the super-

position of the arcs caused by the Earth's limb. The best positional information on a source is obtained when the occultation angle is 45° as this produces two orthogonal arcs for the rise and set.

3.3.4 LAD response normalisation

The LADs do not measure the actual spectrum of the source but photon counts in each energy channel. Each LAD has a different response and so are not instantly comparable. Harmon et al. (2002) took the approach of normalising the behaviour of each LAD using the Crab as a calibration source. The Crab Nebula occultation data for each detector and energy channel was investigated using the standard technique at a range of orientations. An example of this is given in Fig.3.4 (Figure 13 of Harmon et al. (2002)).

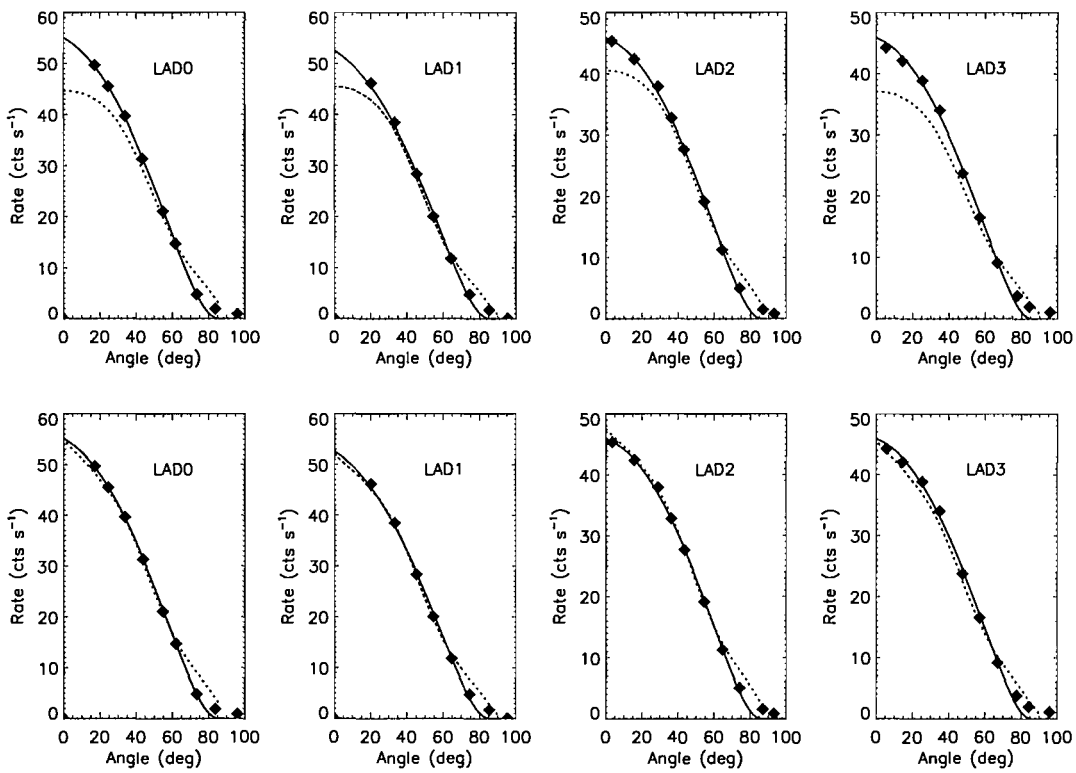

Figure 3.4: Crab Nebula count rates in CONT channel 3 (40–50 keV) for LADs 0, 1, 2, & 3 as a function of aspect angle. In the top 4 panels the dotted curves represent the original detector response function, folded with the known Crab spectrum. The bottom four panels, the dotted curves represent the response function after a correction for the entrance window was applied. The solid curves are an empirical fit to the Crab data, (Harmon et al., 2002).

The empirical function fit to the LADs to represent the response, R, is described by

an equation containing 4 parameters, A_1, A_2, A_3 and A_4, which are unique for each energy channel and detector. Harmon et al. (2002) give the equation for the response as:

$$R = A_1 \cos(\theta) \exp^{\left(\frac{-A_2}{\cos(\theta)} + \frac{A_3}{\sin(\theta + A_4)}\right)} \tag{3.10}$$

This calibration gives maps of α in units of the normalised Crab Nebula response.

3.3.5 Summing of images

The LIMBO code is computationally limited to generating images on a daily basis. However, this is attractive as it allows images to be summed together over desired periods, allowing for the investigation of source variability. The limiting sensitivity of a map may be decreased by summing up over time and energy. However, it is not possible to add together likelihood images in a linear fashion. This can be seen in the dependence of Eq. 3.5 on Eq. 3.8, as α is the ratio of two sums:

$$\alpha_{top} = \sum_i \frac{o_i e_i}{\sigma_i^2} \tag{3.11}$$

$$\alpha_{bot} = \sum_i \frac{e_i^2}{\sigma_i^2} \tag{3.12}$$

However it is feasible to sum up the individual components of α_{top} and α_{bot} prior to taking the ratio of the two to get the total flux α_{Tot}. So, if we have a number of maps created for individual days then:

$$\alpha_{Tot} = \frac{\sum_d \alpha_{top}}{\sum_d \alpha_{bot}} \neq \sum_d \alpha_d \tag{3.13}$$

where d is the index of each daily map.

Significance maps can be regained by dividing the total flux by its statistical uncertainty, i.e. $\alpha_{Tot}/\Delta\alpha$, where the uncertainty is given by Eq. 3.9. This method also possible allows the combination of images made from individual energy channels.

An all-sky map for 489 days in the period TJD 09448 - 09936, produced from 7 CONT energy channels (30 – 160 keV), is shown in Fig. 3.5. Using simple statistical arguments, and neglecting any systematic background, the map has a 3σ sensitivity of 3 mCrab. It is easy to see the brightest sources in the sky, such as the Crab Nebula and Cygnus X-1. However, it is also clear that the imaging process produces a very large, and complicated point spread function (PSF) for each source. The origin of the PSF is clearly from the ~140° arcs of the Earth's limb. The far reaching effects of the PSFs of the bright sources

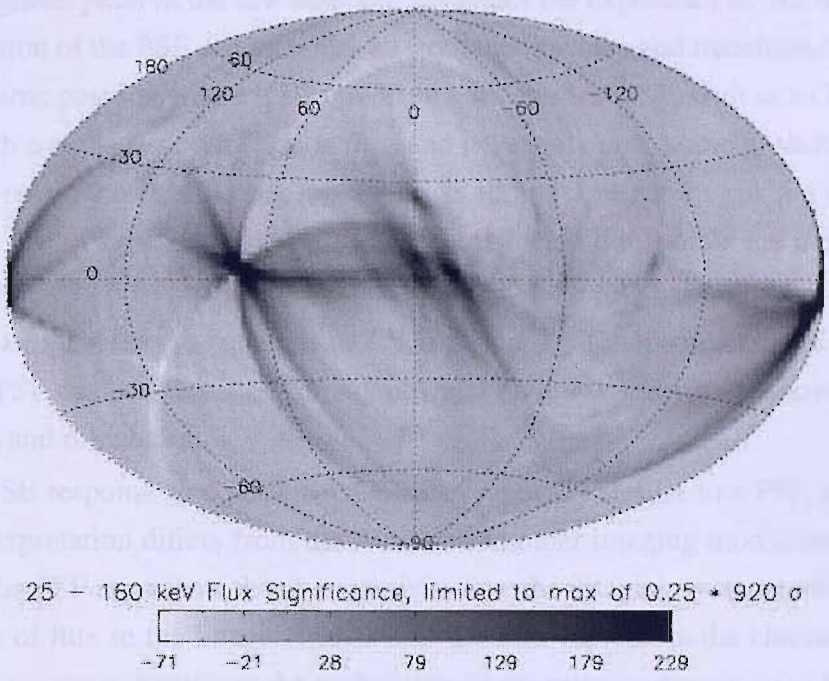

Figure 3.5: Map of the significance of 30 – 160 keV flux from the whole sky for a total of 489 days from TJD 09448 to TJD 09936 made using LIMBO. The colour scale of the map has been limited to a quarter of the peak in order highlight details at lower significance. The peak significance of 920 σ is consistent with the position of the Crab Nebula. regions.

negates the possibility to detect weaker sources. The problem is made worse in crowded regions, such as the Galactic Centre where many PSFs overlap and are indistinguishable as separate entities.

The artifacts present in the maps at the extremities of the brightest source PSFs dominate over the fainter source populations. In order the exploit the imaging capability a method of removing these source artifacts is required.

3.4 The image cleaning algorithm

All imaging systems have an inherent PSF. In the cases of optical systems the instrument is designed to produce source PSFs which are symmetric and as narrow as possible. In other wave bands where designers have less control over the instrument PSF another approach must be taken. In the case of radio interferometry a CLEAN algorithm is used to remove artifacts from radio maps (Högbom, 1974).

The CLEAN algorithm works by defining two data spaces; the raw map and the clean

map (of the same dimensions as the raw map, but initially empty). The algorithm first finds the brightest pixel in the raw map and generates the expected PSF for this position. A small fraction of the PSF is then removed from the raw map and transferred to the clean map at the same position where it is convolved with an ideal PSF, such as a Gaussian distribution with a realistic width. This is repeated iteratively until some predefined criteria, such as the minimum significance of the brightest pixel remaining in the raw map, is reached. At this point the remnants of the raw map should resemble the intrinsic noise, and can be added to the clean map to produce a realistic final image.

This process can also be applied to LIMBO maps. The parameters of the BATSE occultation PSF can be calculated for any position on the sky using the knowledge of the CGRO orbit and orientation.

The BATSE response to a point source is conceptually similar to a PSF, although the physical interpretation differs from the PSF used in other imaging modalities. In optical astronomy the PSF represents the characteristic way the imaging system redistributes the point source of flux in the image. In LIMBO the PSF represents the characteristic way the imaging system redistributes the probability of the estimated position of the source; a point source in the sky produces an image that is consistent with emission from a number of different, but mutually exclusive, positions.

The PSF for any particular sky position is highly complex. An example of this is shown in Fig. 3.6; this is the case of a Crab PSF for channel 2 summed over ~500 days. However, the PSF of a selected source position can be calculated and so it is possible to subtract that source's contribution to the total image.

It is possible to reduce the computing resources required in the calculation of the LIMBO PSF using the method developed by Westmore (2002). This uses knowledge of the position of the Earth's limb over time to restrict the number of pixels LIMBO tests for a response from. For each time bin during the occultation, the pixels through which the Earth's limb passes can be identified. Once all of the relevant pixels have been identified LIMBO can be run on this smaller set. In the case of a 2°×2° grid of sky positions this approach leads to a reduction in the number of pixels for which the MLR is calculated from 16,471 to ~ 1000, resulting in a significant reduction in the amount of computing time required.

Section 3.3.5 discussed the problems of summing images together due to the fact that likelihood maps cannot be summed linearly. In a similar fashion, the CLEAN algorithm must operate on a linear parameter if it is to subtract flux from a raw map and transfer it to a clean map. However, α_{top} can be considered linear. The flux maps themselves are not linear. Since α_{bot}, is a constant it is possible to run the cleaning algorithm on α_{top} and

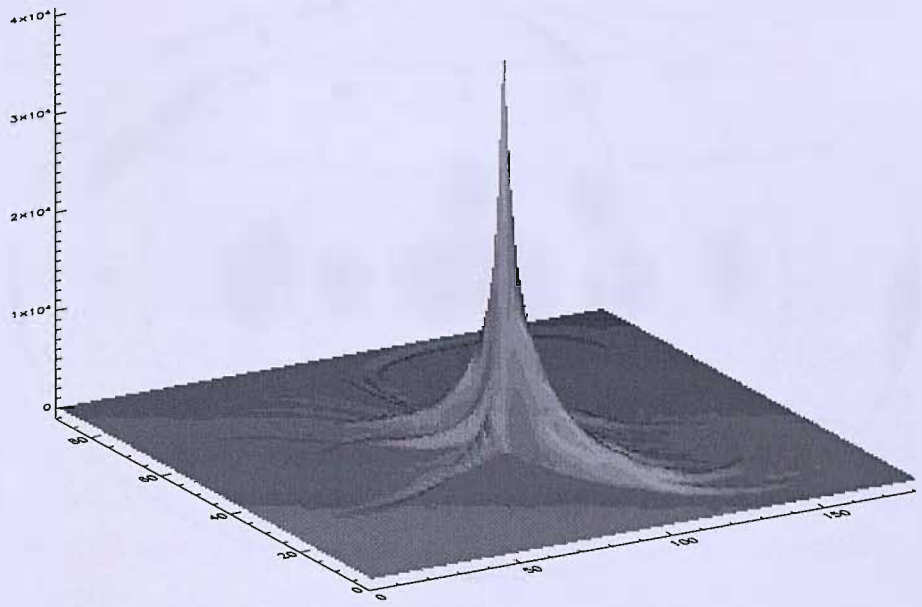

Figure 3.6: This is the simulated BATSE occultation PSF which would be observed of a source at the location of the Crab Nebula over the course of ~500 days in CONT energy channel 2.

then re-derive the cleaned flux and likelihood maps.

3.4.1 Identifying which pixel to clean

Prior to cleaning commencing the location of the source to be cleaned must be ascertained. In traditional imaging systems this is usually trivial, the source position corresponding to that of the brightest pixel. In the LIMBO imaging system the brightest pixel of the PSF does not necessarily correspond to the true location of the source. If the wrong point is chosen then the shape of the PSF will be incorrect. As the PSF is so complex cleaning with the wrong PSF will create artifacts and noise in the maps. For this reason the pixel at which to clean is found by first generating the PSF for the most significant pixel and then cross-correlating this on a grid surrounding the most significant pixel. The pixel position with the highest correlation coefficient is then assumed to be the correct pixel. The PSF is then re-generated at this position and a fraction of the source flux is cleaned out and transferred to the clean map.

As the pixels are 2°× 2°the PSF is prone to being slightly incorrect if only as a result of a source not lying directly at the central location of the pixel. However, choosing the

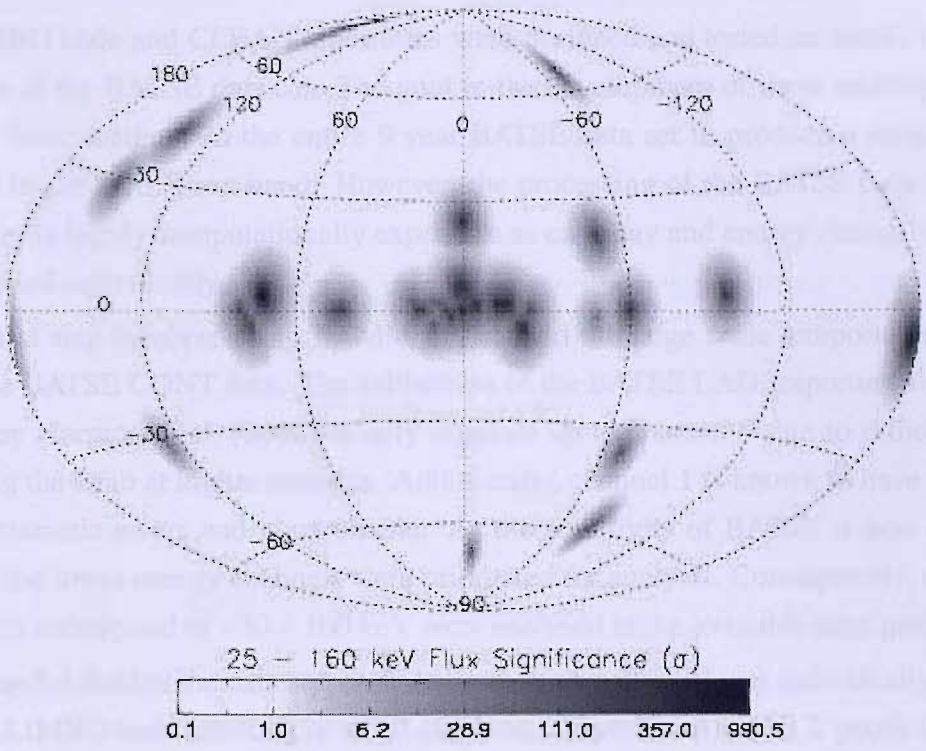

Figure 3.7: The results of performing the image cleaning technique on the all-sky map of Fig. 3.5. This image is of the CLEAN map prior to any residuals being added back in. A simple Gaussian PSF has been convolved with the extracted fluxes.

wrong pixel entirely will result in very bad systematics being introduced, especially in the case of the brighter sources. To address these problems two approaches are taken. The first involves a pre-cleaning stage. Prior to the iterative process the majority of the flux contributions of the brightest sources can be cleaned out immediately. This typically corresponds to ~95% of the signal from sources such as the Crab Nebula and Cyg X-1. These sources are cleaned out at their known locations on the sky. Secondly, a catalogue of possible sources is passed to the cleaning algorithm. When the cleaning pixel is identified its location is compared to the catalogue of sources to see if it belongs to a known source. If a source is identified it adopts the catalogue position for which to generate the PSF. The catalogue comprises of among others, the HEAO catalogues, known AGN, and transient Galactic sources.

An example of the application of the CLEAN algorithm to the raw map in Fig. 3.5 is shown in Fig. 3.7. Approximately 25 sources are clearly detected including both galactic and extragalactic sources. The Crab is detected at a significance of ~950σ.

3.5 Imaging and cleaning the 9 year data set

The LIMBO code and CLEAN algorithms were designed and tested on small, ~50 day, segments of the BATSE data set. The goal in the development of these techniques was to apply these methods to the entire 9 year BATSE data set to produce a sensitive all-sky map in the hard X-ray band. However, the processing of the BATSE data by these techniques is highly computationally expensive as each day and energy channel needs to be processed individually.

The first step involves using BAMM to flat-field the large scale temporal variations out of the BATSE CONT data. The calibration of the BATSE LAD response to the Crab Nebula by Harmon et al. (2002) is only accurate up to channel 9 due to difficulties in observing the Crab at higher energies. Additionally, channel 1 is known to have unquantified systematic errors and is unreliable. As the sensitivity of BATSE is best at lower energies the lower energy channels were prioritised for analysis. Consequently, channels 2–7 which correspond to ~30 – 160 keV were analysed in the available time period.

Having flat-fielded the data set, each day and energy channel was individually imaged with the LIMBO code resulting in an all-sky image constructed of 2°× 2°pixels for every day and energy channel. Each energy band was summed up in ~500 day sections to produce more significant all-sky maps. The maps were produced in segments of time for two reasons. One reason is that this allows the maps to be allocated to different computing resources to allow for parallel cleaning to occur. Secondly, these shorter timescale maps allow for easier checking of the cleaning process. After cleaning the maps can be summed up to cover the entire 9 year time-span.

In the course of summing up over the maps some days will be found to have particularly noisy images and will be rejected by the summation software. Combining these losses with days in which the background model didn't fit and those in which the energy channel boundaries were altered from the standard look-up table represents ~20–25% of the 9 year data set. The days which are not included in the summed maps are recorded so that the CLEAN algorithm does not incorporate them when it generates a simulated source PSF.

The ~500 day maps for each energy channel are individually cleaned down to the ~4σ level. It is possible to sum maps over energy prior to cleaning. However, the occultation PSF is variable with energy and the cleaning algorithm can only use a single PSF. Typically the PSF for the lowest, and hence presumed most dominant, energy channel is used. Tests performed on individual energy band maps where the wrong energy PSF is used by the CLEAN algorithm indicated that large systematics were added into the map and the algorithm could not be relied upon to find all of the sources present in the field.

Consequently, we clean each energy channel separately with the corresponding energy channel PSFs. Although, this slows down the processing of the images it does allow for crude spectral information to be extracted out at a later date. Once cleaned all of the maps are summed together over time and energy to produce the most sensitive map possible.

The residuals are added to the clean components to produce the most realistic map possible. However, the clean components alone provide a record of everywhere the CLEAN algorithm believed there to be a source and consequently cleaned. However, there may be residual sources below the individual cleaning thresholds, when summed together these may become significant and hence the residuals may still contain source information. Maps of significance, flux and variance are produced at the end of the process. An overview of the procedure applied to the 9 year data set is indicated in the flow diagram shown in Fig. 3.8.

3.6 The statistical properties of the final all-sky maps

Prior to extracting and identifying sources in the maps it is important to ascertain the statistical behaviour of the maps in order to understand if there are any systematic errors present and therefore how reliable the map data is. The final map spans ~9 years of BATSE observations over the 30–160 keV energy band, the cleaned components and complete significance map is shown in Figs. 3.9 & 3.10. The point of highest significance is at ~2100σ and corresponds to the expected position of the Crab Nebula. This increase in significance is exactly what would be expected from the extrapolation of the significance observed of the Crab Nebula in an individual 500 day map. A number of other points of high significance are also clearly evident as are a number of features in the map.

Artifacts of the occultation PSF are clearly visible although at a much reduced level in comparison to what they were prior to the application of the CLEAN algorithm. However, plotting the histogram of the summed flux map reveals unexpected results. The image histogram, shown in Fig. 3.11 clearly shows an approximately Gaussian noise distribution. The source population exists as a low-level extended tail at high fluxes. What is clear is that the noise distribution is not centred about zero, it is centred around a value which would correspond to ~-20 mCrab. This also, shows that the vast majority of the residuals left over from the CLEAN algorithm have negative flux values since the CLEAN algorithm only operates on positive points. This raises the question of whether the CLEAN algorithm has damaged the underlying flux distribution.

An investigation of all of the individually cleaned energy channels shows the same type of pixel distribution. An examination of the raw maps prior to cleaning (see Fig. 3.5

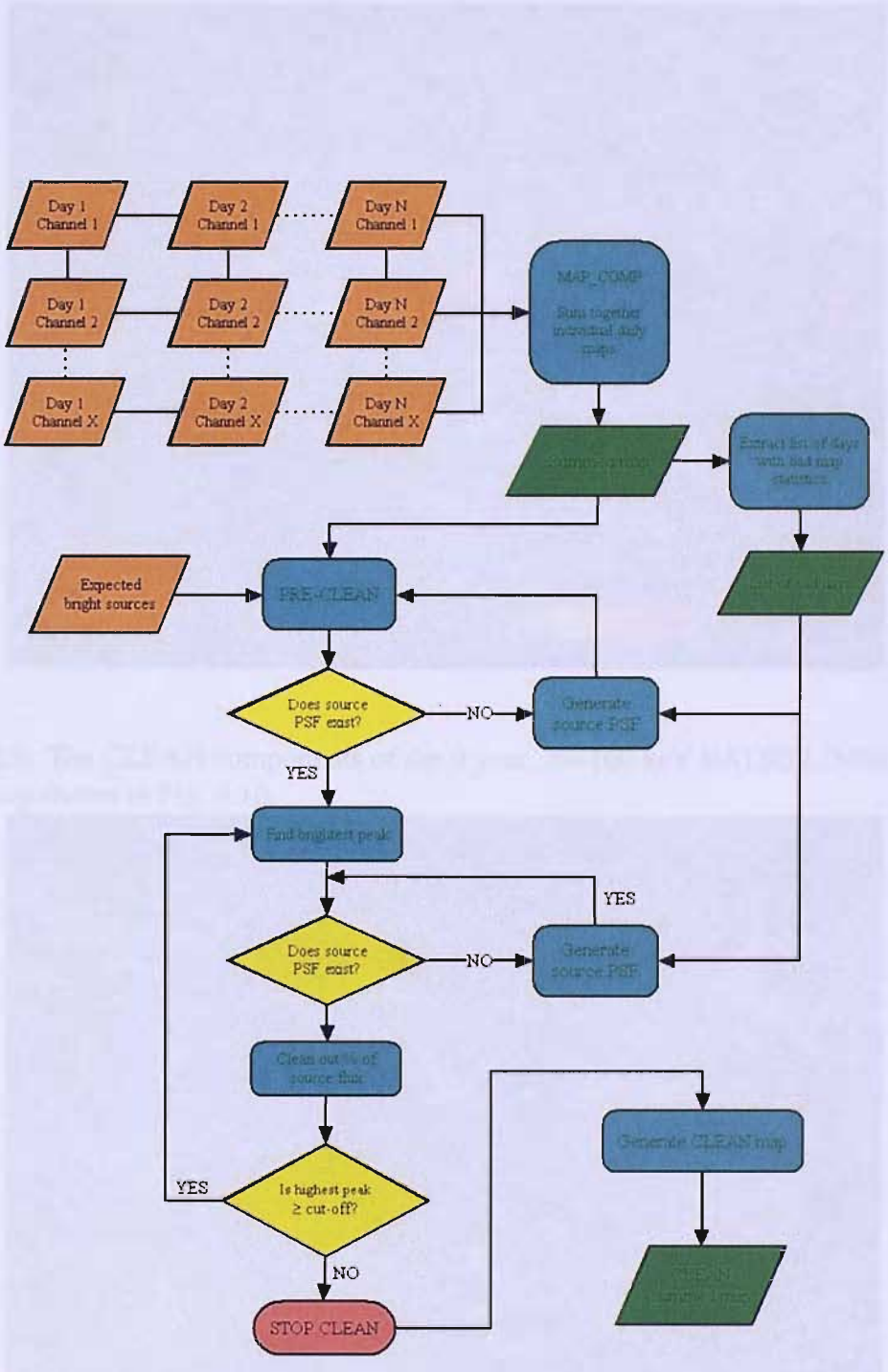

Figure 3.8: Organisational chart showing the steps involved in producing and cleaning a summed BATSE all-sky map.

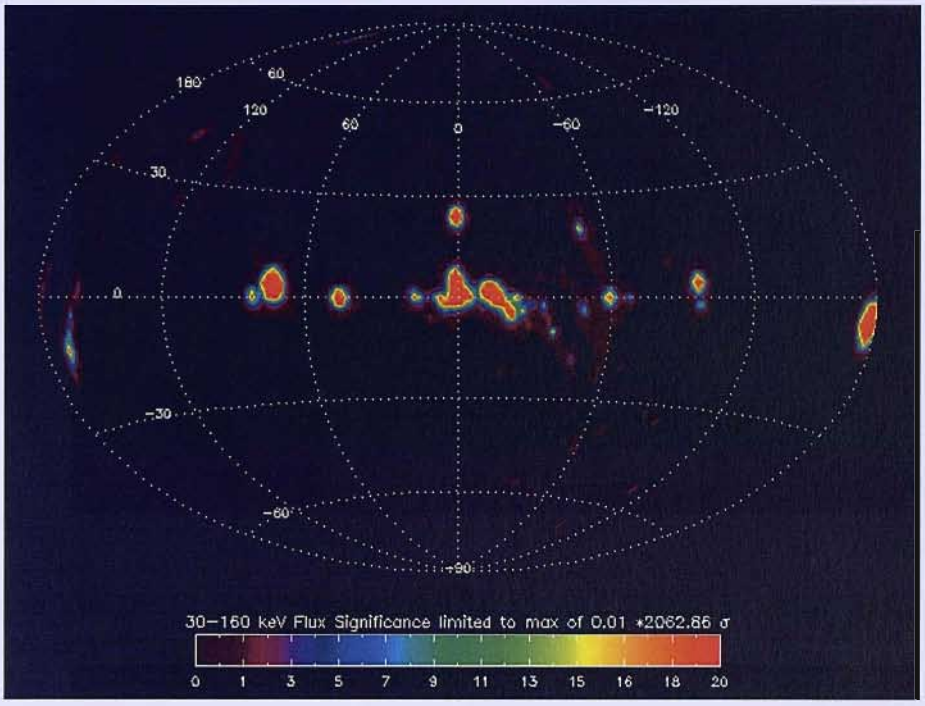

Figure 3.9: The CLEAN components of the 9 year, 30–160 keV BATSE LIMBO significance map shown in Fig. 3.10.

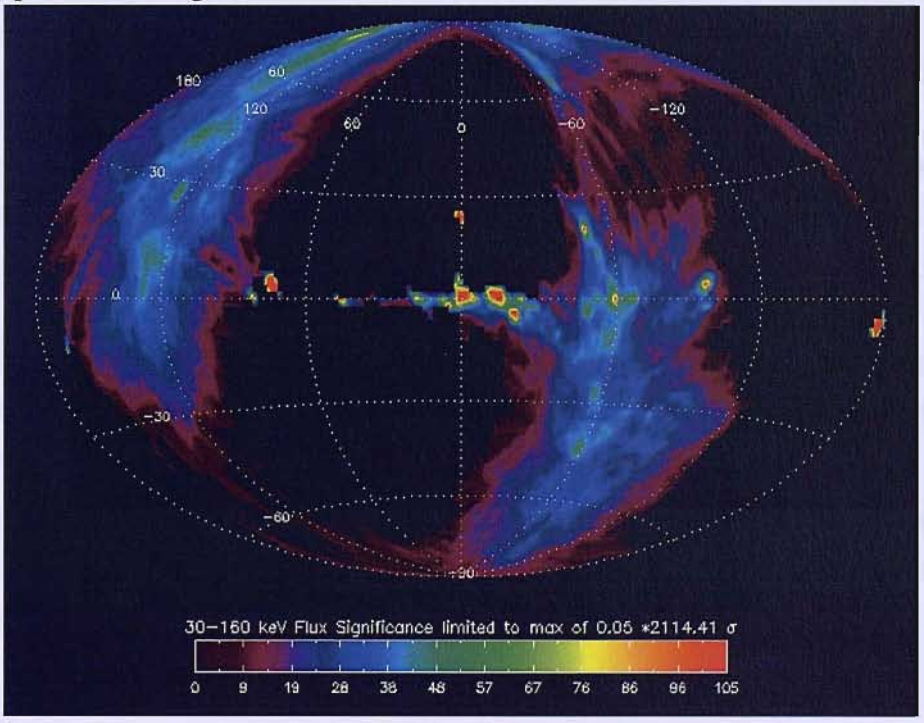

Figure 3.10: The CLEAN 9 year, 30–160 keV BATSE LIMBO significance map. The cleaning residuals have been included in the final image. The low-level artifacts are clearly evident, especially around the celestial polar regions.

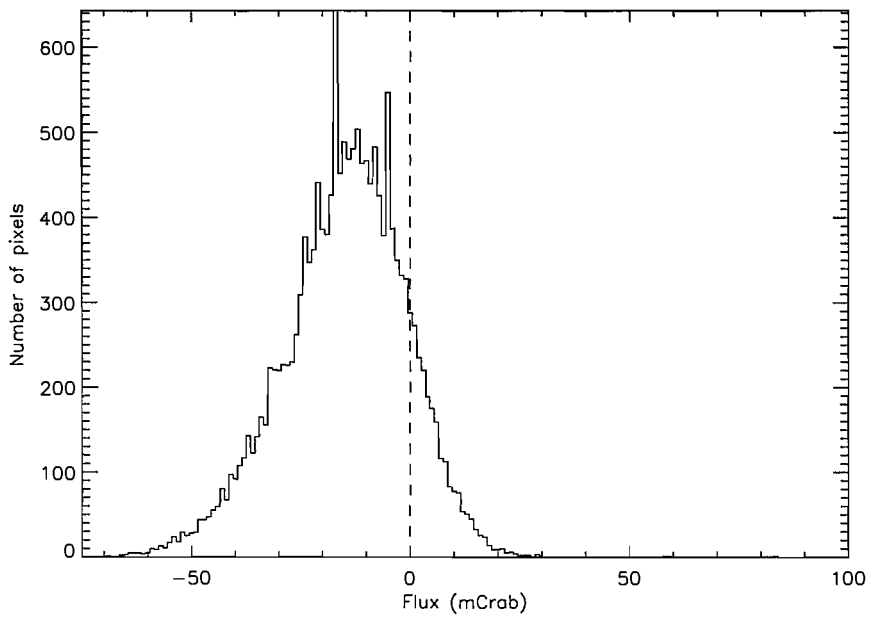

Figure 3.11: Histogram of the 30–160 keV flux map corresponding to the significance map shown in Fig. 3.10. The dashed line reprexents the zero flux point

for an example), also show the same distribution. This implies that the CLEAN algorithm has not created this distribution of negative residual pixels and they were, in fact, already included in the images. Looking at the individual daily maps proves difficult as the fluxes on a daily timescale are very small, as would be expected. However, it is possible to take the mean flux value of each daily map and see how it behaves. A plot of the mean value of ~1000 days of BATSE images is shown in Fig. 3.12. It is evident, that even on a daily timescale, the fluxes in the map are predominantly negative. This means that no procedure or algorithm applied after the creation of the daily images can be responsible for the negative pixel distribution observed in the final summed maps.

The daily maps are produced using the Maximum Likelihood imaging approach described in Section 3.3.3. The daily flux images are constructed from the measurement of the scaling factor, α

$$\alpha = \frac{\alpha_{top}}{\alpha_{bot}} \tag{3.14}$$

$$= \frac{\sum_i \frac{o_i e_i}{\sigma_i^2}}{\sum_i \frac{e_i^2}{\sigma_i^2}} \tag{3.15}$$

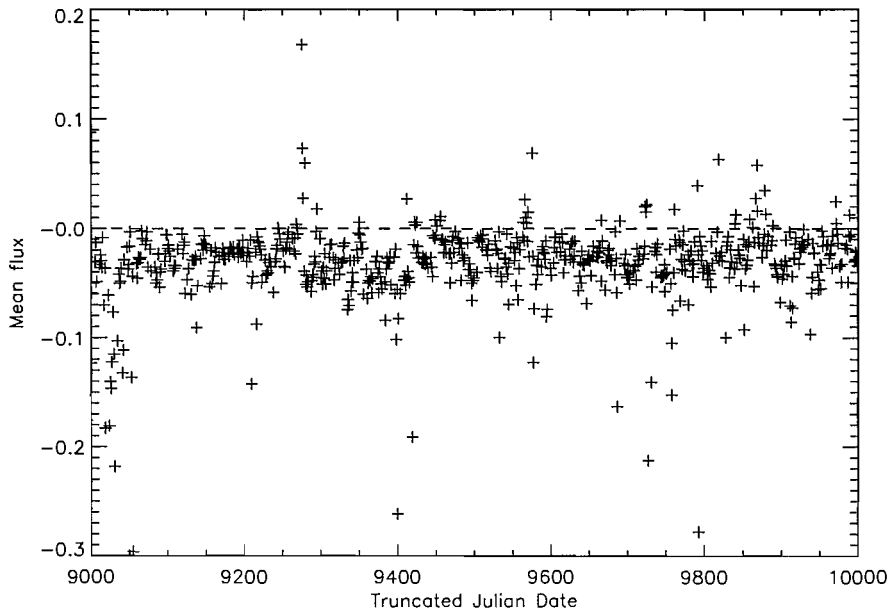

Figure 3.12: A plot of the mean flux value of each daily image of energy channel 2 over 1000 days. The dashed line indicates the zero flux line.

α_{bot} is purely the calculated response for any given position of the sky and cannot be negative. Looking at the α_{bot} distribution of a number of the maps confirms this. Hence, α_{top} must be negative in order to explain the observed pixel flux values. The key calculation of α_{top} is the product of the observed filtered data set, o_i, and the response vector for that portion of the sky, e_i. The response vector comprises of the expected positive and negative spikes expected for the anticipation rises and troughs in the BATSE count rate for a given source position. The filtered data set consists of what is actually observed. For a negative value to be produced the response vector and filtered data would have to comprise of occultation spikes out of phase, i.e. one positive and one negative.

The fact that negative flux values are in the majority of pixels implies that they are not associated with sources, which would be few in number, but somehow with the sky background. This is possible if the original BATSE count rate has a gradual negative gradient, hence all of the sources sit on a decreasing background. When the data set is differentiated this would appear as a continual setting source and would explain the observed negative fluxes.

3.6.1 Origin of the negative background gradient

This negative gradient in the BATSE count rates is explained by the passage of BATSE through the South Atlantic Anomaly. The BATSE detectors are turned off during the passage, however, the spacecraft is bombarded by protons during this time and becomes active. Once the passage is complete the BATSE detectors are turned back on however the residual spacecraft activity can still be observed in the LAD count rates. A test of this can be performed by simply re-ordering the time stamps of a single day of BATSE data, this will effectively reverse the SAA decay to a positive gradient. The statistics of the image produced by this method mirrors that of the original image shifting the mean of the pixel distribution to positive fluxes.

The scale of this background variation is very small on a daily basis and the temporal variations modelled by BAMM are much more significant. Consequently during the development of the LIMBO and CLEAN techniques the SAA decay was considered negligible. On the short timescales on which the code was tested this is a valid assumption. However, the SAA decay produces a systematic effect which is additive when summing maps together. Hence, the summing together of 9 years of BATSE observations in this manner has produced such a drastic result.

3.6.2 Correcting the maps for the negative distribution

As the origin of the typically negative background fluxes can be attributed to the mathematics of the imaging process we can account for this by assuming that the source population effectively exists on top of a negative distribution. We therefore scale each map to centre the noise distribution at zero and rescale all map fluxes to the Crab Nebula measured flux. This scaling has to occur to the linear parameter, α_{top}, prior to the final flux maps being generated. This is obviously an approximation as the gradient of the SAA decay changes with time and is not a simple linearly decreasing function. This correction is applied at the end of the analysis procedure and raises questions about the validity of the significances measured in the original maps. These significances may have been underestimated and must be used with care.

The only way to accurately correct for SAA decay is to model it out of the detector count rates at the same time as removing the background with the BAMM model. The data would then need to be imaged, cleaned and re-analysed again from scratch. The time this would take does not currently make it feasible to perform within the context of this thesis.

3.7 Extracting sources from the map

One of the effects of rescaling the maps is that the noise distribution is now much more evident and such that it limits source extraction down to the 20–30 mCrab level. Sources were extracted from the map consisting of all the data for 9 years, across the 30–160 keV energy band with both cleaned components and residuals present, using the SExtractor 2.2.2 (SE) software, developed by Bertin & Arnouts (1996). A wavelet pass-band filter to assist in extraction in crowded regions of the map was used. For a detailed description of this software see Chapter 4. Sources were extracted down to a very low flux before being cut-off at the 20 mCrab threshold dictated by the scale of the noise distribution. The sources were then inspected by eye and those associated with clear residual structures rejected. One point to note is that two sources of fluxes, ~30 mCrab are apparent at the celestial poles. These are an artifact of the rescaling correction. The celestial poles are very rarely occulted and so are typically set to zero in the map and so never experience the negative background flux. Rescaling these points artificially makes them appear as sources. They are easily identified as they represent a grouping of 4 neighbouring pixels all of identical flux values.

The extracted source list is shown in Table 3.1. The errors quoted on the source fluxes are entirely based upon the statistical errors of the imaging method and take no account of the much more dominant systematic errors present in the map. The sources extracted by SExtractor were compared to the INTEGRAL Science Data Centre (ISDC) catalogue of high energy sources (Ebisawa, et al., 2003), which contains over 1000 sources with flux estimates in the 20 - 200 keV band. Points of emission in the map have been identified with sources from the catalogue, based on their positions and estimated brightness. Any source which lies within 2.8° of its catalogue position is within the diagonal size of one image pixel. The angular resolution of the LIMBO images is limited by the 2° grid spacing. Hence there are some cases where it is not possible to associate the detection with only one known source, in these cases the source which is expected to be brightest is listed. Source confusion is always likely to be a problem, especially in the Galactic Centre, with a technique such as Earth Occultation Imaging.

Approximately 36 sources are visible in the final map. The limiting factor in the process of source detection is not however due to a statistical nature but more a systematic effect. The rescaled noise distribution becomes very dominant at fluxes below ~20 mCrab and makes it impossible to identify source emission with any confidence. However, those sources identified with fluxes of > 30 mCrab are all confidently associated with known sources. Due to the original negative nature of pixels below 20 mCrab they

Table 3.1: List of sources detected by BATSE with LIMBO in the 30 - 160 keV band for the 9 years of observations. The quoted flux error is derived on a statistical basis and takes no account of the much more dominant systematic errors in the map.

Source Name	RA (°)	Dec (°)	BATSE Flux (mCrab)	Flux error (mCrab)	Dist from known position (°)
Crab	83.13	22.34	1000.0	0.5	0.56
CygX-1	299.24	36.12	883.8	0.4	0.97
Galactic Centre (a)	266.40	-28.94	168.2	0.4	-
4U1700-377	255.66	-38.87	167.6	0.4	1.05
ScoX-1	245.35	-14.86	150.5	0.4	0.86
VelaX-1	136.14	-40.91	113.3	0.5	0.59
GRS1915+105	288.72	10.91	99.1	0.4	0.09
GX301-2	186.45	-62.73	98.9	0.5	0.11
GX339-4	255.71	-48.84	62.6	0.5	0.04
CygX-3	308.34	40.42	60.4	0.4	0.56
Galactic Centre (b)	264.26	-30.13	50.7	0.4	-
GRS 1758-258	270.38	-25.10	48.7	0.4	0.09
GROJ0422+32	65.88	33.69	48.0	0.4	0.98
CenA	201.93	-42.69	46.6	0.4	0.53
GX354-0	262.64	-34.01	44.1	0.5	0.34
GX1+4	260.72	-25.69	39.8	0.4	2.27
NGC4151	182.64	38.86	38.5	0.4	0.54
AXJ1631.9-4752	248.29	-47.92	37.7	0.4	0.20
GX17+2	273.99	-14.45	34.8	0.4	0.41
CenX-3	171.50	-60.97	33.2	0.5	0.68
NGC3252	166.35	72.34	28.9	0.5	2.67
Circinus Galaxy	212.65	-64.66	27.8	0.5	0.74
SMCX-1	17.15	-73.60	27.5	0.5	0.63
3C273	187.16	2.05	27.2	0.5	0.13
H1608-522	245.29	-52.82	26.2	0.5	1.31
NGC4945	197.07	-49.91	23.7	0.5	0.63
4U1323-62	201.16	-62.63	23.5	0.5	0.55
Vela Pulsar	129.14	-43.80	23.5	0.5	1.40
NGC4388	186.55	12.26	22.9	0.5	0.39
4U1626-67	244.30	-66.31	22.8	0.5	1.88
QSOB1156+295	181.71	28.92	21.9	0.5	1.63
LMCX-4	83.56	-67.02	21.8	0.5	0.67
3C390.3	285.51	78.38	21.4	0.5	1.68
Ginga1826-24	277.55	-23.64	20.4	0.5	0.23

were never cleaned and consequently occultation PSF artifacts are still evident. Table 3.1 lists amongst it's sources, Galactic Centre (a) and (b). These are detections of either side of the Galactic Centre, the resolution of the LIMBO imaging is such that the individual sources in this region cannot be resolved, hence it is observed as an extended source which SExtractor attributes to two seperate sources. The flux of these two sources represents the combined flux of all sources observed in the Galactic Centre region.

3.8 The BATSE All-Sky Survey source population

An ideal test of the success of the LIMBO technique and CLEAN algorithm can be made rather simply by comparison to the catalogue constructed by Harmon et al. (2004) using the traditional Earth occultation method to search for known and new sources. The catalogue of Harmon et al. (2004) contained three lists, persistent sources, transient sources and a deep sample. In the deep sample 179 sources where searched for; 83 were classed as definite detections, 36 sources were classified as possible detections, 45 sources were undetected and 15 were indeterminate.

The LIMBO technique should be most sensitive to persistent sources. Of the 23 persistent sources observed using the traditional method 4 are not seen in the clean LIMBO map: 4U 1705-440; OAO 1657-415; Her X-1; 4U 0614+091. These 4 sources are all galactic sources and so are susceptible to falling within one of the map pixels occupied by a brighter source. This is the case for the first two sources which lie very near to the Galactic Centre and 4U 1700-377. The latter two sources, Her X-1 and 4U 0614+091, exist away from the Galactic Plane. At their expected positions a flux of ~4 mCrab is measured. However, the statistical properties of the all-sky image is such that such a low flux measurement cannot be considered a detection. The location of these sources whilst off the Galactic Plane places them near to the artefacts of some of the brighter γ-ray sources, consequently the CLEAN algorithm may have removed excesive flux from this region rendering these sources undetectable.

We expect to be most sensitive to persistent sources of emission, especially with the negative background. However, we detect 3 of the 39 transient sources listed by Harmon et al. (2004). A number of the remaining ~20 sources are listed as possible detections in the deep sample made using the standard techniques. However, this would represent the first confirmed detection of these sources by BATSE. The strength of the LIMBO technique lies in that it makes no assumptions as to what sources it expects to detect and produces images of the entire sky over which to search for source emission. The strength of the traditional occultation techniques is in the analysis of known source variability

or the detection of bright transients. Consequently these are complimentary approaches which will yield differing results when compared. The poorer angular resolution of the LIMBO maps makes it impossible to identify all the sources of emission in the Galatic Plane whilst having more success in the extragalactic sky.

3.8.1 Comparing the BATSE and INTEGRAL views of the sky

The current observations and survey activities of the INTEGRAL γ-ray mission are also an obvious candidate for cross-comparison of results. For a detailed discussion of the INTEGRAL/IBIS survey see Chapter 4. The 2^{nd} IBIS/ISGRI Survey Catalogue is constructed from observations taken over the first two years of the INTEGRAL mission. The 20–100 keV mosaic used in the production of the IBIS survey catalogue was degraded to the BATSE angular resolution and the fluxes for the corresponding BATSE sources were extracted. The fluxes taken from the INTEGRAL map were calibrated to the observed flux of the Crab Nebula. Neglecting source variability, if the BATSE All-Sky Survey source fluxes are reasonably accurate we may expect there to be some level of linear correlation between the fluxes observed by BATSE and those observed by INTEGRAL.

The plot demonstrating the correlation between the BATSE and INTEGRAL fluxes is shown in Fig. 3.13. The source population listed in Table 3.1 is indicated by the red circles. A broad correlation can be seen indicating that the BATSE flux measurements are reasonable for the sources we believe we have detected. Also plotted are a number of the excesses which were rejected in the construction of the BATSE All-Sky Survey (BASS) catalogue (excesses > 20 mCrab are shown as blue squares, excesses < 20 mCrab are represented by black crosses). The bunching, and random scatter below ~20 mCrab is an indicator of excesses being found in the noise distribution of the BATSE image which do not have valid counterpart in the INTEGRAL image.

3.8.2 An alternative method of source cleaning

Prior to the implementation of the CLEAN algorithm another method for removing artefacts from LIMBO images was investigated. This was achieved by making two passes of the likelihood calculation. By first calculating the response function for a particular source position, the effect on the entire image of a source at this position can be removed by adding the inverse of this response to the likelihood calculation. This method is very effective at removing sources, however, the iterative removal of sources by this method is not practical not least because it requires repeated imaging calculations each time a source is removed.

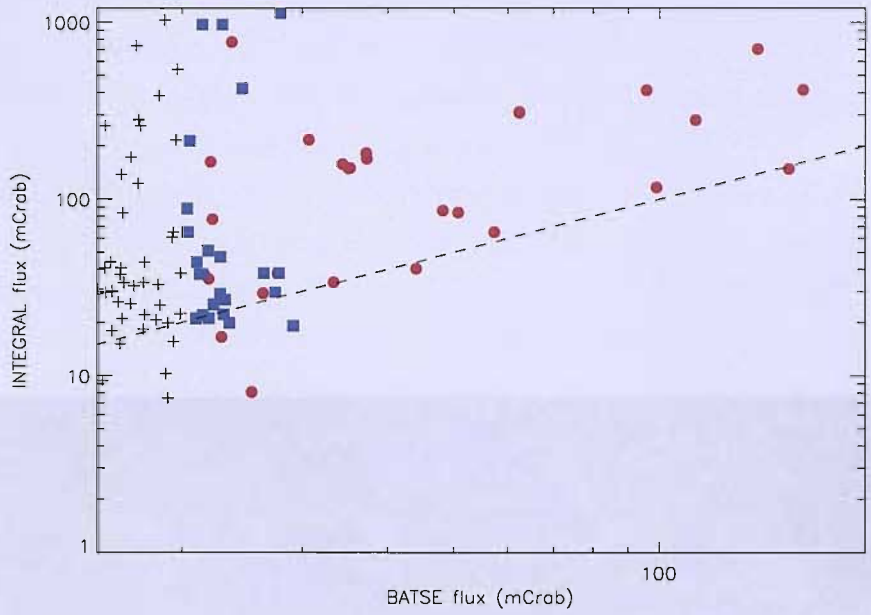

Figure 3.13: The correlation between source fluxes in the BATSE map and INTEGRAL mosaic degraded to the BATSE resolution.

However, this method can be applied to see if inaccuracies in the PSF generated for cleaning the bright galactic sources added additional systematics to the maps. To achieve this the 1^{st} IBIS/ISGRI Survey Catalogue was used as a list of all the galactic γ-ray sources above 30 mCrab. Approximately five hundred days, from TJD 09448 – 09936, was re-imaged in energy channel 2 with the alternative cleaning algorithm removing all of the sources selected from the INTEGRAL catalogue. The final image is shown in Fig. 3.14. The final image shows little evidence of sources left in the image, especially not at high galactic latitudes where no sources were assumed to exist. There is some evidence to suggest that some sources remain in the galactic centre, however, the 2° resolution still makes it all but impossible to identify the specific sources repsonsible in this highly crowded region. The pixel distribution of the map shows the highly negative distribution previously observed.

3.9 Conclusion

The Southampton LIMBO technique combined with the CLEAN algorithm has provided a new and novel investigation of the BATSE data set. This has resulted in all-sky images of the γ-ray sky in the 30 – 160 keV energy band. These are the first all-sky images of

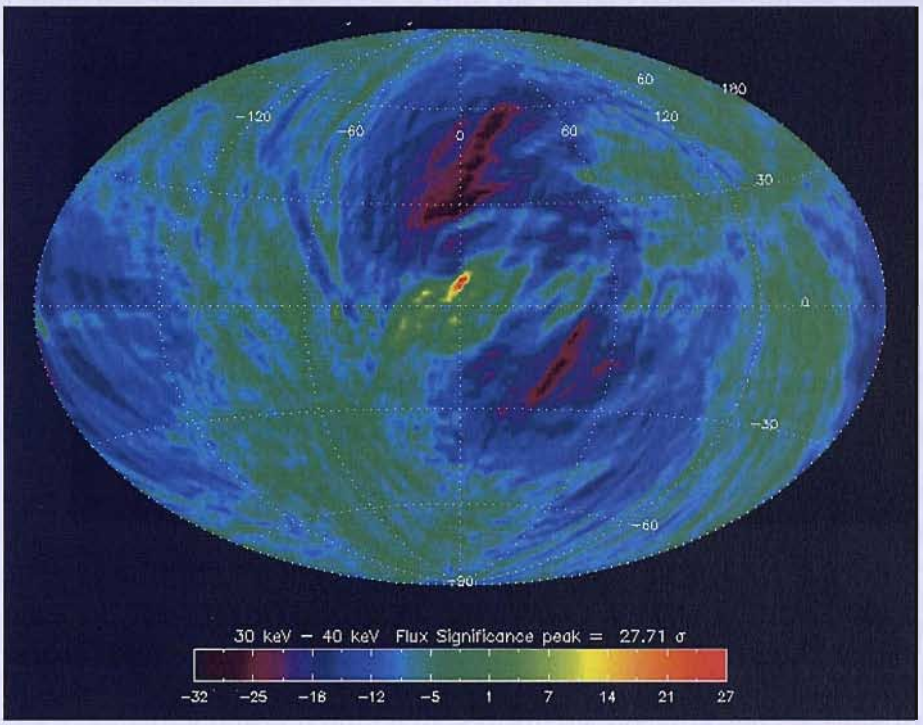

Figure 3.14: The LIMBO map of 30–40 keV over ~500days (TJD 09448–09936) by automatically removing all sources observed above 30 mCrab in the 1st IBIS/ISGRI Survey Catalogue.

this energy regime to be produced since the HEAO-1 A4 experiment in the late 1970's. In addition to the imaging techniques an accurate background model for the BATSE experiment (BAMM; Shaw et al. (2003)) had to be produced in order to remove the large temporal fluctuations in the detector background count rates.

The all-sky map is based on 9 years of data and shows the location of approximately 40 known γ-ray sources, including several extragalactic objects. In all cases, emission from within one pixel has been attributed to a source from the ISDC high energy catalogue. However, whether all the detections from the LIMBO map are real sources of γ-ray emission, that have been associated with the correct object from the catalogue, can not be determined at present.

It is clear that the images presented here suffer from the coarse 2° resolution of the imaging grid, which makes identification of sources in crowded regions, such as the Galactic Centre, very difficult. However, the bigger limiting factor is the identification of a systematically negative background resulting from fluctuations of the background count rate. These fluctuations are attributed to the decay of satellite activity associated with passage through the South Atlantic Anomaly (SAA).

Both of these limitations can be conceivably overcome. The negative noise present in the image can be removed by fitting the decay observed as a result of the SAA and then flat-fielding this effect out of the data set prior to running the LIMBO code. This should remove a large quantity of the systematic attributable to the SAA and allow for the performance of the imaging to come closer to its statistical detection limit. The problem of imaging crowded regions can be improved significantly by simply increasing the resolution of the imaging grid toward the theoretical imaging limit of 0.5°. This however increases the computing power required to perform the imaging and cleaning by a factor of 16. Although the available processing power has increased since the beginning of this project it has not increased by this quantity and hence larger computing resources would be required to re-image the entire BATSE data set in a reasonable space of time.

The theoretical imaging limit of 0.5° is attributable to the finite time taken for a γ-ray source to be occulted by the Earth's atmosphere. Even, at this limit the PSF generated by the CLEAN algorithm is therefore an approximation of the true source PSF. The scale of the PSF across the sky is such that errors in the PSF calculation for bright galactic sources can impact upon the sensitivity in the detection of extragalactic sources away from the plane. The significance of this effect is unknown as the negative pixel distribution is a more dominant effect identifiable in the maps generated to date. Only through further analysis and investigation after the dominant effect has been removed can the effect of slight errors in the source PSF be quantified.

Chapter 4

The IBIS/ISGRI Soft Gamma-Ray Survey

4.1 Introduction

The INTErnational Gamma-Ray Astrophysics Laboratory (INTEGRAL) was successfully launched in October 2002 on board a Russian Proton rocket. This ESA observatory is designed to observe the celestial γ-ray sky in the energy range 15 keV – 10 MeV using the on-board γ-ray spectroscopy and imaging instruments, SPI and IBIS respectively (Winkler et al., 2003). As a return to the individual scientists and collaborations responsible for the development and running of INTEGRAL, a fraction of the total observing time is used for Core Programme observations. The remaining fraction of the observing time is available to the scientific community through the General Programme.

INTEGRAL is the most advanced imaging and spectroscopic γ-ray astronomy mission launched to date. The 12' angular resolution and the sensitivity of the on-board imager, IBIS, allows the detection and identification of a large number of γ-ray sources. The capability to detect a 1 $M_{\odot}$ neutron star emitting at the Eddington limit from 10 kpc in a ksec allows for a meaningful survey of γ-ray sources to be performed. The only all-sky hard X-ray survey to date was performed by the HEAO 1 A4 experiment. This catalogue contained a list of 72 sources visible down to 14 mCrab in the 12–180 keV energy band (Levine et al., 1984). The SIGMA telescope on-board the GRANAT mission identified 15 sources in the Galactic Centre down to a sensitivity of ~26 mCrab (Vargas et al., 1997). In contrast IBIS has a 3σ sensitivity of 1mCrab at 100 keV in a 1 Msec exposure (Goldwurm et al., 2003).

The role of the IBIS survey team is to reduce the available Core Programme and Gen-

eral Programme data sets and analyse them to produce an accurate, sensitive catalogue of the γ-ray sources visible by INTEGRAL/IBIS. Prompt and regular data releases are made by the survey team providing the best source location and spectral responses available at each release. It is the goal of the survey team to continually refine and improve the data analysis methods until a complete survey of the soft γ-ray sky visible by INTEGRAL is complete. A secondary goal of the survey team is the identification and understanding of any new sources identified in the course of completing the survey.

4.2 INTEGRAL observing programme

The Core Programme consists of 35% of the observing time (9.3×10^6s) in year 1, decreasing to 30% in year 2 (8.0×10^6s) and then to 25% in year 3 and onwards (6.7×10^6s) (Winkler et al., 2001). The Core Programme has three main science components: a deep exposure of the Galactic Centre; regular scans of the Galactic Plane; pointed observations. The remaining time in each year is awarded as the General Programme to the scientific community. Guest Observer (GO) proposals are selected based upon scientific merit by the Time Allocation committee (TAC) (Winkler et al., 2003). The deadline for the first call (AO-1) for proposals was 16 February 2001. AO-1 observations ran for 12 months from January 2003. AO-2 observations ran for 12 months from January 2004.

4.2.1 The Galactic Centre Deep Exposure (GCDE)

During the first year of operations INTEGRAL spent ~4.3×10^6s performing observations of the Galactic Centre region. The Galactic Centre was observed twice a year to build up this level of exposure. Earlier space missions, such as BeppoSAX and GRANAT / SIGMA, have previously identified a large population of high energy emitters in this region (Ubertini et al., 1997; Vargas et al., 1997). The high sensitivity, 12′ angular resolution and large field of view of the IBIS instrument allows the detection and identification of this source population. This allows for a sensitive, accurate survey of the Galactic Centre providing information on the spectral and temporal behaviour of a large selection of sources. Additionally, this allows for a study of the diffuse continuum hard X-ray/γ-ray emission observed from the Galactic Plane.

4.2.2 The Galactic Plane Scans (GPS)

The Galactic Plane is scanned regularly, on an approximately weekly basis. During the first year of operations INTEGRAL spent ~2.3×10^6s performing observations of the

Galactic Centre region (Winkler et al., 2001). The principal reason behind these observations is the detection and localisation of transient sources. These sources may then be potentially observed as targets of opportunity. Additionally, these regular scans allow for exposure to be built up gradually across the entire galactic plane and hence is a valuable resource for surveying the γ-ray galactic source population in general.

4.2.3 Pointed observations

The remaining ~2.7×10^6s of Core Programme observations in the first year was devoted to the observation of transient events, from both known and unknown sources. In the first year a survey of the Vela region was also included in the pointed observations.

4.2.4 General Programme

General Programme observations become publicly available twelve months after the data has been issued to the guest observer. The combination of all of the Core Programme data sets, in addition to Guest Observer observations as they become public, provides a large and powerful data set which will eventually cover the entire sky. This allows for a detailed and sensitive survey of the entire γ-ray sky. The sky locations of the GO observations for the first and second year of observations, as well as the fields included in the GPS and GCDE are shown in Fig. 4.1 and Fig. 4.2.

4.3 The challenges of constructing the survey

The generation and production of the IBIS survey is a challenging task which inevitably is solved by breaking it down into several constituent components. The scale of the project is such that many people are involved in the different individual task components. The Responsible Scientist for the IBIS survey, Dr. A. J. Bird oversees and manages the entire project. The individual components include:

- Reduction of data using the standard OSA software. There are many different parameters involved in the generation of images from IBIS observations. The effects and optimisations of these parameters require investigation. The Author was responsible for exploring the effects of the different search modes used to fit and remove ghost sources from the images. The Author worked with Dr. A. J. Bird on the construction of an input catalogue for the image processing of the second survey.

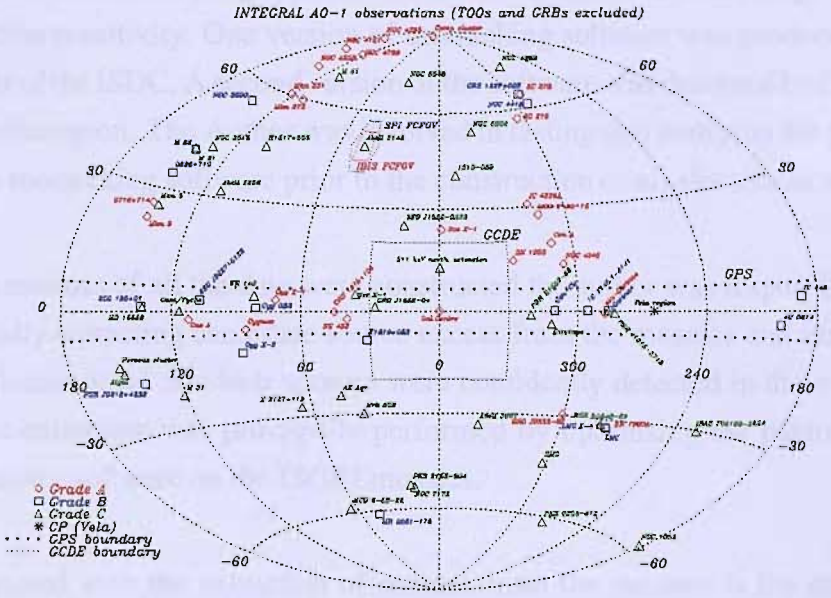

Figure 4.1: The location of the approved AO-1 Guest Observer observations and their associated grade. Additionally the regions designating the Galactic Plane Scans and the Galactic Centre Deep Exposure are displayed. Targets of opportunity (TOOs) and GRBs are not shown.

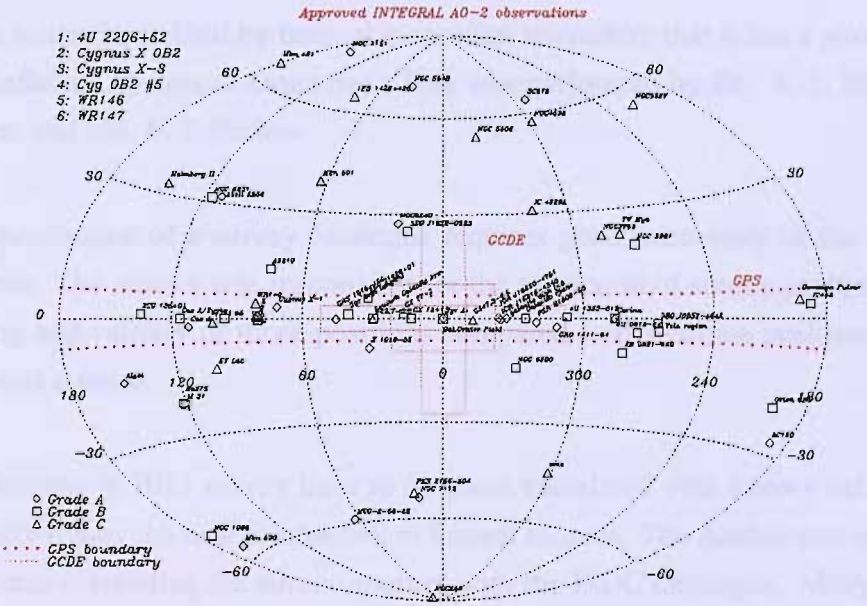

Figure 4.2: The location of the approved AO-2 Guest Observer observations and their associated grade. Additionally the regions designating the Galactic Plane Scans and the Galactic Centre Deep Exposure are displayed. Targets of opportunity (TOOs) and GRBs are not shown.

- The individual IBIS images need to be summed over time and energy to maximise detection sensitivity. One version of mosaicking software was produced by Dr. R. Walter of the ISDC. A second version of the software was designed by Dr. A. J. Bird at Southampton. The Author was involved in testing and verifying the performance of the mosaicking software prior to the construction of all-sky mosaics.

- Once mosaics of all the data were constructed the author was responsible for automatically extracting candidate source excess from the mosaics and identifying the significance level at which sources were confidently detected in the mosaics. The source extraction was principally performed by optimising the parameters of the SExtractor software on the ISGRI mosaics.

- Associated with the extraction of sources from the mosaics is the deblending of sources in confused regions. The Author was responsible for the optimisation of SExtractor to isolate sources in confused regions. Ms. E. J. Barlow was responsible for using the inherent variability of the Galactic Centre sources to resolve individual source components.

- Each source is verified by manual inspection to confirm that it has a good PSF and is unaffected by source structures. This was performed by Dr. A. J. Bird, Dr. L. Moran and Ms. E. J. Barlow.

- The production of a survey catalogue requires good astrometry of the individual sources. The Author was responsible for the extraction of source positions and the testing and validity of those positions compared to the known positions of astrophysical sources.

- All sources in IBIS survey have to be cross correlated with known catalogues to identify if they are new discoveries or known sources. The Author was responsible for cross-correlating the survey sources with the ISDC catalogue. Many members of the IBIS survey team were responsible for cross correlating with wider catalogues.

All of these individual challenges must be overcome in order to compile an accurate unbiased survey of the γ-ray sky as observed by INTEGRAL.

4.4 The 1st IBIS/ISGRI Survey Catalogue

The first IBIS/ISGRI soft gamma-ray Galactic Plane survey catalogue was the first data release of results from the IBIS Galactic Plane survey based upon the Core Programme (CP) observations made during the first year of INTEGRAL observations. As GO observations are private up to one year after being performed the 1st IBIS/ISGRI Survey Catalogue was restricted to CP observations only. The GPS scans are performed approximately once every twelve days. The 1st year GCDE observations are the dominant source of data for the survey, hence the survey is heavily biased toward the detection of sources in the Galactic Centre.

Observations are broken down into 'Science Windows' (ScWs), these are exposures of typically 2150 seconds and cover ~900 degrees^2 (Bird et al., 2004). Hence the large fov and sensitivity of the IBIS instrument to easily detect, resolve and locate persistent and transient sources (Ubertini et al., 2003). Images generated by IBIS have an angular resolution of ~12′. The 1st IBIS/ISGRI Survey Catalogueuses only data from the ISGRI detector of IBIS and gives source fluxes integrated over two energy bands, 20–40 keV and 40–100 keV. The limiting sensitivity in the central radian of the Galaxy is ~1 mCrab.

4.4.1 Observations

The data set comprises observations made within the Core Programme between 28 February 2003 and 10 October 2003, revolutions 46 and 120 respectively. This consists of 2529 individual science window observations. Observations prior to revolution 46 were part of the Performance and Verification (PV) phase of the mission when many of the instrument configurations were adjusted and hence were not included within the survey data set.

4.4.2 Data reduction

The data was processed using the Offline Standard Analysis (OSA) software version 3 provided by the INTEGRAL Science Data Centre (ISDC) (Courvoisier, et al., 2003). Images were produced for each observation in 10 narrow energy bands: 15–20; 20–30; 30–40; 40–60; 60–80; 80–100; 100-150; 150–300; 300–500; 500–1000 keV. This was done to allow flexible data analysis.

One of the key difficulties in reducing data from IBIS is the production of source ghosts in images. As the coded aperture mask pattern is symmetric, up to eight source ghosts can be produced by a source in the centre of the field of view. These ghosts are distributed at the corners and mid-points of a square with sides of length ~21° centred on the actual

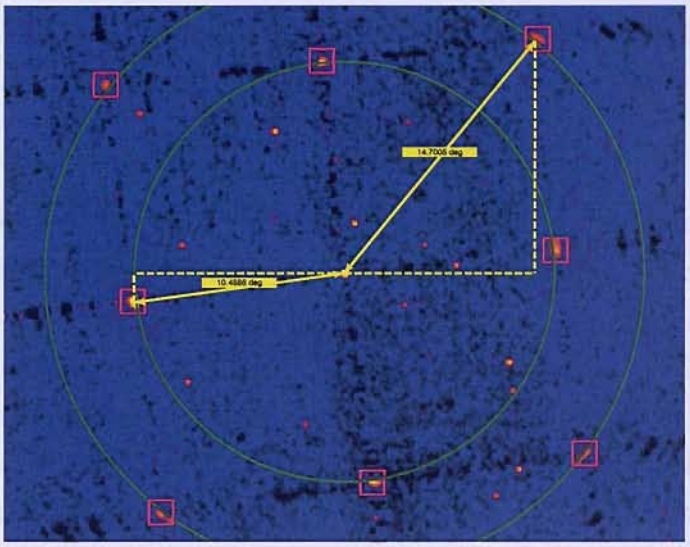

Figure 4.3: A mosaic of 29 Science Windows from revolution 60 processed with OSA using search mode 1. The catalogue used to fit to sources has been edited to remove the source IGR J17464-3213, which is expected to be in this field. The mosaic clearly shows the uncleaned ghost sources attributable to IGR J17464-3213. The 8 ghosts are distributed symmetrically around IGR J17464-3213 with 4 lying ~10.5° away and the remaining 4 lying ~14.7° away.

source. An example of source ghosts is shown in Fig. 4.3, eight ghosts surrounding IGR J17464-3213 are clearly visible. To prevent this a catalogue of sources likely to be visible is provided to the OSA software to allow it to clean out ghost sources. It is also possible to set the software to detect new sources and clean the associated ghosts. However, the software occasionally fails and either leaves in ghosts or may keep a ghost and remove the true source. The OSA software has three search modes:

- Search mode 1: This mode only searches for sources supplied in the input source catalogue and ignores any other source detections. Hence, any unlisted sources will show numerous ghost sources in the output image.

- Search mode 2: This mode searches for an optional number of sources within the image without any knowledge of the catalogue. This mode will detect and attempt to clean new sources however, it has to rely on its own source fit positions even for bright, well known sources. This often results in badly cleaned images.

- Search mode 3: This mode searches for all of the input catalogue sources, plus it will search for an optional number of new sources as well. This typically, produces

the cleanest images, it is however the most CPU intensive and takes the longest to generate images.

Prior to the launch of INTEGRAL, a catalogue of high-energy sources which would potentially be visible to the on-board instruments was compiled. The ISDC catalogue contains sources which have been seen to be brighter than ~1 mCrab at energies above 3 keV. The initial catalogue contained 1122 sources (Ebisawa, et al., 2003). The ISDC catalogue includes HMXBs taken from Liu et al. (2000), LMXBs from Liu et al. (2001), Gamma-ray sources from Macomb & Gehrels (1999), the 4th Uhuru catalogue of Forman et al. (1978) and the HEAO1 A4 catalogue of Levine et al. (1984). As new sources are detected by INTEGRAL they are added to the ISDC catalogue.

The survey data was initially processed using the ISDC catalogue however, a source catalogue was built iteratively as the data was processed until it finally included all of the sources visible. Source ghosts were cleaned out of every image even when a source was not independently significant in an individual observation.

4.4.3 Mosaicking

The images generated from the individual observations were combined together to produce all-sky mosaics. The mosaics were produced using proprietary software written by Dr. Roland Walter at the ISDC. The all-sky mosaics are constructed using an Aitoff projection and have a pixel size of 2.4′× 2.4′ at the centre of the mosaic. The mosaics are centred on the Galactic Centre. By summing together all of the observations the significance of detection of persistent sources is emphasised.

In the construction of the mosaics the number of counts in each pixel is weighted according to the variance of the signal in the associated pixel. Sources which are observed outside of the fully coded field of view are seen to be less bright than those in the fully coded field of view due to the off-axis response of the telescope. To correct for this when generating the mosaics the total number of counts in each pixel is divided by the overall effective exposure of each pixel. This produces an accurate count rate image of the sky. Significance, variance and exposure maps are also produced by the software.

The production of images in the aforementioned narrow energy bands allows multiple energy band mosaics to be easily produced. Examining the statistical properties of the mosaics of different energy bands allows the for optimisation of source detection.

4.4.4 Source Extraction

Two energy bands were used to detect excesses in the final all-sky mosaics. The 30–50 keV energy band was used as the principal band for detection as it was found to be the 'cleanest', having the best understood background with minimal detector systematics. Hence, many objects in this band have good signal-to-noise ratios and there is minimal structure to confuse with 'real' sources.

However, a number of well known sources were not apparent in this energy band due to the soft nature of their intrinsic spectrum. As a result it was necessary to additionally search the 20–40 keV bands for sources with these 'soft spectrum' characteristics. Additionally, due to the uneven level of exposure across the sky, source excesses were searched for in the significance mosaics rather than the flux maps. All excesses, down to a pre-defined cut-off level, were considered as potential sources. Two methods were used to identify excesses in the maps.

4.4.4.1 Identifying detection cut-off significance

The complex nature of the background in the mosaics complicates the detection of sources as simple Poisson statistics no longer apply. Consequently, a high significance does not necessarily correspond to a detection in the case of there being high levels of local structure. Hence, in order to identify an excess as a source, it is necessary to identify the significance level at which the source population dominates over the noise distribution. To this end a form of 'LogN - LogS' is produced. The number of excesses above a certain significance is plotted against significance. An example of one of these plots for the 30–50 keV map is shown in Fig. 4.4.

The distribution of number of sources as a function of significance is fit by a Gaussian and power law function. The power law fits to the true source population and is clear at the higher significance levels. The Gaussian fits to the noise induced by both statistical and systematic effects. From the parameters of the fit it is possible to calculate the significance at which 90% of the excesses come from the underlying source population and 10% from the noise distribution. This level is 6.6σ in the 20–40 keV band map and 5.6σ in the 30–50 keV band map. The lower significance level in the 30–50 keV map is an indication of the lower level of image structure.

An alternative method of investigating the cut-off significance is to look at the pixel histogram of the entire map. This produces a large Gaussian noise distribution around zero with a power-law tail at positive significances attributable to the source population. The advantage of this investigation is that the Gaussian can be easily fitted and gives some

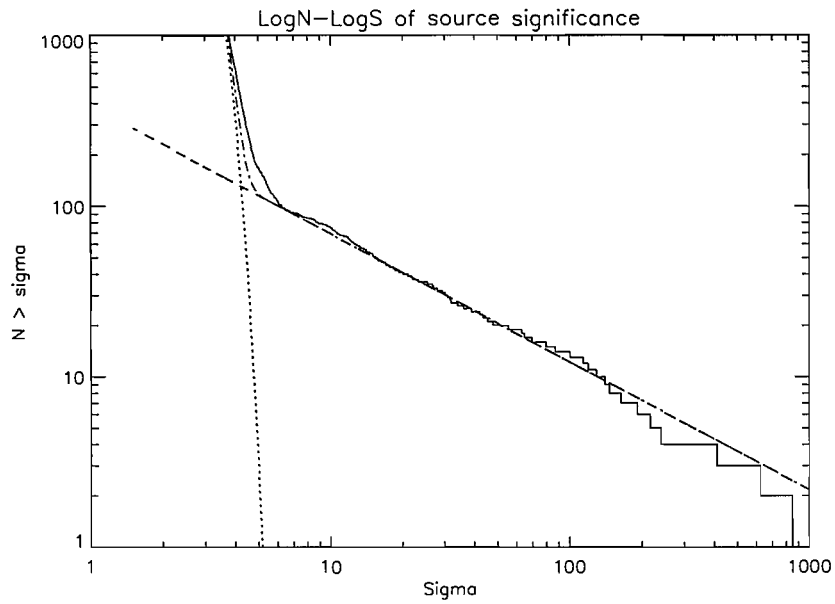

Figure 4.4: Distribution of the number of excesses as a function of significance in the 30–50 keV map. The dotted and dashed line represents the fitted model; the dashed line represents the extrapolated power law component of the fit; the dotted line represents the Gaussian component of the fit.

statistical information regarding the quality of the maps. However, as the source PSF has a finite size it covers a number of pixels and consequently contributes to the histogram multiple times. This has the effect of changing the power-law at the low significance levels where the noise becomes important. This makes it very difficult to identify the point at which the noise becomes dominant over the source significance.

Ideally, a method which removes the contribution of sources prior to the measurement of the background would produce a much more accurate estimation of the statistical properties of the background, allowing the cut-off significance to be determined. Another method would be to recalculate the significance of individual sources based upon the variations in the map in the surrounding vicinity. Both methods should be explored in future exploitations of the IBIS survey data set to allow for more automatic, confident determination of excesses as actual sources of γ-ray emission.

4.4.4.2 Peak find

Peak find is a search algorithm written at the University of Southampton. The algorithm takes a minimum threshold and searches the map for a triangular point spread function whose peak lies above the threshold. This simple algorithm easily finds the brightest

sources, however, the simple deblending routine cannot cope with overly crowded regions such as the Galactic Centre and high levels of systematic image structure. The source positions returned by Peak Find correspond to the centre of the brightest pixel in the source PSF.

4.4.4.3 SExtractor

SExtractor (Source Extractor) is proprietary software designed to build catalogues of objects from an astronomical image (Bertin & Arnouts, 1996). The power of SExtractor lies in its ability to handle large images, to deblend overlapping objects in crowded fields and in real-time filtering of images to improve detectability. SExtractor version 2.2.2 was used in the analysis.

The software functions by making two passes across the map. In the first pass a model of the background is estimated and the statistical properties of the map are calculated. In the second pass the map is background subtracted, filtered and thresholded. The list of sources is then automatically deblended and astrometry and flux measurements taken before writing out to the final catalogue.

Detection is obviously limited at the faintest flux levels by background noise. The spatial power spectrum of the noise and the source signal can be significantly different and hence, detection can be optimised by linearly filtering the data set. In the case of the INTEGRAL/IBIS mosaics we expect the sources to be point-like and hence have the same underlying point spread function (PSF). This simplifies the matter in selecting an appropriate filter. However, the matter is complicated by the AITOFF projection of the mosaics distorting the PSF of sources located far from the Galactic Centre. The observations used in the 1^{st} IBIS/ISGRI Survey Catalogue are significantly constrained to the Galactic Plane and hence this distortion is minimal and the PSF is not distorted sufficiently to remove the advantages gained by filtering. An additional problem, which may be encountered in crowded fields is the convolution of the filter may decrease the contrast between two objects. This is the case when using a low-pass filter but it may be overcome using the inbuilt deblending algorithm. In extremely crowded fields it is advisable to use a bandpass filter to overcome this problem.

To enhance the detectability in the IBIS/ISGRI mosaics a filter was constructed which matched the source PSF in the mosaics. To this end an isolated, undistorted bright source near the centre of the map was chosen as the prototypical PSF and hence duplicated in the filter. The filter corresponded to a 5×5 grid centred on Gaussian PSF with 5 pixel FWHM. A three dimensional rendering of this filter can be seen in Fig. 4.5.

Although filtering improves the detectability of sources it fundamentally changes the

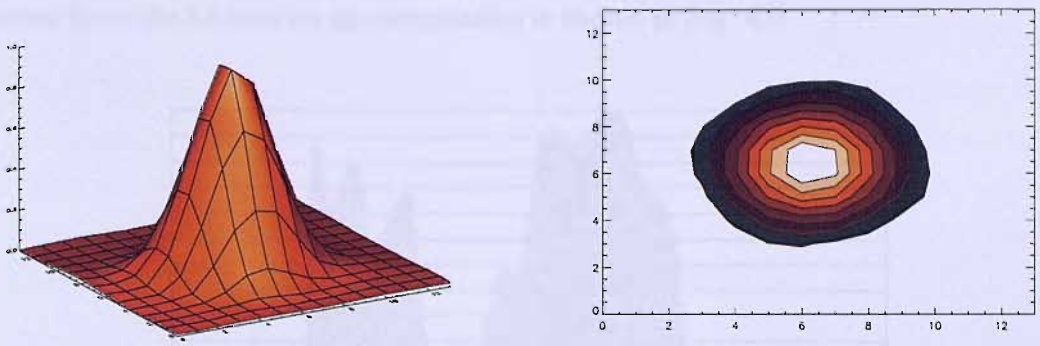

Figure 4.5: IBIS/ISGRI PSF used to filter the mosaics by SExtractor. This PSF represents a bright undistorted source close to the centre of the map. The PSF is normalised by the peak value. *Left panel*: 3D rendering of the normalised PSF. *Right panel*: Contour plot of the normalised PSF.

properties of the map. It distorts the shape of the sources as well as correlating the noise. As a result filtering is only employed in the detection of sources. Beyond the detection and location of sources the filtered data is not used in the extraction of source properties, principally the flux (or significance in the case of the ISGRI mosaics). This information is taken from the original un-filtered data set.

Segmentation is the actual action of separating sources from the sky background. This is achieved by identifying a group of pixels above the designated threshold (see Section 4.4.4.1). SExtractor operates with two key parameters to govern this process. The first DETECT_THRESH, indicates the actual threshold above the local background which the pixel group has to be above. The second is DETECT_MINAREA, which dictates the minimum number of adjacent pixels required to be above the threshold. In the case of the latter parameter we require only one pixel to be above the threshold as we are attempting to extract out sources to the lowest detection threshold possible. It should be noted that the IBIS mosaics are correlation images and hence no aperture photometry should be used, the significance of a detection is the value of the brightest pixel of the PSF, this is also true in the flux and variance maps. Hence, we are only ever concerned with the value of the fitted peak of any individual source PSF.

Deblending occurs whenever a source has been identified and extracted from the mosaic. SExtractor attempts to split the source into individual overlapping components. A multi-thresholding approach is applied in which the set of associated pixels are re-thresholded at multiple levels between the DETECT_THRESH value and the peak value of the group. If saddle points are found then the algorithm will separate out the individual sources based upon the constructed tree-structure. The schematic diagram illustrating this

function from the SExtractor documentation is shown in Fig. 4.6.

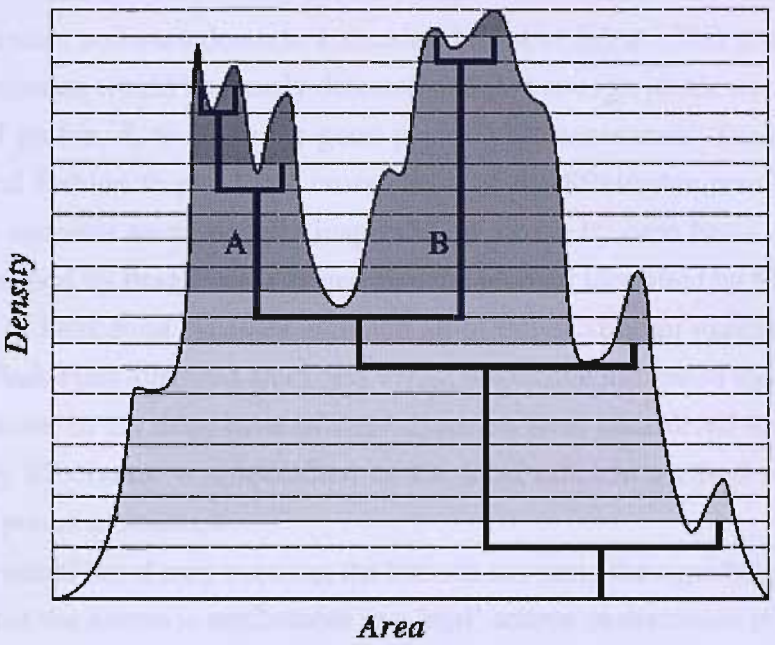

Figure 4.6: A schematic diagram of the method used to deblend a composite object. The area profile of the object (smooth curve) can be described in a tree-structured way (thick lines). Taken from the SExtractor manual.

SExtractor is capable of producing a number of different types of position for the sources it detects. Positions in both image coordinates (pixel x & y) and in world coordinates (RA & Dec) are extracted. For the measurement of positions SExtractor examines the spatial distribution S of connected pixels above the pre-defined detection threshold. The centroid coordinates, X and Y, are used to identify the position of peak source emission. This is perfectly adequate in the case of point source emission. These coordinates are given by:

$$X = \overline{x} = \frac{\sum_{i \in S} I_i x_i}{\sum_{i \in S} I_i} \tag{4.1}$$

$$Y = \overline{y} = \frac{\sum_{i \in S} I_i y_i}{\sum_{i \in S} I_i} \tag{4.2}$$

SExtractor can also provide the coordinates of the centre of the pixel which corresponds to the brightest component of the source profile, this is identical to the measurement returned by Peak Find.

4.4.4.4 Compiling the list of excesses

The 30–50 keV and 20–40 keV significance maps were both searched independently using the SExtractor software down to a threshold limit of 3.5 σ. This guaranteed that all significant excesses would be clearly detected and that enough pixels would be attributed to the spatial profile, S, to allow for good position measurements. Peak Find was used in an identical fashion to provide a cross-check of the SExtractor results. In instances of doubt the excesses were visually inspected on a case by case basis. The number of excesses identified by Peak Find is larger than the number identified by SExtractor. However, the list of Peak Find excesses included all of the SExtractor excesses. In the cases where only Peak Find identifed an excess visual inspection attributed the excess to either noise or structure in the map; none of these excesses were considered to be real sources. Consequently SExtractor was identified as the most efficient method of generating an initial list of potential sources.

From this initial list of map excesses the list was cut using the significance threshold for confidence that the excess is attributable to a 'real' source as discussed in section 4.4.4.1. Hence, the 20–40 keV and 30–50 keV source lists were used to excesses brighter than 7σ and 6σ respectively. These two lists were amalgamated into a single list of excesses. The use of both of these bands for source detection does not bias the source selection procedure as a result of the bands overlapping because no requirement is made for excesses to be detected in both bands. Each band is searched independently and then amalgamated into a single list. Each excess was visually inspected and those identified as resulting from image structures around some of the bright sources, principally the Crab and Sco X-1, were removed by hand. This left 123 excesses in the final source list.

4.4.5 Sources of the 1st IBIS/ISGRI Survey Catalogue

From the centroid positions of the sources derived from the significance mosaics the mean source fluxes and their associated errors were extracted from the 20–40 keV and 40–100 keV flux and variance mosaics. The flux errors only account for the statistical uncertainty upon the flux measurements and take no account of systematics. Hence, if the flux is less than 6σ in an energy band the 2σ upper limit is quoted. The off-axis response of IBIS/ISGRI has not been fully calibrated, however, this should result in a systematic uncertainty of no greater than 10% for a source with an exposure of a few tens of ksec. The final catalogue of 123 sources is shown in Appendix A. Images extracted from the 30–50 keV mosaic are shown in Appendix B. The first year of survey data accumulation has resulted in a catalogue with a limiting sensitivity of ~1 mCrab in the central radian of

the galaxy.

The 1st IBIS/ISGRI Survey Catalogue is dominated primarily by the galactic binary population as would be expected. Within the binary population we have detected members of all different classes including 23 HMXBs and 53 LMXBs. Additionally, a number of pulsars with and without supernova remnants as well as a number of black hole candidates. The concentration of exposure along the galactic plane minimises the likelihood of detecting extragalactic sources, none the less the 1st IBIS/ISGRI Survey Catalogue includes 5 Active Galactic Nuclei. Of the 123 sources detected in the first year of survey data 28 of them, ~23%, are not associated with any one type of object. A number of the unidentified sources have ROSAT All-Sky Survey counterparts. A detailed cross-correlation of the 1st IBIS/ISGRI Survey Catalogue and the ROSAT All-Sky Bright Source catalogue by Stephen et al. (2005a) indicated that 75 of the IBIS/ISGRI sources had ROSAT counterparts of which 10 of the sources were of an unknown nature. Using the ROSAT error boxes Stephen et al. (2005a) provide tentative identifications of 8 of these 10 sources.

4.5 Position errors of the 1st IBIS/ISGRI catalogue

As discussed earlier, two independent source search algorithms were used to identify sources in the survey significance mosaic; SExtractor and Peak Find. The two methods both detect the same strong sources however, at lower significances they begin to behave differently. Of the 123 sources detected in the 1st IBIS/ISGRI galactic plane survey, 69 of the sources have well defined positions obtained in different wavebands according to the SIMBAD/NED database. Measuring the spherical distance between the measured positions and those according to SIMBAD gives a measurement of the source position errors. The mean location accuracy of the two methods are 0.8' and 1.1' for the centroid and brightest pixel positions respectively. The pixels in the survey mosaic are 2.4' in size. From a statistical standpoint the mean error using positions based upon the location of the brightest pixel will be half a pixel, 1.2'. As this is what is observed in the brightest pixel measurements it is indicative that this is the dominant systematic effect in this method of source location.

As a result, the centroid positions were used in the IBIS/ISGRI survey whenever available. No correlation between the source sky location and the associated error was found. This indicates that distortion of the source PSF due to the map projection of the survey mosaic does not introduce a noticeable systematic error to the capability to locate the centroid of the source profile.

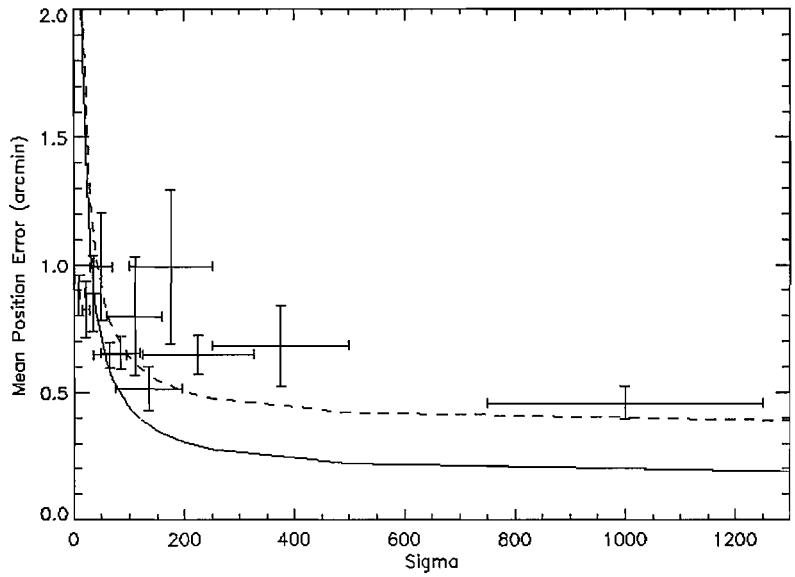

Figure 4.7: The mean source positional error of 69 sources from the 1st IBIS/ISGRI galactic plane survey catalogue (Bird et al., 2004). The solid line represents the PSLE measured by Gros et al. (2003). The broken line shows the PSLE function with a 0.2 arc min offset.

The IBIS/ISGRI point source location error (PSLE) is defined in Gros et al. (2003) as 3'-20" depending upon the significance of detection with 1' accuracy for S/N > 30. Averaging the position errors of survey sources of similar significance allowed the comparison of the centroid position error to the ideal instrument location accuracy and is seen in Figure 4.7. In making this comparison we are assuming that we have correctly identified our 69 detections as previously identified sources. However, those sources of 30σ or greater are highly unlikely to have been mis-identified. Additionally, when searching the SIMBAD/NED database for counterparts a positional uncertainty of 3' was used and the nearest known source was associated with the detection. As a result the mean location error of sources < 30σ in our sample will typically be less than 3' away from its known position.

In Figure 4.7 it can be seen that the mean measured position errors for sources > 30σ lie above the PSLE function but are compatible with the general trend with significance only offset by ~0.2' (portrayed by the broken line in Fig. 4.7). However, the PSLE function is derived from fields with few detected sources and for crowded fields may behave differently (Gros et al., 2003). This indicates that the process of generating a mosaic of the entire galactic plane and extracting all of the known source positions has added a systematic error of approximately ~0.2' to the source location accuracy of the system.

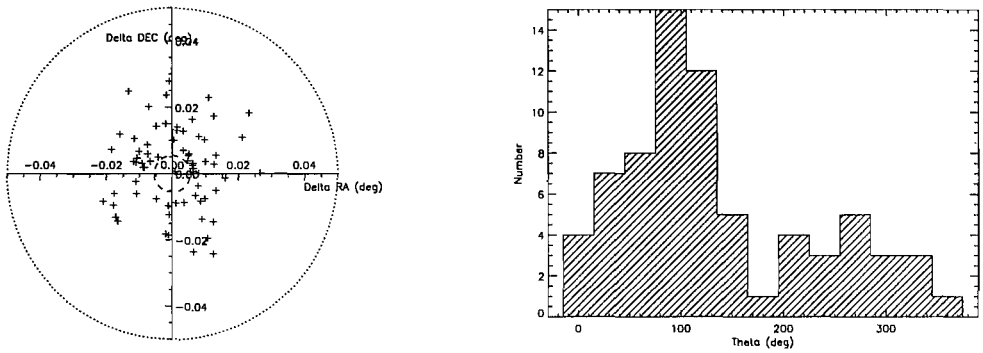

Figure 4.8: *Left panel*: The scatter in positional error, using the SExtractor positions, of 70 of the ISGRI sources. The two circles indicate the limits of the PSLE (3'-20"). *Right panel*: A histogram of the angular distribution of the left hand scatter plot.

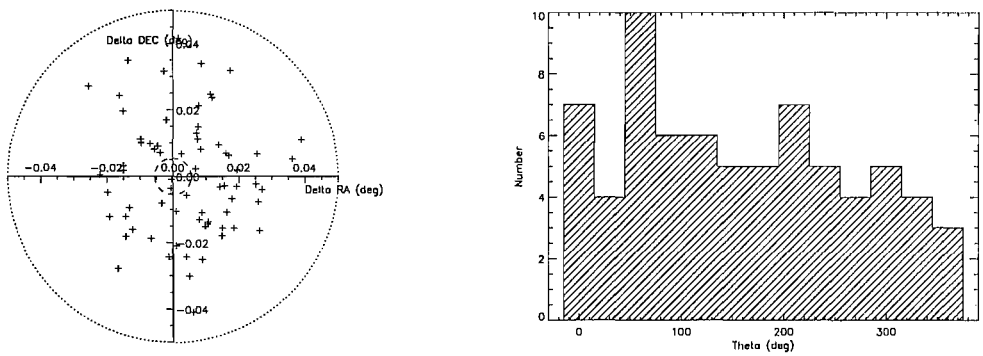

Figure 4.9: *Left panel*: The scatter in positional error, using the Peak Find positions, of 70 of the ISGRI sources. The two circles indicate the limits of the PSLE (3'-20"). *Right panel*: A histogram of the angular distribution of the left hand scatter plot.

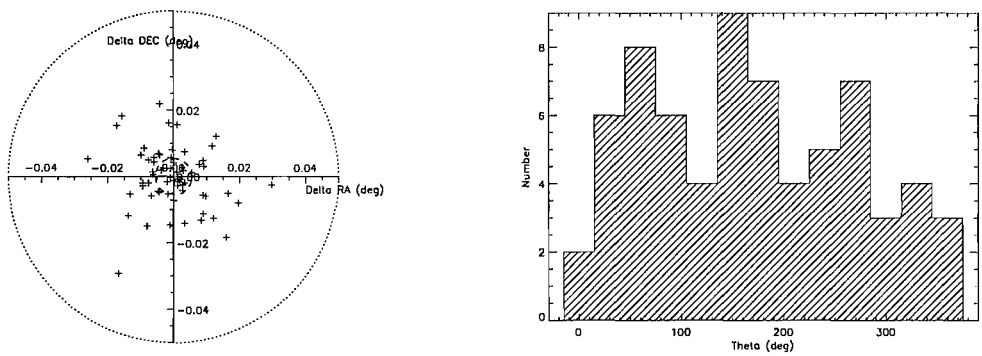

Figure 4.10: *Left panel*: The scatter in positional error of 70 of the ISGRI sources. The two circles indicate the limits of the PSLE (3'-20"). *Right panel*: A histogram of the angular distribution of the left hand scatter plot.

This systematic is made obvious when plotting the actual scatter of the source position errors and when looking at their distribution about zero. Figures 4.8 & 4.9 show the errors in RA and Dec of the two methods. Figure 4.9 shows the random scatter of positional errors is evenly distributed over all angles for the Peak Find algorithm. Figure 4.8 indicates that the source position errors from SExtractor are not uniformly distributed and that there is an over concentration of sources in the upper quadrants. The systematic was found to be due to an asymmetric PSF model used by SExtractor when detecting the sources. The sample PSF extracted from the IBIS/ISGRI mosaic to use as a filter by SExtractor was not perfectly centred on a pixel unsurprisingly. Hence, the filter was slightly asymmetric and introduced a systematic shift to all of the SExtractor derived positions. Using a symmetric modelled PSF removes the systematic. The new error distribution is indicated in Fig. 4.10 and shows no signs of an uneven distribution. An example of the position derived using the original PSF and the new modelled PSF is shown in Fig. 4.11. It is clear that the original PSF filter introduced a systematic which shifted the detection position away from the profile peak.

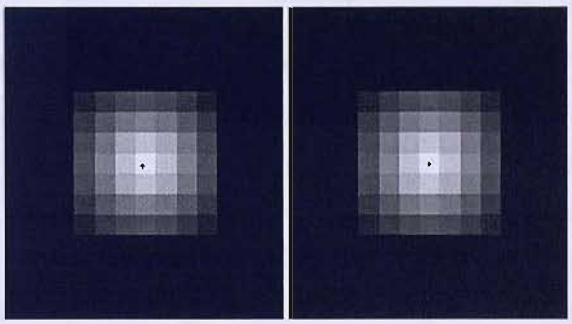

Figure 4.11: Extracting the positions of perfectly symmetric modelled sources. *Left panel*: SExtractor extracted position using the original asymmetric PSF filter. The cross indicates that the position is clearly off centre. *Right panel*: SExtractor extracted position using the new symmetric PSF filter.

Having corrected the positions of the survey sources for this systematic we achieve a mean positional error of 37" with a standard deviation of 27", based upon the bright 70 sources. This is well within the expected PSLE measured by Gros et al. (2003). However, the nature of this measurement neglects any measurements of the weakest sources which are dominated by the new, unclassified population. Hence, we assume that these sources have the typical weak source error of ~3'. It should be noted that the source positions published in the 1st IBIS/ISGRI Survey Catalogue and which are listed in Table A.1 are the original source positions which have not been corrected for systematic error.

4.5.1 The positions of the Russian survey

Simultaneously to the production of the 1st IBIS/ISGRI Survey Catalogue Revnivtsev et al. (2004) released a catalogue of INTEGRAL sources detected in the Galactic Centre region from deep Guest Observer observations. Revnivtsev et al. (2004) primarily use their own software in the reduction and analysis of IBIS data as opposed to the standard OSA software used by the IBIS survey team. For those sources detected by Revnivtsev et al. (2004) for which there are well known positions from other wave bands the same analysis was performed as described above. The positions were seen to have a mean positional error of 1' with a standard deviation of 50". This implies that the IBIS survey is achieving much better source positions than the methods employed by Revnivtsev et al. (2004), however due to the much smaller sample of sources available this is only indicative. An analysis of the angular distribution of the position errors indicates the possible presence of a systematic effect in the measurement of source RA.

4.6 The 2nd IBIS/ISGRI Survey Catalogue

The 2nd IBIS/ISGRI soft γ-ray survey catalogue was the second data release of results from the Core Programme GPS and GCDE observations performed up to September 2004. The ESA/INTEGRAL scientific policy to render all scientific data publicly available a year after the original observation provided an additional data set to roll into the survey. The net result was an excess of 10 Msec of exposure across the entire sky. Hence, this catalogue comprises the first 2 years of Core Programme observations and the first year of General Programme observations. Whereas, the 1st IBIS/ISGRI Survey Catalogue provided coverage principally of the Galactic Plane, the 2nd IBIS/ISGRI Survey Catalogue covers 50% of the sky down to an exposure of >10 ksec.

4.6.1 Observations & data reduction

The data set consists of all available observations from February 2003 to June 2004. This covers revolutions 46-209 and includes ~6300 individual science window observations. Standard processing of the science windows was performed using the OSA version 4.1 software to produce images of each individual observation. Images were produced in 10 narrow, adjacent energy bands; 15–20, 20–30, 30–40, 40–60, 60–80, 80–100, 100-150, 150–300, 300–500 and 500–1000 keV to allow future flexibility data analysis.

Version 4.1 of OSA included improvements in the production of IBIS images and the cleaning of ghosts. Prior to the processing of the entire data set the effects of the different

search modes, discussed in section 4.4.2, was tested. During revolution 60 a GCDE observation took place so a subset of 29 science windows from this revolution was used as a field with a large source population. The data was reduced initially using search mode 1 and the 1st IBIS/ISGRI Survey Catalogue, hence the location of all sources in the field are known in advance. This produced a very clean image visible in the upper left panel of Fig. 4.12. Problems are expected to arise when a bright unknown source appears in a field, as might be expected of a transient source. To simulate this the input catalogue was edited to remove two of the bright sources in the field of view, IGR J17464-3213 and 4U 1700-377. Processing the data with the edited catalogue in search mode 1 produces the image seen in the middle panel of Fig. 4.12. It is clear that a large quantity of structure is generated, and the 8 ghosts surrounding IGR J17464-3213 are clearly visible.

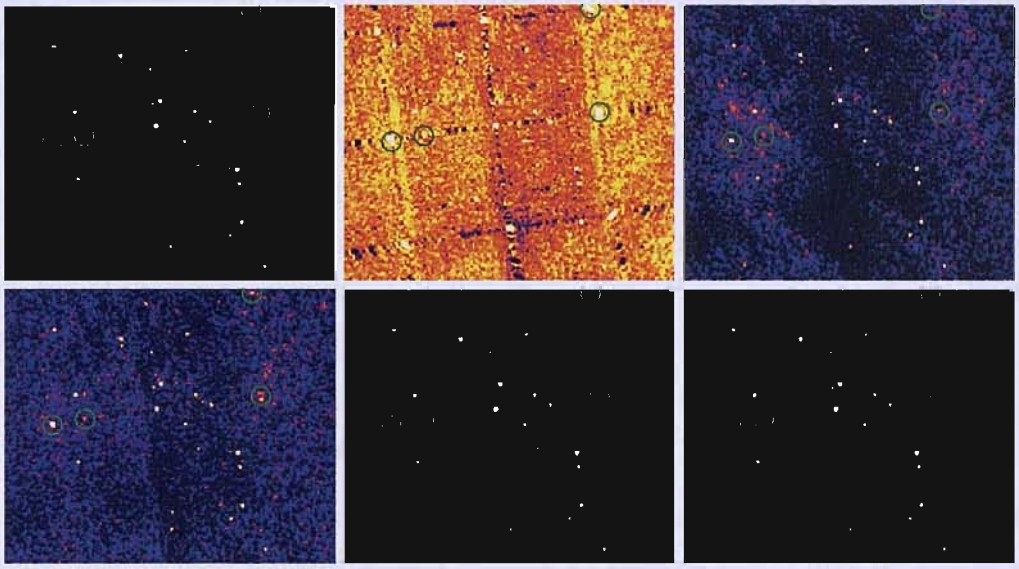

Figure 4.12: A mosaic of 29 science windows from revolution 60 processed with OSA using different search modes and input catalogues. The circles correspond to the same regions in each image, and identify the location of structure attributable to ghosts. *Upper left*: Search mode 1 with a complete catalogue of all sources in the field of view. *Upper middle*: Search mode 1 with an incomplete catalogue of all sources in the field of view; the bright sources IGR J17464-3213 and 4U 1700-377 have been removed from the catalogue. *Upper right*: Search mode 2 allowing for 10 sources in the field of view. *Lower left*: Search mode 3 using the aforementioned incomplete catalogue and allowing for 10 additional unlisted sources. *Lower middle*: A second iteration using search mode 3 and the sources found in the first iteration with search mode 3 as the catalogue. *Lower right*: Search mode 1 using the catalogue based upon the sources found using search mode 3.

Search modes 2 and 3 allow the software to fit to new sources in the field which are not listed in the catalogue. The images produced using search mode 2 and 3 are indicated

in the upper right and lower left panels of Fig. 4.12 respectively. Both of these search modes produce very similar images however, some structures and importantly, at least one of the ghosts remain strong and bright (these are indicated by circles in Fig. 4.12). The key difference between the search modes is that search mode 2 does not use the input catalogue source positions and instead fits each source in each science window where the PSF may not be well defined. Search mode 3 however, uses the input catalogue to clean out any known sources and then fits to any additional excesses detected in the image. Hence, in general search mode 3 should be using better source positions to clean known sources.

The bright ghost visible in the lower right panel of Fig. 4.12 is a problem because in an all-sky mosaic it is indistinguishable from a real source without concentrated study which is impractical to perform on a large list of sources. When using search mode 3 to process the data a source list file is produced in combination with the final mosaic. Reprocessing the data using this source list and search modes 3 and 1 produces the images shown in the lower middle and lower right panels of Fig. 4.12 respectively. It is clear that the ghost source has now been successfully cleaned and that the level of structure in the image has been reduced to the same level as obtained by processing the data initially with complete knowledge of the source population visible in the field of view. Hence, the catalogue 2 data set was processed twice to minimise ghosts and structures in the images.

4.6.1.1 The Cleaning catalogue

As has been shown the input catalogue is a key component in the operation of the OSA software. Ideally the catalogue should include all sources which may be visible in an individual science window and which require the cleaning of ghosts. However, additional sources in the catalogue which are not visible slow the processing of the data.

Prior to the release of OSA 4.1 the 2^{nd} survey data set was processed using OSA 4.0. The mosaics of the OSA 4.0 data in the 20–40, 30–60, 20–100 and 30–100 keV bands were searched for excesses potentially attributable to sources using SExtractor down to a significance of 4.5σ. The 30–60 keV mosaic excesses were used as the basis for the cleaning catalogue as this was the mosaic with the least image structure. The lists of excess were cross-correlated to guarantee that no duplicates existed. The final cleaning catalogue consisted of ~400 excesses combined from:

- The list of excesses from the OSA 4.0 mosaics.
- All sources from the 1^{st} IBIS/ISGRI Survey Catalogue.

- All of the published IGR sources at the time of processing.
- A list of transient sources obtained by searching the individual OSA 4.0 processed science window images.

An illustration of the construction of the cleaning catalogue is shown in Fig. 4.13. This catalogue was then used as the input catalogue to process the entire 2^{nd} survey data set using OSA 4.1 with search mode 3.

4.6.2 Generating mosaics

The individual observation images are combined together to create all-sky mosaics in an equal-area Aitoff projection. The mosaic production algorithm is proprietary software written at the University of Southampton designed to produce all-sky galactic maps from an input of several thousand science window observations. The mosaics have a pixel size of 3.6'×3.6' at the image centre.

4.6.2.1 Mapping pixels

The mosaic pixels are intentionally smaller than the raw science window image pixels, 3.6' compared to 4.8', as oversampling is required in order to combine the different orientated images into a single mosaic. If all four vertexes of a mosaic pixel lie within science window pixel then the mosaic pixel value is assigned the value of the science window pixel. If the mosaic pixel is not entirely contained within a science window pixel then the mosaic pixel is subdivided into 4 equal areas. If the subdivided area lies entirely within a science window pixel then a quarter of the science window pixel value is assigned to mosaic pixel.

This subdivision continues to a maximum of four levels with the fraction contribution adjusting appropriately. An illustration of the sub-division of pixels is shown in Fig. 4.14.This method obviously results in an approximation of the original value in some mosaic pixels in the cases where the final level of subdivision does not successfully lie within a single science window pixel. However, four levels of subdivisions only results in an underestimate of ~5% in these pixels.

These losses can be minimised by reducing the size of mosaic pixels and by increasing the number of allowed subdivisions. However, this comes at the cost of available RAM and CPU processing power respectively. The mosaicking algorithm was optimised to use 3.6' mosaic pixels and four levels of subdivision with available computing resources.

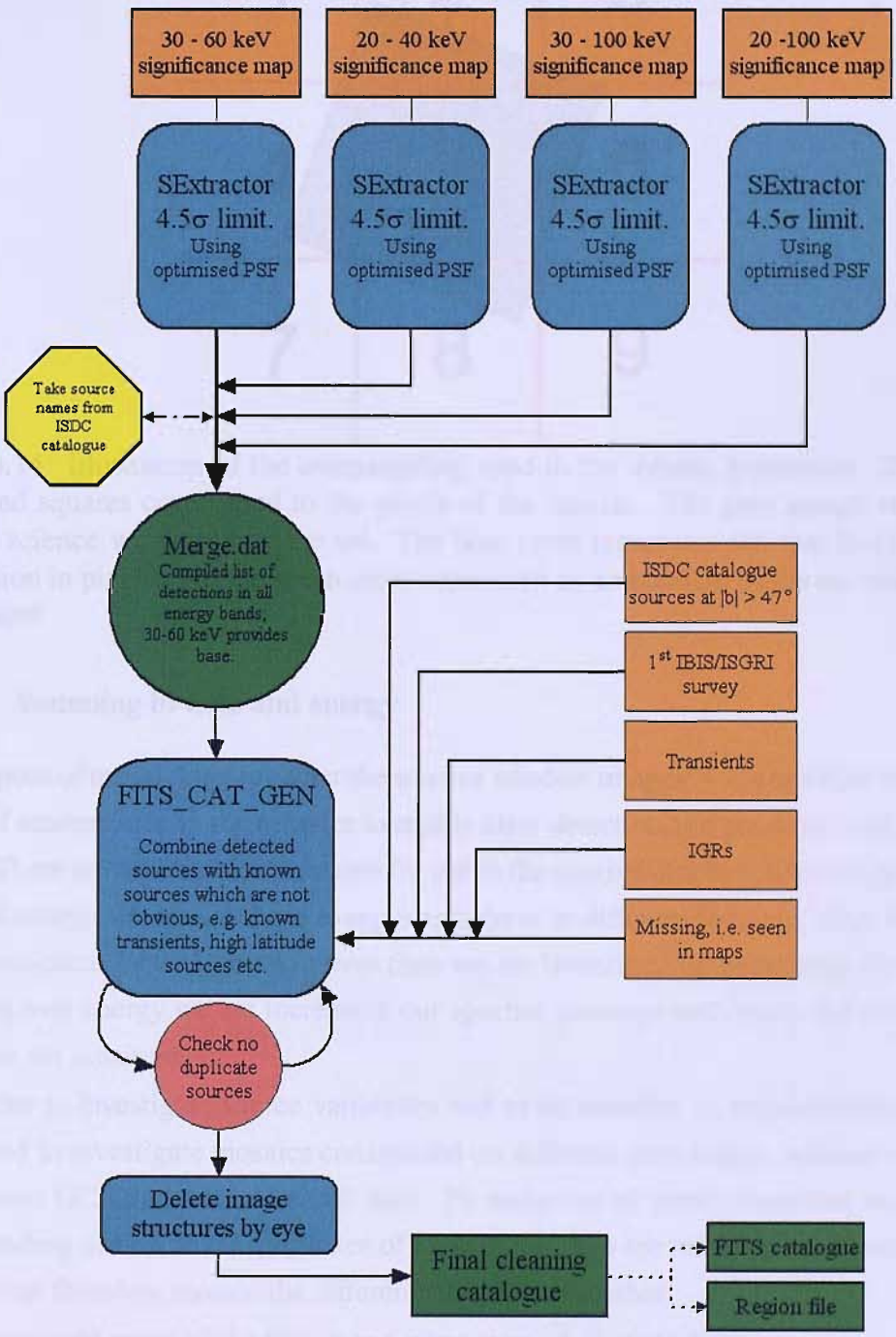

Figure 4.13: Organisational chart showing the steps involved in producing a cleaning catalogue

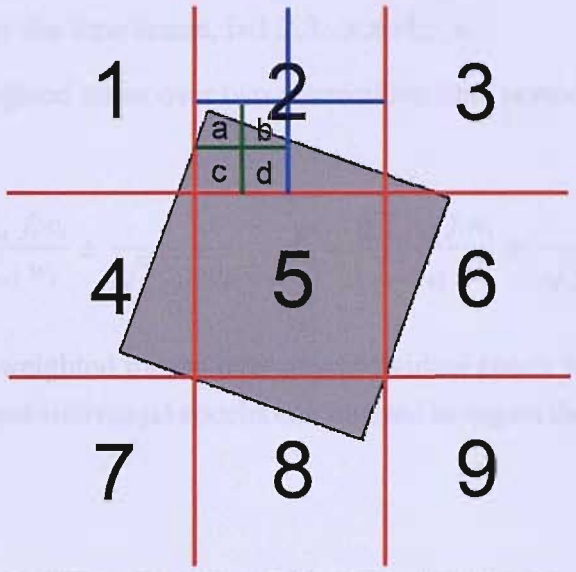

Figure 4.14: Illustration of the oversampling used in the mosaic generation. The numbered, red squares correspond to the pixels of the mosaic. The grey square represents a single science window image pixel. The blue cross represents the first level of pixel subdivision in pixel 2 and the green cross represents an an element of the second level of subdivision.

4.6.2.2 Summing in time and energy

The purpose of mosaicking together the science window images is to maximise the significance of sources seen in the mosaics to enable clear detection and good position determination. There are two regimes available for use in the maximisation of source significance, time and energy. However, these to regimes behave in different fashions when they have been mosaicked. When summing over time we are investigating the average flux. When summing over energy we are increasing our spectral coverage and hence, the total flux to which we are sensitive.

In order to investigate source variability and to be sensitive to transient behaviour, it is required to investigate mosaics constructed on different time scales: science windows; revolutions; GCDE observations; all data. To make use of these timescales requires an understanding of how the mean fluxes of these timescales are related to one another, and how we can therefore mosaic the different timescales together.

The weighted mean of the flux over a given time, $\overline{f}$, is given by:

$$\overline{f} = \frac{\sum_{i=1}^{n} f_i w_i}{\sum_{i=1}^{n} w_i} \pm \frac{1}{\sqrt{\sum_{i=1}^{n} w_i}} \tag{4.3}$$

where f_i is the flux measured at time t_i and w_i is the weight of the measurement, $w_i = \frac{1}{\sigma_i^2}$, σ_i is the error on the associated with the measurement of f_i. The weighted

mean is calculated over the time frame, i=1,2,3...x,x+1,...n.

Calculating the weighted mean over two consecutive time periods gives:

$$\overline{f}_a = \frac{\sum_{i=1}^{x} f_i w_i}{\sum_{i=1}^{x} w_i} \pm \frac{1}{\sqrt{\sum_{i=1}^{x} w_i}} \qquad \overline{f}_b = \frac{\sum_{i=x+1}^{n} f_i w_i}{\sum_{i=x+1}^{n} w_i} \pm \frac{1}{\sqrt{\sum_{i=x+1}^{n} w_i}} \tag{4.4}$$

The calculation of weighted means over any individual epoch is trivial, however, the question is whether these individual epochs can be used to regain the weighted mean over all observations.

$$\overline{f}_{a+b} = \frac{\overline{f}_a w_a + \overline{f}_b w_b}{w_a + w_b} \pm \frac{1}{\sqrt{w_a + w_b}} \tag{4.5}$$

$$= \frac{\frac{\sum_{i=1}^{x} f_i w_i}{\sum_{i=1}^{x} w_i} \sum_{i=1}^{x} w_i + \frac{\sum_{i=x+1}^{n} f_i w_i}{\sum_{i=x+1}^{n} w_i} \sum_{i=x+1}^{n} w_i}{\sum_{i=1}^{x} w_i + \sum_{i=x+1}^{n} w_i} \pm \frac{1}{\sqrt{\sum_{i=1}^{x} w_i + \sum_{i=x+1}^{n} w_i}} \tag{4.6}$$

$$= \frac{\sum_{i=1}^{n} f_i w_i}{\sum_{i=1}^{n} w_i} \pm \frac{1}{\sqrt{\sum_{i=1}^{n} w_i}} \tag{4.7}$$

$$= \overline{f} \tag{4.8}$$

Hence, it is possible to calculate the overall weighted mean from individual weighted means calculated over smaller segments of time.

The case of summing over energy bands, however, is entirely different as a it is a summation and not an average. Defining the energy bands j→k and j→l with corresponding weighted mean fluxes, $\overline{f}_{jk}$ and $\overline{f}_{kl}$ respectively. The weighted mean flux for the broad band j→l is given by:

$$\overline{f}_{jl} = \frac{\sum_i f_{jl_i} w_{jl_i}}{\sum_i w_{jl_i}} \pm \frac{1}{\sqrt{\sum_i w_{jl_i}}} \tag{4.9}$$

$$= \frac{\sum_i \left[(f_{jk_i} + f_{kl_i}) \frac{w_{jk_i} w_{kl_i}}{w_{jk_i} + w_{kl_i}} \right]}{\sum_i \frac{w_{jk_i} w_{kl_i}}{w_{jk_i} + w_{kl_i}}} \pm \frac{1}{\sqrt{\sum_i \frac{w_{jk_i} w_{kl_i}}{w_{jk_i} + w_{kl_i}}}} \tag{4.10}$$

$$\tag{4.11}$$

Calculating the broad band flux using the individual bands results in:

$$\overline{f}_{jk} + \overline{f}_{kl} = \frac{\sum_i f_{jk_i} w_{jk_i}}{\sum_i w_{jk_i}} + \frac{\sum_i f_{kl_i} w_{kl_i}}{\sum_i w_{kl_i}} \pm \sqrt{\frac{\sum_i w_{jk_i} + \sum_i w_{kl_i}}{\sum_i w_{jk_i} \sum_i w_{kl_i}}} \quad (4.12)$$

$$= \frac{\sum_i f_{jk_i} w_{jk_i} \sum_i w_{kl_i} + \sum_i f_{kl_i} w_{kl_i} \sum_i w_{jk_i}}{\sum_i w_{jk_i} \sum_i w_{kl_i}} \pm \sqrt{\frac{\sum_i w_{jk_i} + \sum_i w_{kl_i}}{\sum_i w_{jk_i} \sum_i w_{kl_i}}} \quad (4.13)$$

$$\neq \overline{f}_{jl} \quad (4.14)$$

So it is not possible to combine mosaicked energy bands into broad energy band mosaics except for in the special case where all weights are equal. To maximise source detection significance requires the summation of energy bands at the science window level before mosaicking these summed images together over time. However, to produce average spectra of sources observed in the final mosaic requires the mosaicking of each energy band separately.

4.6.2.3 Science window selection

Some individual science window observations can contain large levels of noise and structure. When these are included in the mosaics these structures do significant damage to the image statistics making weak source detection difficult. These 'bad' science windows are attributable to a number of factors including:

- Space weather, for example solar flares.
- Periodic high levels of background at the beginning or end of a revolution when INTEGRAL is near the radiation belts.
- The location of a bright source near to the edge of the partially coded field of view.

The rms statistic of these 'bad' science windows is significantly higher than science windows without these problems. The rms statistic is used to automatically filter out the 'bad' science windows and these are not included into the final mosaic. The allowed range of rms statistic is dependent upon energy band and so was independently set for each band. Overall this removes ~5% of the total data set.

4.6.3 Improving source identification and location

As in the first survey the 30–60 keV and 20–40 keV band mosaics were found to have the highest image quality and were the primary resource for identifying new sources. An

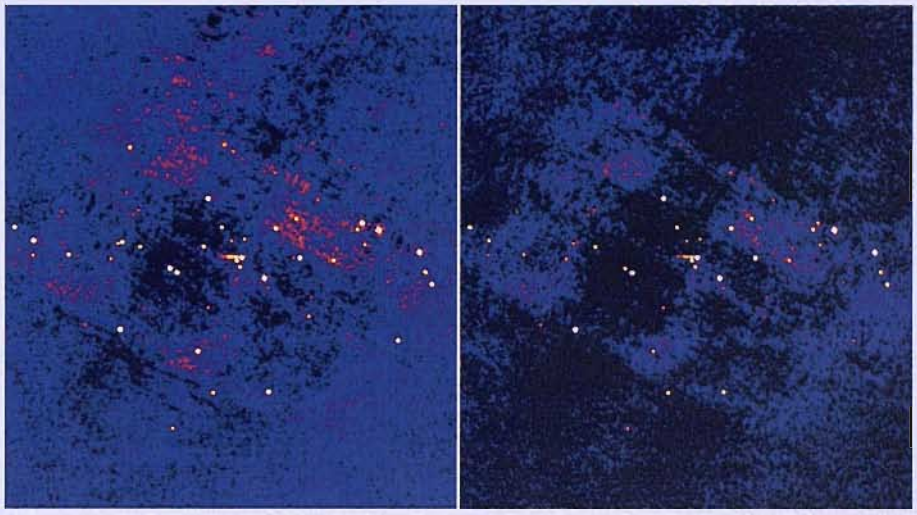

Figure 4.15: A comparison of the level of image structure surrounding the Galactic centre region in two different energy channels. *Left panel*: The 20–40 keV significance mosaic. *Right panel*: The 30–60 keV significance mosaic. Both images have the same scaling and colour bars. The 20–40 keV map evidently has a larger level of structure associated with this region of the map

example of the difference in image quality is indicated in Fig. 4.15. The 30–60 keV band generally shows a lower level of structure in its images. Fig. 4.15 shows the Galactic Centre region of the 20–40 and 30–60 keV mosaics, the image structures are apparent to the upper left and lower right of each image. Given the larger sky coverage of the second survey more extragalactic sources were expected. The spectral nature of extragalactic sources is such that broader energy bands, e.g. 20–100 keV, are better suited to detect these objects.

The level of structure within a mosaic can, to some extent, be seen in the statistical properties of the mosaic. In an ideal mosaic the any fluctuations would be entirely due to statistical effects. Hence a significance mosaic would have a pixel distribtuion with a mean of zero and a standard deviation of one. Adding a source population to this mosaic should not noticeably change this distribution if the number of sources is small compared to the total number of pixels in the mosaic. This should be the case for the survey mosaics. If a sufficient amount of image structure is added to the mosaic then the image statistics will be altered.

Table 4.1 shows the measured means and standard deviations of the pixel distributions in a number of the mosaics. The all-sky 30–60 keV mosaic, which by eye we consider less affected by image structure, shows the narrowest distribution of pixels approximately about zero. This is a verification that there is less image structure in theis map than in the 20–40 and 20–100 keV mosaics. However, if we examine the polar projection maps

Table 4.1: The mean and standard deviations of the mosaic pixel distributions in different energy bands and projections.

Mosaic :	Mean	Standard deviation
All-sky 20–40 keV	0.06	4.1
All-sky 30–60 keV	0.02	2.7
All-sky 20–100 keV	0.05	4.0
Polar 20–40 keV	0.007	1.1
Polar 30–60 keV	-0.009	1.1
Polar 20–100 keV	0.007	1.1

we find that the statistics are remakably better with a mean of approximately zero and standard deviation of one across all energy bands. This is explained by the low density of sources in the polar regions and the fact that those present are noticebaly weaker than those found on the Galactic Plane. The image structure in the mosaics is attributable to the poor fitting and cleaning of sources performed by the reduction software. In the Galactic Centre region where there is a very high density of very bright sources this is very damaging. At the galactic poles the effect is not observable. Consequently, it is easier to detect sources of lower significance in the polar mosaics.

The combining of all the data into a single mosaic maximises the likelihood of detecting weak persistent sources. However, using all of the data can have the effect of washing out brief transient events which appear significant on different timescales. In order to detect these events the individual science windows and mosaics of each revolution and each GCDE observation are also searched for sources.

4.6.3.1 SExtractor

SExtractor version 2.3.2 was used to search each of the mosaics for excesses (Bertin & Arnouts, 1996). Source detectability is limited at the faintest levels by background noise and can be improved by the application of linear filtering of the data. In addition, source confusion in crowded fields can be minimised by the application of a bandpass filter. To this end, the mexhat bandpass filter was used with the SExtractor software to search the mosaics for excesses. The mexhat filter is a 'wavelet' filter constructed from a Gaussian with negative side lobes; the FWHM of the Gaussian is matched to that of the PSF of mosiac sources. The convolution of the filter with the mosaics alters the source significances, hence SExtractor uses the source positions identified from the filtered mosaic to extract source significances from the original mosaic.

Fig. 4.16 demonstrates the effectiveness of the bandpass filter in separating sources in close proximity. In this specific case 1E 1145.1-6141 and 2E 1145.5-6155, which have an angular separation of ~15', close to the telescope angular resolution. If a simple Gaussian filter is used, as in the case of the 1^{st} survey, only a single extended source is identified at a position which lies between the two sources. This location is indicated by the diamond symbol in the figure. In comparison the mexhat filter successfully identifies both sources, although the weaker source, 2E 1145.5-6155 is shifted ~1 pixel away from the expected SIMBAD location of the source.

As described previously the SExtractor calculates the centroid of each source it detects. However, the Aitoff projection heavily distorts the PSF of sources at high galactic latitudes i.e. $|b| > 60°$. To guarantee that the best possible positions for sources in these regions were obtained additional mosaics using the polar, Arc, projection were generated. Using SExtractor to search all of the mosaics of all the different timescales and energy bands yielded an initial list of 1019 excesses.

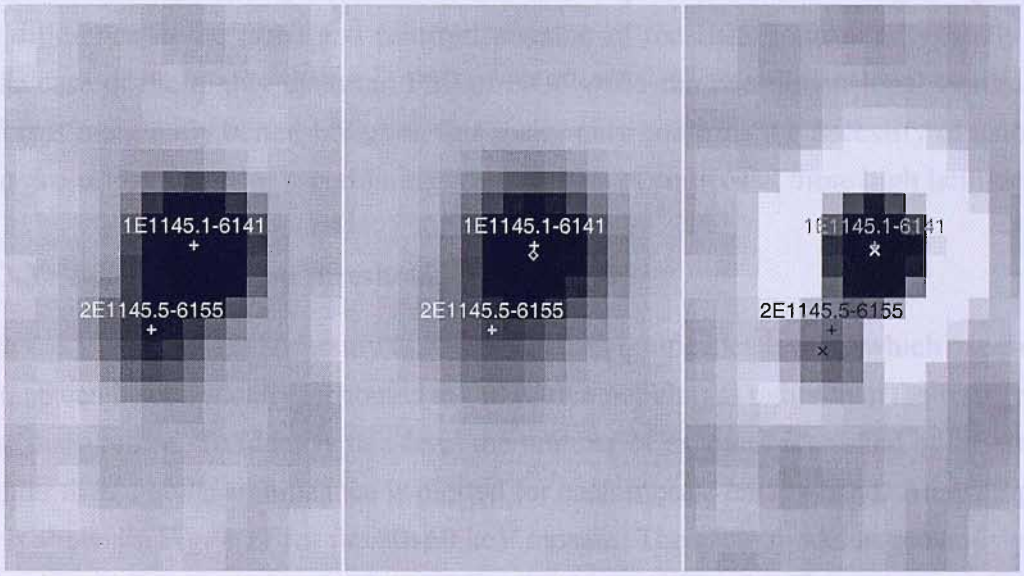

Figure 4.16: Results of using the SExtractor software on a region containing the blended sources, 1E 1145.1-6141 and 2E 1145.5-6155. *Left panel*: The region in the original 20–60 keV mosaic. *Middle panel*: The region in the Gaussian filtered 20–60 keV mosaic. *Right panel*: The region in the bandpass filtered 20–60 keV mosaic. The diamond symbol represents the source position found using the Gaussian filter; the x symbols represent the source positions found by the mexhat filter; the + symbols indicate the SIMBAD source locations.

Table 4.2: The angular distance of the Crab and NGC 4151 from their nominal positions according to the SIMBAD/NED database

Distance from :	Crab Nebula	NGC 4151
Gauss fit	0.438'	1.42'
centroid	0.447'	1.45'

4.6.3.2 Source PSF fitting

In theory the source coordinates of the survey sources can be found more precisely by fitting a two-dimensional Gaussian function to the source PSF. The previously used method makes use of the inbuilt centroid routines of SExtractor. A number of sources at different locations of the map were fit with a Gaussian function and their positions compared with the known positions and the centroid positions of these sources. The distance of the nominal SIMBAD position for the Crab Nebula and NGC 4151 from the positions obtained by fitting the PSF and the centroid method are shown in Table 4.2. It is clear, that the differences in the positional error obtained by these two methods is insignificant. The difference in the fitted and centroid position of the IBIS sources is typically ~4". In the case of the highly distorted PSF of NGC 4151 the two-dimensional Gaussian fit performs marginally better, however, this really only confirms the necessity of using the polar projection maps for ascertaining the positions of sources at these high latitudes.

4.6.3.3 Source detection threshold

As in the 1^{st} survey it is necessary to determine the significance level at which excesses in the map can be confidently attributed to the source population rather than the background noise distribution. To identify this level the number of excesses identified by SExtractor brighter than a given significance is plotted for each mosaic energy band. An example of this is shown in Fig. 4.17 for the 30–60 keV mosaic. The same model as previously is fit to the data, a Gaussian + power-law. Using the fit model the significance at which 1% of the excesses are attributable to the noise distribution is calculated and used as a filtering threshold.

The thresholds corresponded to 5σ in the 30–60 keV and 20–100 keV mosaics, 5.5σ in the 20–40 keV mosaic and 6σ in any single revolution mosaic. The lower thresholds when compared to those used in the 1^{st} survey is indicative in the improvements in the imaging processing software and hence the lower level of noise and structure in the final mosaics. These thresholds were used to filter down the initial list of 1019 excesses. The excesses

were then visually inspected to verify an appropriate PSF. Obvious map structures were deleted upon inspection. Any excesses in regions of high structure were required to have an appropriate PSF and be 3σ brighter than any structures in the immediate vicinity. Having performed all of these checks the source list was reduced to 209 sources.

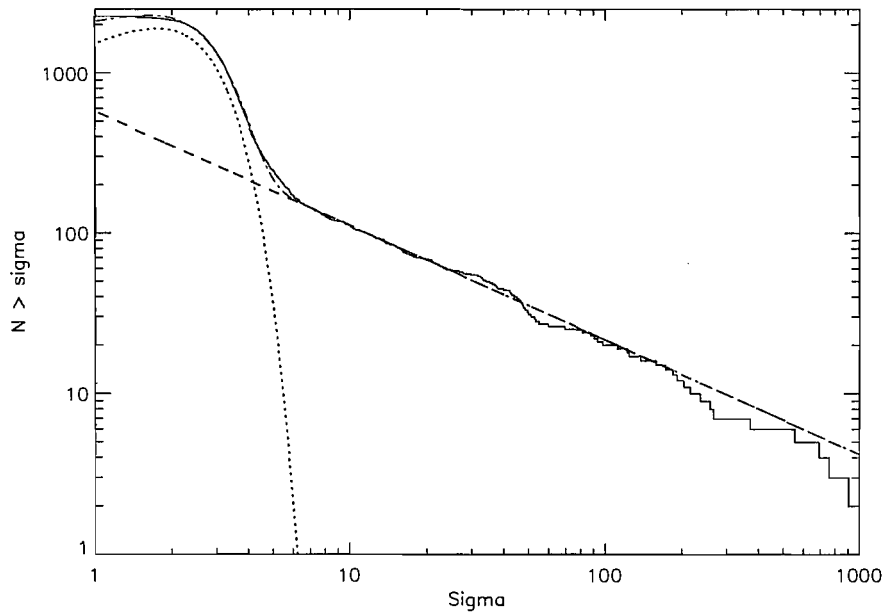

Figure 4.17: Distribution of the number of excesses as a function of significance in the 30–60 keV map. The dotted and dashed line represents the fitted model; the dashed line represents the extrapolated power law component of the fit; the dotted line represents the Gaussian component of the fit.

4.6.3.4 Galactic Centre sources

The galactic centre is a highly crowded and confused region of the Galaxy. With the 12' angular resolution of INTEGRAL it is impossible to disentangle all of the individual sources within this region. However, the highly variable nature of these γ-ray sources assists in the disentangling of the individual sources. To this end, each individual revolution in which the Galactic Centre was observed, was individually inspected. Examples of the usefulness of this approach are evident in the cases of SAX J1747.0-2853 which appears in a single revolution and SLX 1744-299 which is detected in all but 9 of all the revolutions.Using this method ten individual sources were identified, including the six sources previously identified by Bélanger et al. (2004) in an 850 ksec exposure of this region.

4.6.4 Sources of the 2^{nd} IBIS/ISGRI Survey Catalogue

The filtered, final source list of 209 objects is given in Appendix C. A selection of images extracted from the all-sky mosaics are shown in Appendix D. The astrometric coordinates of the sources are those extracted by SExtractor. However, as discussed in section 4.6.2.1, the mosaicking of images results in a loss of ~5% of source flux. For each source in the catalogue a light curve in the 20–40 keV and 40–100 keV bands was extracted. Taking the weighted mean flux of the light curve in principle repeats the same process as performed by the mosaicking software but without the oversampling of pixels and hence does not incur any flux loss. These represent the present most accurate average fluxes for sources observed in the first two years of the INTEGRAL mission.

The advances in the OSA imaging software include a better understanding of the off-axis response of the IBIS instrument in versions 4.0 and onward. This successfully reduces the previous systematic uncertainty in flux measurements which were made using earlier versions of the software and which were discussed with regards to the first IBIS survey. This improved understanding of the instrument and the correction for mosaicking losses combined with the intrinsically variable nature of γ-ray sources makes it impossible to expect there to be similar sources fluxes in the first and second IBIS/ISGRI survey catalogues.

For each of the sources in the second catalogue a complete light curve in each of the energy bands and an average spectrum is automatically generated for future investigation and analysis of the individual source properties and behaviours.

4.6.5 Data Validity

The data provided by the survey catalogues is principally a list of the detected γ-ray sources with an associated position and average flux. It is therefore impotant to ascertain the quality and validity of these measurements.

4.6.5.1 Point source location error

The astrometric coordinates of the source positions were extracted from the mosaics by the centroid routines built into SExtractor 2.3.2. Of the 209 sources listed in the 2^{nd} IBIS/ISGRI catalogue, 179 have well-defined positions obtained in different wavebands according to the SIMBAD/NED database. Measuring the angular distance between the measured positions and those provided by the SIMBAD database gives an indication of the source position errors.

An analysis similar to that described in Section 4.5 was performed. Fig. 4.18 shows the error in the measured RA and Dec of the 179 identified sources. The error distribution is well centred around zero and the angular distribution shows an even distribution of sources across all angles. Examining the measured and expected positions of some of the sources on an indiviudal basis also shows no sign of any systematic shift in positions. The mean position error of all sources detected at a 10σ level or higher is ~0.7′. However, the point source location error of IBIS is highly dependent upon the significance of the source detected (Gros et al., 2003).

By binning together sources of similar significance and calculating the mean source position error we can see how the source positioning accuracy varies with significance; this is shown in Fig. 4.19. The data is fit by a power-law model with a constant offset:

$$\delta x = 11.6S^{-1.36} + 0.51 \tag{4.15}$$

where δx is the error in the source position (in arc minutes) and S is the source significance. This indicates that for the most significant detections we do not, on average, obtain a source location better than 0.51′. For sources which have a significance of $\sim 5\sigma$ we have a mean accuracy of $< 2'$. From Equ. 4.15 the 1σ position errors for each of the catalogue sources was calculated and is listed in Appendix C.

Gros et al. (2003) gives the range of the 90% confidence level error radius as $3' - 20''$, with an error better than 1′ for $\sigma > 30$, and they note that these results are derived from fields with few detected sources and may not be accurate in crowded fields. The source location accuracy of the source positions in the 2^{nd} IBIS/ISGRI catalogue is better than predicted by Gros et al. (2003) with an error better than 0.7′ for $\sigma > 10$.

4.6.5.2 Off-axis flux errors

Despite the improved corrections for the off-axis response of the IBIS/ISGRI instrument available in the OSA 4.0 and later software the off-axis response is still not fully understood (Barlow, 2006). The uncertainty in off-axis fluxes needs to be recognised when attempting to analyse data in the survey. When a source flux is measured at a large off-axis angle it tends to have a larger associated error than at smaller angles hence when taking weighted mean fluxes the off-axis uncertainty does little damage. In methods which do not take these errors into account this systematic can be very damaging.

A case in point is the use of the Lomb-Scargle periodogram method to search for periodicities (see section 6.4.1 for details of this method). An example of the effect of off-axis angle flux uncertainty is shown in the case of a periodic, weak, persistent INTEGRAL

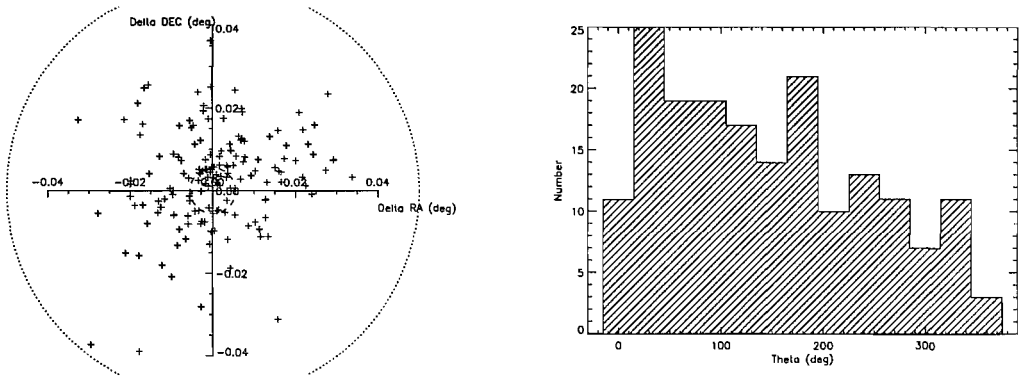

Figure 4.18: *Left panel*: The scatter in positional error, using the SExtractor positions, of 179 of the 2nd ISGRI catalogue sources. The two circles indicate the limits of the PSLE (3'-20"). *Right panel*: A histogram of the angular distribution of the left hand scatter plot.

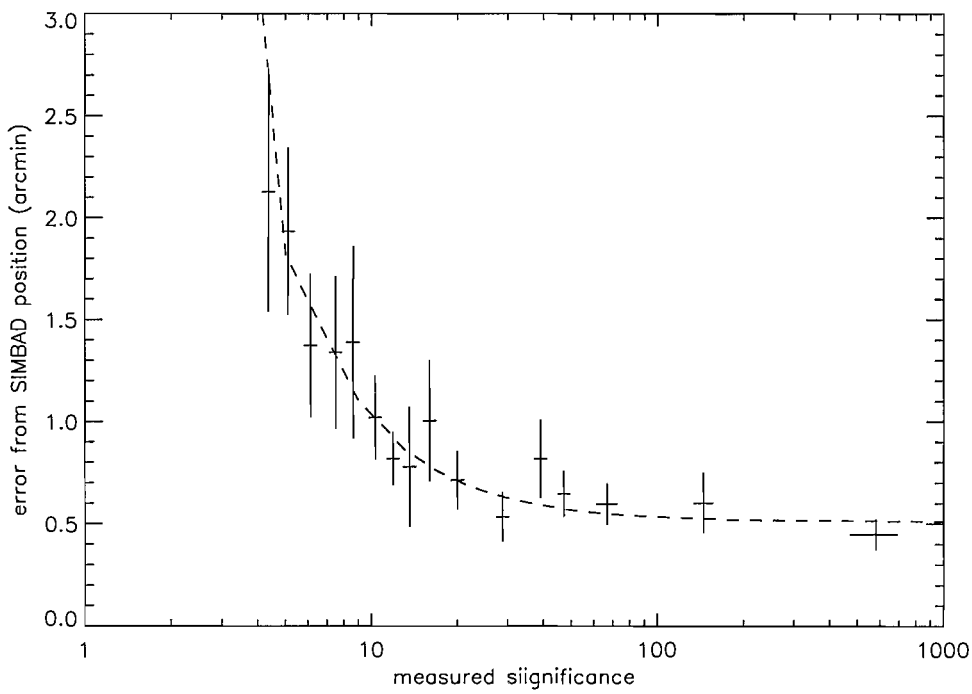

Figure 4.19: The binned mean source position error of sources as a function of source significance. Each bin contains 10 sources. The dashed line indicates the model shown in Equation 4.15.

source in Fig. 4.20 & 4.21. Fig. 4.20 indicates that the correct periodicity corresponds to the periodogram peak of maximum power until there are less than ~250 points in the light curve, i.e. < 20% of the available data is used.

Fig. 4.21 shows the histogram of the power in the highest peak of the periodogram for different off-axis angle exclusions normalised to the maximum power found in any of the periodograms. Also shown, by the dashed line, is the fraction of the total data available at less than any given off-axis angle. From this figure it can be seen that the periodic signal of the source is clearest when the light curve input into the Lomb-Scargle periodogram is restricted to observations taken at an off-axis angle of less than 10–13°. This is despite only using 50–80% of the data for this range of angles. If observations at larger off-axis angles are included then the systematic error in these fluxes damages the periodic signal to the extent that using all observations reduces the periodogram peak to 30% of its maximum.

If we restrict the light curve to data observed when the source is only in the fully-coded field of view (FCFOV) then the periodogram peak is again reduced to 30% of its maximum. At these angles the light curve comprises of fewer observations. Consequently the restricted data set does produces a much less significant peak in the periodogram making it harder to identify the periodic signal. This is confirmed by Fig. 4.20, as using only the FCFOV limits the light curve to less than 20% of the available data which corresponds to the point at which the Lomb-Scargle periodogram method can no longer detect the system periodicity.

These tests were performed on the weak, persistent source IGR J18027-2016 for which an off-axis angle limit of 12° optimises the detection of the system periodicity. The systematic error attributable to off-axis angle is obviously most damaging in sources where this error is a large fraction of the amplitude of the periodic signal. This is dependent on the individual source so it is necessary to investigate each system independently when performing this type of analysis.

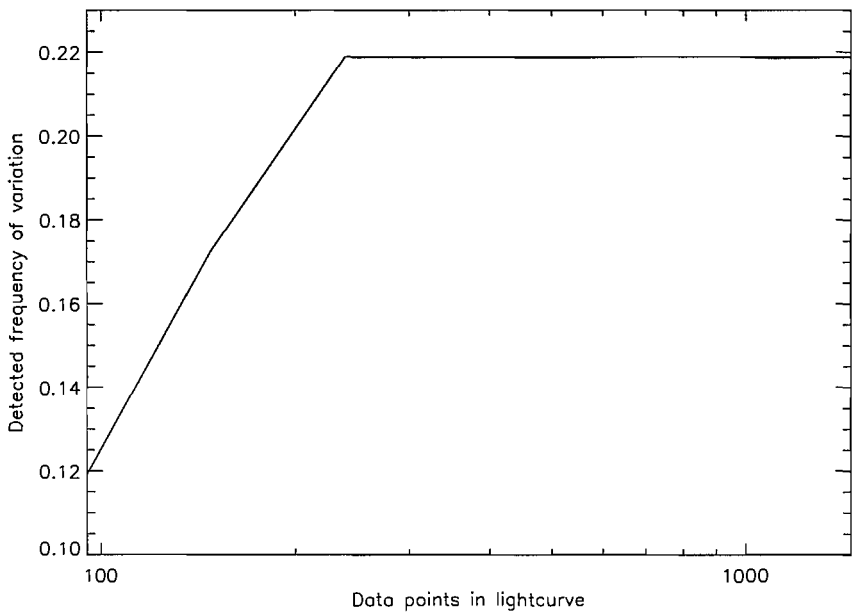

Figure 4.20: The detected frequency at which the Lomb-Scargle periodogram has maximum power for light curves of varying levels of completeness. A source with a known periodicity of frequency 0.2188 was used. The number of points in the input light curve was varied by restriction the allowed off-axis angle of the source, i.e. the maximum number of data points exist when all observations of the source are used.

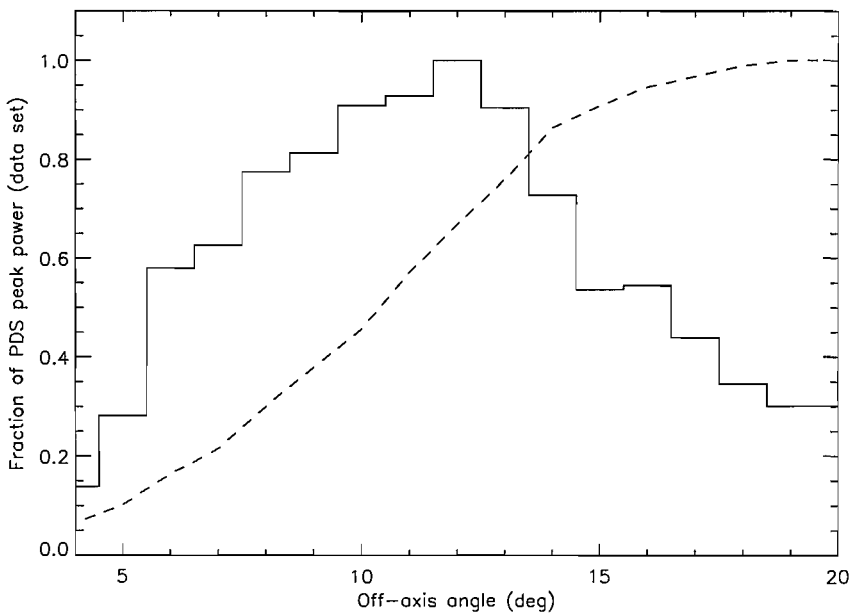

Figure 4.21: A histogram of the power of the maximum peak in the Lomb-Scargle periodogram as a function of the off-axis angle limit placed on the input light curve. The histogram is normalised to the highest power achieved. The dashed line represents the fraction of the total observations which occur at less than each off-axis-angle.

4.7 Conclusions

The IBIS/ISGRI soft γ-ray survey is an ongoing project which will continue until the end of the INTEGRAL mission and all observations have been analysed. To date the first two releases of survey catalogues corresponding to the first and second years of observations have already provided invaluable information on the source population of the γ-ray sky. Between the release of the first and second survey catalogues the number of available observations increased the total exposure of the sky by more than a factor of two to ~10 Msec. This combined with the improved imaging software and a better understanding of the instrument behaviour and response almost doubled the number of sources in the survey catalogue to a total of 209.

Table 4.3 compares some of the properties if the 1^{st} and 2^{nd} catalogues. The increased quantity of data is very significant, specifically in expanding the quantity of the sky observed with an exposure of 100 ksec from 5% to 32%. As the survey continues to include more observations this can only increase both in sky coverage and level of exposure. However, it is also clear that the sensitivity of the exposure has not increased drastically. The 1^{st} catalogue had a sensitivity of 1 mCrab in the Galactic Centre. The 2^{nd} catalogue expands this to cover the entire Galactic central radian but does not push down any further despite the drastically increased exposure. This is explained by the level of source structure which is left residual in the image. The Galactic Centre is a crowded field of bright sources, as a result any failure in the reduction software to fit and clean source ghosts results in high levels of structure in the moasics. This is the factor which currently prevents the survey from reaching a higher sensitivity, as the source structure builds with the exposure. This can only be resolved by future improvements in the OSA analysis software. Once sources are cleaned better these structures should be reduced and lower sensitivities obtained.

Table 4.3: A comparison of the properties of the 1^{st} and 2^{nd} catalogues.

	Catalogue 1	Catalogue 2
Number of sources	123	209
Number of ScWs	2529	6304
Exposure	~4 Msec	~10 Msec
% of sky > 10^5 sec exp.	~5%	~32%
Sensitivity	~1 mCrab in GC	~1 mCrab central radian
Mean source location error	0.7'	0.7'

Of the 209 sources of the 2^{nd} IBIS/ISGRI Survey Catalogue ~25% of them are new high-energy, INTEGRAL source detections. This introduces the possibility that INTEGRAL has discovered a new class of previously unseen binary systems. Early follow up studies of a number of individual objects indicates that a large number of these systems have a high level of intrinsic obscuration (Walter et al., 2004; Hill et al., 2005). Only through follow-up studies and statistical analysis of this population can we hope to understand the physical processes which are in action and understand the place of these systems in the global scheme of binary system evolution.

The catalogue of Macomb & Gehrels (1999) is the most recent pre-INTEGRAL catalogue of sources emitting at energies above 50 keV. They list 309 sources in the energy range 50 keV – 1 TeV which have been detected by at least one instrument; they do not include any γ-ray bursts or emission from the Sun. Of these sources 183 have only been detected at energies above 1 MeV. Out of the 309 sources 126 are classified objects which have been detected at 50 keV – 1 MeV. These include 83 accreting objects, 22 Seyfert galaxies, 14 blazars, 7 pulsars, 6 galaxy clusters and 3 supernova remnants. The second IBIS/ISGRI catalogue sees a similar number of sources, especially galactic systems. Future catalogues should see a larger source population with the increased sky coverage and exposure.

The second IBIS catalogue included ~6,300 science window observations. By the end of the third year of operations, in December 2005, over 19,000 science window observations were available. An early analysis of the processed observations to date has increased the total source population to over 250 discrete sources. Specifically the extragalactic source population is increasing in size. Over 60 AGN have now been detected by INTEGRAL, double the population announced in the 2^{nd} IBIS/ISGRI Survey Catalogue (Bassani et al., 2006). With the funding of INTEGRAL extended to 2010 the IBIS survey is anticipated to cover the entire sky with a source list of ~500 sources.

Chapter 5

The Global Characteristics of the 1^{st} IBIS/ISGRI Survey

5.1 Introduction

The IBIS/ISGRI survey produces regular catalogues of the soft γ-ray sky, making use of all of the data available to the IBIS survey team at the time of catalogue release. The processes and methods used in the production of all-sky mosaics and the generation of source catalogues from these mosaics is discussed in Chapter 4. These survey catalogues are based upon unbiased search techniques and so are not pre-disposed to finding any specific class of source in the γ-ray band. This provides γ-ray selected samples of source populations which can be investigated for differences from the parent populations and hence yield important information about the origins and processes of these sources.

The 1^{st} IBIS/ISGRI Survey Catalogue is based upon the 1st year of Core Programme observations of the Galactic Plane and Galactic Centre. This totals ~5 Msec of exposure across the galaxy, however, the majority of this exposure is concentrated in the central radian due to the Galactic Centre Deep Exposures. The nature of the exposure results in the vast majority of the source catalogue consisting of galactic stellar γ-ray sources although a few, ~6, extragalactic sources are reported. The 1^{st} IBIS/ISGRI Survey Catalogue comprised of a total of 123 discrete sources.The complete source list is given in Appendix A. All of these sources were identified in either the 20–40 keV or the 30–50 keV energy band mosaics at a significance of $> 7\sigma$. Positions for previously known sources were cross-checked against archive positions, and found to match the expected point source location accuracy well(Gros et al., 2003). The typical point source location error range is 20"–3', with a 1 arc minute error circle for a source $>10\sigma$(90% confidence). The precision of the

source locations allow for the clear identification/association to sources seen by previous missions and hence source classification is possible. Additionally, those sources without previously seen high energy counterparts can be confidently identified as newly discovered INTEGRAL γ-ray sources. Fluxes for each source were obtained by extraction of values from the all-sky mosaics at the positions of best fit provided by the SExtractor software. As the survey mosaics are time-averaged maps the source fluxes quoted are weighted means dependent upon the total accumulated flux averaged over the time each source was observed. Hence, no level of variability is indicated.

The number of galactic γ-ray sources in the 1^{st} IBIS/ISGRI Survey Catalogue is comparable to the early X-ray source catalogues; the Ariel V survey detected 109 X-ray sources (Warwick et al., 1981). This is a sufficient sample for a preliminary investigation of their global characteristics on a statistical basis. The γ-ray selected nature of the objects is interesting as source emission is insensitive to typical obscuration at these energies. Hence, objects highly photo-absorbed in the classical X-ray band are clearly visible at γ-ray energies, a factor borne out by the large sample of previously undetected sources being identified by INTEGRAL.

5.1.1 Source populations

The 123 sources of the 1^{st} IBIS/ISGRI Survey Catalogue include:

- 54 Low Mass X-ray binaries (LMXBs)
- 24 High Mass X-ray binaries (HMXBs)
- 4 Cataclysmic Variables (CVs)
- 4 radio pulsars
- 3 supernova remnants
- 28 unclassified sources

From the list of sources observed it is clear that only the LMXB, HMXB and unclassified sources are of sufficient numbers to explore the properties of these populations in a statistical fashion. The unclassified source, IGR J17460-3047 was identified as a false detection of the 1^{st} survey attributed to an uncleaned image ghost. Hence, we only include the remaining 27 unclassified sources in any analysis. The LMXBs in our sample are classified as having a primary star with a mass < 1 $M_{\odot}$ (Liu et al., 2001) and the HMXBs

having a primary star with M > 10 $M_{\odot}$ (Liu et al., 2000). The unclassified source population is likely to consist of a number of different classes of object, however, the possibility exists that they are dominated by a single class. To this end, the unclassified sources are treated as a single population.

The goal of analysing the statistical properties of these different source populations is to identify and explain any difference between this γ-ray selected set and the known properties of the parent populations. Additionally, contrasting the unclassified population properties with those of the HMXB and LMXB populations will shed light onto whether either of these source types dominate the unclassified population or whether they are something entirely different.

An understanding of these unclassified sources is a primary goal of the IBIS survey team. By exploring the statistical properties of the population and combining this knowledge with the classification of individual sources through targeted follow-ups at other wavelengths it is possible to build up a detailed image of how these sources fit into the global scheme of stellar evolution.

5.2 The LogN-LogS Distributions

Investigating the number flux distribution of the IBIS survey sources is an obvious avenue to explore the basic distribution of the sources across the sky. In simple euclidean geometries a source population, with a uniform luminosity, distributed isotropically across the whole sky would be found to have a power-law distribution with an index of -1.5. In the case of a two-dimensional disc population the index should correspond to -1. Finally, for a one-dimensional, linear distribution of sources the power-law index will be -0.5.

In the case of the IBIS survey populations the survey exposure is concentrated in the Galactic Plane hence, we expect them to be distributed in a similar fashion to the disc population. However, if the sources are not evenly distributed across the disc then the index of the power-law distribution will be < -1.

Assuming that the flux-density distribution is represented by the power-law:

$$N(S) = kS^{-\alpha} \tag{5.1}$$

we can describe the distribution of the source populations. N(S) is taken as the number of sources brighter than the luminosity S, where S exists in the the range $S_{min} \leq S \leq S_0$. S_0 corresponds to the source of the brightest flux observed and S_{min} the minimum observed flux. Using the 20–40 keV fluxes the source population number flux distribu-

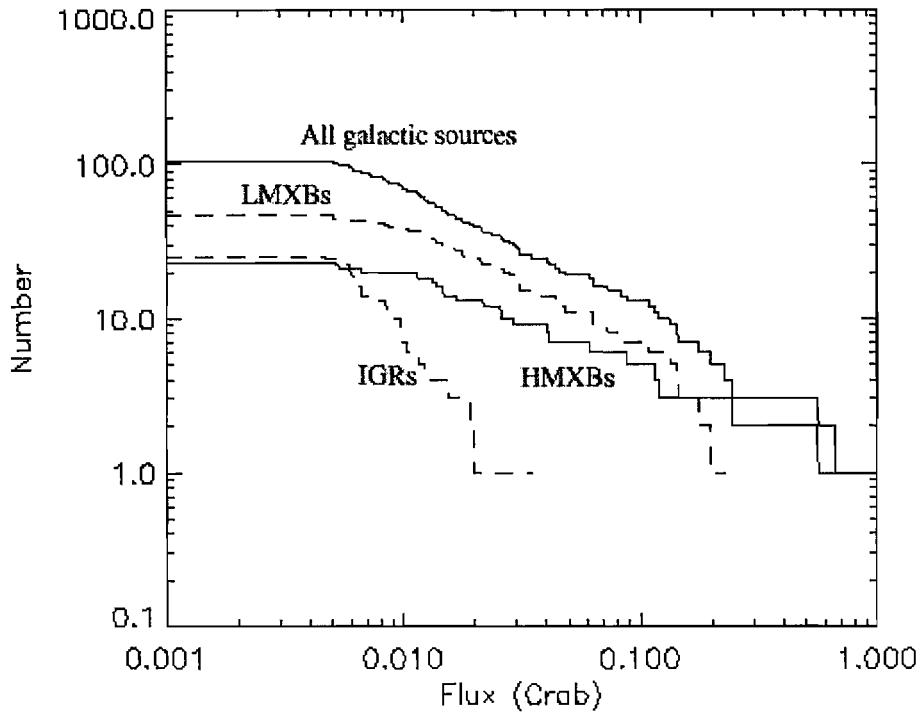

Figure 5.1: The raw Number-Flux relationship for the sources in the 1st INTEGRAL/IBIS survey. The curves shown are for, All galactic sources; LMXBs, HMXBs and the unclassified sources.

tions are plotted in Fig 5.1. The entire galactic source population, the HMXB population, LMXB population and unclassified population distributions are all plotted. The break in the power-law at low fluxes indicates the level of completeness of the samples. At the lowest fluxes we have not observed all of the sources due to exposure and sky coverage limitations, hence the samples are incomplete. The IBIS survey source populations are complete down to a flux level of ~5 mCrab, this corresponds to ~3.5×10^{-11} erg s^{-1} cm^{-2} for a Crab-like spectrum.

5.2.1 Correcting and fitting the LogN-LogS

The incompleteness of the population samples can be corrected by examining the levels of exposure and sky coverage of the survey hence, obtaining slopes indicative of the true population distributions. This correction is complicated by the systematic noise and structures which exist in the IBIS OSA 3.0 images. However, by using the flux error and exposure distributions it is possible to calculate the minimum detectable flux (MDF) as a function of sky exposure. Combining this effect with the actual sky exposure allows the calculation of the effective area of the sky observed down to the minimum detectable flux. This is shown in Fig. 5.2 where sky area, in square degrees is plotted against MDF,

in Crab flux units. The threshold for source detection is defined to be 6σ, corresponding to the level of significance defined as the cut-off for detection in the 1st IBIS/ISGRI survey catalogue (see Chapter section 4.4.4.1).

The effective area of the sky observed by the 1st IBIS/ISGRI survey can then be used to correct the observed number flux distributions shown in Fig. 5.1. The corrected LogN-LogS distributions are shown in Fig.5.3.

Crawford, et al. (1970) showed that the best method for measuring the slope of the number-flux distribution is the maximum-likelihood method. This is an appropriate method for the IBIS data set as all of the detections are of $> 6\sigma$. The best value of α is given by maximising the likelihood function (Murdoch & Crawford, 1973):

$$L = N \ln \alpha - \ln \sum_j A_j (S_{0j}^{-\alpha} - S_{uj}^{-\alpha}) + \sum_j n_j \ln A_j - (\alpha + 1) \sum_i \sum_j \ln S_{ij} \qquad (5.2)$$

where N is the total number of sources, n_j is the number of sources in area A_j, A_j is the area in which the limiting sensitivity is $S_{0j} < S < S_{uj}$ and S_{ij} is the flux of the ith source in the jth area.

This method is applied to each of the individual source populations before and after correction for the sky exposure and MDF. The slope, α, of the fits to each source population are shown in Table 5.1.

Table 5.1: Slope of Number/Flux relation calculated using the maximum likelihood method.

Source Class	Uncorrected Slope	Corrected Slope
All Galactic Sources	-0.81±0.10	-0.91±0.09
LMXB	-0.81±0.13	-0.95±0.13
HMXB	-0.65±0.15	-0.81±0.15
Unclassified Sources	-1.79±0.37	-2.11±0.46

5.2.2 Interpreting the LogN-LogS distributions

Comparing and contrasting the fitted LogN-LogS distributions of the different source classes allows us to see if they are distributed in similar fashion across the sky as compared to one another as well as to the populations of sources observed by other missions. The corrected slope of the galactic source population observed by IBIS has an index of -0.91 ± 0.09. Within the estimated errors is perfectly compatible with the expected slope

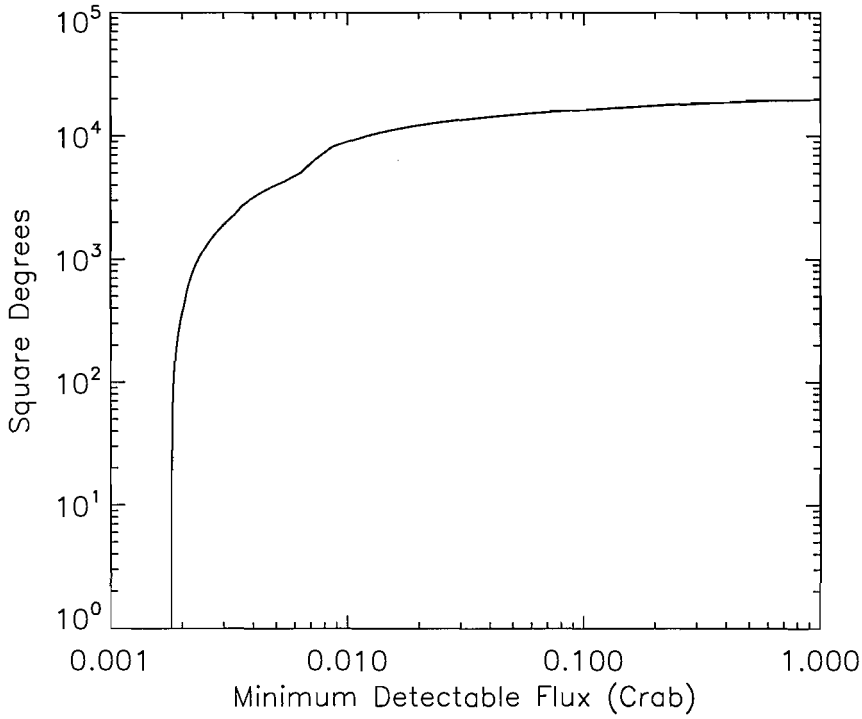

Figure 5.2: The area of sky observed in the survey as a function of the minimum detectable flux (6σ). The flux is in equivalent Crab units.

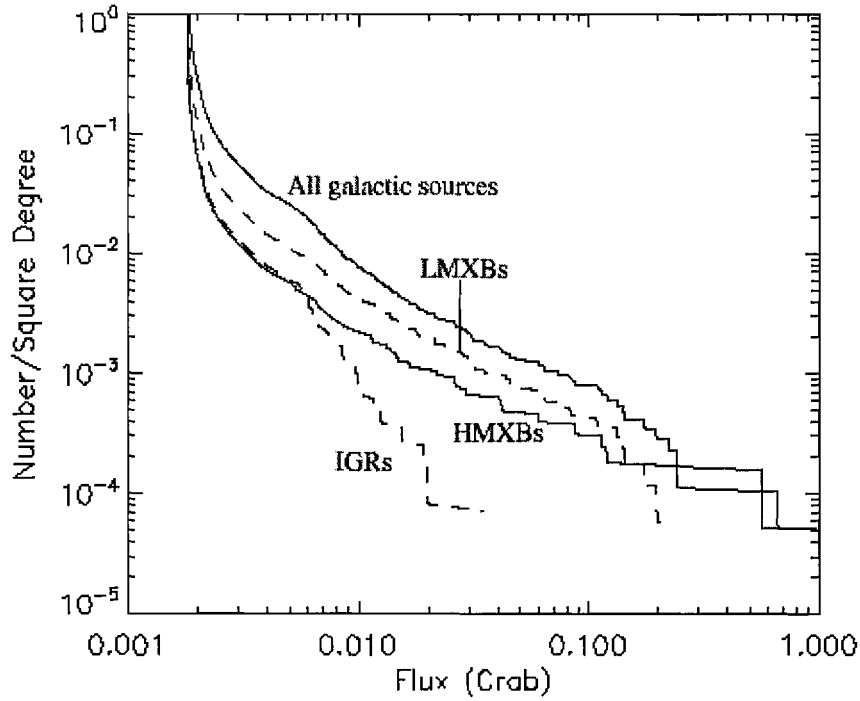

Figure 5.3: The Number-Flux relationships as shown in Figure 5.1 but corrected for exposure and sky area observed.

for a two-dimensional disc population.

The 4U catalogue of sources detected by the Uhuru mission contains 339 sources detected in the 2–6 keV band (Forman et al., 1978). Of these sources ~186 are at low galactic latitudes, $|b| < 20°$. The fitted LogN-LogS is fitted with a power-law of slope -0.4. The Ariel V, 3A catalogue contains 109 sources detected in the 2–10 keV band at $|b| < 10°$ (Warwick et al., 1981). They find a power-law of index -0.62 ± 0.15. In comparison the observed IBIS/ISGRI hard X-ray source population shows a noticeable steeper distribution which is much more consistent with a disc population than either of these early X-ray missions.

More recent X-ray surveys are more consistent with the IBIS/ISGRI measurement. The ASCA Galactic Plane survey (Sugizaki et al., 2001) observed a logN-logS distribution with a power-law index of -0.79 ± 0.04 for sources observed in the 2–10 keV band at $|b| < 0.4°$. The Einstein Galactic Plane survey (Hertz & Grindlay, 1984) finds that the galactic source population is fit with an index of -1.10 ± 0.16. The IBIS/ISGRI measurement falls between both of these values.

It is interesting to note that the early X-ray missions observed power-law indexes of ~0.5 which is consistent with a linear population of sources. Due to the lower sensitivities of these missions it is clear that the brightest high energy sources clearly have a flatter distribution than a disc population. This may explain why the IBIS/ISGRI galactic population appears slightly flatter than the perfect two-dimensional disc population.

5.2.2.1 The X-ray binary populations

It is clear that the 'all galactic source' population is dominated by the LMXB population, which comprises over 40% of the total number of sources in the 1st IBIS/ISGRI Survey Catalogue. Fitting the logN-logS of the LMXB population yields a power-law index of -0.95 ± 0.13, again consistent with a two-dimensional population of sources. This is not unexpected as LMXBs are typically found in the Galactic Bulge and the plane of the disc.

In contrast the HMXB population is observed to have a slightly flatter distribution, with an index of -0.81 ± 0.15. However, the precision of the measurement is such that this measurement is within 2σ of the expected values of both a one-dimensional linear distribution and a two-dimensional disc population. High mass systems are typically located in star formation regions which, within the galaxy, are associated with the spiral arms and so are expected to have a distribution consistent with a linear source distribution. Additionally, the level of precision in the measurements of the slopes of both classes of X-ray binary makes it impossible to distinguish between them based on the available data.

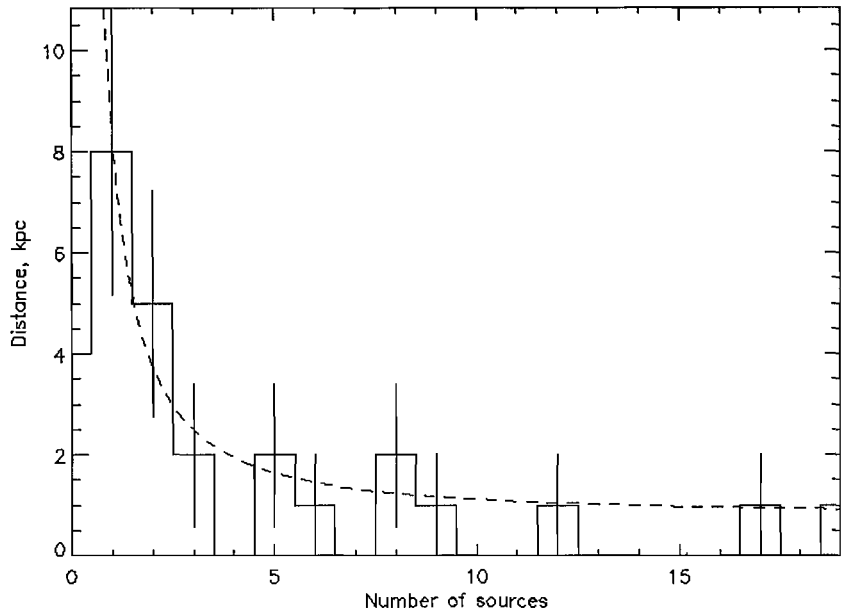

Figure 5.4: A histogram of the absolute distance of unclassified sources away from the galactic centre perpendicular to the line of sight (assuming they are ~8 kpc away). The dashed line represents a power-law fit to the histogram.

5.2.2.2 Properties of the unclassified sources

An exceptionally steep slope is observed for the unclassified INTEGRAL source population. The fit to the index is -2.11 ± 0.46, much steeper than would expected even for contamination by an extragalactic population. However, it must be remembered that these are generally the weakest sources in the 1^{st} IBIS/ISGRI Survey Catalogue and there are not large numbers of sources in this group and so care must be taken when interpreting this measurement. This is is however, reflected in the precision of the fit, and in fact the measurement is within 3σ of the expected disc population slope. The angular distribution of the sources (see Section 5.3.1) indicates that the unclassified sources are concentrated in and around the Galactic Centre. An increase in the space density of these sources in this region could explain the steeper nature of their logN-logS slope.

Working on the assumption that all of the unclassified sources are located in the galactic bulge region we can estimate their spatial distribution along the line of sight by approximating it to the observed distribution orthogonal to our view of the Galactic Centre. The zero point is set to be at the peak of the distribution and take absolute values of the distance of sources from this point because of the low number of statistics. The resulting distribution is shown in Fig. 5.4. The decay in the number of sources away from the Galactic Centre can be fitted by a power law with an index of ~1.3 ± 0.8. This distri-

bution, coupled with the fact that the sensitivity of the first IBIS/ISGRI catalogue does not extend appreciably beyond the galactic centre region, would imply that for a disc population the sources would have a logN-logS distribution with a slope of 1.7 ± 0.4, approximately 1 standard deviation away from the value observed for this population. In general due to the limited number of sources in the first catalogue, and also the remaining systematics affecting the imaging process these results are necessarily subject to several sources of error. This can only be overcome by future editions of the survey which have a larger and more complete sample of this source population. Nevertheless they provide qualitative information on the behaviours of galactic source populations above 20 keV.

5.3 The Angular Distributions

The galactic locations of the γ-ray emitting sources detected in the 1st IBIS/ISGRI Survey Catalogue are shown in Fig. 5.5. The sources are shown in a restricted AITOFF projection with the Galactic Centre located at the origin of the co-ordinate system. The open circles correspond to the positions of LMXBs, the filled circles to HMXBs, the unclassified sources are represented by the triangles. Superimposed on this sky map are contours of the sky exposure. It is readily apparent that the first year of INTEGRAL observations have been strongly biased toward the study of the Galactic Plane and in particular the Galactic Centre, hence the first IBIS/ISGRI catalogue is essentially a survey of galactic sources.

Also apparent from Fig. 5.5 is the level of non-uniformity in the exposure of the Galactic Plane and especially the dominance of exposure in the Galactic Centre. However, despite the uneven levels of exposure, the HMXBs observed in the 1st IBIS/ISGRI Survey Catalogue are clearly well constrained to the Galactic Plane. The LMXB population, however, shows a much wider distribution consistent with a population associated with the galactic bulge region. Also evident, is the pre-disposition of the unclassified sources to lie in and around the galactic centre region, however this may be an effect of exposure.

5.3.1 Galactic longitudinal distributions

Looking at how the sources lie along the Galactic Plane gives an indication of their angular distribution from which we can infer implications regarding their actual spatial distribution. However, it must be remembered that the Earth lies approximately 8 kpc from the centre of the galactic disc. Hence, sources at $|l^{II}| = 0°$ lie toward the Galactic Centre, whereas $90° < |l^{II}| < 180°$ exist behind the Earth with respect to the Galactic Centre. An

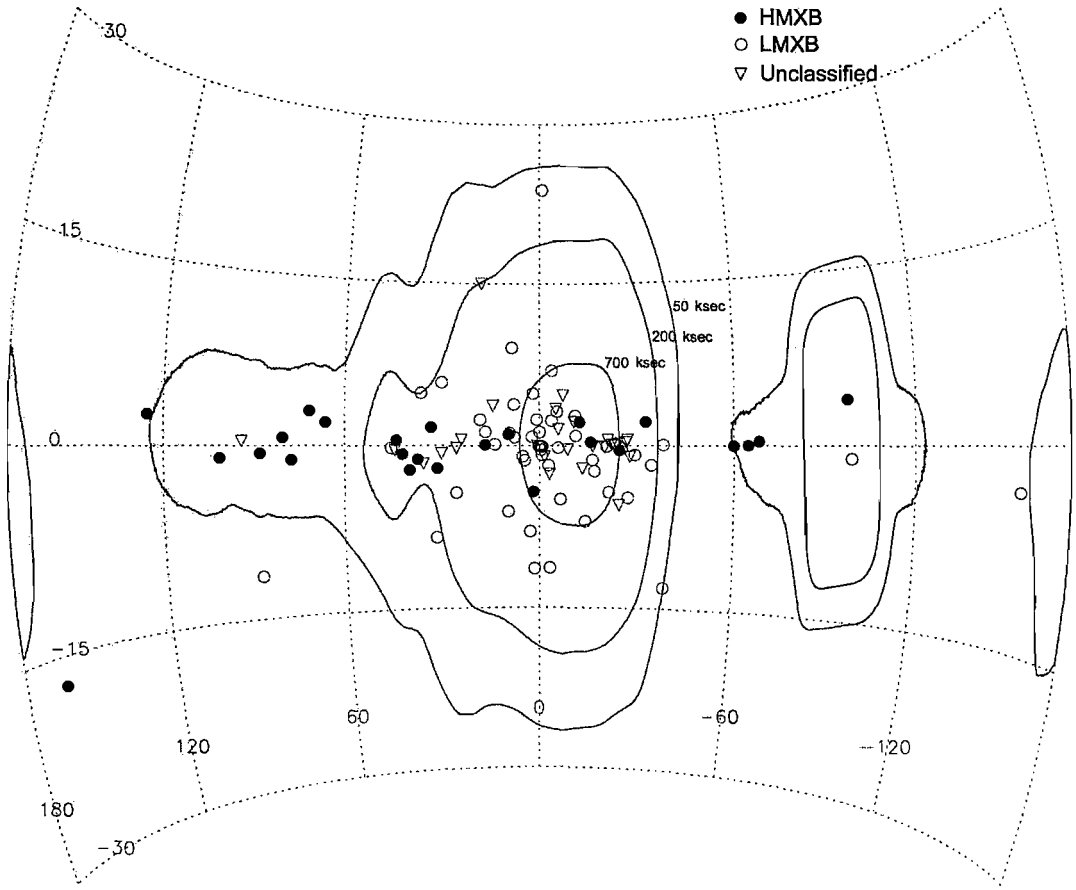

Figure 5.5: The galactic distribution of sources in the 1st IBIS/ISGRI catalogue. Filled circles represent HMXBs; open circles represent LMXBs; triangles represent unclassified INTEGRAL sources. Overlaid are contours of exposure time, 50, 200 and 700 ksec.

obvious important feature of the Galactic disc is the presence of the spiral arm structures. When viewed in the two-dimensional angular plane from the Earth, the arms are most evident in spiral arm tangent regions. The locations of the spiral arm tangents are given by Englmaier & Gerhard (1999):

- The Sagittarius arm, l^{II} ~49°
- The Scutum arm, l^{II} ~30°
- The 3-kpc arm, l^{II} ~-21°
- The Norma arm, l^{II} ~-31°
- The Centaurus arm, l^{II} ~-51°

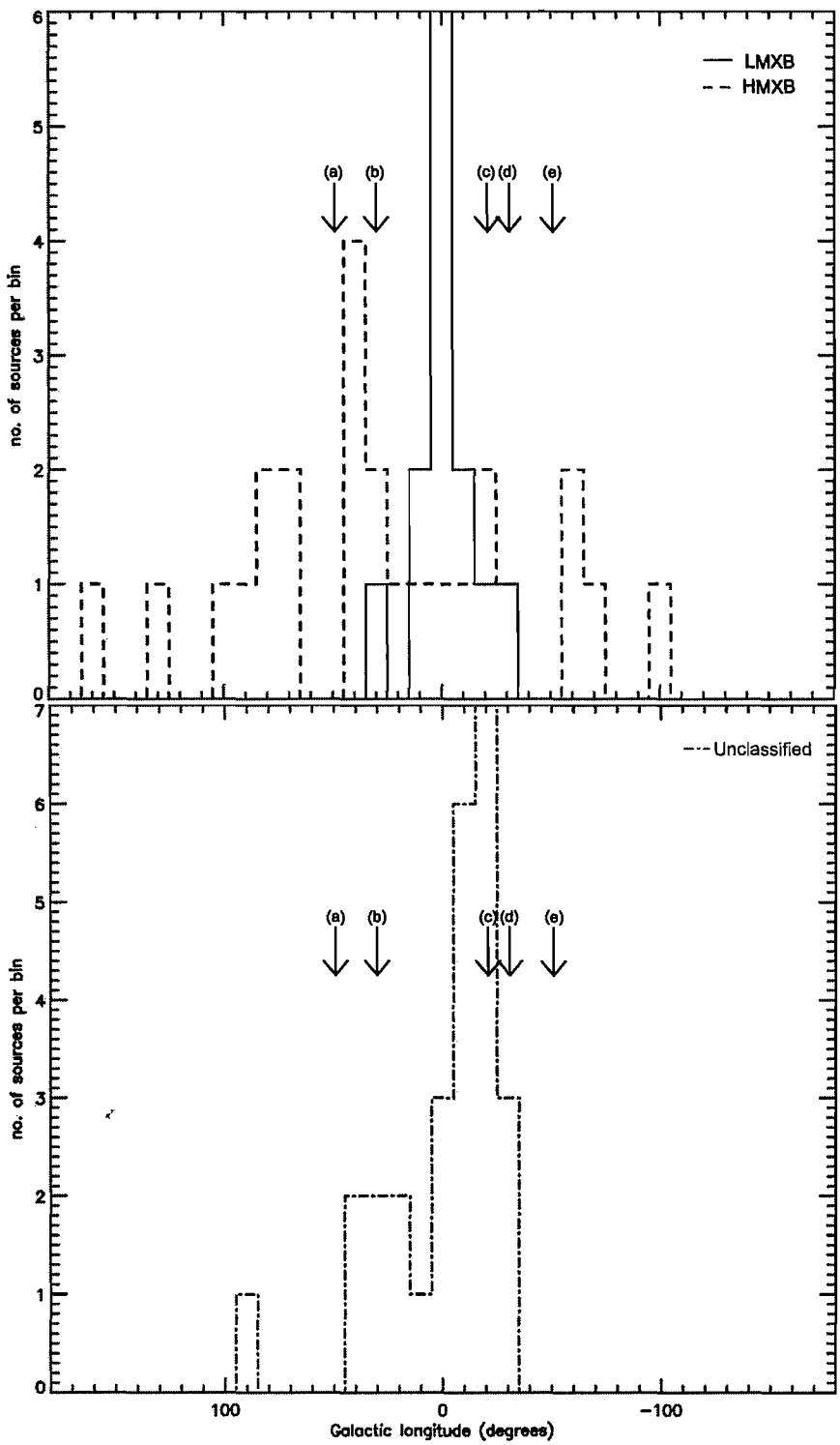

Figure 5.6: The Galactic longitude distribution of HMXBs, LMXBs and unclassified sources. Labelled are the locations of the spiral arm tangents: (a) - Sagittarius; (b) - Scutum; (c) - 3-kpc; (d) - Norma; (e) - Centaurus, as given by Englmaier & Gerhard (1999).

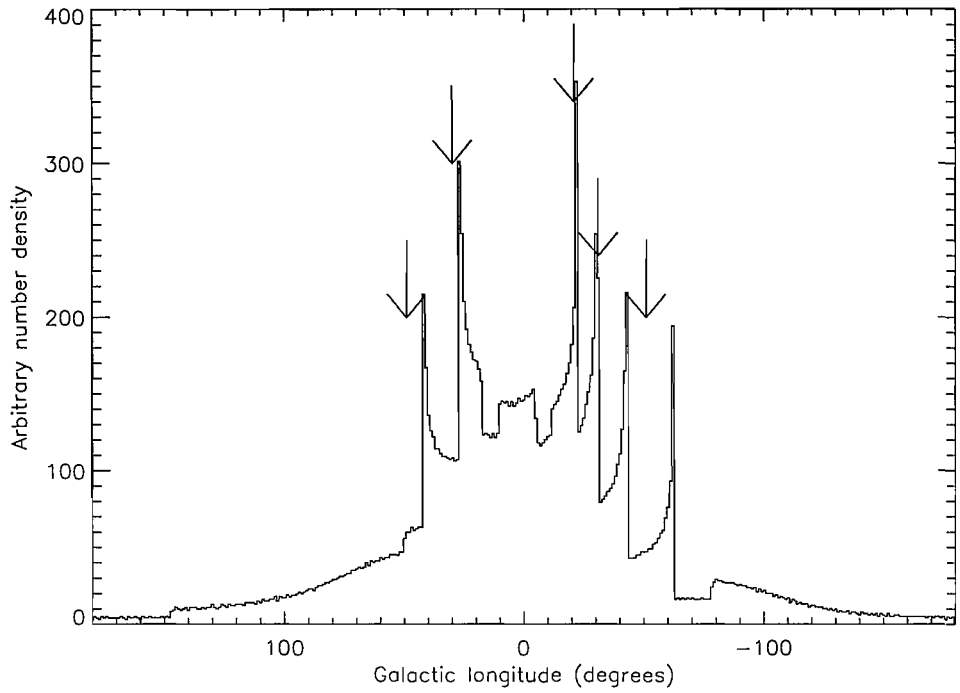

Figure 5.7: The angular density distribution resulting from the spiral arms of the galaxy. The 4-arm spiral model of Vallée (2002) is collapsed into an angular distribution, assuming the Earth is 8 kpc from the Galactic Centre. The density is in arbitrary units assuming that the spiral arms have a constant mass density. the arrows indicate the known locations of the spiral arm tangents (Englmaier & Gerhard, 1999).

The angular distributions of the HMXB and LMXB source populations is shown in the upper histogram in Fig. 5.6. It is immediately clear that these two source populations are not distributed in the same fashion along the Galactic Plane. The LMXBs are concentrated in the region surrounding the Galactic Centre, in a symmetric fashion, which is completely to be expected for a population associated with the Galactic Bulge.

The HMXB distribution is spread out much more across the entire Galactic Plane, however, in a non-uniform fashion. Also, plotted on Fig. 5.6, are the locations of the spiral arm tangents as obtained from radial velocity measurements of gas along the Galactic Plane (Englmaier & Gerhard, 1999). The non-uniformity of the HMXB distribution appears to include an over-density of sources at longitudes near to the spiral arm tangents. Additionally, a number of HMXBs are seen at $l^{II} \sim \pm 90°$, which is indicative of systems located within our particular spiral arm.

Associations with spiral arms is to be expected for high mass systems as these are young stellar systems with limited life spans and hence should be correlated with areas with levels of star formation activity. This association has previously been identified

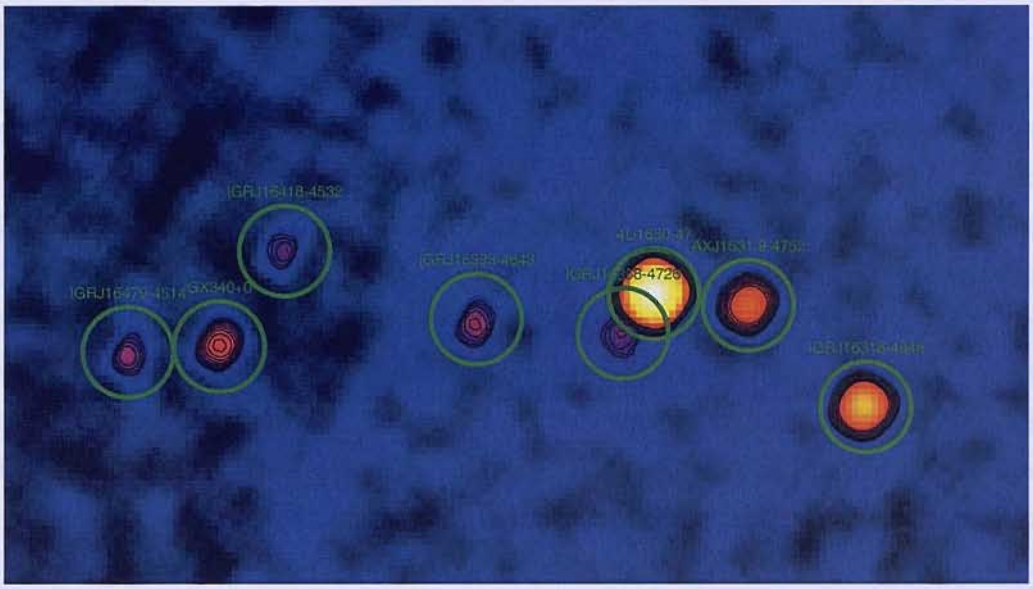

Figure 5.8: The Norma spiral arm tangent region of the 30–50 keV significance map produced in the 1st IBIS/ISGRI Survey Catalogue. Contours indicate significances between 6 and 20 σ. This area contains the highest concentration of newly detected sources by INTEGRAL.

by inspection of data obtained by the Ginga mission (Koyama et al., 1990) and by the RXTE/ASM instrument (Grimm et al., 2002).

Fig. 5.7 indicates the modelled distribution of HMXB systems assuming that they are uniformly distributed along spiral arms in significant numbers. This was achieved by collapsing the 4-arm logarithmic spiral model of Vallée (2002) into an angular distribution. This is obviously an over-simplified model as it does not take into account any decay in the mass distribution in the spiral arms, any width the the arms or account any luminosity/extinction corrections. However, it does clearly show an over-density would be expected at the spiral arm tangents. The only way to confirm an HMXB association with this is to be obtain, deeper sampling of the Galactic Plane and hence a more statistically significant sample population to compare to modelled distributions.

5.3.1.1 The locations of the unclassified sources

The longitudinal distribution of the unclassified sources is shown in the lower panel of Fig. 5.6. Upon first inspection the unclassified INTEGRAL sources appear to have a longitude distribution concentrated around the Galactic Centre, similar to that of the LMXBs. This is somewhat misleading as the Galactic Centre region has had the largest exposure and hence is the area in which we are most sensitive and therefore most likely to discover these new, weaker sources. A closer examination these sources are not symmetrically

distributed about the Galactic Centre. In fact the peak of the distribution correlates rather well with the locations of the 3-kpc and Norma spiral arm tangents. This is not surprising as the Norma spiral arm region has been reported to have an over-abundance of newly detected INTEGRAL sources by Walter et al. (2004). An image extracted from the 1^{st} IBIS/ISGRI Survey Catalogue 30–50 keV significance mosaic of this region is shown in Fig. 5.8; five INTEGRAL sources are clearly visible in close proximity to one another.

The unclassified sources are in no way expected to belong entirely to one class of object and some may be associated with the Galactic Bulge, whilst others are associated with the disc and spiral arms. However, due to the small number of sources it is impossible to see if there is definitely a dominant association. As in the case of the HMXB population this can only be resolved by a larger population sample and a more uniform exposure.

5.3.2 The galactic latitudinal distribution

The angular distribution off the Galactic Plane of the sources is shown in Fig. 5.9. The Low mass X-ray binary systems show a broad distribution perpendicular to the plane of the Galaxy. Again, this is expected for a source population comprising of old stellar systems and hence belonging to the Galactic bulge population of sources. In contrast, the high mass systems have a much sharper cut-off at a smaller angle from the Galactic Plane as per a population associated with the disc of the galaxy.

The unclassified systems have a latitude distribution which, by eye, appears more like that of the HMXBs. It is a narrow distribution cut-off at approximately 5° from the Galactic Plane. The Kolmogorov-Smirnov test (KS-test) can be used to determine if two datasets differ significantly. The advantage of the KS-test is that it is non-parametric and distribution free, hence it makes no assumptions about the distribution of the sample data. Additionally, the KS-test is able to cope with uneven sample sizes, making it ideal to compare the latitude distributions.

Application of the KS-test yields the following:

- An 83% probability that the HMXBs and unclassified sources are drawn from the same sample distribution.
- A 29% probability that the HMXBs and LMXBs are drawn from the same sample distribution.
- A 55% probability that the LMXBs and unclassified sources are drawn from the same sample distribution.

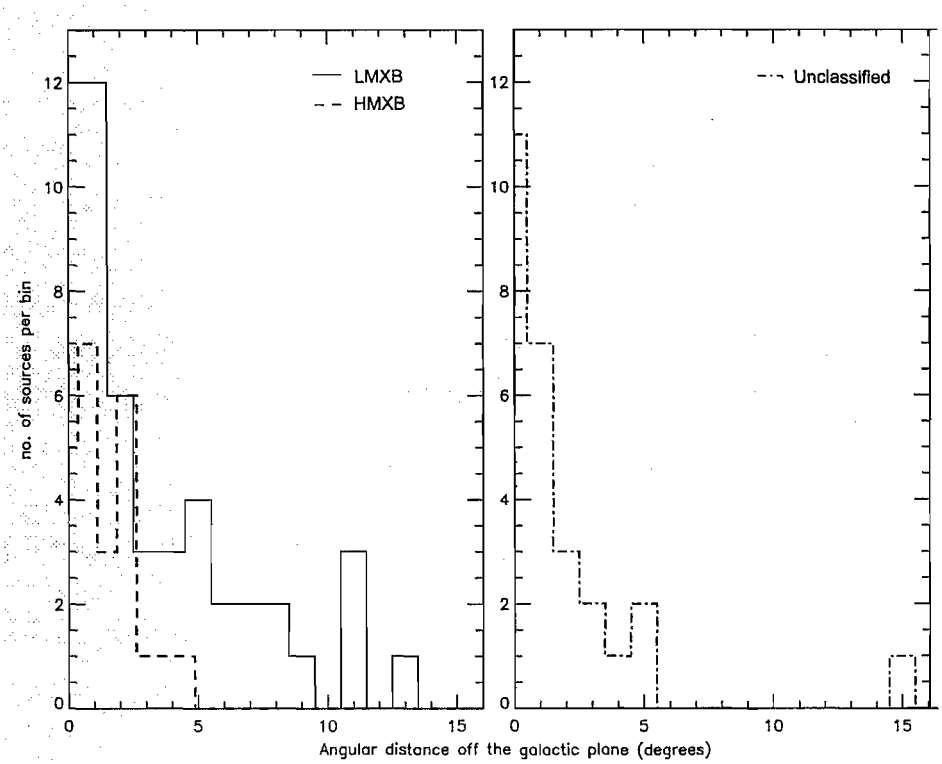

Figure 5.9: Angular distribution of the source populations away from the Galactic Plane.

The results of the KS-test are not significant in the comparison of any of the source populations and consequently we cannot reject the null hypothesis that they are all drawn from the same underlying distribution. It is expected that the LMXB and HMXB latitudinal distributions should differ however the available sample size does not yield a significant result to confirm this. Comparing the unclassifed sources with the known HMXB and LMXB populations may not yield a significant result beecause the unclassified population could consist of a mixture of both HMXB and LMXB sources, or be a separate generic set. Only if there is a significantly dominant sub-group could a clear result ever be expected.

Although the longitude distribution is not entirely dissimilar to the LMXBs, this is probably distorted by an effect of exposure and the source concentration around spiral arm tangents suggests a potential association with high mass systems. This association is further supported by their latitude profile that more closely resembles that of the HMXB. However the unclassified sources are very much associated with the Galactic Centre region, this association may be generic in some way and possibly an artifact of the fact that this is a γ-ray selected set of sources and consequently is not sensitive to the effects of higher photo-absorption generally suffered through conventional soft X-ray observations.

5.4 The spatial distributions

To investigate the actual spatial distributions of the sources requires knowledge of their distances from the Earth. Accurate distance estimates of sources is an important piece of astronomical information and yet it is one of the hardest attributes to establish. This difficulty lies in the lack of availability of 'standard candles' within our own galaxy. For extragalactic sources distances can be obtained from redshift measurements based upon recession velocities, observations of Cepheid Variables and type I supernovae. However, for galactic distances either an observable parallax is required or the intrinsic source luminosity must be known. In the case of X-ray binaries an estimate of distances is often made by assuming that transient bursting behaviour is at the Eddington luminosity limit.

The available published literature was searched for information on the distances to the sources of the 1^{st} IBIS/ISGRI Survey Catalogue (White & van Paradijs, 1996; Macomb & Gehrels, 1999; Kuulkers et al., 2003). Of the 109 catalogue sources distance estimates were found for ~70 sources including a large proportion of the HMXB and LMXB sources. A key resource in identifying distances to the neutron stars and black holes in known LMXB systems came from the work of Jonker & Nelemans (2004). Obviously, there are currently no distance estimates for the INTEGRAL unclassified source population.

5.4.1 Distance measurement methods

Different methods were used across the literature to estimate distances, with each method having its own limitations and assumptions. For those neutron stars exhibiting type I bursts a distance can be inferred from observations of Eddington limited bursts. As discussed in Section 1.5.1.1, type I bursts in LMXBs result from thermonuclear flashes on the surface of the neutron star resulting from the build-up and fusion of hydrogen (Lewin et al., 1993). The maximum luminosity of these bursts is 2–4 $\times$ 10^{38} ergs cm^{-2} s^{-1}, corresponding to the Eddington luminosity of a neutron star. The radiation pressure of the thermonuclear flash forces the photosphere of the neutron star to expand and is followed by a subsequent contraction. During this time the luminosity stays approximately constant at the Eddington limit. The large number of bursts from both newly detected and previously known sources by the Wide Field Camera on-board the BeppoSAX mission allowed this property to be taken advantage of in the cases of many sources (e.g. Cocchi et al. (2001); Kuulkers et al. (2003); in't Zand et al. (2004)).

In the cases of systems where an optical identification of the companion star has been made it is possible to identify the spectral type of the companion. Based upon the ob-

served and expected magnitudes of these stars it is the possible to estimate distances to the systems. Jonker & Nelemans (2004) compared the distances obtained for sources where both methods were viable and found that the differences between the two methods implied that using Eddington limited bursts over estimated the source distance whilst spectral measurements could be seen to be underestimating the distance. In some respects this is to be expected, in the case of type I burst it must be assumed that the bursts are Eddington limited and hence are really an upper limit to the distances and hence on average should be seen to be an over estimate. Errors in classifying the spectral type or in estimating the extinction in the line of sight can equally lead to errors in the case of the optical method. However, in this case the errors should equally lead to an under estimate as an over estimate of the distance.

In the cases of the black hole candidate systems there are two other possible distance methods. One method is the estimation of the distance based upon the observed interstellar absorption properties. The other is from measurements of the observed proper motions of the receding and approaching lobes in systems where symmetric jets are present. An example of this method is applied by Fender et al. (1998) in the case of radio observations of GRS 1915+105.

5.4.2 Modelling the galaxy

To model the spiral arm structure of the galaxy we use the work of Vallée (2002). Using all of the published results from 1995–2001 they estimate that the Milky Way incorporates a 4-arm spiral pattern with a mean pitch angle of 12° inwards. This was achieved by fitting logarithmic model arms to the observed spiral arm tangent points and the position angle of of the Galaxy's central bar.

A schematic of this model is shown in Fig. 5.10. The position of the Sun is indicated by the five-pointed star. The locations of those X-ray binaries for which distance measurements are available are also indicated; HMXB systems are represented by filled circles and LMXB systems are represented by open circles. It is immediately obvious from Fig. 5.10 that these two classes of binary system are not distributed across the plane of the galaxy in the same fashion. As was indicated by their angular distribution (see Section 5.3.1) the LMXBs are concentrated in the Galactic Centre. However, their distance measurements now confirm this to a higher degree, showing that the majority of the low mass systems, ~60% are in fact clustered within ~3 kpc of the Galactic Centre.

The high mass X-ray binaries are typically seen to be outside of this 3 kpc radius. This is to be completely expected if the HMXBs are associated with the spiral arms as the arms

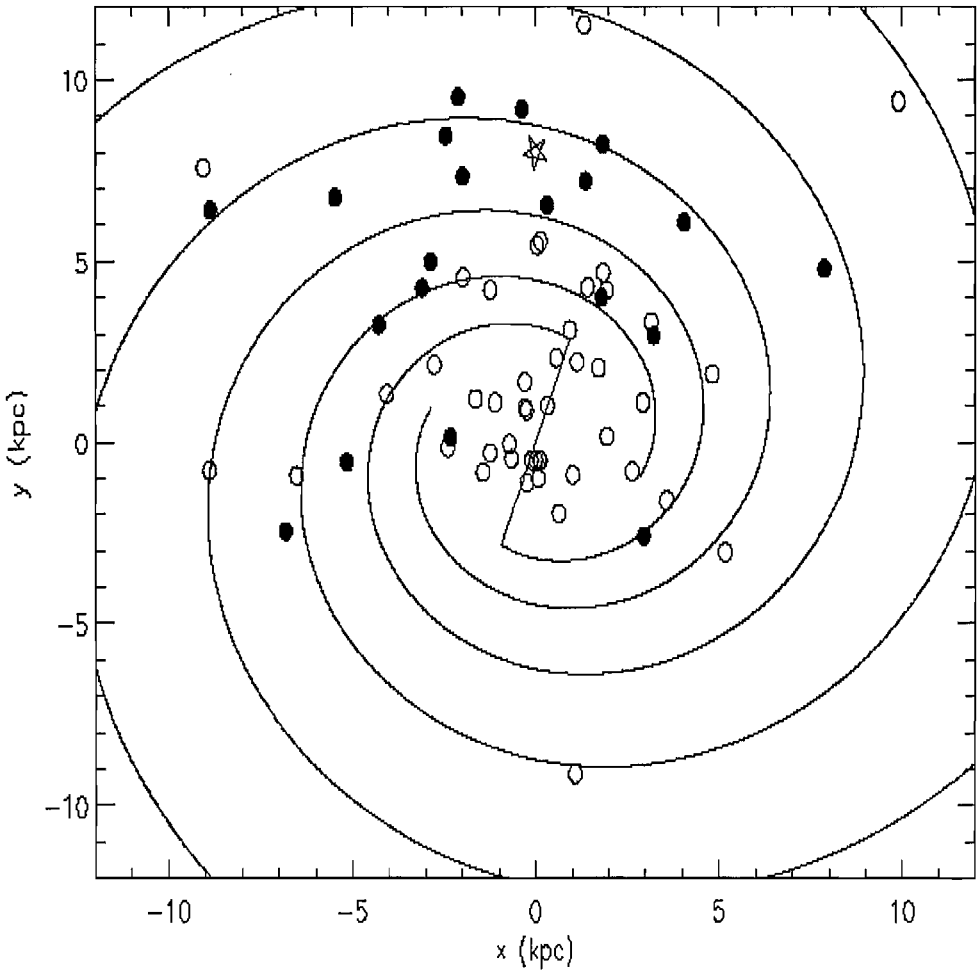

Figure 5.10: The galactic distribution of the subset of HMXBs (filled circles) and LMXBs (open circles) for which distance estimates are available in the literature. The Sun is represented by the star symbol and is 8 kpc away from the galactic centre. Superimposed is the 4-arm spiral model of Vallée (2002). Source distance errors are on average of the order of a kpc.

in the model of Vallée (2002) begin at ~3 kpc from the centre of the Galaxy. However, for those systems >3 kpc from the Galactic Centre, it is impossible to say whether LMXB or HMXB follow the spiral structure more strongly. For a useful quantitative measurement of the correlations of the two classes of binary to the spiral arm pattern a larger sample set of systems and a more complex model would be required.

Theoretically the appearance of the HMXB epoch should lag behind the leading edge of spiral arms. This is brought about by the density wave inducing star formation and the HMXB phase subsequently developing some time later after one of the binary components has evolved into a compact object. A broad time window is to be expected since the period of elapsed time from star formation to the appearance of a HMXB system is

dependent upon the initial masses of its components, and any time lag would naturally reflect this spread. For example Tauris & van den Heuvel (2004) calculate an age of 24.6 million years for a system which starts with 14.4 $M_\odot$ and 8 $M_\odot$ stars, and van den Heuvel & Heise (1972) calculate an age of 15 million years for a system which starts with a 16 $M_\odot$ and 3 $M_\odot$ star.

An investigation of this systematic time lag is not possible with the available data set. An analysis of this would require a larger population of HMXBs with well defined distance measures and a model of the galaxy which incorporates the quasi-stationary spiral structure hypothesis proposed by Lin et al. (1969). The key parameter in modelling the spiral structure is Ω_P the angular velocity of the spiral pattern. Recent measurements of Ω_P based upon observations of open clusters by Dias & Lepine (2005) strongly indicate that the spiral pattern rotates as a rigid body with Ω_P ~25 km s^{-1} kpc^{-1} at the distance of the Sun from the galactic centre. This implies that the Sun will effectively remain within its spiral arm, whilst systems inside the radius of the Sun's orbit will move ahead of their spiral arms at a velocity dependent upon their distance from the Galactic Centre.

5.4.3 Estimating population scale heights

Combining the source distance estimates with the galactic latitude distribution allows an estimation of the physical scale height of the high and low mass systems with respect to the Galactic Plane. The distribution of the HMXB and LMXB distances out of the Galactic Plane are shown in the top and middle panels of Fig. 5.11 respectively. In each case the distribution was fit with a simple exponentially decreasing function of the form:

$$N = ke^{-\alpha z} \tag{5.3}$$

where N is the number of sources found at a height, z kpc, off the plane. The result of fitting this function to the different source distributions is shown in Table 5.2. If we make the assumption that all of the unclassified sources are located close to the galactic bulge region, i.e. they have a distance of ~8 kpc, then we can construct a pseudo scale height distribution for this group of sources. This is shown in the lower panel of Fig. 5.11.

It is anticipated that the scale heights of the HMXB and LMXB populations are different, and that the vertical distributions reflect the age disparity of their parent stars. Unfortunately, the precision of the observed scale heights shown in Table 5.2 is such that the HMXB, LMXB and unclassified sources have scale heights which are within one sigma of each other and are hence indistinguishable. However it is interesting to note that the scale height of this γ-ray selected HMXB set is consistent with the value of 150pc found

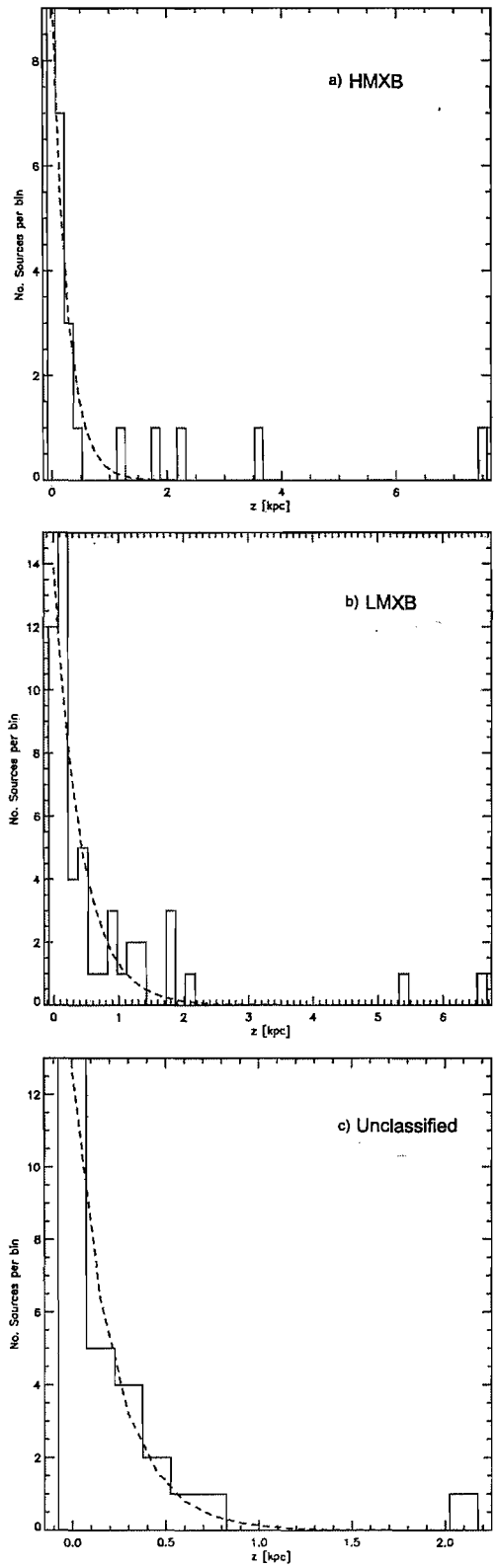

Figure 5.11: The distribution of the height off the plane of the different source populations seen by INTEGRAL: a) HMXBs; b) LMXBs; c) Unclassified sources (assuming they are ~8 kpc away). The dashed lines represent exponential fits.

Table 5.2: Summary of the characteristics of the principal populations of the IBIS-ISGRI sources in terms of their distributions above the Galactic Plane.

Source type	k	α	Scale Height (pc)
HMXBs	9 ± 3	4 ± 1	240^{+90}_{-40}
LMXBs	13 ± 3	2.9 ± 0.6	350^{+90}_{-60}
Unclassified sources	12 ± 3	4 ± 1	240^{+90}_{-40}

for the HMXBs selected from RXTE/ASM data (Grimm et al., 2002). The lack of errors on the HMXB scale height as measured by Grimm et al. (2002) make it difficult to accurately compare the values. Likewise the vertical distribution of the γ-ray selected LMXBs is compatible with the 410^{+100}_{-80} pc scale height of the RXTE/ASM sample of the LMXB disc population however, our HMXB scale height lies only $\sim 2\sigma$ from this measurement as well. If we take the unclassified source "scale height" at face value, then it is very interesting to note that, whilst they appear to conglomerate in the galactic bulge region, their vertical distribution is the same as the HMXB systems, reflecting the similarities found in their longitude distributions.

5.5 Source Luminosity Functions

In addition to allowing an exploration of the spatial distributions of the different INTEGRAL source populations the distances to the sources can be used to construct the luminosity function for each distribution. However to construct an accurate luminosity function a number of corrections are required to account of the uneven level of sky exposure, the flux limited nature of the population sample and any incompleteness in the identification of object classes.

5.5.1 The luminosity function correction

To correct the apparent luminosity function requires the construction of a model of the stellar mass distribution of the galaxy as performed by Grimm et al. (2002). We construct a model of the galaxy comprising of two components; one representing the galactic disc and the other the bulge. Dehnen et al. (1998) derive the following functions for the disc and bulge components:

$$\rho_{Bulge} = \rho_{0,Bulge} \cdot \left(\frac{\sqrt{r^2 + \frac{z^2}{q^2}}}{r_0} \right)^{-\gamma} \cdot exp\left(-\frac{r^2 + \frac{z^2}{q^2}}{r_t^2} \right) \tag{5.4}$$

$$\rho_{Disc} = \rho_{0,Disc} \cdot exp\left(-\frac{r_m}{r} - \frac{r}{r_d} - \frac{|z|}{r_z}\right) \tag{5.5}$$

where $\rho_{0,Bulge}$ and $\rho_{0,Disc}$ are the normalisations, r is the distance in the plane to the galactic centre, z is the distance out of the galactic plane and R is the distance from the Galactic Centre in spherical coordinates. The other parameters are: q, the oblateness of the bulge; r_0, the scale length of the bulge; r_t, the truncation radius of the bulge; r_d, the scale length of the disc; r_z, the vertical scale of the disc; r_m, the inner disc cut-off

The INTEGRAL source sample is insufficient to derive these parameters. Hence we use the parameters obtained by the fitting of RXTE/ASM XRBs to the galactic model by Grimm et al. (2002). However we adjusted r_z to match our measured scale heights. The parameters obtained by Grimm et al. (2002) are given in Table 5.3. All of the distances are in kilo-parsecs. The standard galaxy model uses a mass ratio of 2:1 for disc:bulge. We use the same normalisations as Grimm et al. (2002); $\rho_{0,Disc}$ is taken as 0.05 $M_\odot$ pc^{-3} observed in the solar neighbourhood (Zombeck, 1990). To correct the LMXB population both model components were used whereas the HMXB population uses only the disc component.

Table 5.3: The parameters of the standard Galaxy model used by Grimm et al. (2002).

Parameter	Meaning	Value	
		HMXB	LMXB
q	oblateness of bulge	–	0.6
γ	–	–	1.8
r_0	scale length of bulge	–	1 kpc
r_t	truncation radius of bulge	–	1.9 kpc
r_d	scale length of disc	3.5 kpc	3.5 kpc
r_m	inner disc cut-off	6.5 kpc	6.5 kpc
R_{mass}	mass ratios Disc:Bulge	1:0	2:1

To correct the observed luminosity function we calculate the fraction of the galactic mass which is observable at any given luminosity. The correction is taken from Grimm et al. (2002) and is shown below:

$$\frac{dN}{dL} = \left(\frac{dN}{dL}\right)_{obs} \times \frac{M_{tot}}{M(< D(L))} \tag{5.6}$$

Where $\frac{dN}{dL}$ is the true luminosity function, $\left(\frac{dN}{dL}\right)_{obs}$ is the observed luminosity function, M_{tot} is the total mass of the galaxy, M(<D) is the mass of the galaxy inside a distance D from the Sun. D(L) is defined as:

$$D(L) = min\left(\sqrt{\frac{L}{4\pi F_{lim}}}, D_{max}\right) \tag{5.7}$$

where F_{lim} is the limiting flux of the sample and D_{max} is the maximum distance from the Sun of the sources used in constructing the luminosity function. We take F_{lim} as ~5mCrab in the 20-100 keV energy band which corresponds to ~8.5×10^{-11} ergs cm^{-2} s^{-1}. The maximum distance at which we detect sources approximates to the galactic centre distance. Consequently this means that it is only at relatively low luminosities that D_{max} does not correspond to D(L). As previously discussed the majority of our exposure is in the vicinity of the Galactic Centre. To compensate for the uneven exposure we modified F_{lim} for the four quadrants of the galactic plane. As the sensitivity is proportional to the square root of the exposure and that the maximum depth of our sample is ~8 kpc the change in the luminosity function correction within our range of exposures is <10%.

5.5.2 The corrected luminosity functions

The population of accreting X-ray binaries are the brightest, persistent sources of X-ray and soft γ-ray emission in the sky. The emission properties of these systems are dictated, principally, by the nature of the compact object in the system. In the case of neutron stars the strength of the magnetic field is also an important factor in the determination of the accretion flow geometry and hence the high energy emission properties of the system. Those with high magnetic fields, B ~ 10^{12} Gauss, will disrupt the accretion disc at several hundred neutron star radii and channel the accreting material down the magnetic field lines onto the neutron star poles. In the case of low magnetic fields, B < 10^{10} Gauss, an accretion disc can form almost to the neutron star surface.

As discussed in Section 1.5 the majority of neutron stars in low mass X-ray binaries are not observed to be pulsars. This is believed to be associated with LMXBs being an old population in which the magnetic field of the neutron star has diminished. Hence, these systems are believed to generally have low magnetic fields. These are also the systems from which type I X-ray bursts are observed. In fact it is thought that type I X-ray bursts are suppressed in systems in which the neutron star has B > 10^{10} Gauss (Lewin & Joss, 1983).

High mass X-ray binaries on the other hand are regularly observed to have an X-ray pulsar. This is explained by the relative youth of these systems. As HMXBs are expected to live for ~10^7 years a neutron star is expected to have a magnetic field closely resembling that which it was born with. That these systems have such high magnetic fields also then explains why type I X-ray bursts are not observed from these systems. The detection of

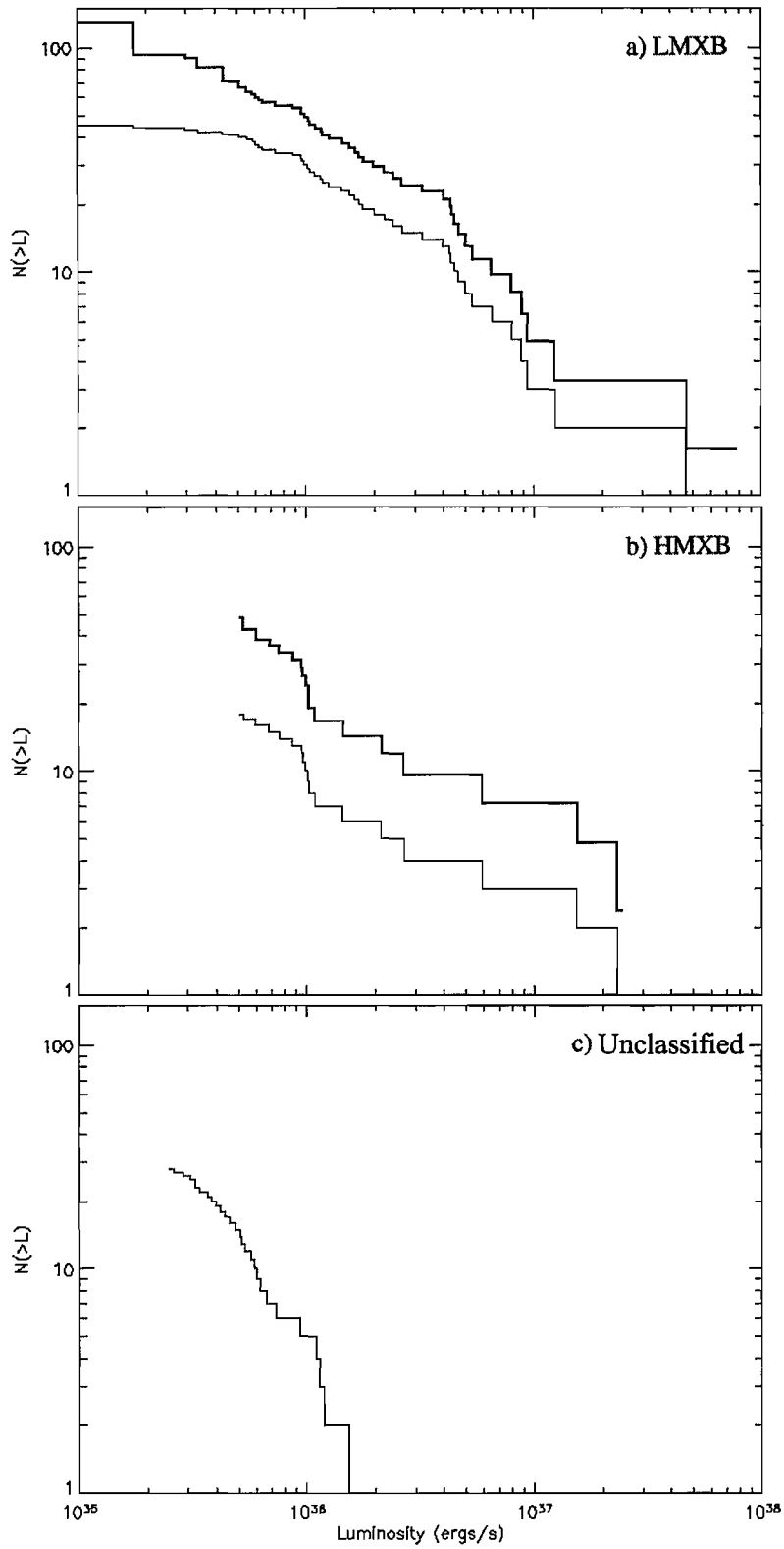

Figure 5.12: The 20 – 100 keV luminosity functions of: a) LMXBs; b) HMXBs; c) Unclassified sources (assuming a distance of ~ 8 kpc). The thin line represents the uncorrected luminosity function. The thick line represents the corrected luminosity function as described in the text. The unclassified sources are uncorrected as their source population is undetermined.

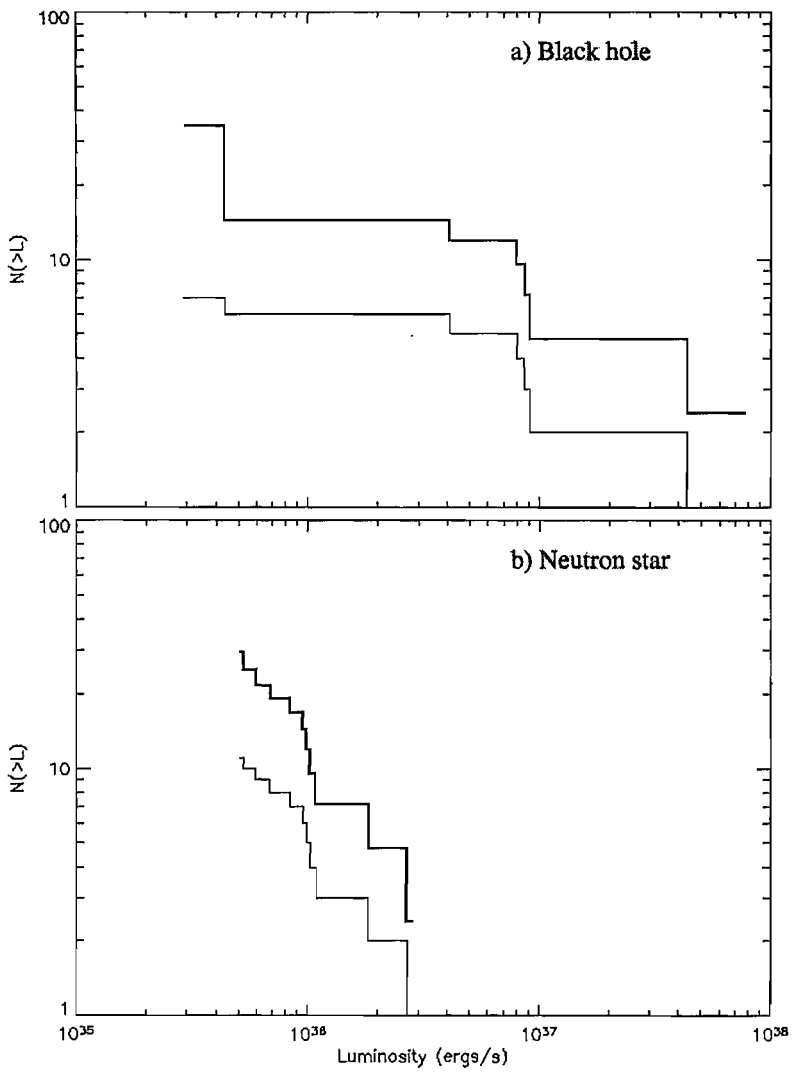

Figure 5.13: The 20 – 100 keV luminosity functions of the IBIS/ISGRI sources separated according to the nature of the compact object: a) black holes; b) neutron stars. The thin line represents the uncorrected luminosity function. The thick line represents the corrected luminosity function as described in the text.

cyclotron lines in the high energy spectra of these sources can be used to directly measure the magnetic field of the neutron star in these systems (Psaltis, 2004; Coburn et al., 2002).

The apparent and corrected luminosity functions for the high mass and low mass systems are shown in Fig. 5.12. Also shown is the apparent luminosity function for the unclassified sources assuming, again, that they lie in the region around the Galactic Centre. No correction is made for this group as we do not know their origin and hence do not know their relationship with the different galactic model components. These luminosity functions are given for the 20–100 keV energy band.

The LMXBs are seen to spread their 20 – 100 keV luminosities relatively consistently up to and beyond 10^{37} ergs cm^{-2} s^{-1}. The vast majority of the high mass systems appear to have luminosities of approximately 10^{36} ergs cm^{-2} s^{-1}. This luminosity is unsurprising as this is typical expected luminosity of an HMXB where the source of accretion is the stellar wind. This implies that the majority of the X-ray emission by the HMXBs is generated by this form of accretion. The distribution of the unclassified sources exhibits the low luminosity characteristics of the low mass systems, but also a tendency to favour luminosities close to 10^{36} ergs cm^{-2} s^{-1}.

Rather than using the overall classification of the system as a discriminator we can also construct luminosity functions based upon the nature of the compact object, i.e. black hole candidate or neutron star. In Fig. 5.12 the γ-ray luminosity functions of the black hole candidate and neutron star systems are presented. As only a sub-set of the γ-ray sample are systems in which the nature of the compact object has been defined these luminosity functions are based on small numbers. Despite this, there are noticeable differences between these two luminosity functions. The majority of the 20–100 keV luminosities of black hole systems appear to exist around 10^{37} ergs cm^{-2} s^{-1}. The neutron star systems do not appear to emit γ-ray fluxes much in excess of 10^{36} ergs cm^{-2} s^{-1}. It is interesting to note that comparing Fig. 5.12c and Fig. 5.13 the unclassified sources appear more like the neutron star systems than the black hole candidates. Similarly, looking at the overall system classifications these may also be pre-dominantly high mass systems. The use of a $\sim 10^{37}$ ergs cm^{-2} s^{-1} soft γ-ray boundary to separate neutron star and black hole systems is not a new concept. Barret et al. (1996) found for high luminosity, high energy emitters, the ~100 keV luminosity of black hole systems is commonly in the range $1 - 6 \times 10^{37}$ ergs cm^{-2} s^{-1}, whereas for neutron star systems it is $\leq 10^{37}$ ergs cm^{-2} s^{-1}.

5.6 Conclusions

The INTEGRAL Galactic Plane Survey and the 1st IBIS/ISGRI Survey Catalogue has offered for the first time the possibility to investigate the global γ-ray characteristics of galactic sources on a reasonable statistical basis. The generalised observational features of γ-ray selected, HMXBs, LMXBs and the class of previously unclassified objects have been investigated and compared with one another. Although the sample of sources has been γ-ray selected the logN-logS, angular and spatial distributions of the known classes emulate those of X-ray selected sets, for example the RXTE/ASM sample of Grimm et al. (2002). However there appear to be subtle differences. Of great interest however are the 27 "unidentified" objects, which naturally have overhanging questions such as what are they and how do they fit into mainstream stellar evolution?

It is unsurprising that INTEGRAL should discover a new class of object. The γ-ray energy regime in which INTEGRAL observes is insensitive to photoelectric absorption. Hence a source observed by INTEGRAL to be bright in the γ-ray band can be rendered much weaker in the classical X-ray band if a large column density is associated with the source. Individual follow-ups of a number of INTEGRAL sources have indicated that a large number of them are heavily absorbed (Walter et al., 2004). Investigation of the absorbing column density of the sources is only possible by individual follow-up observations of sources and not by investigating the global statistical properties of the set as presented here.

However, the statistical investigation presented here lends itself to suggest that the large majority of the new INTEGRAL sources may be high mass X-ray binaries with a neutron star companion. The broad angular distribution and logN-logS of the unclassified sources initially indicates that these sources inhabit the central 3–4 kpc of the galaxy, this is similar to the LMXB population. However, the details of the angular distribution are not reminiscent of sources belonging to the galactic bulge, the distribution is seen to be asymmetric and offset from the Galactic Centre. In fact, the concentrations of sources at specific galactic longitudes, which are similar to the spiral arm tangents, indicate a population which may be associated with star formation regions and young stellar systems. This leads to the potential that a large number of the unclassified sources are indeed high mass X-ray binaries. Similarly the latitude distribution of the unclassified sources is much more tightly associated with the plane of the galaxy than is expected or observed for the low mass systems. The high mass systems, however, have a very similar latitude profile, close to the Galactic Plane.

The luminosity function of the sources can also give us clues as to their origin. How-

ever, using this as a discriminator requires the assumption that the unclassified sources are at the distance of the Galactic Centre. This, assumption obviously weakens any indicators that the luminosity function may provide. A comparison of the unclassified source luminosity function with those of known objects shows similarities in the properties of both high mass X-ray binaries and those systems in which the compact object is a neutron star. On its own this argument is very tenuous, however, collectively all of the statistical investigations performed have implied a potential association of the unclassified systems with HMXBs.

The only possible way of confirming the type of system is by multi-wavelength follow-ups of the individual sources. These investigations have been underway since INTEGRAL first began discovering new sources. However, there is an obvious time delay between source identification, proposing for follow-up observations and then receiving, analysing and interpreting the data. A number of the new sources identified in the 1^{st} IBIS/ISGRI Survey Catalogue have now been followed up. Walter et al. (2003); Hill et al. (2005); Revnivtsev (2003); Matt & Guainazzi (2003); Rodriguez et al. (2003) have all performed follow-ups of INTEGRAL sources which identify them as potential high mass X-ray binaries with a high level of intrinsic absorption and neutron star compact object. For a detailed analysis of one of the new INTEGRAL sources see Chapter 6.

The HMXBs are a sensible candidate for the unclassified systems for two reasons. The stellar wind accretion mechanism can be used to explain the dense shroud of circumstellar material which must be present in these systems to explain the high level of intrinsic absorption which is observed and hence diminish the observed X-ray emission. Secondly, the recent release of the 2^{nd} IBIS/ISGRI Survey Catalogue indicates that all of the known high mass supergiant systems containing accretion powered pulsars have been detected by the IBIS survey, except for one which has not yet had a significant level of exposure ($<$ 75 ksec) (Bildsten et al., 1997; Bird et al., 2005). That only $\sim$10 supergiant HMXBs were known prior to INTEGRAL would imply that they were not being observed due to some form of selection effect. If that selection effect is that the large majority of these sources have high levels of intrinsic absorption then their detection by INTEGRAL was inevitable.

5.6.1 Future work

Obviously the limiting factor in performing a statistical analysis of the IBIS survey sources is the size of the available data set. However, the 2^{nd} IBIS/ISGRI Survey Catalogue is now available as well as detections of many other sources which have since been detected in

the ever increasing INTEGRAL data set. This includes over 100 new sources which INTEGRAL has discovered to be high energy emitters.

The 2nd IBIS/ISGRI Survey Catalogue is based upon the first 2 years of available INTEGRAL observations and yields 209 sources identified in an unbiased manner. As in the 1st IBIS/ISGRI Survey Catalogue the source population is dominated by Galactic sources, specifically X-ray binary systems. However, the added exposure off of the Galactic Plane has drastically increased the number of detected extragalactic sources. The source populations of the second catalogue consist of:

- Galactic systems:
  - 38 High Mass X-ray binaries
  - 67 Low Mass X-ray binaries
  - 8 Cataclysmic Variables
  - 4 isolated pulsars
  - 4 supernova remnants
  - 1 Symbiotic Star
- Extragalactic systems:
  - 22 Seyfert galaxies
  - 3 Blazars
  - 2 Galaxy clusters
  - 6 AGN with unconfirmed classifications
- Unclassified sources:
  - 39 sources of unknown nature
  - 17 sources with unconfirmed, tentative classifications

Of the galactic systems the compact object is predominantly a neutron star. This is the case in ~84% of the high mass systems and ~70% of the low mass systems. Four of the X-ray binary systems have confirmed black hole candidates whilst another four systems are tentatively identified as such based upon their observed X/γ-ray characteristics. Two of the unconfirmed source classifications are associated with known molecular clouds although recently Bassani et al. (2005) identified the γ-ray emission as originating from an AGN lying behind the molecular cloud NGC 6334.

The number of confirmed extragalactic sources has increased five fold since the 1^{st} IBIS/ISGRI Survey Catalogue and now comprises ~20% of the catalogue sources. The number of unknown sources has doubled since the first catalogue, although this represents approximately the same proportion of the overall catalogue. This is obviously a much improved sample over that based solely upon the 1^{st} IBIS/ISGRI Survey Catalogue. A more detailed statistical analysis is now feasible with more quantifiable results in the correlations between system types. Also, an extragalactic population is available for analysis. As a number of the newly discovered INTEGRAL sources have now been detected off the Galactic Plane it is now possible to compare these prospective AGN with their confirmed counterparts.

Working on the ever increasing sample sizes will hopefully allow us to answer some of the key questions which INTEGRAL is raising, principally how the γ-ray selected highly absorbed systems fit into the overall picture of binary star evolution. A key difficulty is due to the requirement of a suitable companion able to provide a sufficiently strong stellar wind mass loss rate ($\dot{M} \geq 10^{-4}$ M$_{\odot}$ yr^{-1}) that is capable of generating a suitably dense gas surrounding the compact object to stifle the X-ray emission. We need to understand why they are different to "normal" HMXBs. Do these highly absorbed systems relate to the mass/giant nature of the primary star, or to the orbit configuration, or are they experiencing a phase the binary systems routinely pass through; but have not been exposed at other wavelengths? Do they need to be HMXBs? Clearly a series of dedicated observations are required to solve this problem. If they are not all HMXB systems, then could some of them be intermediate mass X-ray binaries (IMXBs) (van den Heuvel, 1975). Some of the sources could be systems that are passing through, or close to the common envelope phase (Iben & Livio, 1993; Taam & Sandquist, 2000). However on statistical grounds this seems unlikely due to the requirement that their relative numbers need to compatible with the relatively short timescale ($\leq 10^3$ yr) of this phase, which is dictated by the drag force created as the compact star moves through the envelope of the extended companion.

On a statistical basis INTEGRAL will provide a clearer picture of the relative numbers of the various sub species of X-ray binary systems, and consequently a more balanced understanding of the rather murky final stages of binary star evolution and by implication eventually more reliable estimates for the relative numbers of black hole and neutron stars.

Chapter 6

The nature of IGR J18027-2016

6.1 Introduction

One of the key discoveries of the INTEGRAL mission to date has been the detection of previously unknown high-energy emitting sources. In excess of 95 new sources have been identified by INTEGRAL to date. The majority of these sources have been discovered during Core Programme galactic plane scans (GPS) and the Galactic Centre Deep Exposure (GCDE). However, a number of these sources have also been serendipitously discovered in private, general observer time. As the vast majority of observations, to date, have concentrated on the Galactic Plane it is reasonable to assume that the majority of these new sources are Galactic in origin. As discussed in the previous chapter, considering the global properties of this class of sources and comparing them to known source populations can lead to an indication of the dominant class of source of the new INTEGRAL population. However, the only way to ascertain the nature of any individual source is to study that source in detail at multiple wavelengths. This chapter presents a detailed analysis of the INTEGRAL source IGR J18027-2016.

6.2 The discovery of IGR J18027-2016

IGR J18027-2016 was first detected in April 2003 at the INTEGRAL Science Data Centre (ISDC) during a Core Programme exposure of the Galactic Centre. Shortly after its discovery it was included in an XMM observation proposal (under the ID IGR J18029-2016). The source has been independently reported in both core programme GCDE (Galactic Centre Deep Exposure) observations (Bird et al., 2004) and in guest observer data (Revnivtsev et al., 2004). Shortly after the discovery of IGR J18027-2016, Augello

et al. (2003) reported the discovery of of a new X-ray pulsar, the serendipitous source SAX J1802.7-2017. However, it was Lutovinov et al. (2005) who announced the spatial association of these two sources.

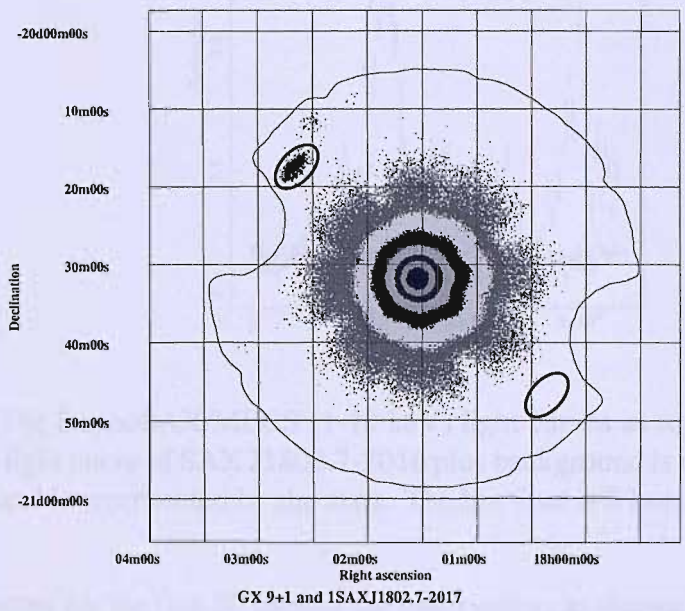

Figure 6.1: The BeppoSAX/MECS (1-10 keV) image as reported by Augello et al. (2003). GX 9+1 is at the centre and SAX J1802.7-2017 is located toward the upper left. The ellipses indicate where the source and background counts were extracted.

6.2.1 BeppoSAX observations

Augello et al. (2003), hereafter *Au03* , identified SAX J1802.7-2017 after re-analysing archival BeppoSAX observations of the GX 9+1 field. BeppoSAX observed the GX 9+1 field from 02:01:30.0 UTC, September 16 2001 to 03:00:08.5 UTC, September 20. The position of SAX J1802.7-2017 was given as R.A.(2000.0) = $18^h02^m39.9^s$ and Dec. = -20°17′13.5″ with a positional uncertainty of 2′. The position was extracted from the MECS instrument 1-10 keV image and is shown in Fig. 6.1. SAX J1802.7-2017 lies ~22′ from the position of GX 9+1. The source plus background light curve obtained by the MECS instrument is show in in Fig. 6.2.

A temporal analysis of the MECS data by *Au03* identified a pulse period of 139.612 seconds, indicating that the source was an X-ray pulsar. Additionally, phase delays in the arrival times of the pulsations were observed. The phase delays were explained as modulation brought about by an approximately circular orbit of ~4.6 days. The source

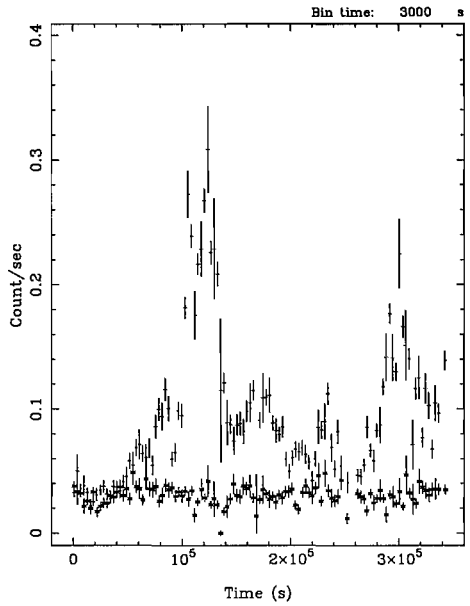

Figure 6.2: The BeppoSAX/MECS (1-10 keV) light curves as reported by Augello et al. (2003). The light curve of SAX J1802.7-2016 plus background is indicated by the crosses; the background is represented by the stars. The bin time is 3 ksec.

was not detected for the first 50 ksec of the observation, as shown in Fig. 6.2, which *Au03* interpreted to indicate that this was likely an eclipsing binary system. Table 6.1 lists the derived phase delay fit and system parameters. The total duration of the observation, ~4.0 days, was such that the data does not cover a complete orbit and hence the measurement of the orbital period through the delays in the pulse arrival times was associated with a 9% error. This contributed to other system parameters having errors of ~30%. The conclusion arrived at by *Au03* was that SAX J1802.7-2017 is thus an accreting X-ray pulsar in a (possibly eclipsing) high-mass X-ray binary.

6.2.2 Early INTEGRAL observations

Lutovinov et al. (2005) identified SAX J1802.7-2017 and IGR J18027-2016 as the same source based upon guest observer observations made by the IBIS instrument, on-board INTEGRAL, during August 23 to September 24, 2003 and March to April of 2004. The 18-60 keV flux of the source was found to be almost constant over the two observing epochs and the hard X-ray spectrum was observed not to vary. The spectrum was described by a power law with an exponential cut-off at high energies. The IBIS data was not of sufficient quality to constrain the photon index, hence it was fixed at the value estimated by *Au03* , however, the cut-off energy was found to be E_{cut}=18 keV.

Table 6.1: Estimated phase delay fit parameters and system parameters of SAX J1802.7-2017 (*Au03*). [MJD = JD - 2400000.5, a_0, a_1, and B are phase delay fit parameters defined in Section 6.4.3.]

Parameter	Value
a_0	$0.04^{+0.12}_{-0.09}$
a_1	0.02 ± 0.03 days^{-1}
B	$0.50^{+0.07}_{-0.05}$
P_{orb}	$4.6^{+0.4}_{-0.3}$ days
$a_x \sin i$	70^{+10}_{-7} lt-s
$T_{\pi/2}$	$52168.22^{+0.10}_{-0.12}$ MJD
P_{pulse}	$139.612^{+0.006}_{-0.007}$ s
$f(M)$	$17 \pm 5\ M_\odot$
θ_ϵ	0.64 ± 0.14 rad
M_C	$\gtrsim 11\ M_\odot$
R_C	$\gtrsim 14\ R_\odot$

6.3 Observations

Presented in this chapter is an analysis of the INTEGRAL/IBIS observations of IGR J18027-2016 contained within core programme observations or public data as of September 2004 (i.e. the data used in the 2^{nd} IBIS/ISGRI Survey Catalogue). Also presented is an analysis of the XMM-Newton follow up observation obtained, and a re-analysis of the BeppoSAX data.

6.3.1 INTEGRAL core programme observations

IGR J18027-2016 has been observed by INTEGRAL on multiple occasions during the core programme by the IBIS detector as it lies on the galactic plane, approximately 9° from the Galactic Centre. IBIS observed IGR J18027-2016 over three epochs during the first two years of core programme observations: 28 Feb. – 28 Apr. 2003; 27 Sept. – 12 Oct. 2003; 17 Feb. – 20 Apr. 2004. ISGRI images were generated for each selected pointing in 10 narrow energy bands with the ISDC Offline Scientific Analysis (OSA) software version 4.1. The individual images were combined to produce mosaics of the region in broader energy bands using the system described in Bird et al. (2005).

Fig. 6.3 shows the IBIS/ISGRI 20–40 keV image of the region around IGR J18027-2016 and GX 9+1. The 12′ angular resolution of ISGRI (Winkler et al., 2003) allows us to easily resolve these two sources as they lie ~22′ apart. In the 20–40 keV band IGR J18027-2016 is seen as a 30.5σ detection and is located at R.A. (2000.0) = $18^h02^m46.1^s$

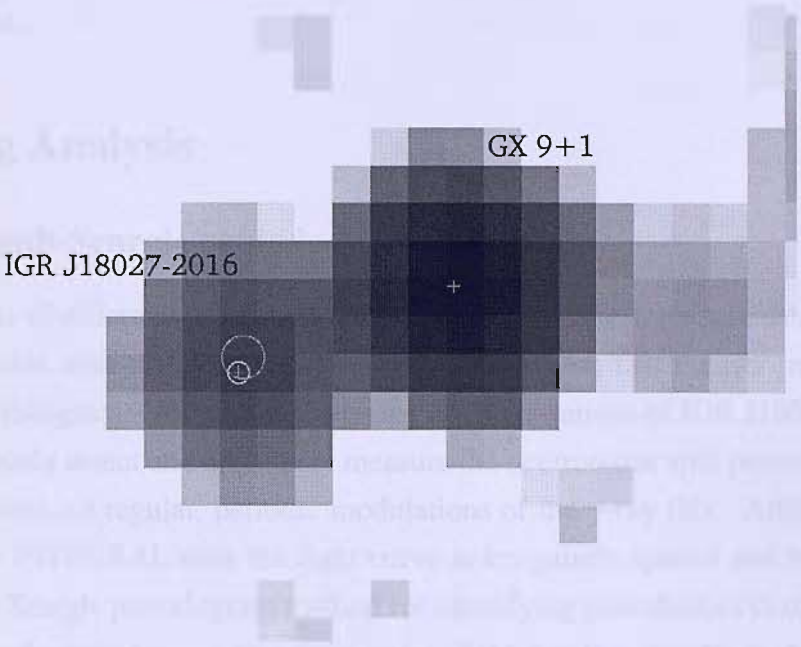

Figure 6.3: ISGRI 20-40 keV image of the field containing IGR J18027-2016 and GX 9+1. The crosses correspond to the source positions; the larger circle is the BeppoSAX error circle (Augello et al., 2003); the smaller circle is the ISGRI 90% error circle (Gros et al., 2003).

and Dec. = -20°17′37.1″ with a positional uncertainty of ~1′ (Gros et al., 2003). This position is consistent with the position of SAX J1802.7-2017 according to *Au03* and has a smaller associated error. The source flux is seen to be persistent throughout all of the observing epochs and does not exhibit any large degrees of variability. IBIS observes it as a weak persistent γ-ray source with an average 20–40 keV flux of $F_{20-40keV} = 0.58 \pm 0.02$ counts sec^{-1}, which corresponds to ~6.4 mCrab.

6.3.2 XMM-Newton Observations

IGR J18027-2016 was observed by XMM-Newton from 06:54:40.0 – 09:44:38.0 UTC, 2004 April 06, giving a net effective exposure of 7.6 ksec. A single X-ray source was found, within the ISGRI error circle, in the EPIC PN and MOS cameras (Strüder et al., 2001; Turner et al., 2001). The XMM Science Analysis System (SAS), software version 6.0, was used to extract light curves and spectra for IGR J18027-2016. Standard SAS tools were used to calculate the instrumental response and the effective area for the extracted spectra. The extracted position of IGR J18027-2016 is R.A. (2000.0) = $18^h02^m42^s$ and Dec. = -20°17′18″, with a positional uncertainty of 4″. This is the most precise position known for this source and is compatible with both the ISGRI and BeppoSAX

measured positions.

6.4 Timing Analysis

6.4.1 The Lomb-Scargle periodogram method

There are a number of different methods applied to detect periodic signals in data including: phase dispersion minimisation; discrete Fourier transform; fast Fourier transform; Lomb-Scargle periodogram. Our goal in analysing the observations of IGR J18027-2016 was to unambiguously detect and accurately measure the neutron star spin period and the system orbital period, i.e regular, periodic modulations of the γ-ray flux. Additionally, in the case of the INTEGRAL data the light curve is irregularly spaced and hence we employ the Lomb-Scargle periodogram method for identifying periodicities in the data.

The Lomb-Scargle periodogram of a time series, $X(t_i), i = 0, 1, 2, ...N_0$, is defined as (Scargle, 1982):

$$P_X(\omega) = \frac{1}{2}\left\{\frac{\left[\sum_j X_j \cos\omega(t_j-\tau)\right]^2}{\sum_j X_j \cos^2\omega(t_j-\tau)} + \frac{\left[\sum_j X_j \sin\omega(t_j-\tau)\right]^2}{\sum_j X_j \sin^2\omega(t_j-\tau)}\right\} \tag{6.1}$$

where τ is defined by,

$$\tan(2\omega\tau) = \frac{\sum_j \sin 2\omega t_j}{\sum_j \cos 2\omega t_j} \tag{6.2}$$

One of the desirable properties of the discrete Fourier transform method is that the probability that a peak of power between z and z+dz could be generated by random white noise is given by,

$$P_z dz = e^{-z} dz \tag{6.3}$$

Horne & Baliunas (1986) showed that in the case of the Lomb-Scargle periodogram the exponential distribution can be regained if the periodogram is normalised to the noise variance, σ_0. This must be the total variance of the entire data set, not after any detrending has been performed.

$$P_N(\omega) = \frac{P_X(\omega)}{\sigma_0} \tag{6.4}$$

In this instance it is now possible to use the False Alarm Probability (FAP) to place confidence limits on the detection of periodicities. The FAP is the probability that a period

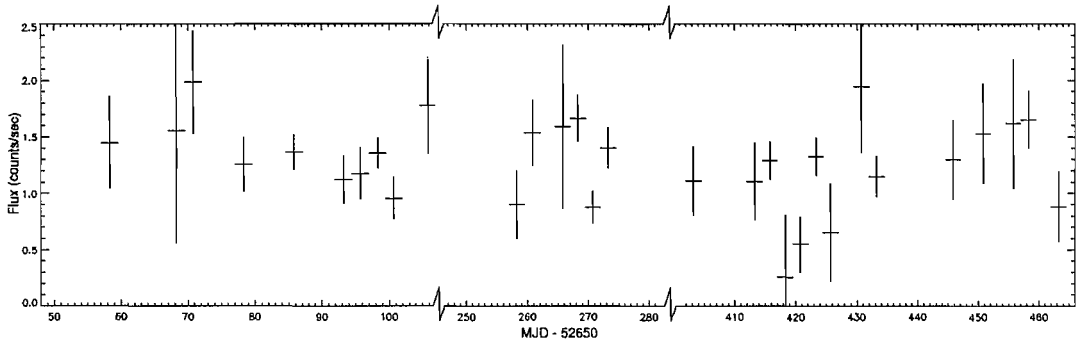

Figure 6.4: 20-80 keV light curve of IGR J18027-2016 covering the three observed epochs. The light curve has been re-binned to 2.5 day averages.

is not real. If M independent frequencies are examined then the FAP is:

$$FAP = 1 - (1 - e^{-z})^M \tag{6.5}$$

However, this is only true in the case of white noise and when the variance is known in advance. This is rarely the case, such that the variance must be estimated from the data. If these instances the exponential distribution does not hold, it may be used as a guide to identify possible periods but it will not accurately give the statistical significance of the peaks in the periodogram. In these instances Monte-Carlo techniques can be applied to identify the statistical properties of the periodogram.

6.4.2 Identifying the orbital period of IGR J18027-2016 from ISGRI data

The flux of IGR J18027-2016 was extracted from each ISGRI pointing image to generate light curves in different energy bands, the re-binned 20–80 keV light curve spanning ~417 days is seen in Fig. 6.4. It is clear that the source appears as a weak persistent source throughout the INTEGRAL observations. The source is not especially strong above 40–50 keV and to minimise systematic effects the 20–40 keV light curve was searched for periodicities using the Lomb-Scargle periodogram method by means of the fast implementation of Press & Rybicki (1989). Additionally, as the far off-axis response of the ISGRI detector is not well understood, the light curve was constructed from observations when IGR J18027-2016 was within 14° of the centre of the field of view. The resulting Lomb-Scargle power spectrum is shown in Fig. 6.5. The peak power of 52.6 corresponds to a frequency of 0.2188 days^{-1}. The error on the angular frequency (Horne & Baliunas, 1986) is:

$$\delta\omega = \frac{3\pi\sigma_N}{2\sqrt{N}TA} \tag{6.6}$$

where $\sigma_N{}^2$ is the variance of the noise, N is the number of data points, T is the total length of the data set and A is the amplitude of the signal given by:

$$A = 2\sqrt{\frac{z_0\sigma_s^2}{N}} \tag{6.7}$$

where z_0 is the Lomb-Scargle power and $\sigma_s{}^2$ is the variance of the light curve.

This frequency corresponds to a period of 4.570 ± 0.003 days which is consistent with the orbital period indirectly measured by *Au03*.

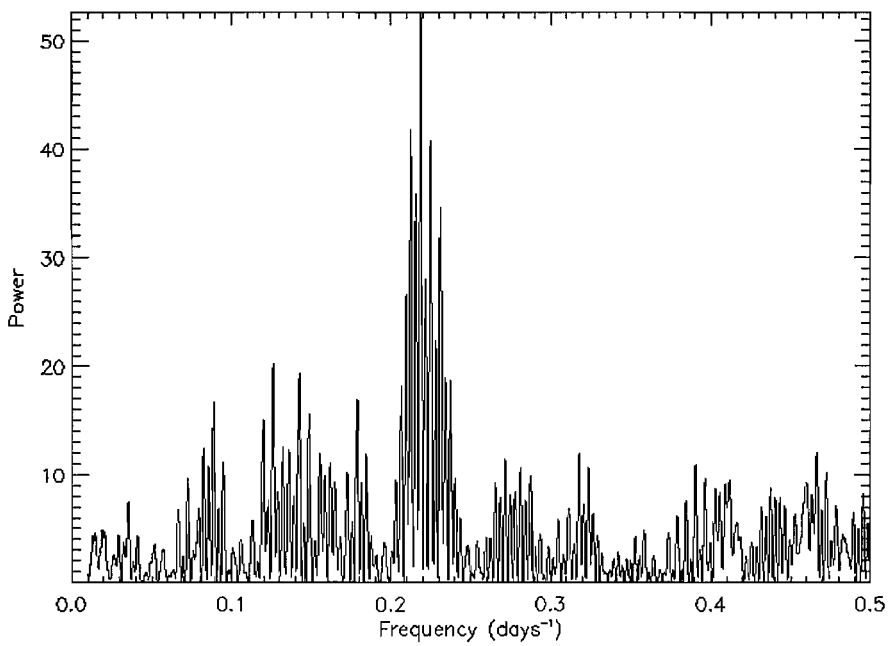

Figure 6.5: Lomb-Scargle periodogram generated from the 20-40 keV light curve of IGR J18027-2016.

6.4.2.1 The Randomisation Test

As previously discussed without knowing in advance the variance of the noise distribution the significance and hence the precision of any measured periodicities are subject to error. The significance of this peak was confirmed by applying a randomisation test. The time stamps for each flux measurement were randomly reordered and the periodogram of the resulting light curve generated. Five thousand light curves were simulated in this fashion. The histogram of the distribution of the power of the most significant peak is shown in

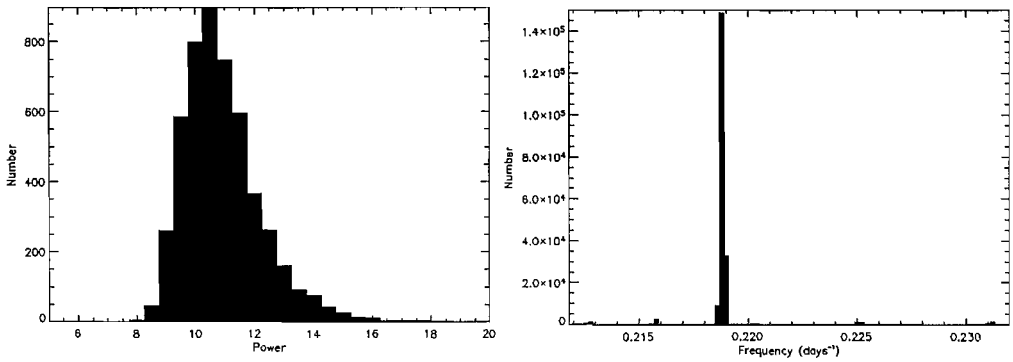

Figure 6.6: *Left*: The histogram of the peak power of 5000 periodograms generated from randomised light curves simulated from the original IGR J18027-2016 data. *Right*: The histogram of the frequency of the highest power peak in the periodograms of 200,000 bootstrapped light curves simulated from the original IGR J18027-2016 data.

Fig. 6.6. The mean maximum power found in the randomised data sets was 10.9 with a standard deviation of 1.3, and highest power recorded was a single instance of 19.5. It is immediately obvious that a peak of power ~53 is extremely unlikely to occur by chance and hence our detection is highly significant. From Fig. 6.6 it can be seen that the distribution of power is not perfectly Gaussian, however using Gaussian statistics, the significance of the peak in the periodogram of IGR J18027-2016 is ~42σ.

6.4.2.2 The Bootstrap Method

Upon close examination of the periodogram it can be seen that there is some aliasing around the frequency of the detected period. This raises the question of whether we have selected the correct peak and hence the correct frequency/period. The higher power of our selected frequency is such that we can be confident that this is the true frequency of the system, however to more rigorously confirm this a monte-carlo approach must be taken.

One method of investigation is the Bootstrap method (Kawano & Higuchi, 1995). The strength of the Bootstrap method is that it provides a method to non-parametrically estimate the statistical properties of data whilst making few assumptions about the distribution of the variable and hence is of use when analysing non-Gaussian distributions. The Bootstrap method does however, require high computing power to provide meaningful results.

Assuming that the light curve provides a good representation of the underlying distribution a simulated data set, called the bootstrap sample, is generated on the principal that each data point has equal probability. This is done by randomly sampling the source light curve with replacement. Consequently the each bootstrap sample will, in general,

be subtly different from the original light curve with some points being omitted and other points being counted more than once.

The Lomb-Scargle periodogram of the simulated light curve is generated and the frequency of the peak with maximum power is measured. The histogram of the results of 200,000 simulations is shown on the right in Fig. 6.6. The peak distributed around the frequency of 0.2188 days^{-1} indicates that in 95% of the simulations this periodicity is apparent. The next most likely periodicity is only selected in ~1.5% of the simulations. This demonstrates that the chosen frequency is the dominant periodicity in our sample and hence can be confidently chosen as being the true frequency of the system. If the aliasing pattern is entirely a result of the window function, i.e. the sampling pattern of the light curve, then the Bootstrap method should weaken the aliasing by subtly changing the sampling pattern in each of the simulations.

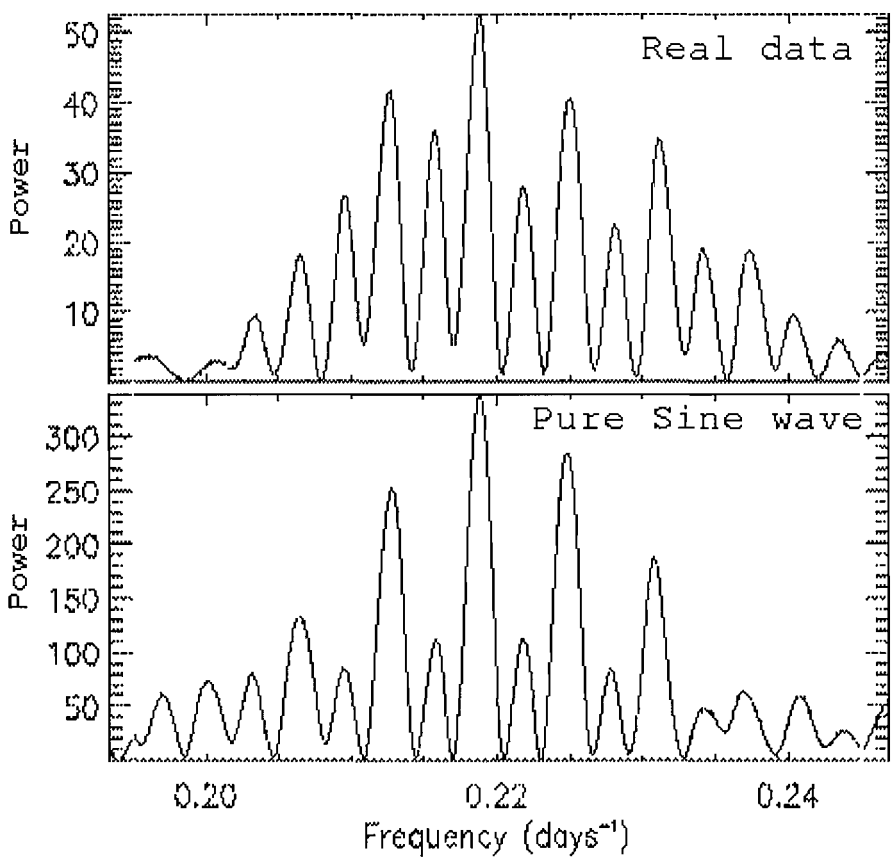

Figure 6.7: *Top*: Zoom on the peak of the periodogram of IGR J18027-2016, shown in Fig. 6.5. *Bottom*: Lomb-Scargle periodogram generated from a sine wave with a period of 4.570 days and sampled identically to IGR J18027-2016.

Additionally, using the Bootstrap method we can estimate the error on the measured frequency (Kawano & Higuchi, 1995). Examining the peak of the histogram centred at

a frequency of 0.2188 days^{-1} the identified period and associated error can be estimated as 4.570 ± 0.002 days. This is essentially the same as that calculated using the equations of Horne & Baliunas (1986), indicating that the statistics of our light curve essentially behave sufficiently like those assumed in the error equations.

To investigate the origin of the aliasing pattern a pure sine wave of our chosen frequency was sampled in an identical fashion to that of the original data set. The corresponding periodogram (Fig. 6.7) can be seen to exhibit broadly the same aliasing pattern as observed in the data. The peak of maximum power corresponds to the frequency of the input sine wave and the aliases are spaced in an identical manner to that of the original data set. Also, as discussed in section 6.4.3, folding the ISGRI light curve on a period of 4.570 days indicates an eclipse of the system exactly when it would be expected to be observed if this was an eclipsing binary as suggested by *Au03* . Hence, the peak of maximum power in the data can be confidently attributed to the true frequency of the system.

6.4.3 Re-analysis of the BeppoSAX observed timing properties

The orbital period as measured by ISGRI can be used to re-analyse the BeppoSAX data presented by *Au03* . Originally, phase delays in the pulse period of the pulsar measured by SAX were fitted without any prior knowledge of the orbital period. The incomplete orbital coverage, of the SAX observation, resulted in 10% error in the measured orbital period which resulted in large errors on a number of other system parameters. Performing an identical analysis of the phase delays assuming an orbital period of 4.570 days should result in more precise measurements of the system parameters.

The modulation of the phase delays can be explained by the propagation delays resulting from the orbital motion of the neutron star around its companion star. The phases were fit with

$$\Delta\phi = a_0 + a_1 t_n + B\cos\left[\frac{2\pi(t_n - T_{\pi/2})}{P_{orb}}\right] \tag{6.8}$$

where t_n is the arrival time of the nth pulse, $T_{\pi/2}$ is the epoch of NS superior conjunction of the NS, the linear term $a_1 = \Delta P_{pulse}/P^2_{pulse}$ and $P_{orb} = 4.570 \pm 0.003$ days. The χ^2_ν of the fit was 1.3, the fit parameters are listed in Table 6.2 and the fit is shown in Fig. 6.8. As $a_x \sin i = P_{pulse} B$, then $a_x \sin i = 68 \pm 1$ lt-s; P_{pulse} ~139.612 s (*Au03*). All of the fit parameters are consistent with those originally measured by *Au03* , however they are considerably better constrained due to the independent and precise measurement of P_{orb} by IBIS/ISGRI. The epoch measurements are all quoted as Modified Julian Dates (MJD).

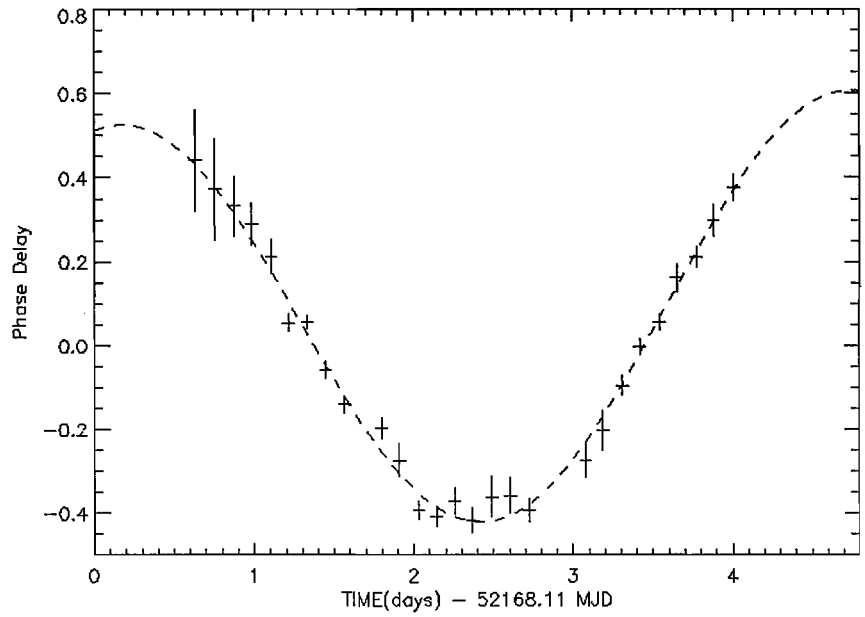

Figure 6.8: Phase delays as a function of time as measured by BeppoSAX. The dashed line is the best-fit function (Eq.[6.8]).

MJD is defined as JD - 2400000.5, where JD is the Julian date of the measurement.

Table 6.2: Phase delay fit parameters

Parameter	Value
a_0	0.03 ± 0.07
a_1	0.02 ± 0.03 days^{-1}
B	0.49 ± 0.003
$T_{\pi/2}$	52168.26 ± 0.04 MJD

Using the measured orbital period and the epoch of superior conjunction of the NS, $T_{\pi/2}$, obtained in the fit, the IBIS/ISGRI light curves were phase-folded in the 20-30 keV and 30-40 keV energy bands. These are shown in Fig. 6.9 and clearly show a sharp eclipse as suggested by *Au03*. The fuller phase coverage of the IBIS/ISGRI data unambiguously confirms the orbital period and the presence of an eclipse in the system. The time of mid-eclipse occurs at the time of superior conjunction of the NS, $T_{\pi/2}$.

6.4.4 Refining the orbital period & an accurate ephemeris

Taking the zero epoch as the time of superior conjunction of the NS, $T_{\pi/2} = 52168.26 \pm 0.04$ MJD and the orbital period, $P_{orb} = 4.570 \pm 0.003$ days the number of orbital cycles

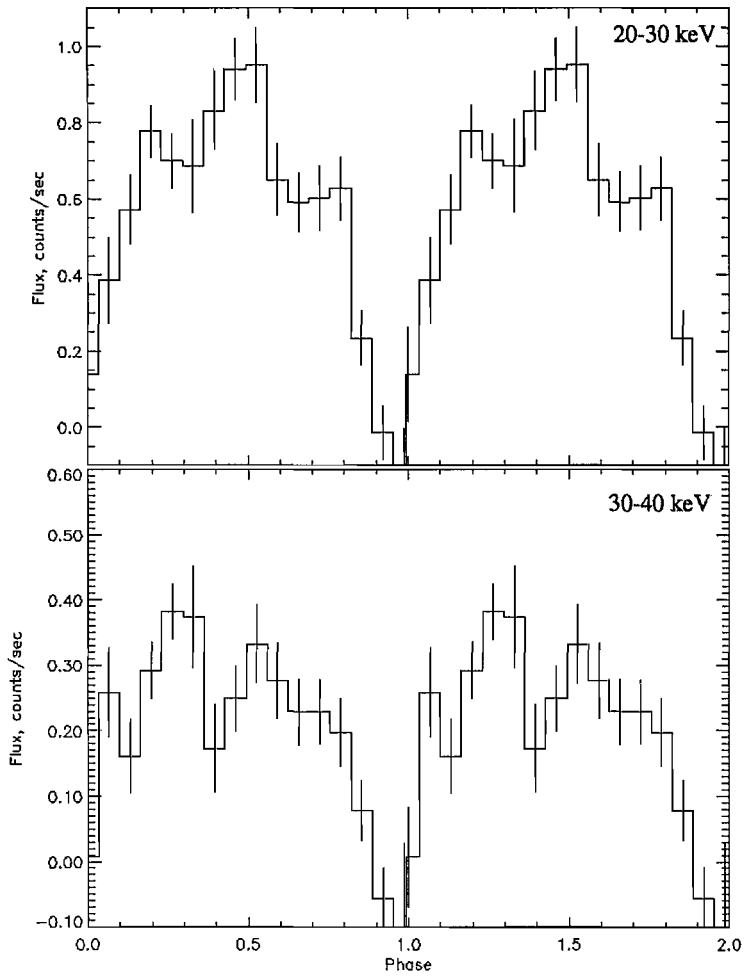

Figure 6.9: Folded light curves in the 20-30 and 30-40 keV energy bands of IGR J18027-2016. The folding is performed for an orbital period of 4.570 days, and the zero epoch was assumed at the superior conjunction of the NS,$T_{\pi/2}$ = 52168.26 MJD .

which have occurred by the time of the last ISGRI observation is E = 207.2 ± 0.1. Hence, over this timescale, we can confidently identify which cycle we observe. This is borne out by Fig. 6.9, as the eclipse is evident very near zero phase when the ISGRI data is folded with the BeppoSAX zero epoch. From the folded ISGRI light curves the time of an eclipse around the mid point of the ISGRI observation is calculated, $T_{eclipse}$ = 52931.4 ± 0.2 MJD. This would correspond to the beginning of the 167^{th} orbital cycle. Linearly fitting between these two times of eclipse measurements yields a refined orbital period estimate of P_{orb} = 4.5696 ± 0.0009 days. This allows the calculation of an accurate mid-eclipse ephemeris from:

$$T_{mid} = T_0 + P_{orb} \times E \tag{6.9}$$

where T_0 is the time of the 1^{st} eclipse seen by BeppoSAX and E is the cycle number. This gives an ephemeris of, T_{mid} = 52931.37 ± 0.04 MJD.

6.4.5 XMM timing properties

The timing mode of the PN camera allows the collection of timing data with a resolution of 30 μs (Strüder et al., 2001). The arrival time of all events were corrected to the solar system barycentre, using the SAS task "barycen". A 2–10 keV band light curve consisting of 1 second bins was generated for the duration of the observation, ~7.6 ksec. The Lomb-Scargle periodogram method performed described in section 6.4.1 was applied to search for periodicities. The resulting power spectrum is shown in Fig. 6.10. A peak of power ~504 is clear at a frequency of 7.17 mHz, the second harmonic of this frequency is also clearly visible with a power of ~220. This corresponds to a pulse period of, P_{pulse} = 139.47 ± 0.04 seconds. This is consistent with the range of pulse periods (139.44 – 139.86 s) detected by *Au03* . At the time of the XMM observation the system is expected to be at a phase of ~0.2 in its orbital cycle. Hence, the pulse period should be Doppler shifted by the orbital motion. Correcting the measured pulse period to the rest frame of the pulsar yields, P_{pulse} = 139.61 ± 0.04 seconds. The XMM measurement is consistent with the pulse period, P_{pulse} = 139.612 ± 0.006 seconds, measured by BeppoSAX.

Folding the XMM data on this pulse period yields the pulse period phase folded light curve seen in Fig. 6.11. The main pulse occurs around phase 0.63. A secondary peak is visible around phase 0.05. The pulse fraction, $(I_{max} - I_{min})/I_{max}$, where I_{max} and I_{min} are the maximum and minimum count rates, is ~68% ± 10%. The pulse period phase folded light curve matches well with the folded light curves of *Au03*, the pulse fractions are consistent and the locations of the primary and secondary peaks also agree.

6.5 Analysis of the XMM and IBIS/ISGRI spectra

The ISGRI spectrum was extracted from narrow energy band mosaics and hence represent the long term average spectrum of the source. Phase resolved spectra were extracted from the XMM-EPIC data set. Using the pulse profile (Fig. 6.11) a spectrum of the source during the primary pulse and a spectrum outside of the primary pulse were generated. *Au03* reported that the low statistics of the BeppoSAX data did not allow for an accurate spectral analysis. Additionally, the BeppoSAX PDS data is difficult to analyse as the data is contaminated by the bright atoll source GX 9+1, which also appears in the field of view.

The EPIC PN and ISGRI average spectra were simultaneously fit, in XSPEC v11.3, by

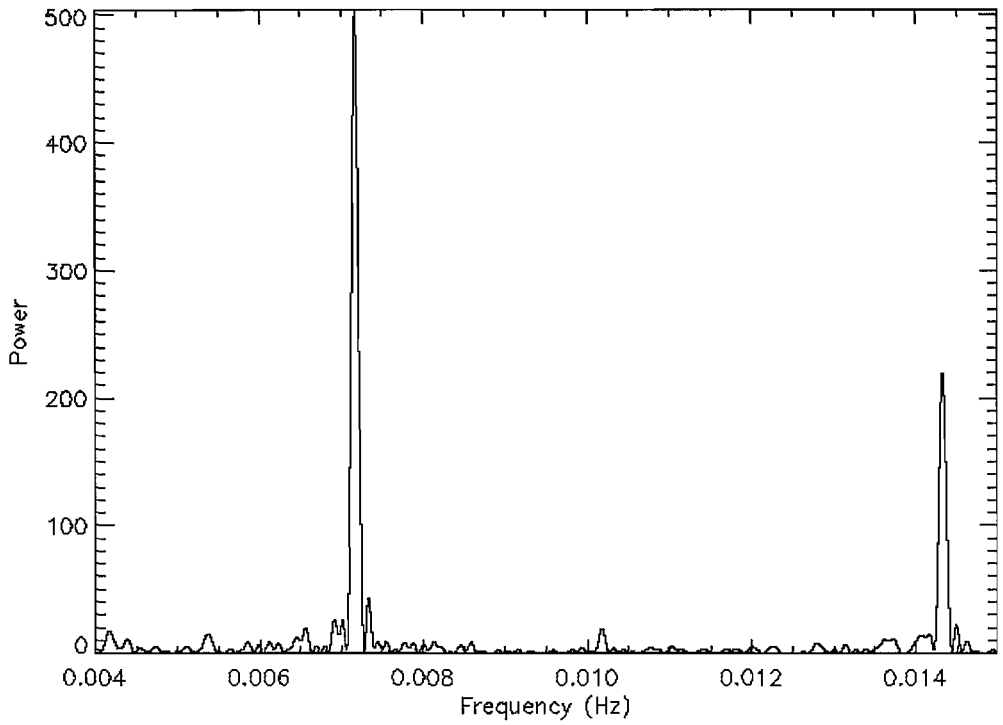

Figure 6.10: The Lomb-Scargle periodogram generated from the XMM EPIC 2–10 keV light curve of IGR J18027-2016.

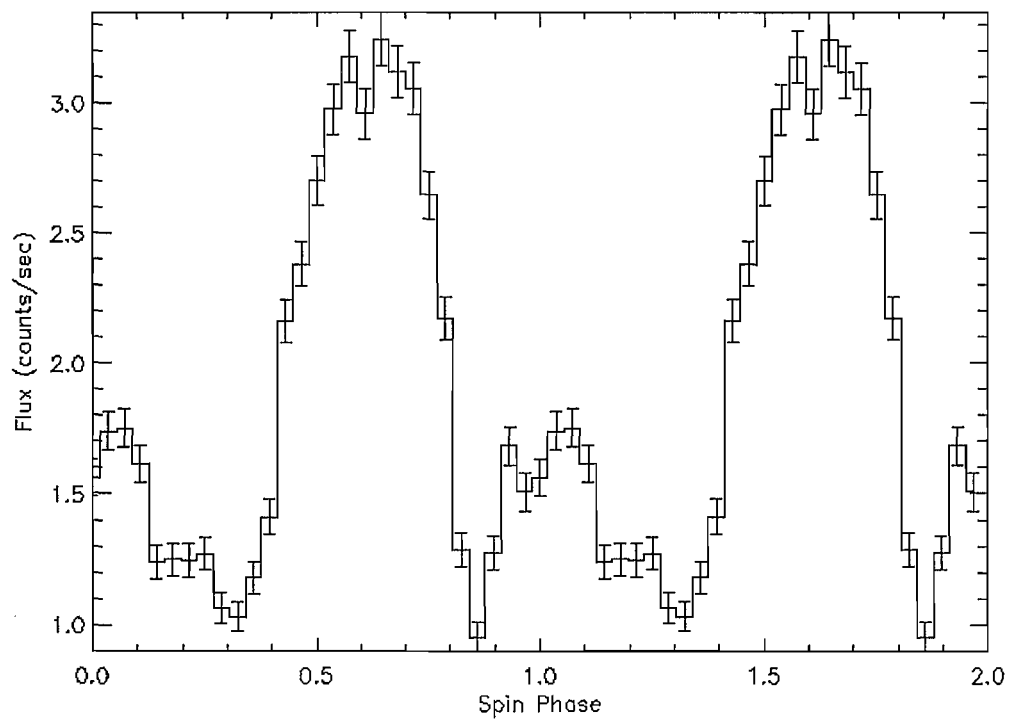

Figure 6.11: Pulse period phase folded light curve in the 2–10 keV energy band. The folding is obtained for a pulse period of 139.47 seconds and the zero epoch is taken at the superior conjunction of the NS, $T_{\pi/2}$ = 52168.26 MJD.

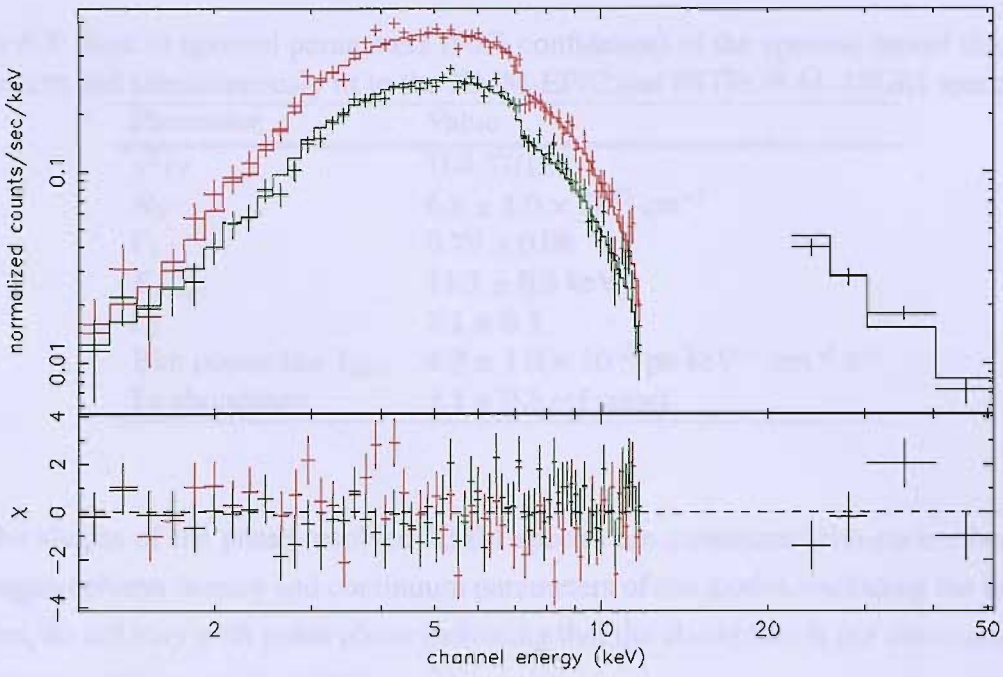

Figure 6.12: The phase resolved XMM (*upper left: EPIC PN spectrum of primary pulse. Lower left: EPIC PN spectrum outside of the primary pulse*) and INTEGRAL photon spectra (*right: ISGRI spectrum*)of IGR J18027-2016 with the best fit model.

a photoelectric absorbed, broken power law model with a single Gaussian emission line (gauss + zvphabs*bknpower). A broad Gaussian line is used to account for soft X-ray residuals that mostly concentrate at low energy. This soft excess contributes 7 $\times 10^{-14}$ ergs cm^{-2} s^{-1} below 3 keV. Elemental abundances of the spectral model, excluding Fe, are frozen to solar quantities and the redshift is frozen to 0, all other parameters are free. The fit has $\chi^2_\nu = 1.29$. The best fit parameters are listed in Table 6.3. The broken power law indices were found to be $\Gamma_1 = 0.79 \pm 0.08$ and $\Gamma_2 = 3.1 \pm 0.1$, with a break at E_{Break} = 11.3 ± 0.6 keV. A column density of $N_H = 6.8 \pm 1.0 \times 10^{22}$ cm^{-2} is found compared to the expected galactic column density of 1.0×10^{22} cm^{-2}. The Fe edge is ~3 times that of solar abundances, this may indicate that large amounts of Fe are present or that the N_H is underestimated. The shape of the spectrum is typical of X-ray pulsars which are characterised by a flat power law with a slope of between 0 and 1 up to a high energy cut-off at 10-20 keV after which the slope becomes much steeper (White et al., 1995). Fitting Fe lines at 6.45 and 7.1 keV improves the overall fit, however the F test indicates that they are significant at only the 95% confidence level. The ISGRI spectrum flux is, $F_{20-100keV} = 5.9 \times 10^{-11}$ ergs cm^{-2} s^{-1}, the XMM unabsorbed fluxes are, $F_{2-10keV} = 8.9 \times 10^{-11}$ ergs cm^{-2} s^{-1} within the primary pulse, and $F_{2-10keV} = 5.1 \times 10^{-11}$ ergs cm^{-2} s^{-1} outside the primary pulse.

Table 6.3: Best fit spectral parameters (90% confidence) of the spectral model discussed in the text and simultaneously fit to the XMM-EPIC and INTEGRAL-ISGRI spectra.

Parameter	Value
χ^2/ν	164.57/128
N_H	$6.8 \pm 1.0 \times 10^{22}$ cm^{-2}
Γ_1	0.79 ± 0.08
E_{Break}	11.3 ± 0.6 keV
Γ_2	3.1 ± 0.1
Bkn power law I_{1keV}	$4.9 \pm 1.0 \times 10^{-3}$ ph keV^{-1} cm^{-2} s^{-1}
Fe abundance	3.1 ± 0.8 (of solar)

The shapes of the phase resolved XMM spectra are consistent with each other. The hydrogen column density and continuum parameters of the model, excluding the normalisation, do not vary with pulse phase indicating that the absorption is not associated with the neutron star accretion column.

It is possible to fit the data with a Comptonization model or a cut-off power law, however to do so requires the introduction of a particularly small normalisation constant to the spectral model, C_{ISGRI}~0.2, to account for cross-calibration uncertainties of the ISGRI and EPIC observations. This would indicate that XMM had observed IGR J18027-2016 while it was in a high state when compared to the average ISGRI flux. However, the ISGRI light curve (Fig. 6.4) at the time of the XMM observation show no indication of a large change in flux of the source. The fitting of system N_H is highly dependent upon the spectral shape of the continuum assumed in the spectral model, a softer spectrum (e.g. the comptt model describing Comptonization of soft photons in a hot plasma) results in an N_H twice as large as listed in Table 6.3.

6.6 Discussion

From the IBIS/ISGRI and BeppoSAX observations we have directly and precisely measured the orbital period for IGR J18027-2016 of 4.5696 ± 0.0009 days. This is consistent with the implied orbital period of SAX J1802.7-2017, and as it is the only known X-ray source within 10′ according to the SIMBAD/NED database the two sources are confirmed as the same source. Additionally, we have observed that this is an eclipsing system confirming the hypothesis of *Au03*. The ephemeris of the mid-eclipse time is measured as, T_{mid} = 52931.37 ± 0.04 MJD. The ~139 s pulse period measured by BeppoSAX and XMM combined with the 4.5696 day orbital period, situates IGR J18027-2016 in the

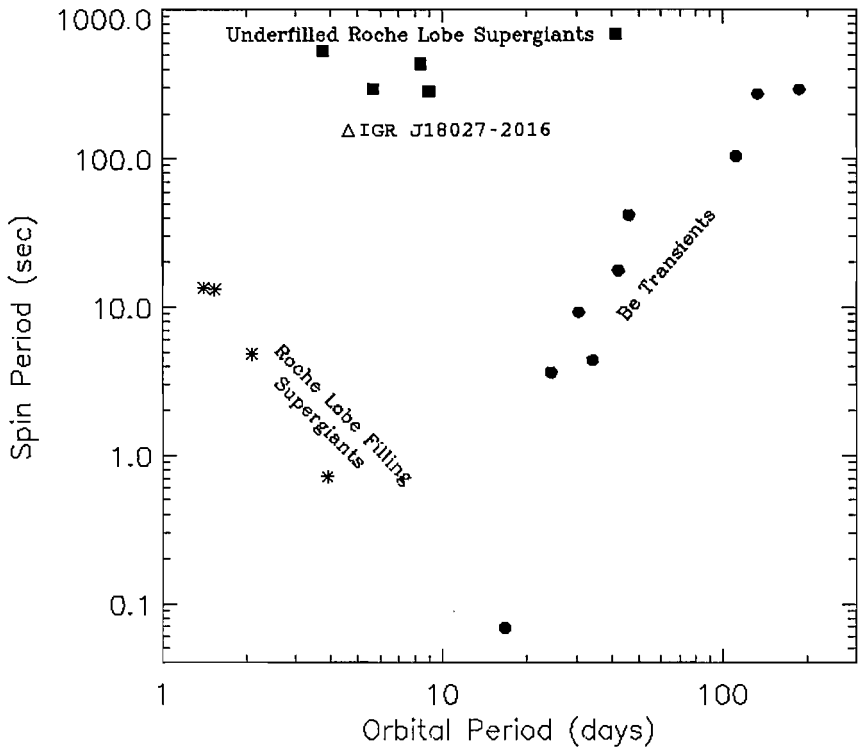

Figure 6.13: The Corbet diagram of HMXBs. The locations of Be X-ray binaries (filled circles), Supergiant Roche lobe filling (stars) and under-filling (filled squares) X-ray binaries are labelled. The region occupied by IGR J18027-2016 is indicated by a triangle.

region of the Corbet diagram (Corbet, 1986) occupied by under-filling Roche lobe supergiant systems (see Fig. 6.13). Hence, the system appears to be a neutron star that is accreting material through the stellar wind of the companion supergiant star.

6.6.1 Source variability

The ISGRI 20-80 keV light curve, shown in Fig. 6.4, indicates that this is a weak, persistent source with no evidence of flaring in any of our observations. Lutovinov et al. (2005) also reported that the 18–60 keV fluxes observed by IBIS in September 2003 and March 2004 of IGR J18027-2016 were nearly constant and equal. The absence of strong hard X-ray variability contrasts with what has been observed in other HMXBs in which flares by a factor of 10 have been detected. This may indicate that the stellar wind is rather homogeneous, at least on time scales longer than a few days. The persistent nature of the source suggests that the NS is continuously accreting, and, combined with the sinusoidal modulation of the pulse arrival times this implies that the NS is in an approximately cir-

cular orbit about its companion. This is consistent with the eccentricity upper limit of $e \lesssim 0.2$ given by *Au03*. The absence of apparent transient behaviour and circularity of the orbit further suggests that this is a supergiant system and not a Be X-ray binary (Liu et al., 2000). However, the fact that IGR J18027-2016 has not been reported by previous X-ray telescopes may indicate some level of transient behaviour. Notably there was no detection by the ROSAT mission. Transient behaviour would indicate the absence of Roche lobe overflow but would suggest that this was an atypical Be X-ray binary as its orbital and pulse period do not locate it in the expected region of the Corbet diagram and it has a very low eccentricity orbit. The lack of previous detection may be explained by the high column density measured by XMM.

During the XMM observation the X-ray flux increased by 50% with constant pulse fraction. Spectra derived for both periods do not show any significant variation in the spectral parameters. This is notable as one could expect to see a significant increase in N_H for large flux differences. The observed properties of IGR J18027-2016 appear to be very stable on timescales of a few days, as seen by ISGRI, and ~8 ksec, as seen by XMM.

6.6.2 Deriving the Mass Function

From Kepler's 3rd law it is possible to derive the mass of each component of a binary system from observations of both stars. In this case only the X-ray pulsar has been observed and hence, the mass function for the donor star can be calculated. The mass function of the system donor is given by:

$$f(M) = \frac{M_C \sin^2 i}{(1+q)^2} = \left(\frac{2\pi}{P_{orb}}\right)^2 \frac{(a_x \sin i)^3}{G} \sim 16 \pm 1 M_\odot \tag{6.10}$$

where M_C is the supergiant companion star mass, $q = \frac{M_x}{M_C}$, is the ratio of the NS mass to the supergiant companion mass and G is the gravitational constant.

Fig. 6.9 clearly shows an eclipse occurring in the 20–30 and 30–40 keV energy bands. Future observations of the ingress and egress of the NS eclipse may provide information regarding the donor star's atmosphere and indicate any evidence of extended high energy emission in the region around the NS. There are two methods to determine the half angle of eclipse, θ_ϵ, which we define as the half width half height of the eclipse. We assume that the NS behaves as a point source in a circular orbit about a spherical star. Hence, the measured duration of the eclipse corresponds to a half angle of eclipse of $\theta_\epsilon = 0.66 \pm 0.2$ radians in both energy bands. Additionally, the mid-eclipse time corresponds to the epoch of NS superior conjunction of the NS, $T_{\pi/2}$, derived from our fit. This corresponds to the

period in the BeppoSAX data when the count rate was consistent with the background count rate. Taking the time at which the eclipse ends as 52,168.69 MJD (*Au03*), then the half-angle of the eclipse corresponds to $\theta_\epsilon = 0.591 \pm 0.09$ radians. Taking a weighted mean of the half angle of eclipse gives $\overline{\theta}_\epsilon = 0.61 \pm 0.08$ radians. Assuming we have a point source and spherical geometry the duration of the eclipse is related to R_C, the companion star radius, the inclination of the system and a, the separation of the stars by (Nagase, 1989):

$$\frac{R_C}{a} = (\cos^2 i + \sin^2 i \sin^2 \overline{\theta}_\epsilon)^{1/2} \tag{6.11}$$

Assuming that the NS has the canonical mass of 1.4 $M_\odot$ then for any given inclination angle the mass of the companion star can be derived from the mass function (eq. 6.10). Assuming that we have a perfectly circular orbit then $a_x \simeq a$, the phase delay modulation yields $a_x \sin i$ and hence for any given inclination the radius of the companion star can be derived from eq. 6.11. This gives an empirical relationship between the companion star mass and radius. An analytic approximation for the companion star Roche lobe is:

$$R_{Roche} = a\left(0.38 + 0.2 \log \frac{M_C}{M_{NS}}\right) \tag{6.12}$$

(Bowers & Deeming, 1984) (accurate < 1%)

From its low luminosity and its position in the Corbet diagram, we expect the supergiant companion star to be under-filling its Roche lobe hence the Roche lobe radius gives an upper limit to the allowed companion star radius, mass and system inclination. The empirical M_C–R_C relation and the associated R_{Roche} are plotted in Fig. 6.14 along with the neutron star – supergiant separation. The lighter shaded region toward the lower left of Fig. 6.14 indicates the allowed system parameters such that our measurements represent an under-filling Roche lobe supergiant. Also plotted are the masses and radii of a number of known OB supergiants (Wilson & Dopita, 1985; Herrero et al., 1992).

From Fig. 6.14 we can see that the properties of the companion star are: $M_C \sim 21 M_\odot$; $R_C \sim 19 R_\odot$. The complete range of these values is given in Table 6.4 with the other parameters of the system. These mass and radius values are consistent with late O9 – early B1 supergiant stars.

6.6.3 Spin properties of the pulsar

Measurement of changes in the NS pulse period is an independent indicator of the accretion mechanism operating in the system. If the NS is accreting matter from the donor star

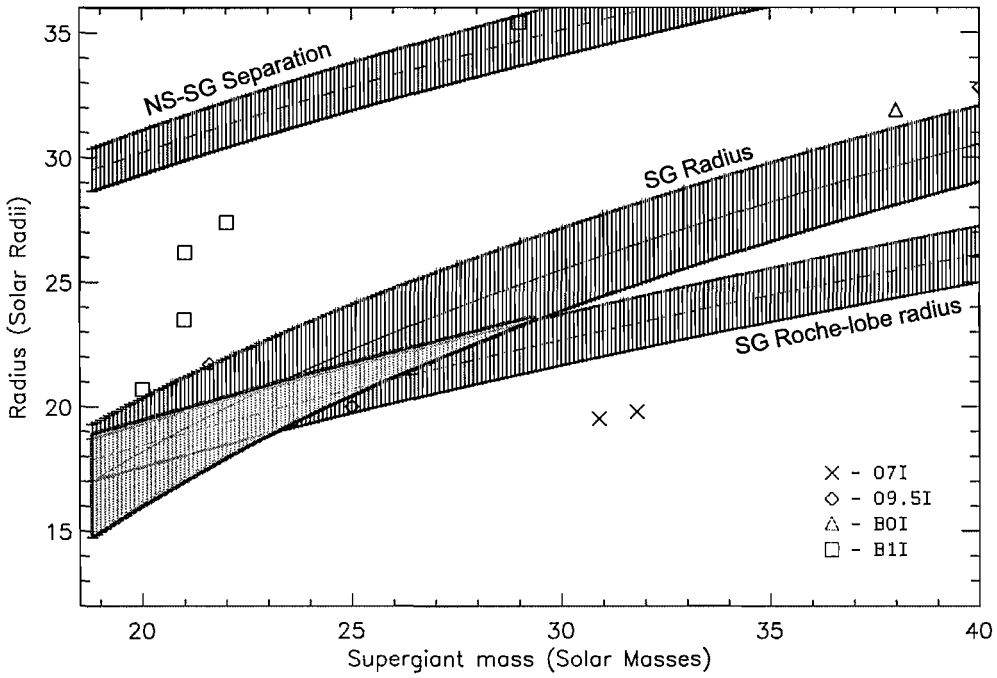

Figure 6.14: The derived mass-radius relationship of the supergiant (SG) in IGR J18027-2016 (assuming a NS mass of 1.4 $M_{\odot}$) is plotted against the SG Roche lobe radius and the NS-SG separation. The lighter shaded area corresponds to the region in which the SG radius is smaller than its Roche lobe radius. Also plotted are the masses and radii of a number of known OB supergiants.

via Roche lobe overflow then torques induced by the accretion disk will cause the pulse period to decrease, i.e. the NS should show evidence of spinning up. The BeppoSAX and XMM measurements of the spin period as 139.612 ± 0.006 s and 139.61 ± 0.04 s respectively, are separated by ~2.5 years and indicate no evidence of a change in spin period. Taking the 1σ limits of these measurements we find an upper limit to the spin-up rate of, $\dot{P}_{pulse}$~0.02 s yr^{-1}. The theoretical spin-up rate for a slow rotator is given by (Frank et al., 1992):

$$\frac{-\dot{P}_{pulse}}{P_{pulse}} \cong 8 \times 10^{-5} M_1^{-3/7} R_6^{6/7} L_{37}^{6/7} \mu_{30}^{2/7} I_{45}^{-1} P_{pulse} yr^{-1} \quad (6.13)$$

where M_1 is the NS mass in M⊙, R_6 is the NS radius in cm, L_{37} is the NS accretion luminosity in units 10^{37} ergs cm^{-2} s^{-1}, μ_{30} is the magnetic moment in units 10^{30} G cm^3 and I_{45} is the moment of inertia (~MR^2) of the NS in units 10^{45} g cm^2. For a typical neutron star with a magnetic field strength, B~10^{12} G, $\mu_{30} \sim I_{45} \sim R_6 \sim 1$. The theoretical spin-up of a neutron star accreting via Roche lobe overflow with a luminosity in the range 10^{35}–10^{38} ergs cm^{-2} s^{-1} is shown in Table 6.5 with the associated source distance for

Table 6.4: System parameters of IGR J18027-2016

Parameter	Value
P_{orb}	4.5696 ± 0.0009 days
P_{pulse} (BeppoSAX)	139.612 ± 0.006 s
P_{pulse} (XMM)	139.61 ± 0.04 s
$a_x \sin i$	68 ± 1 lt-s
$T_{\pi/2}$	52168.26 ± 0.04 MJD
T_{mid}	52931.37 ± 0.04 MJD
$f(M)$	16 ± 1 $M_\odot$
$\overline{\theta}_\epsilon$	0.61 ± 0.08 rad
M_C	$18.8 \lesssim M \lesssim 29.3\ M_\odot$
R_C	$14.7 \lesssim R \lesssim 23.4\ R_\odot$
a	$28.4 \lesssim a \lesssim 35.8\ R_\odot$
i	$59° \lesssim i \lesssim 88°$

each luminosity. If Roche lobe overflow is the source of accretion then a luminosity of 10^{38} ergs cm^{-2} s^{-1}, close to the Eddington luminosity, is expected (Kaper et al., 2004). Table 6.5 illustrates that this would locate the source outside of the galaxy and would result in a clear spin-up of the pulsar of ~24 seconds between the BeppoSAX and XMM observations, which is not seen. The limit of $\dot{P}_{pulse}$~0.02 s yr^{-1}, would imply that the source has a luminosity upper limit of 10^{35} ergs cm^{-2} s^{-1} which is very much lower than expected from a Roche lobe overflow system but would be typical of a wind accretion system. Hence, this is another indication that the donor star has not filled its Roche lobe and that the pulsar is powered entirely by wind fed accretion and thus lending further credence to the constraints on the donor star given by the shaded region of Figure 6.14.

Table 6.5: Theoretical $\dot{P}_{pulse}$ and distance for different source luminosity

Luminosity, (ergs cm^{-2} s^{-1})	10^{35}	10^{36}	10^{37}	10^{38}
$\dot{P}_{pulse}$, (s yr^{-1})	0.02	0.2	1.4	9.7
Distance, (kpc)	3.1	9.7	31	421

6.6.4 Spectral characteristics

The soft excess (< 3keV) evident in the XMM-EPIC data is identical in the on and off pulse spectra implying that the soft excess may not be pulsed. Performing timing analysis on the events below 3 keV does not show any period, however, the event rate is not high enough to reach a definitive conclusion. Soft X-ray excess have been found in other

HMXB sources, e.g. Vela X-1, and have been explained by scattering or partial ionisation of the stellar wind.

The equivalent width of the 6.4 keV Fe line has a 3 sigma upper limit of 40 eV and 25 eV for the off pulse and on pulse spectra respectively. Such values are consistent with $N_H < 5.0 \times 10^{22}$ cm^{-2} for a spherical geometry. The non-detection of the Fe line is therefore consistent with the absorbing column density which is observed.

The spectral fit of the EPIC and ISGRI spectra indicate a column density of $N_H = 6.8 \pm 1.0 \times 10^{22}$ cm^{-2}. This is much greater than the expected line of sight column density. The expected line of sight hydrogen column density is given by the NASA HEASARC nH tool and corresponds to $N_H = 1.0 \times 10^{22}$ cm^{-2}, and suggests that the absorption is intrinsic to the source and not the line of sight. This could be explained by the stellar wind from the OB supergiant accreting onto the neutron star forming a dense spherical shell. As the column density is not seen to change when the pulsar is observed inside and outside of the primary pulse indicates that the high level of absorption cannot be explained by the accreting column. The low statistics of the BeppoSAX data used by *Au03* did not allow an accurate spectral analysis. They inferred a luminosity of ~5.6 $\times$ 10^{35} ergs s^{-1} over the 1.8-10 keV range by fitting their data to a power law with Γ = -0.1 $\pm$ 0.1 and $N_H = 1.7^{+0.8}_{-0.9} \times 10^{22}$ cm^{-2}, and assumed a source distance of 10 kpc. The XMM spectral fit indicates that the column density is much higher and hence the source luminosity was previously underestimated.

Assuming that IGR J18027-2016 is 10 kpc away the 2-10 keV flux during the primary pulse of $F_{2-10keV} = 8.9 \times 10^{11}$ ergs cm^{-2} s^{-1} gives an estimate of the source luminosity of ~1.1 $\times$10^{36} ergs s^{-1}, a typical luminosity for a non-Roche lobe filling Supergiant HMXB (Negueruela, 2004). A useful comparison is provided by 4U 1538-52, which is a typical HMXB accreting from a stellar wind and shows similarities to IGR J18027-2016. 4U 1538-52 has a long spin period of ~529 s, an orbital period of 3.75 days and undergoes a well defined X-ray eclipse. The companion is a 19.9$M_\odot$ B0 star (Reynolds et al., 1992) and the X-ray flux has been estimated as ~2 $\times$ 10^{36} ergs s^{-1} for a distance of 6.4 kpc (Robba et al., 2001). Hence the luminosity of IGR J18027-2016 appears to be typical of wind accreting HMXBs assuming it has a distance which approximates to the far side of the Galactic Centre.

6.7 Conclusions

Through the analysis of observations of the INTEGRAL discovered source IGR J18027-2016 by the BeppoSAX, INTEGRAL and XMM-Newton missions it has been possible

to identify the nature of the source and to identify a large number of the systems physical parameters. IGR J18027-2016 is seen to be an eclipsing HMXB system comprising an X-ray pulsar accreting matter from the stellar wind of a late O – early B supergiant.

The source is persistent in the soft γ-ray band, showing no evidence of extreme variability. Pulsations are observed in the 1-10 keV X-ray band by both BeppoSAX and XMM-Newton. The pulse period is measured to be 139.61 seconds. Measurements of the pulse period separated by ~2.5 years give no indication of a change in the spin rate of the pulsar. This implies that there are no accretion torques present, hence accretion is via the stellar wind only. However, the pulse period is modulated by the orbital motion of the neutron star around the supergiant companion. Timing analysis of the INTEGRAL observations reveals a periodicity of 4.5696 days which is attributed to the orbital period of the binary system and fits the observed modulation of the pulse arrival times. The folded orbital light curve indicates a sharp eclipse, indicating that this is a relatively high inclination system. The pulse period and orbital period place this system in the region of the Corbet diagram occupied by Supergiant HMXBs which are under-filling their Roche lobe.

From the system orbital period and neutron star pulse period a donor mass function of ~18 $M_{\odot}$ is found. Assuming a canonical 1.4 $M_{\odot}$ neutron star the mass function and the duration of eclipse indicate a range of donor star potential masses and radii of 18.8 $M_{\odot}$ $\lesssim M \lesssim$ 29.3 $M_{\odot}$ and 14.7 $R_{\odot} \lesssim R \lesssim$ 23.4 $R_{\odot}$. These correspond to a system inclination angle of $59° \lesssim i \lesssim 88°$. These values are typical of a late O – early B supergiant.

An investigation of the 1–50 keV spectra of IGR J18027-2016 identifies a very high intrinsic photoelectric absorption, ~7 times the expected line of sight column density, which is not attributable to the accretion column. The origin of this absorption is not fully understood, however, IGR J18027-2016 shares this nature with a large number of other newly discovered INTEGRAL sources (Walter et al., 2004). The mechanism by which these sources become highly obscured is a question of much debate, although the prevailing idea currently is that the companion star is producing a wind of sufficent density to cocoon the neutron star in material. This is one of the greates mysteries identified by INTEGRAL and the results of these investigations should enhance our understanding of the evolution of X-ray binary systems.

Of these new obscured sources, IGR J18027-2016, is now the best understood, however it is by no means fully understood and further studies of it may shed light onto the properties of this new family of objects. Currently proposals have been submitted to observe IGR J18027-2016 and IGR J17252-3616, another eclipsing obscured HMXB, in the X-ray band at multiple epochs around the orbit and eclipse to probe the obscuring mate-

rial. If the stellar wind is strongly clumped then during eclipse fluorescence lines should be evident in the X-ray spectra. Besides resolving the issue of the high obscuration in these systems, these sources are extremely valuable as they drastically increase the number of supergiant High Mass X-ray binary systems known in our galaxy. These systems are extremely important in the 'weighing' of neutron stars and hence may be used in the constraining of an equation of state for these objects.

Chapter 7

Conclusions

The work presented in this thesis has focused on the production of surveys of the hard X-ray and γ-ray sky taking advantage of new techniques and instrumentation. The technical challenges and difficulties in observing at these high energies has led to a lack of information and understanding of the properties of astrophysical objects which emit radiation in this regime and make them a ripe sample of objects for current study. The work presented in this thesis has attempted to explore this energy regime and specifically through the use of the INTEGRAL satellite gain some knowledge and understanding of the γ-ray source populations in or galaxy.

7.0.1 The BATSE All-Sky Survey

The BATSE All-Sky Survey (BASS) presents a novel and new approach to the exploitation of BATSE data to construct all-sky images of the high-energy sky. Although the use of the Earth occultation technique has long been used with BATSE data to monitor sources and construct images of a limited size it has not been used in the construction of all-sky images. The LIMBO software developed at Southampton in conjunction with the CLEAN algorithm has produced the capability to build all-sky images and clean the complex point-spread functions of the sources allowing an all-sky survey to be constructed.

The results of the BATSE survey identify ~36 sources down to a limiting sensitivity of ~20 mCrab in the 30–160 keV energy band. The survey is limited by the angular resolution of the imaging grid ($2^\circ \times 2^\circ$) and by the presence of an imaging systematic attributed to passage through the South Atlantic Anomaly (SAA). With improvements in computing power it is possible to reduce the imaging grid down to improve the angular resolution of the imaging process, however it is limited to a $0.5^\circ \times 0.5^\circ$ imaging grid due to the finite time of an occultation transition through the Earth's atmosphere. None the

less this would vastly improve the resolution currently available.

The systematic arising from passage through the SAA can theoretically be corrected. Just as temporal variations in the detector backgrounds were removed from the data set by Mass Modelling, modelling of the SAA activity decay would allow for its removal from the data set. Removing this temporal variation will allow the LIMBO code to produce maps which would be more statistical in nature and have a lower level of systematic noise. The combination of these two improvements could vastly improve the effectiveness of the BATSE survey.

However, these techniques are not purely of use in the analysis of BATSE data. The burst monitor on-board the GLAST mission, which is due for launch August 2007, can be used to observe occultations of γ-ray sources by the Earth. This is also potentially true on the EXIST mission if an all-sky monitor is included. Application of the standard Earth occultation technique has already been discussed for these two missions. The only major requirement to apply the Southampton imaging techniques to these missions would be the construction of a Mass Model Monte-Carlo to simulated the detector backgrounds to allow flat-fielding.

7.0.2 The IBIS/ISGRI survey

The IBIS survey team have to date released two catalogues of sources. This thesis has shown the difficulties in this task and the development of techniques to maximise the source detection and science capability of the IBIS survey and its subsequent data products. The last catalogue to be publicly released contained 209 sources detected in the 20–100 keV energy regime. This is a vast improvement on any prior mission which has observed in this energy band and has included the discovery of an entirely new set of astrophysical objects.

The INTEGRAL mission is funded until 2010. Already, more than three times the quantity of data is available than was used in the construction of the 2^{nd} IBIS/ISGRI Survey Catalogue. Additionally, there have been recent improvements and developments in the standard OSA reduction software. These combine to produce an increasingly powerful data set which can be used in the production of a survey which will cover ever increasing sky down to a higher sensitivity. The source populations identified by the survey team allow for an understanding of their statistical properties as classes of objects as well as their individual properties when combined with the observations in other wavebands.

7.0.3 Global properties

An analysis of the global characteristics of the sources observed in the 1st IBIS/ISGRI Survey Catalogue are presented in this thesis. The high mass X-ray binary and low mass X-ray binaries observed to emit in γ-rays are seen to exhibit similar properties to their counterparts observed in the traditional X-ray band.

The high mass source population is seen to have a number density distribution which is consistent with a population which is not distributed uniformly within the galactic disk. They are also observed to be tightly constrained to the Galactic Plane and often are observed in the vicinity of the spiral arm tangent points. These properties are entirely expected of a young, galactic source population.

Conversely, the low mass systems are seen to cluster in the Galactic Centre region and have a much more uniform distribution throughout the plane of the disk. They are also observed to have a much larger scale height than the HMXB population. Again, this is expected of a source population which is old and associated with the Galactic Bulge.

The unclassified objects detected in the IBIS survey show many interesting characteristics despite their small numbers. They show a tight correlation to the plane of the disk and are seen to cluster in the Galactic Centre region. However, there is also a large concentration of them in the Norma spiral arm tangent. These angular and spatial characteristics are very reminiscent of the high mass X-ray binary population. A comparison of the luminosity function of these sources with those of the known classes also shows similarities with the known HMXBs. However, the small sample number combined with the exposure bias of the Galactic Centre makes it very difficult to analyse these results.

Follow-up observations of individual sources has indicated that a large number of the unclassified sources are indeed high mass systems. More importantly however, they have also been observed to have high intrinsic absorptions explaining why they have previously gone unnoticed by earlier X-ray missions. A better understanding of these source populations can only be achieved by the examination of a much larger un-biased γ-ray sample. The continued survey activities of INTEGRAL will readily produce this data.

7.0.4 IGR J18027-2016

Work in this thesis goes a long way in identifying and ascertaining the nature of one of the newly discovered, unclassified INTEGRAL sources, IGR J18027-2016. An examination of the IBIS survey data for this source identified an orbital period of ~4.56 days. Combined with the spin period measurement of the BeppoSAX instrument this placed IGR J18027-2016 in the region of the Corbet diagram occupied by supergiant high mass

X-ray binaries which are under-filling their Roche-lobe. Further measurements by the XMM-Newton mission confirmed the pulse period and identified a column density of ~7 $\times 10^{22}$ cm^{-2}. Hence, the source appears to be a highly obscured HMXB, as have many other new INTEGRAL sources.

Combining the data from all three missions allows for the detailed analysis of the parameters of the binary system. A mass function of ~16 $M_{\odot}$ is indentified. Assuming a canonical 1.4 $M_{\odot}$ neutron star the mass function and the duration of eclipse indicate a range of donor star potential masses and radii of 18.8 $M_{\odot} \lesssim M \lesssim$ 29.3 $M_{\odot}$ and 14.7 $R_{\odot} \lesssim R \lesssim$ 23.4 $R_{\odot}$. These correspond to a system inclination angle of 59° $\lesssim i \lesssim$ 88°. These values are typical of a late O – early B supergiant.

The clear eclipses evident in the γ-ray band make this an interesting source to follow-up further. X-ray measurements made throughout the orbit and during the eclipse can be used to map the obscuring material which is present in the system and lead to an explanation of the origins of this material as well as helping to explain how these new binaries fit into the global scheme of stellar evolution.

7.0.5 Future Work

The work presented here shows the scientific value of exploring the soft γ-ray energy domain. The discoveries that have been made and which continue to be made increase the breadth of our scientific knowledge of the astrophysical sources and the extreme environments which are involved in the production of this high energy emission.

The INTEGRAL mission is currently funded until 2010. As long as the instrument is operational there will be more work for the IBIS survey team to perform, more sources to be discovered and more follow-ups to be performed. Simultaneously, only by further observations of the current sample of sources can we hope to gain an insight into the processes which are in operation and the properties of these systems. The current existence and operation of Swift and the imminent launch of GLAST make this a highly productive time to explore the mysteries of the γ-ray sky. The results and discoveries made today will only pave the way for the missions of tomorrow.

"There is one thing even more vital to science than intelligent methods; and that is, the sincere desire to find out the truth, whatever it may be."

– Charles Sanders Pierce

Appendix A

The 1st IBIS/ISGRI Survey Catalogue

Listed in Table A.1 are the 123 sources detected in the 1st IBIS/ISGRI Survey Catalogue. The methodology used in the generation of this list of sources is given in Chapter 4.

Table A.1: The 1st IBIS catalogue : 20–100 keV

No.	Name	RA (deg)	Dec. (deg)	F_{20-40} (count/s)	F_{40-100} (count/s	Sig[a]	Exp[b] (ks)	Type[c]
1	1A0114+650	19.545	65.298	0.87±0.09	<0.59	9.3‡	43	HMXB
2	4U0352+30	58.842	31.038	11.40±0.58	9.72±0.75	14.9	7	HMXB,XP
3	Crab	83.640	22.009	93.64±0.07	69.12±0.08	1,021.2	94	PWN,PSR
4	4U0614+091	94.284	9.109	2.90±0.14	2.21±0.19	15.6	29	LMXB,B,A
5	Vela Pulsar	128.836	-45.196	0.84±0.08	0.74±0.11	8.4	61	PWN,PSR
6	4U0836-429	129.355	-42.908	1.68±0.08	1.35±0.11	16.9	64	LMXB,T,B
7	Vela X-1	135.537	-40.561	21.09±0.09	3.78±0.12	116.5	58	HMXB,XP
8	Cen X-3	170.334	-60.610	2.84±0.08	<0.40	11.6	55	HMXB,XP
9	A1145.1-6141	176.863	-61.971	2.75±0.09	1.09±0.11	22.2	54	HMXB,XP
10	GX 301-2	186.682	-62.767	22.46±0.09	2.00±0.12	89.3	51	HMXB,XP,T
11	Cen A	201.376	-43.059	20.51±2.75	<14.65	6.5	1	AGN
12	Cir galaxy	213.292	-65.323	1.77±0.12	1.17±0.16	11.1	29	AGN
13	PSR 1509-58	228.496	-59.141	1.21±0.13	1.62±0.17	9.6	74	PSR
14	4U1516-569	230.174	-57.158	3.05±0.10	<0.72	29.7‡	113	LMXB,T,B,A
15	4U1538-522	235.584	-52.376	2.53±0.05	<0.32	26.4	308	HMXB,XP
16	IGR J15479-4529	237.055	-45.471	0.58±0.03	<0.27	12.6	441	CV
17	XTE J1550-564	237.757	-56.458	0.61±0.06	0.63±0.07	8.6	240	LMXB,T,BHC
18	4U1608-522	243.197	-52.420	2.13±0.03	1.23±0.04	44.6	469	LMXB,T,B,A
19	IGR J16167-4957	244.171	-49.957	0.27±0.03	<0.17	6.2	577	?
20	IGR J16195-4945	244.844	-49.719	0.29±0.03	<0.29	8.7	579	?
21	Sco X-1	244.990	-15.643	90.86±0.12	2.33±0.13	111.6	76	LMXB,Z
22	IGR J16207-5129	245.156	-51.510	0.36±0.03	<0.28	10.0	528	?
23	4U1624-49	246.983	-49.187	0.46±0.03	<0.09	16.3‡	589	LMXB,D
24	IGR J16318-4848	247.953	-48.801	2.31±0.03	0.86±0.03	61.9	658	HMXB
25	AXJ 1631.9-4752	248.009	-47.859	1.69±0.03	0.47±0.03	35.9	683	HMXB?
26	4U1626-67	248.085	-67.480	2.75±0.16	<0.60	17.3‡	46	LMXB,XP
27	4U1630-47	248.524	-47.390	8.32±0.03	4.31±0.03	202.4	713	LMXB,T,U,D
28	IGR J16358-4726	248.990	-47.407	0.44±0.03	0.21±0.03	16.4‡	696	LMXB?,T

Continued on Next Page...

Table A.1 – Continued

No.	Name	RA (deg)	Dec. (deg)	F_{20-40} (count/s)	F_{40-100} (count/s	Sig[a]	Exp[b] (ks)	Type[c]
29	IGR J16393-4643	249.757	-46.676	0.82±0.03	<0.16	12.7	727	?
30	4U1636-536	250.231	-53.739	2.48±0.03	1.13±0.04	49.4	501	LMXB,B,A
31	IGR J16418-4532	250.437	-45.520	0.50±0.03	<0.08	10.1	752	?
32	GX 340+0	251.450	-45.603	3.93±0.03	<0.19	21.8	760	LMXB,Z
33	IGR J16479-4514	251.994	-45.217	0.48±0.03	0.19±0.03	11.9	768	?
34	PSR J1649-4349	252.409	-43.818	0.20±0.03	<0.22	6.3	782	PSR
35	IGR J16558-5203	254.004	-52.075	<0.19	<0.20	6.1	572	?
36	AXJ1700.2-4220	255.075	-42.326	0.20±0.03	<0.19	6.8	798	?
37	OAO 1657-415	255.199	-41.653	9.90±0.03	4.02±0.03	248.3	800	HMXB,XP
38	GX 339-4	255.700	-48.783	0.78±0.03	0.55±0.03	21.9	687	LMXB,T,U,BH
39	4U1700-377	255.982	-37.841	23.49±0.03	10.64±0.03	571.6	793	HMXB
40	GX 349+2	256.439	-36.408	5.46±0.03	<0.14	18.8	781	LMXB,Z
41	4U1702-429	256.557	-43.029	1.42±0.03	0.65±0.03	31.8	794	LMXB,B,A
42	4U1705-32	257.213	-32.333	0.36±0.03	0.32±0.03	10.2	737	?
43	4U1705-440	257.223	-44.090	3.25±0.03	1.49±0.03	74.6	780	LMXB,B,A
44	IGR J17091-3624	257.289	-36.405	0.73±0.03	0.49±0.03	19.7	787	?
45	XTE J1710-281	257.583	-28.145	0.21±0.03	0.33±0.04	7.3	661	LMXB,T,B
46	EXMS B1709-232	258.122	-23.357	0.52±0.03	<0.15	16.5‡	568	Cluster
47	SAX J1712.6-3739	258.136	-37.632	0.52±0.03	0.28±0.03	12.1	800	LMXB,T,B
48	V2400 Oph	258.152	-24.270	0.40±0.03	<0.18	7.5	592	CV
49	NGC6300	259.209	-62.792	0.51±0.06	<0.47	7.6	157	AGN,Sy2
50	IGR J17195-4100	259.878	-41.012	0.23±0.03	<0.15	8.3‡	786	?
51	XTE J1720-318	259.978	-31.748	0.45±0.03	0.50±0.03	15.0	773	LMXB,T,BHC
52	IGR J17200-3116	260.008	-31.274	0.24±0.03	<0.24	6.8	768	?
53	IGR J17252-3616	261.309	-36.274	1.13±0.03	0.27±0.03	20.3	801	?
54	IGR J17254-3257	261.381	-32.961	0.32±0.03	0.28±0.03	8.6	797	?
55	GRS 1724-308	261.879	-30.790	2.33±0.03	1.65±0.03	65.1	788	LMXB,G,B,A
56	IGR J17303-0601	262.594	-6.000	0.28±0.03	<0.18	8.3‡	330	?
57	GX 9+9	262.939	-16.948	1.11±0.03	<0.13	39.8‡	580	LMXB,A
58	GX 354-0	262.990	-33.826	3.19±0.03	0.75±0.03	46.4	800	LMXB,B,A
59	GX 1+4	263.009	-24.735	2.34±0.03	1.34±0.03	64.8	741	LMXB,XP
60	GRS 1734-292	264.369	-29.131	0.64±0.03	0.31±0.03	15.8	796	AGN,Sy1
61	SLX 1735-269	264.571	-26.978	1.04±0.03	0.68±0.03	28.6	787	LMXB,B
62	4U1735-444	264.741	-44.444	3.09±0.03	<0.11	14.1	657	LMXB,B,A
63	SLX 1737-282	265.168	-28.313	0.39±0.03	0.25±0.03	10.8	797	LMXB,B,XP
64	1E 1740.7-2943	265.984	-29.735	4.68±0.03	4.32±0.03	147.3	799	LMXB,BHC
65	M1741-293	266.240	-29.336	0.86±0.03	0.60±0.03	24.4	800	LMXB,T,B
66	1E1742.5-2859	266.490	-28.910	0.57±0.03	0.28±0.03	14.0	800	LMXB
67	1E 1742.9-2929	266.500	-29.491	0.63±0.03	<0.10	22.4‡	797	LMXB,B
68	IGR J17464-3213	266.562	-32.223	7.53±0.03	4.01±0.03	179.8	789	LMXB,T,BHC
69	IGR J17460-3047	266.580	-30.791	0.14±0.03	<0.26	6.0	794	?
70	1E1743.1-2843	266.587	-28.752	0.55±0.03	<0.22	8.9	800	LMXB
71	IGR J17475-2822	266.799	-28.444	0.28±0.03	0.22±0.03	10.0‡	800	?
72	SLX 1744-299	266.844	-30.012	0.85±0.03	0.40±0.03	18.2	796	LMXB,B
73	GX 3+1	266.984	-26.556	1.76±0.03	0.21±0.03	10.2	802	LMXB,B,A
74	IGR J17488-3253	267.206	-32.892	0.22±0.03	<0.25	6.2	774	?
75	4U1745-203	267.208	-20.361	0.25±0.03	<0.25	7.3	766	LMXB,T,G
76	4U1746-37	267.512	-37.044	0.47±0.03	<0.14	16.0‡	717	LMXB,G,B,A
77	IGR J17597-2201	269.943	-22.015	1.03±0.03	0.74±0.03	32.0	809	LMXB,B
78	GX 5-1	270.281	-25.068	4.85±0.03	0.24±0.03	27.1	803	LMXB,Z

Continued on Next Page...

Table A.1 – Continued

No.	Name	RA (deg)	Dec. (deg)	F_{20-40} (count/s)	F_{40-100} (count/s	Sig[a]	Exp[b] (ks)	Type[c]
79	GRS 1758-258	270.301	-25.735	4.18±0.03	3.92±0.03	135.9	800	LMXB,U,BHC
80	GX 9+1	270.387	-20.517	1.79±0.03	<0.04	70.6‡	808	LMXB,A
81	IGR J18027-2016	270.677	-20.278	0.48±0.03	<0.18	10.6	809	?
82	IGR J18027-1455	270.691	-14.903	0.24±0.02	0.21±0.03	8.9	769	?
83	XTE J1807-294	271.744	-29.416	0.48±0.03	0.35±0.03	12.3	744	LMXB,T,XP
84	SGR 1806-20	272.142	-20.385	0.25±0.03	0.26±0.03	8.2	812	SGR
85	GX 13+1	273.624	-17.148	1.57±0.02	0.22±0.03	16.9	813	LMXB,B,A
86	M1812-12	273.774	-12.094	2.47±0.02	1.83±0.03	85.0	783	LMXB,B
87	GX 17+2	274.006	-14.029	5.45±0.02	0.20±0.03	31.3	803	LMXB,B,Z
88	AXJ1820.5-1434	275.131	-14.553	0.50±0.02	0.23±0.03	15.1	808	HMXB,XP
89	4U1820-303	275.926	-30.360	3.82±0.03	<0.24	18.3	622	LMXB,G,B,A
90	4U1822-000	276.350	-0.018	0.23±0.03	<0.15	7.1‡	440	LMXB
91	4U1822-371	276.452	-37.100	3.89±0.04	0.29±0.04	35.9	478	LMXB,D
92	GS 1826-24	277.366	-23.789	8.48±0.03	5.29±0.03	230.1	705	LMXB,B
93	IGR J18325-0756	278.113	-7.937	0.53±0.02	0.27±0.03	15.8	708	?
94	SNR 021.5-00.9	278.383	-10.560	0.28±0.02	0.26±0.03	10.6	757	SNR
95	PKS 1830-211	278.417	-21.079	0.29±0.03	0.29±0.03	9.6	714	AGN
96	RX J1832-33	278.930	-32.980	1.39±0.04	0.91±0.04	30.4	479	LMXB,G,B
97	AXJ 1838.0-0655	279.523	-6.921	0.18±0.02	0.20±0.03	6.3	659	?
98	Ser X-1	279.996	5.038	1.26±0.06	<0.32	20.5‡	192	LMXB,B
99	Kes 73	280.318	-4.932	0.28±0.03	0.34±0.03	9.8	589	SNR,XP
100	Ginga 1843+00	281.412	0.891	0.33±0.04	<0.24	8.2‡	335	HMXB,XP
101	AXJ 1846.4-0258	281.600	-2.959	0.26±0.03	0.26±0.04	6.1	488	SNR,PWN,XP
102	IGR J18483-0311	282.075	-3.161	0.36±0.03	<0.29	7.7	487	?
103	4U1850-087	283.270	-8.705	0.56±0.03	0.31±0.03	13.2	618	LMXB,G,B
104	4U 1849-31	283.762	-31.154	0.93±0.04	<0.33	12.0	349	CV
105	XTE J1855-026	283.873	-2.597	1.57±0.03	0.62±0.04	29.9	426	HMXB,XP
106	XTE J1901+014	285.460	1.464	0.43±0.05	<0.39	7.9‡	254	?,T,BHC
107	4U1901+03	285.914	3.215	9.29±0.07	0.84±0.09	42.6	184	HMXB,T
108	4U1907+097	287.401	9.843	2.40±0.11	<0.56	6.8	54	HMXB,XP,T
109	4U1909+07	287.699	7.598	2.12±0.12	1.08±0.14	14.2	72	HMXB
110	SS 433	287.950	4.990	2.52±0.11	<1.02	13.5	109	HMXB
111	IGR J19140+098	288.512	9.888	1.06±0.11	<0.59	9.5‡	51	?
112	GRS 1915+105	288.796	10.951	31.08±0.11	8.63±0.13	144.9	48	LMXB,T,BHC
113	1916-053	289.720	-5.253	1.20±0.04	<0.30	13.1	321	LMXB,B,D
114	RX J1940.2-1025	295.050	-10.383	0.35±0.05	<0.27	7.3‡	218	CV
115	KS 1947+300	297.390	30.213	3.43±0.09	1.73±0.11	26.8	66	HMXB,T
116	Cyg X-1	299.593	35.208	75.51±0.09	66.37±0.11	676.6	67	HMXB,BH,U
117	EXO 2030+375	308.054	37.645	1.51±0.09	0.74±0.10	11.8	70	HMXB,XP,T
118	Cyg X-3	308.102	40.968	18.07±0.08	5.68±0.10	122.7	71	HMXB
119	SAX J2103.5+4545	315.899	45.757	4.65±0.08	2.04±0.10	41.6	70	HMXB,XP
120	IGR J21247+5058	321.175	50.980	0.51±0.07	0.64±0.10	6.5	70	?
121	1H2140+433	325.687	43.577	0.71±0.10	<0.45	7.0‡	45	Dwarf nova
122	Cyg X-2	326.184	38.338	3.99±0.18	<0.87	21.8‡	24	LMXB,B,Z
123	4U2206+543	331.993	54.527	1.87±0.07	0.96±0.10	17.1	69	HMXB

Continued on Next Page...

Table A.1 – Continued

No.	Name	RA (deg)	Dec. (deg)	F_{20-40} (count/s)	F_{40-100} (count/s	Sig[a]	Exp[b] (ks)	Type[c]

[a]Significance in primary detection band (30–50 keV), or 20–40 keV band if marked ‡

[b]On-source exposure, adjusted for off-axis vignetting effects.

[c]Type identifiers: LMXB=Low Mass X-ray binary, HMXB=High Mass X-ray binary, T=transient, A=Atoll source, B=burster (neutron star), BHC=Black hole candidate, CV=Cataclysmic variable, D=Dipping source, G=Globular cluster X-ray source, PSR=Radio pulsar, PWN=Pulsar wind nebula,SGR=Soft Gamma Repeater, SNR = Supernova remnant, U=Ultrasoft source, XP=X-ray pulsar, Z=Z-type source (neutron stars).

[d]The following unidentified sources may have counterparts in the ROSAT Bright All-Sky Survey: 16, 19, 35, 50, 52, 54, 56, 74.

Appendix B

Images of the 1^{st} IBIS/ISGRI Survey Catalogue

The significance mosaic of the 30–50 keV energy band used in the 1^{st} IBIS/ISGRI Survey Catalogueis shown in segments in figures B.1–B.6. They show 30° × 18° sections of the Galactic Plane. Significance countours at the 5, 6, 8 and 15 σ levels are also shown. The exposure map of the 1^{st} IBIS/ISGRI Survey Catalogue is shown in Fig. D.7.

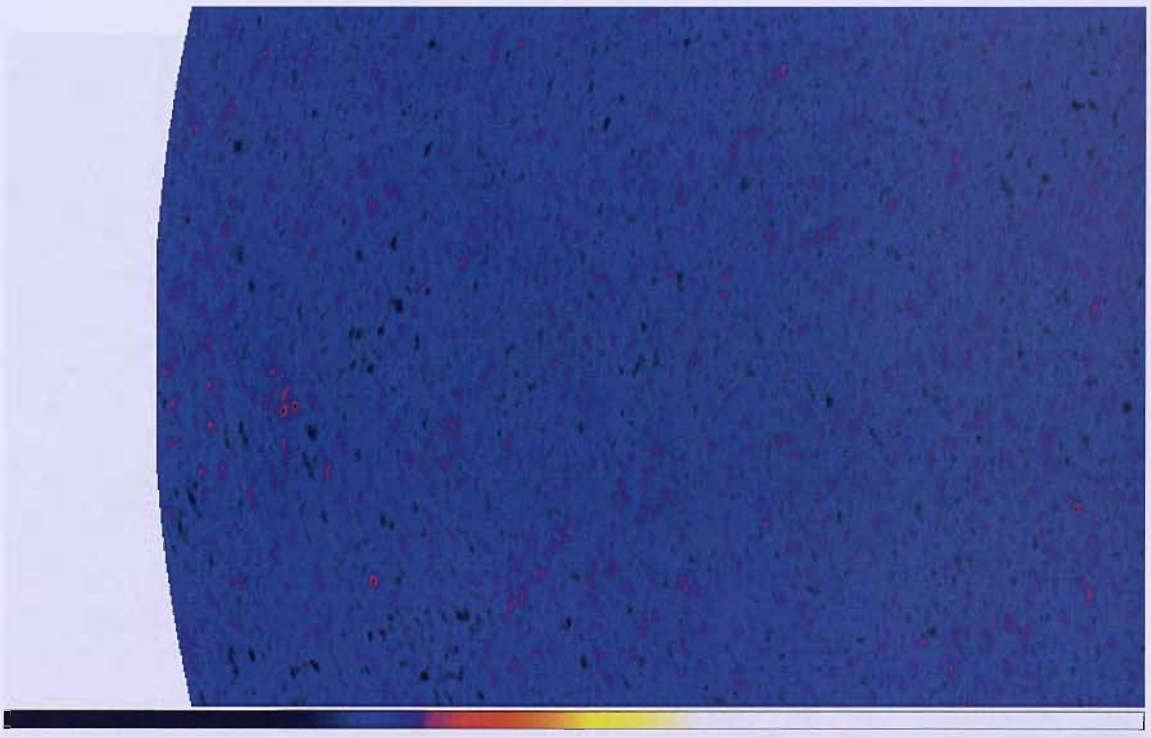

Figure B.1: Significance map of the 1^{st} IBIS/ISGRI Survey Catalogue from 180°< l^{II} <150° and -9.0°< b^{II} <+9.0°

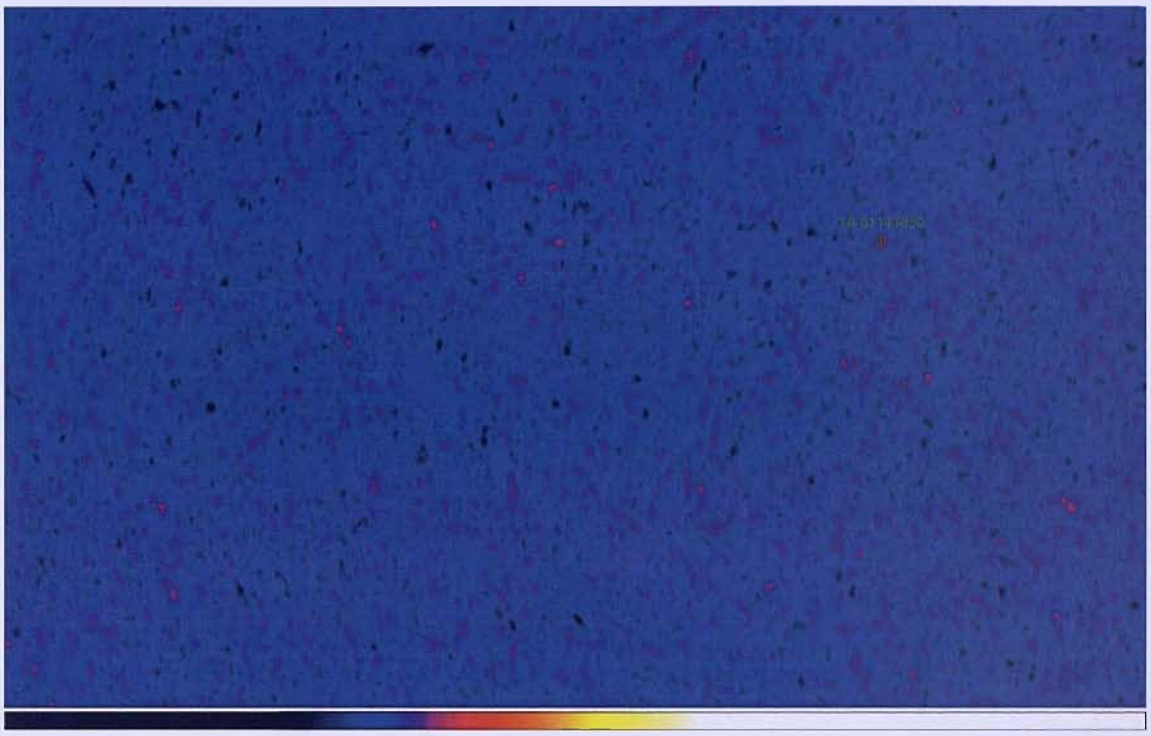

Figure B.2: Significance map of the 1st IBIS/ISGRI Survey Catalogue from 150°< l^{II} <120° and -9.0°< b^{II} <+9.0°

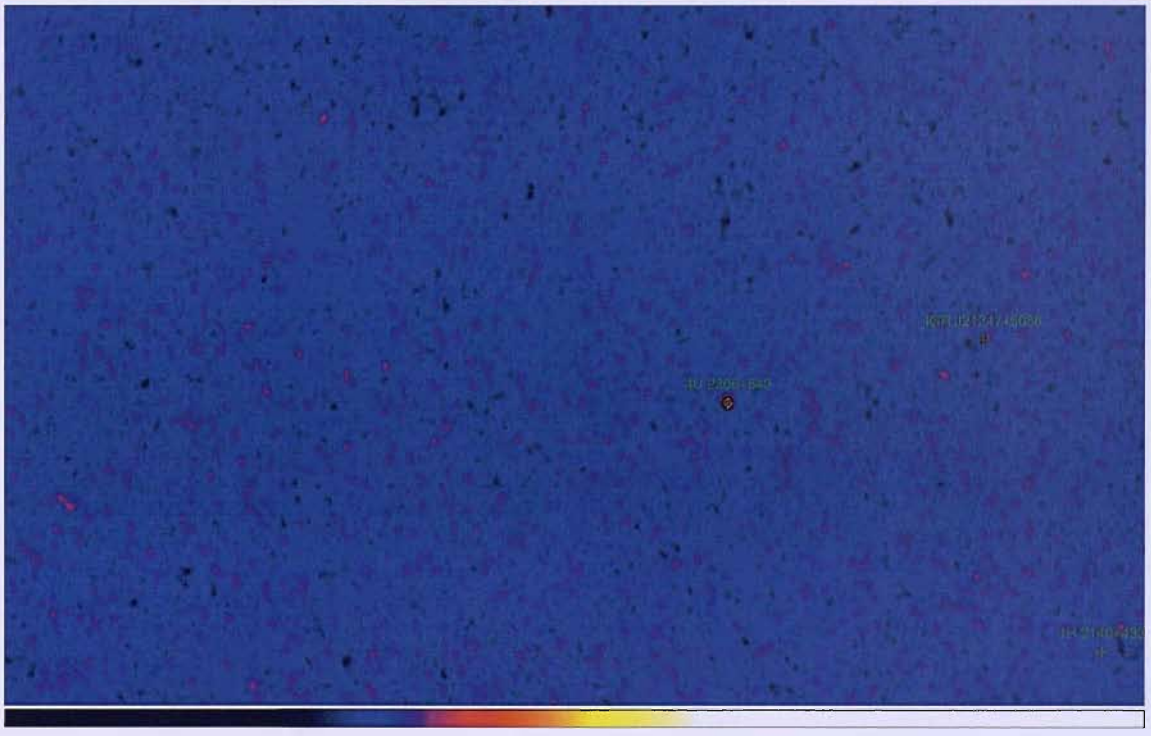

Figure B.3: Significance map of the 1st IBIS/ISGRI Survey Catalogue from 120°< l^{II} <90° and -9.0°< b^{II} <+9.0°

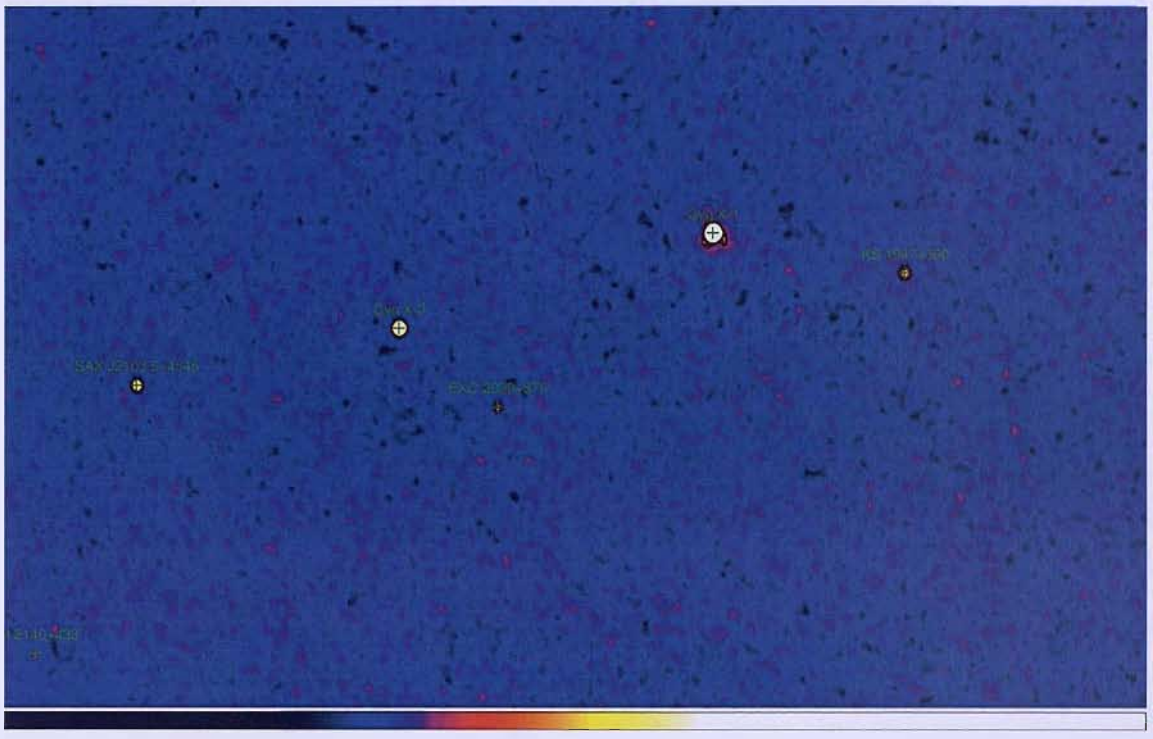

Figure B.4: Significance map of the 1st IBIS/ISGRI Survey Catalogue from 90°< l^{II} <60° and -9.0°< b^{II} <+9.0°

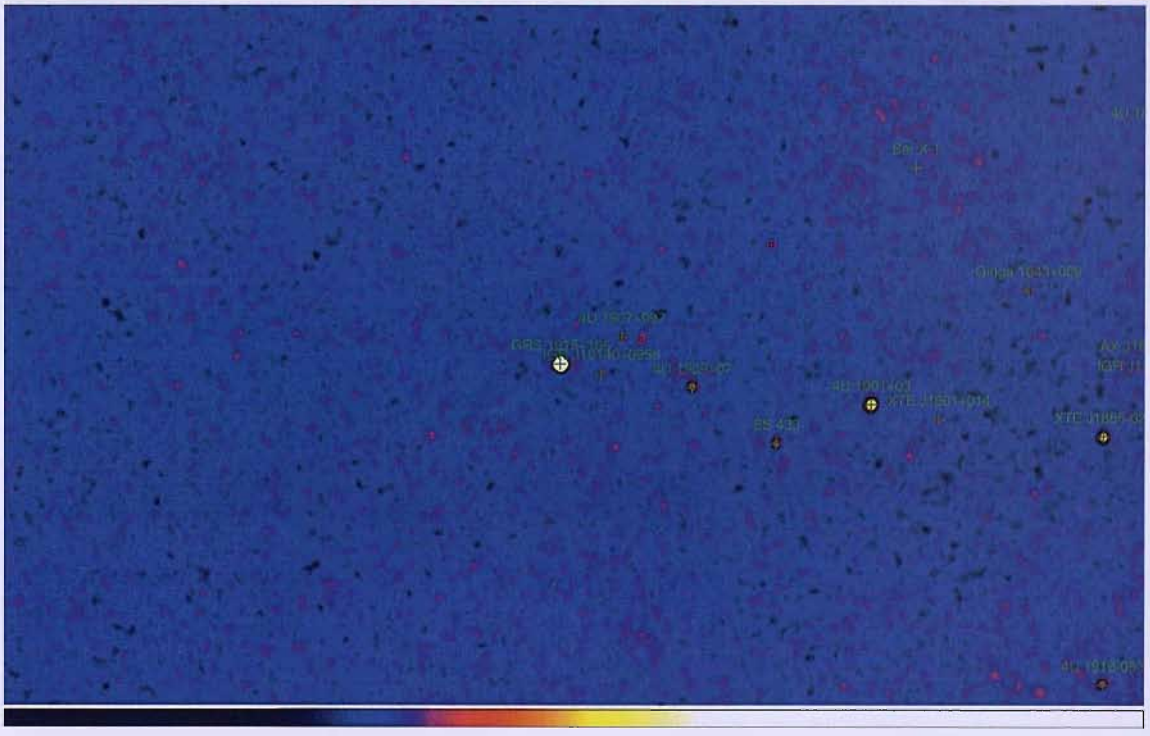

Figure B.5: Significance map of the 1st IBIS/ISGRI Survey Catalogue from 60°< l^{II} <30° and -9.0°< b^{II} <+9.0°

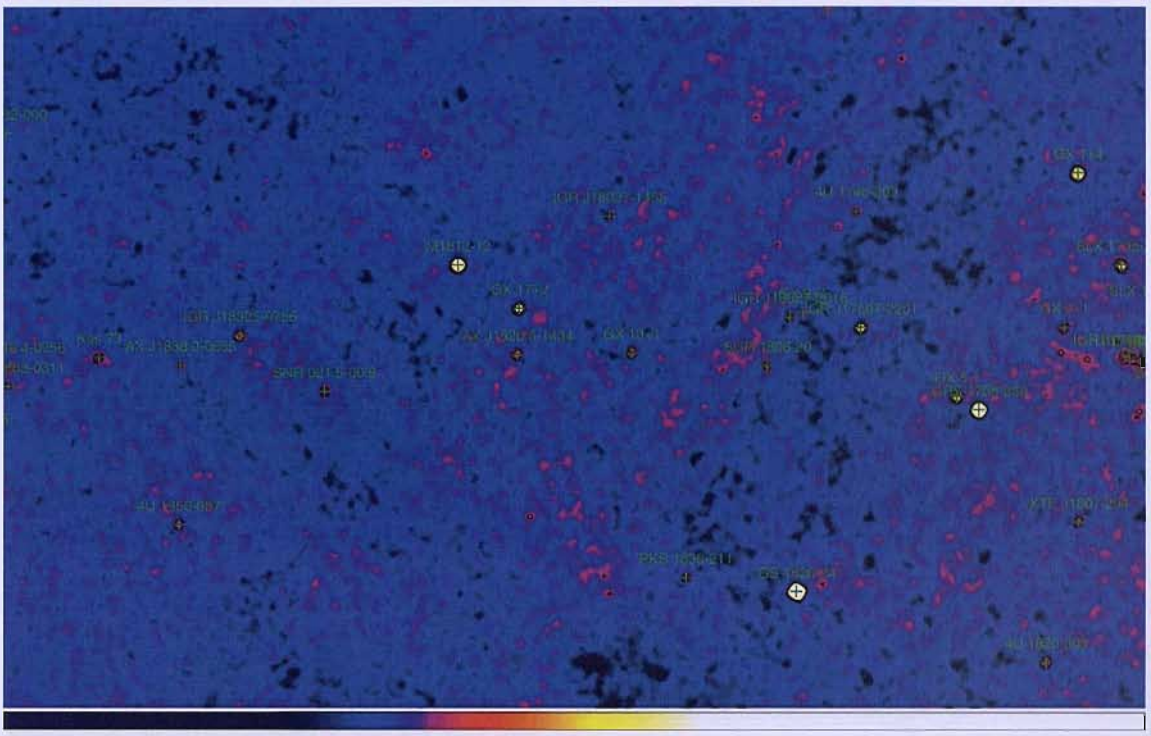

Figure B.6: Significance map of the 1st IBIS/ISGRI Survey Catalogue from 30°< l^{II} <0° and -9.0°< b^{II} <+9.0°

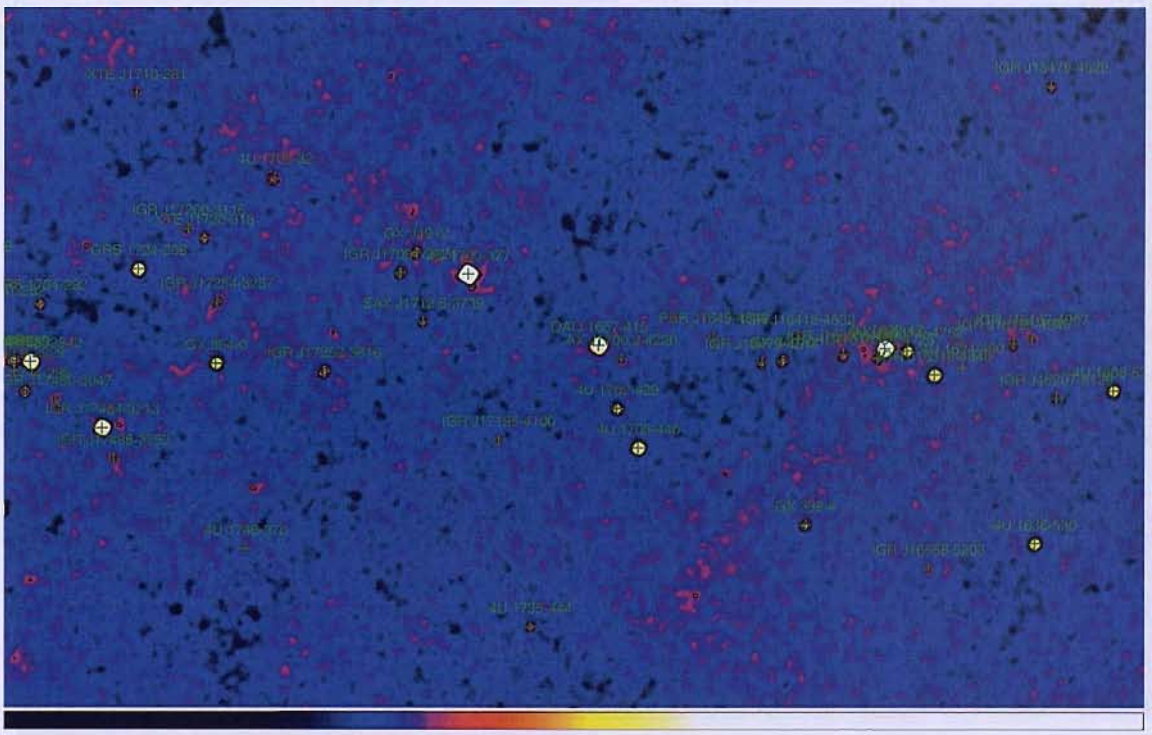

Figure B.7: Significance map of the 1st IBIS/ISGRI Survey Catalogue from 0°< l^{II} <-30° and -9.0°< b^{II} <+9.0°

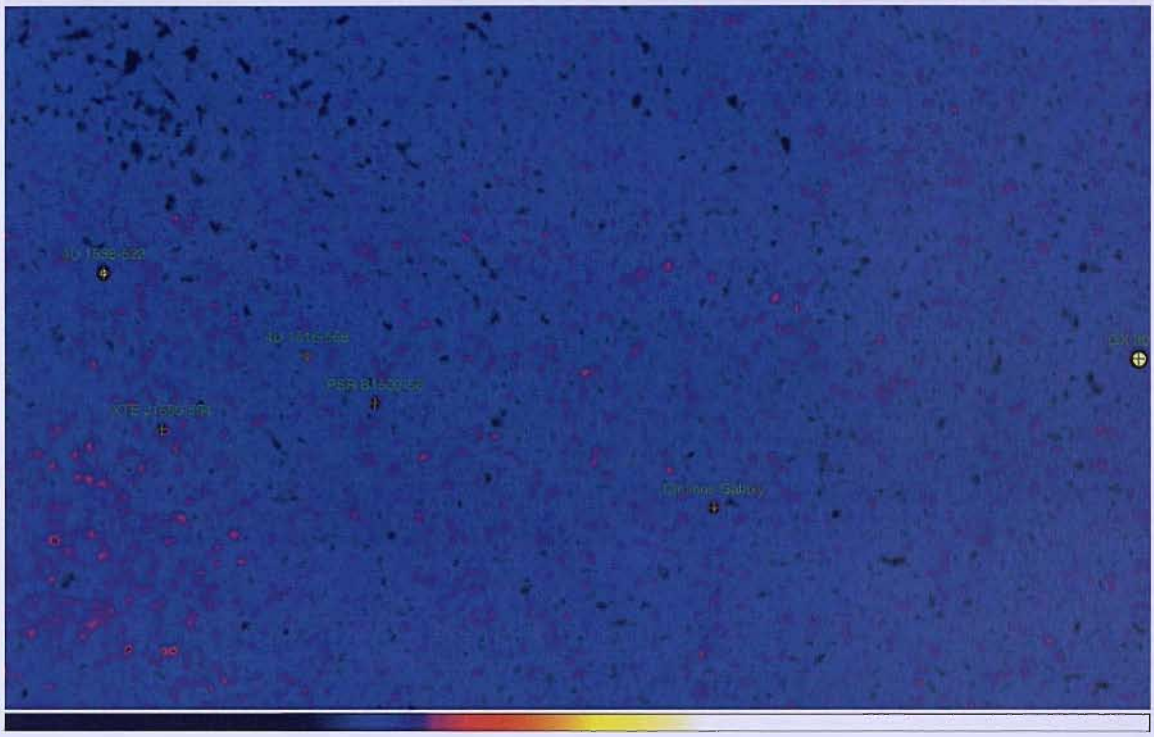

Figure B.8: Significance map of the 1st IBIS/ISGRI Survey Catalogue from -30°< l^{II} <-60° and -9.0°< b^{II} <+9.0°

Figure B.9: Significance map of the 1st IBIS/ISGRI Survey Catalogue from -60°< l^{II} <-90° and -9.0°< b^{II} <+9.0°

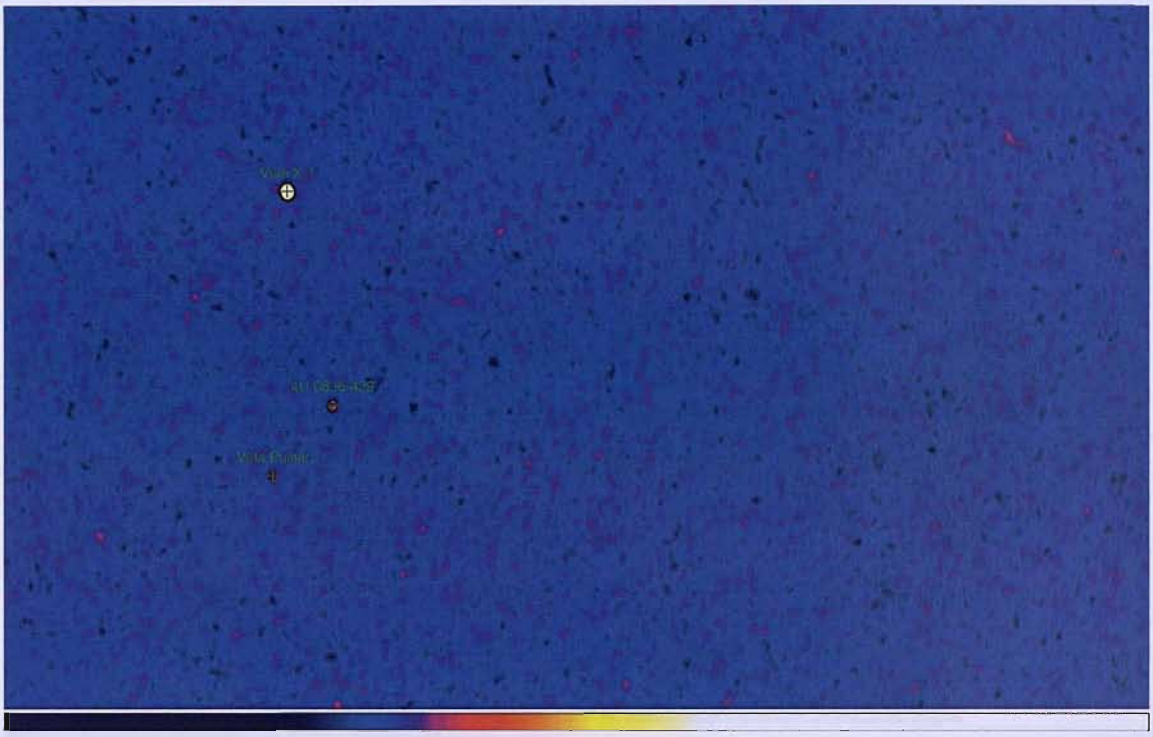

Figure B.10: Significance map of the 1st IBIS/ISGRI Survey Catalogue from -90°< l^{II} <-120° and -9.0°< b^{II} <+9.0°

Figure B.11: Significance map of the 1st IBIS/ISGRI Survey Catalogue from -120°< l^{II} <-150° and -9.0°< b^{II} <+9.0°

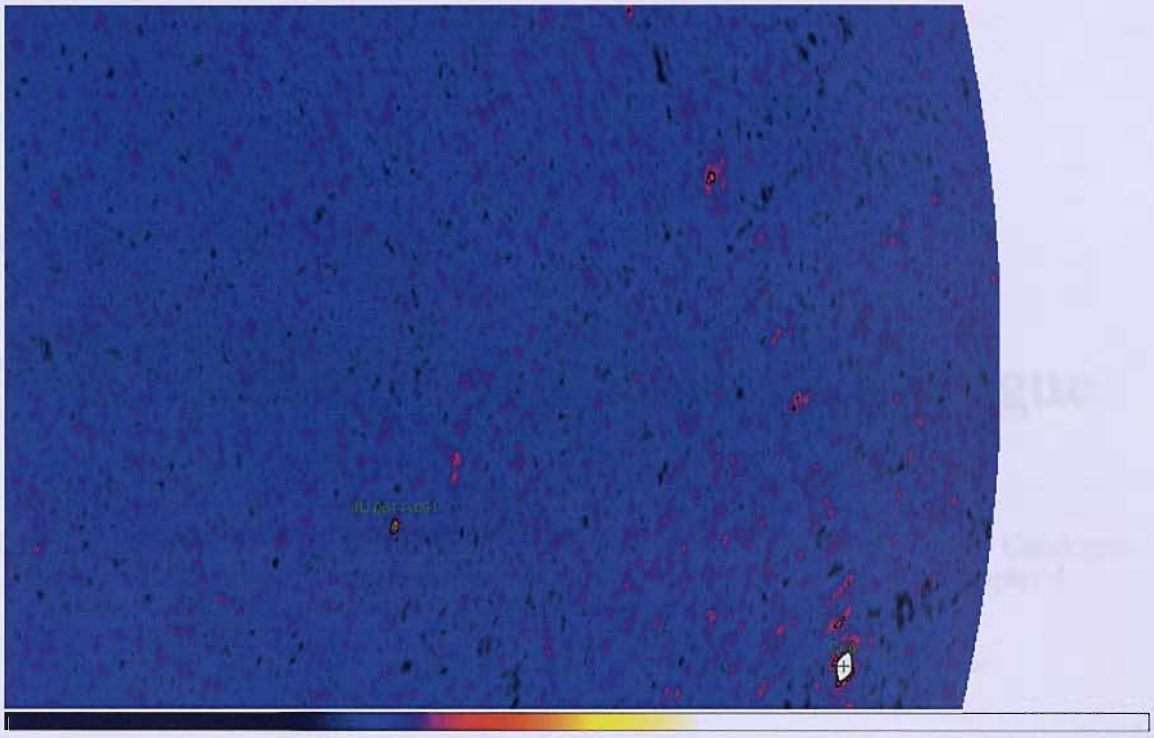

Figure B.12: Significance map of the 1st IBIS/ISGRI Survey Catalogue from -150°< l^{II} <-180° and -9.0°< b^{II} <+9.0°

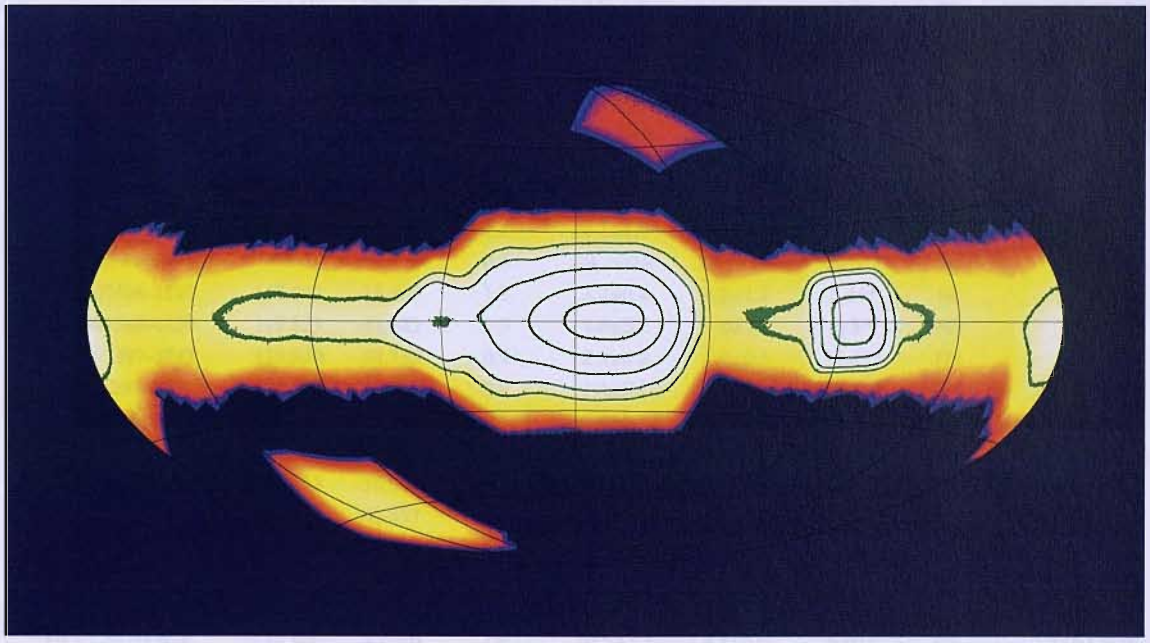

Figure B.13: Exposure map in galactic coordinates for the 1st IBIS/ISGRI Survey Catalogue. The contours represent expsoures of: 50 ksec; 100 ksec; 250 ksec; 500 ksec; 750 ksec.

Appendix C

The 2nd IBIS/ISGRI Survey Catalogue

Listed in Table C.1 are the 209 sources detected in the 2nd IBIS/ISGRI Survey Catalogue. The methodology used in the generation of this list of sources is given in Chapter 4.

Table C.1: The 2nd IBIS/ISGRI catalogue : 20–100 keV. For the footnotes to individual sources (notes 7–35) please refer to Table C.2

Name	RA (deg)	Dec. (deg)	Err (arc min)	F_{20-40} (mCrab)	F_{40-100} (mCrab	Sig	Exp (ks)	Type
V709 Cas	7.252	59.317	1.3	4.1±0.5	<2.9	6.9*	79	CV
RX J0053.8-7226	13.531	-72.426	1.2	3.3±0.4	<2.3	7.6*	106	HMXB, XP, T, Be
gam Cas	14.126	60.702	1.1	5.2±0.5	<2.9	8.8*	77	HMXB, Be
SMC X-1	19.324	-73.444	0.5	39.6±0.4	9.2±0.8	86.7*	106	HMXB, XP
1A 0114+650	19.511	65.288	0.7	10.3±0.5	5.3±1.0	17.5*	78	HMXB, XP
QSO B0241+62	41.184	62.510	1.4	3.7±0.7	5.8±1.2	6.4**	51	AGN,Sy1.2
X Per[7]	58.842	31.036	0.9	50.1±4.8	51.0±7.5	11.2**	2	HMXB, XP, Be
LMC X-4[8]	83.221	-66.365	0.6	50.3±1.5	12.0±2.5	33.5*	23	HMXB, XP
Crab	83.628	22.020	0.5	1000.0	1000.0	1691.0**	97	PWN, PSR
MCG+08-11-011	88.745	46.454	1.4	6.1±1.0	<5.5	6.2*	23	AGN, Sy1.5
4U 0614+091	94.270	9.145	0.6	24.7±0.8	22.8±1.4	29.5**	46	LMXB, B, A
IGR J07506-1547	117.647	-15.788	1.7	2.2±0.6	4.2±1.1	5.3**	64	?
IGR J07565-4139	119.123	-41.642	1.3	1.0±0.2	<0.8	6.8*	949	?
IGR J07597-3842	119.930	-38.730	0.9	2.3±0.2	1.9±0.3	11.4**	774	AGN?
ESO 209-12	120.483	-49.738	0.9	1.4±0.2	1.8±0.3	11.3**	939	AGN, Sy1.5
Vela Pulsar	128.816	-45.184	0.5	6.9±0.1	8.2±0.2	64.8**	1450	PWN, PSR
4U 0836-429	129.338	-42.893	0.5	36.6±0.1	31.1±0.2	240.9**	1400	LMXB, T, B
FRL 1146	129.633	-36.008	1.2	1.3±0.2	0.9±0.3	7.9*	881	AGN, Sy1
Vela X-1	135.512	-40.557	0.5	216.9±0.1	48.1±0.2	1440.1*	1220	HMXB, XP
IGR J09026-4812	135.638	-48.196	1.1	0.9±0.1	0.9±0.2	8.5*	1350	?
4U0919-54	140.050	-55.187	0.7	3.6±0.2	2.6±0.4	16.1**	602	LMXB 6
EXMS B0918-549E[9,10]	140.022	-55.143	0.9	-	-	12.0*	602	?,T
MCG-05-23-016	146.869	-30.930	1.0	10.2±1.4	8.4±2.0	9.9**	27	AGN, Sy1i
GRO J1008-57[11]	152.396	-58.294	0.9	<1.3	<2.2	11.6	130	HMXB, XP, Be, T
IGR J10404-4625	160.095	-46.416	1.5	2.9±0.7	5.9±1.1	5.7**	102	AGN?
IGR J11114-6723	167.854	-67.392	1.7	1.7±0.4	2.3±0.7	5.1**	199	?
Cen X-3	170.300	-60.638	0.5	27.4±0.4	3.6±0.6	71.9*	209	HMXB, XP
1E 1145.1-6141[12,13]	176.866	-61.957	0.5	30.1±0.3	17.5±0.5	83.4**	269	HMXB, XP

Continued on Next Page...

Table C.1 – Continued

Name	RA (deg)	Dec. (deg)	Err (arc min)	F_{20-40} (mCrab)	F_{40-100} (mCrab	Sig	Exp (ks)	Type
2E 1145.5-6155[14]	177.016	-62.199	0.7	7.9±0.3	4.6±0.5	17.5*	274	HMXB, XP, Be, T
NGC 4151	182.640	39.401	0.5	32.7±0.6	40.0±1.0	42.4**	56	AGN, Sy1.5
4C 04.42	185.606	4.239	1.4	1.4±0.4	3.9±0.6	6.5**	213	AGN, QSO
NGC 4388	186.446	12.637	0.6	15.4±0.9	16.7±1.4	21.0**	62	AGN, Sy1h
GX 301-2	186.653	-62.776	0.5	112.8±0.3	14.4±0.4	401.1*	406	HMXB, XP, T
3C 273	187.293	2.027	0.6	7.5±0.3	8.5±0.5	28.2**	279	AGN, QSO
IGR J12349-6433	188.709	-64.570	0.7	4.5±0.3	2.8±0.4	16.8*	437	Symb
NGC 4507	188.912	-39.903	0.7	10.7±0.7	12.2±1.1	17.5**	63	AGN, Sy1h
LEDA 170194	189.796	-16.182	1.2	2.6±0.5	5.6±0.9	7.6**	111	AGN?
NGC 4593	189.927	-5.353	0.7	4.1±0.3	4.0±0.5	16.2**	349	AGN, Sy1
4U 1246-588	192.351	-59.091	1.1	2.0±0.3	2.0±0.4	8.3**	436	HMXB, T
3C 279	194.038	-5.781	1.2	1.9±0.3	2.2±0.5	7.5**	326	Blazar
1H 1254-690	194.361	-69.305	1.2	2.5±0.3	<1.4	7.7*	369	LMXB, B, D
Coma cluster	194.880	27.961	1.3	1.9±0.3	<1.5	7*	251	Cluster
IGR J13020-6359	195.541	-63.925	1.1	2.1±0.2	1.3±0.4	8.4*	501	?
NGC 4945	196.362	-49.476	0.5	11.4±0.4	18.5±0.7	38.2**	226	AGN, Sy2
Cen A	201.364	-43.021	0.5	49.7±0.4	63.8±0.8	129.2**	112	AGN, Sy2
4U 1323-62	201.650	-62.126	0.7	3.8±0.2	2.4±0.4	16.9*	535	LMXB, B, D
4U 1344-60	206.872	-60.604	0.7	3.9±0.2	4.7±0.4	19.9**	526	AGN?
IC 4329A	207.348	-30.323	1.1	10.0±1.1	8.1±1.8	8.6**	29	AGN, Sy1.2
Circinus Galaxy	213.274	-65.343	0.5	14.0±0.2	11.5±0.4	62.3*	487	AGN, Sy1h
IGR J14492-5535	222.305	-55.579	1.5	1.5±0.2	<1.2	5.7*	520	?
PSR B1509-58	228.466	-59.147	0.5	8.6±0.2	11.0±0.4	44.4**	509	PSR
Cir X-1[15]	230.178	-57.174	0.5	15.6±0.2	<1.2	59.6*	512	LMXB, T, B, A
IGR J15359-5750	233.965	-57.832	1.3	1.2±0.2	2.0±0.4	7.0**	505	?
4U 1538-522	235.600	-52.378	0.5	22.6±0.2	3.0±0.4	91.9*	553	HMXB, XP
4U 1543-624	236.947	-62.577	0.9	2.9±0.3	<1.4	10.8*	386	LMXB
IGR J15479-4529	237.033	-45.484	0.6	5.4±0.2	2.4±0.4	20.9*	544	CV
XTE J1550-564	237.746	-56.482	0.5	115.1±0.2	176.5±0.4	628.1**	525	LMXB, T, BH
4U 1608-522	243.175	-52.434	0.5	14.8±0.2	11.9±0.3	68.4**	648	LMXB, T, B, A
IGR J16167-4957	244.139	-49.985	1.0	2.1±0.2	<1.0	9.3*	682	?
IGR J16194-2810	244.858	-28.160	1.5	2.2±0.3	<1.5	6.0*	349	?
AX J161929-4945[16]	244.865	-49.727	0.9	2.2±0.2	1.9±0.3	10.5**	690	HMXB, NS?
Sco X-1	244.988	-15.648	0.5	716.9±0.6	16.3±0.9	1060.0*	110	LMXB, Z
IGR J16207-5129	245.195	-51.504	0.8	3.3±0.2	2.4±0.3	14.9**	676	?
4U 1624-490	247.012	-49.204	0.7	4.2±0.2	<1.0	18.7*	715	LMXB, D
IGR J16318-4848	247.942	-48.824	0.5	29.3±0.2	14.4±0.3	129.1*	724	HMXB, T
AX J1631.9-4752	248.006	-47.870	0.5	17.1±0.2	6.6±0.3	78.3*	737	HMXB, T, XP
4U 1626-67	248.098	-67.456	0.6	16.1±0.5	<2.3	31.0*	181	LMXB, XP
4U 1630-47	248.517	-47.398	0.5	63.5±0.2	44.9±0.3	290.5**	742	LMXB, T, U, D, BHC
IGR J16358-4726	248.970	-47.421	0.7	4.3±0.2	2.4±0.3	19.7*	747	LMXB?, T
IGR J16377-6423[17]	249.420	-64.382	1.6	2.2±0.4	<1.8	5.6*	235	Cluster?
AX J163904-4642[18]	249.763	-46.693	0.6	6.9±0.2	<1.0	32.9*	760	HMXB?, T, XP
4U 1636-536	250.222	-53.755	0.5	24.2±0.2	13.4±0.4	106.5*	641	LMXB, B, A
IGR J16418-4532	250.440	-45.532	0.6	5.2±0.2	1.3±0.3	23.0*	784	?
GX 340+0	251.447	-45.612	0.5	34.9±0.2	2.1±0.3	158.7*	794	LMXB, Z
IGR J16479-4514	252.004	-45.207	0.7	3.9±0.2	2.7±0.3	18.2*	805	HMXB?
IGR J16482-3036	252.040	-30.593	1.1	1.6±0.2	1.6±0.3	8.4**	857	AGN?
IGR J16493-4348[19]	252.381	-43.835	0.8	2.7±0.2	2.2±0.3	13.3**	847	XB?
IGR J16500-3307	252.505	-33.116	1.2	1.7±0.2	<0.9	7.8*	966	?

Continued on Next Page...

Table C.1 – Continued

Name	RA (deg)	Dec. (deg)	Err (arc min)	F_{20-40} (mCrab)	F_{40-100} (mCrab	Sig	Exp (ks)	Type
ESO 138-1[20]	252.938	-59.213	1.3	1.9±0.3	1.6±0.4	6.7**	402	AGN, Sy2
IGR J16558-5203	254.012	-52.052	1.0	1.4±0.2	2.5±0.4	9.1**	660	?
AX J1700.2-4220	255.073	-42.396	1.2	1.4±0.2	1.3±0.3	7.6**	946	?
OAO 1657-415	255.206	-41.661	0.5	85.1±0.2	45.8±0.3	402.6*	980	HMXB, XP
GX 339-4	255.708	-48.791	0.5	22.7±0.2	28.2±0.3	126.1**	710	LMXB, T, U, BH
4U 1700-377	255.988	-37.849	0.5	207.3±0.2	124.6±0.3	1110.2**	1180	HMXB
GX 349+2	256.448	-36.419	0.5	46.0±0.2	1.6±0.3	241.5*	1220	LMXB, Z
4U 1702-429	256.566	-43.055	0.5	14.9±0.2	9.3±0.3	71.1*	921	LMXB, B, A
IGR J17088-4008	257.208	-40.142	0.9	1.1±0.2	2.2±0.3	10.3**	1110	AXP
4U 1705-440	257.226	-44.107	0.5	27.3±0.2	16.4±0.3	124.4*	863	LMXB, B, A
4U 1705-32	257.237	-32.317	0.7	2.9±0.2	3.0±0.3	19.3**	1290	LMXB, B
IGR J17091-3624	257.278	-36.415	0.5	10.0±0.2	13.2±0.3	71.5**	1260	BHC?
XTE J1709-267[21]	257.389	-26.655	0.7	1.0±0.2	<0.8	18.4	1140	LMXB, B, T
XTE J1710-281	257.550	-28.140	0.6	3.0±0.2	4.1±0.3	22.0**	1210	LMXB, T, B
Oph Cluster[22]	258.109	-23.363	0.6	4.9±0.2	1.7±0.3	25.6*	1020	Cluster
4U 1708-40	258.139	-40.850	1.3	1.2±0.2	<0.8	6.9*	1060	LMXB, B
SAX J1712.6-3739	258.146	-37.655	0.6	5.2±0.2	4.5±0.3	31.0**	1250	LMXB, T, B
V2400 Oph	258.170	-24.267	0.7	3.5±0.2	2.1±0.3	19.4*	1070	CV
XTE J1716-389	258.941	-38.835	1.1	1.6±0.2	1.0±0.3	8.8*	1200	?
NGC 6300	259.213	-62.823	1.0	4.3±0.4	3.7±0.7	10.1**	200	AGN, Sy2
IGR J17195-4100	259.931	-41.032	0.8	2.3±0.2	2.2±0.3	13.9**	1060	?
XTE J1720-318	259.976	-31.749	0.5	6.1±0.2	8.1±0.2	49.4**	1410	LMXB, T, BHC
IGR J17200-3116	260.022	-31.290	0.7	3.0±0.2	2.3±0.2	19.4**	1430	?,T
IGR J17204-3554[23]	260.104	-35.900	0.8	1.5±0.2	2.1±0.2	13.1**	1360	mol cloud?
EXO 1722-363[24]	261.288	-36.277	0.5	8.9±0.2	3.2±0.2	51.8*	1360	HMXB, XP
IGR J17254-3257	261.350	-32.968	0.7	2.7±0.2	3.0±0.2	19.9**	1450	?
GRS 1724-30	261.884	-30.812	0.5	18.2±0.2	16.0±0.2	125.6**	1470	LMXB, G, B, A
IGR J17285-2922	262.172	-29.382	1.2	0.7±0.2	1.4±0.2	7.3**	1470	BHC?, T
IGR J17303-0601	262.593	-6.016	0.9	3.7±0.3	2.1±0.5	11.6*	282	LMXB?,CV?
GX 9+9	262.927	-16.974	0.5	12.9±0.2	1.6±0.3	53.8*	722	LMXB, A
GX 354-0	262.988	-33.830	0.5	44.1±0.2	16.8±0.2	264.1*	1460	LMXB, B, A
GX 1+4	263.004	-24.752	0.5	42.5±0.2	31.0±0.2	259.2**	1330	LMXB, XP
4U 1730-335	263.354	-33.390	0.8	2.4±0.2	<0.7	15.0*	1470	LMXB, G, RB, T
GRS 1734-294	264.381	-29.136	0.6	5.4±0.1	3.9±0.2	33.5**	1510	AGN, Sy1
SLX 1735-269	264.567	-26.995	0.5	9.3±0.2	7.5±0.2	61.6**	1460	LMXB, B
4U 1735-444	264.744	-44.451	0.5	29.6±0.2	1.3±0.3	132.3*	767	LMXB, B, A
XTE J17391-3021	264.818	-30.347	1.1	1.3±0.1	0.9±0.2	8.5**	1510	HMXB, NS, Be?, T
XTE J1739-285[25]	264.961	-28.496	1.1	<0.4	<0.7	8.4	1500	LMXB?
SLX 1737-282	265.191	-28.280	0.6	3.2±0.1	3.3±0.2	23.8**	1490	LMXB, B
2E 1739.1-1210	265.463	-12.196	1.1	2.2±0.2	1.8±0.4	8.8**	526	AGN, Sy1
XTE J1743-363	265.751	-36.381	0.8	2.5±0.2	1.9±0.2	14.6**	1340	?,T
1E 1740.7-2942[26]	265.988	-29.745	0.5	26.7±0.1	34.0±0.2	222.0**	1510	LMXB, BHC
IGR J17445-2747	266.132	-27.783	1.5	0.9±0.1	0.8±0.2	6.0*	1480	?
KS 1741-293[27]	266.220	-29.340	0.5	8.8±0.1	7.8±0.2	62.3**	1510	LMXB, T, B
IGR J17456-2901[28,29]	266.410	-29.020	0.6	5.0±0.1	2.7±0.2	30.9*	1500	?
1E 1742.8-2853[29]	266.498	-28.917	0.6	5.4±0.1	3.7±0.2	31.8*	1500	LMXB
1A 1742-294	266.520	-29.510	0.5	14.1±0.1	7.9±0.2	85.7*	1510	LMXB, B
IGR J17464-3213	266.567	-32.232	0.5	66.5±0.2	40.5±0.2	405.1*	1490	LMXB, T, BHC
1E 1742.9-2849[29]	266.570	-28.814	0.6	5.4±0.1	2.8±0.2	31.6*	1500	LMXB
1E 1743.1-2843[29]	266.590	-28.670	0.8	3.8±0.1	1.6±0.2	13.5*	1500	LMXB

Continued on Next Page...

Table C.1 – Continued

Name	RA (deg)	Dec. (deg)	Err (arc min)	F_{20-40} (mCrab)	F_{40-100} (mCrab	Sig	Exp (ks)	Type
SAX J1747.0-2853[30]	266.805	-28.837	1.1	1.4±0.1	<0.7	8.8*	1500	LMXB, B, T
IGR J17475-2822	266.820	-28.445	0.7	2.1±0.1	1.9±0.2	15.1**	1490	mol cloud?
SLX 1744-299	266.860	-30.020	0.5	8.8±0.1	5.7±0.2	56.5*	1500	LMXB, B
GX 3+1	266.989	-26.562	0.5	13.5±0.2	0.8±0.2	84.7*	1440	LMXB, B, A
1A 1744-361	267.057	-36.133	1.2	1.0±0.2	1.3±0.2	7.7**	1340	LMXB, T
IGR J17488-3253	267.206	-32.914	0.7	2.3±0.2	3.3±0.2	19.4**	1460	?
4U 1745-203	267.217	-20.386	0.7	2.1±0.2	3.2±0.3	16.1**	1070	LMXB, T, G
4U 1746-370	267.557	-37.047	0.6	4.7±0.2	1.9±0.3	25.5*	1270	LMXB, G, B, A
GRS 1747-312	267.637	-31.296	1.1	1.1±0.2	1.1±0.2	8.4**	1480	LMXB, G, T
IGR J17513-2011	267.822	-20.188	0.8	2.0±0.2	2.5±0.3	13.4**	1060	?
IGR J17544-2619	268.605	-26.342	1.3	1.1±0.2	<0.7	6.7*	1410	HMXB?, T
IGR J17597-2201	269.939	-22.033	0.5	8.4±0.2	7.8±0.3	52.2**	1190	LMXB, B, D
GX 5-1	270.287	-25.079	0.5	55.3±0.2	3.2±0.2	318.9*	1340	LMXB, Z
GRS 1758-258	270.303	-25.749	0.5	39.5±0.2	48.1±0.2	291.9**	1350	LMXB, U, BHC
GX 9+1	270.388	-20.524	0.5	17.6±0.2	0.9±0.3	93.0*	1080	LMXB, A
IGR J18027-1455	270.690	-14.922	0.7	3.0±0.2	3.3±0.3	15.5**	766	AGN, Sy1
SAX J1802.7-201[31]	270.692	-20.294	0.6	5.8±0.2	2.5±0.3	30.5*	1070	HMXB, T, XP
IGR J18048-1455	271.211	-14.914	1.0	1.7±0.2	2.0±0.3	9.3**	774	?
XTE J1807-294	271.748	-29.410	0.6	3.1±0.2	3.1±0.2	21.6**	1340	LMXB, T, XP
SGR 1806-20	272.156	-20.423	0.6	3.4±0.2	4.7±0.3	23.7**	1060	SGR
IGR J18135-1751[32]	273.363	-17.849	1.1	1.6±0.2	1.2±0.3	8.2**	916	?
GX 13+1	273.618	-17.146	0.5	17.5±0.2	5.0±0.3	84.5*	880	LMXB, B, A
M 1812-12	273.779	-12.102	0.5	25.7±0.2	25.5±0.3	137.7**	735	LMXB, B
GX 17+2	274.007	-14.040	0.5	58.4±0.2	3.2±0.3	263.9*	781	LMXB, B, Z
SAX J1818.6-1703	274.671	-17.055	1.4	1.2±0.2	1.2±0.3	6.5**	869	?,T
IGR J18193-2542	274.820	-25.703	1.5	0.8±0.2	1.1±0.3	5.7**	1130	?
AX J1820.5-1434	275.133	-14.572	0.6	5.1±0.2	3.3±0.3	23.4*	794	HMXB, XP, Be
IGR J18214-1318	275.340	-13.308	0.9	2.1±0.2	2.0±0.3	10.8**	773	?
4U 1820-303	275.928	-30.370	0.5	35.3±0.2	2.3±0.3	186.6*	1070	LMXB, G, B, A
4U 1822-000	276.335	-0.032	1.0	2.4±0.2	<1.1	9.9*	641	LMXB
IGR J18256-1035	276.406	-10.587	1.5	1.2±0.2	<1.0	5.9*	762	?
3A 1822-371	276.462	-37.102	0.5	34.1±0.2	4.3±0.3	162.5*	895	LMXB, D
IGR J18259-0706	276.485	-7.106	1.4	1.2±0.2	1.0±0.3	6.2**	743	?
GS 1826-24	277.367	-23.801	0.5	73.3±0.2	58.6±0.3	359.8**	942	LMXB, B
IGR J18325-0756	278.118	-7.940	0.7	3.9±0.2	2.2±0.3	18.2*	794	?
SNR 021.5-00.9	278.395	-10.558	0.7	2.8±0.2	3.3±0.3	15.9**	785	SNR, PWN
PKS 1830-211	278.405	-21.052	0.7	3.0±0.2	3.7±0.3	17.7**	843	AGN, QSO
RX J1832-330	278.921	-32.989	0.5	11.6±0.2	9.9±0.3	58.6**	823	LMXB, G, B, T
AX J1838.0-0655[33]	279.507	-6.904	0.8	2.1±0.2	3.1±0.3	14.1**	835	?
ESO 103-35	279.578	-65.431	1.4	5.9±0.9	4.5±1.5	6.2**	42	AGN, Sy1.9
Ser X-1	279.992	5.031	0.5	10.1±0.2	<0.9	48.7*	861	LMXB, B
AX J1841.0-0535	280.237	-5.602	1.5	1.0±0.2	1.1±0.3	6.0**	861	HMXB, XP, Be?
Kes 73	280.338	-4.949	0.7	2.0±0.2	3.8±0.3	15.1**	875	SNR, AXP
IGR J18450-0435	281.243	-4.602	1.8	1.0±0.2	<0.9	5.0**	907	?
GS 1843+009	281.418	0.875	0.6	4.3±0.2	3.2±0.3	22.9**	970	HMXB, XP, Be, T
AX J1846.4-0258	281.622	-2.973	0.8	1.9±0.2	2.5±0.3	12.5**	940	SNR, PWN, AXP
IGR J18483-0311	282.064	-3.169	0.7	4.1±0.2	2.7±0.3	20.3*	945	?
3A 1845-024	282.082	-2.424	1.3	1.3±0.2	0.9±0.3	6.7*	956	HMXB, XP, Be?, T
IGR J18490-0000	282.267	-0.025	1.4	1.2±0.2	0.9±0.3	6.4**	998	?
4U 1850-087	283.266	-8.706	0.6	4.6±0.2	3.8±0.3	23.2**	804	LMXB, G, B

Continued on Next Page...

Table C.1 – Continued

Name	RA (deg)	Dec. (deg)	Err (arc min)	F_{20-40} (mCrab)	F_{40-100} (mCrab	Sig	Exp (ks)	Type
IGR J18539+0727	283.477	7.458	0.9	1.9±0.2	1.6±0.3	11.3**	1000	BHC?
V1223 Sgr[33]	283.755	-31.145	0.6	7.8±0.2	3.5±0.4	30.3*	512	CV
XTE J1855-026	283.877	-2.604	0.5	11.8±0.2	6.9±0.3	64.8*	969	HMXB, XP, T
2E 1853.7+1534	284.008	15.621	0.9	2.8±0.2	2.0±0.4	12.0**	578	AGN?
XTE J1858+034[34]	284.686	3.431	0.5	0.8±0.2	<0.8	49.8	1090	HXMB, XP, Be?, T
XTE J1901+014	285.397	1.439	0.6	3.4±0.2	3.0±0.3	21.6**	1070	T, BHC?
4U 1901+03	285.913	3.205	0.5	93.8±0.2	10.5±0.3	552.3*	1090	HMXB, T, XP
XTE J1908+094	287.220	9.390	0.6	3.6±0.2	4.2±0.3	23.7**	998	LMXB, T, BHC
4U 1907+097	287.414	9.836	0.5	16.5±0.2	2.0±0.3	91.4*	980	HMXB, XP, T
4U 1909+07	287.701	7.602	0.5	14.4±0.2	8.7±0.3	81.6*	1060	HMXB, XP
Aql X-1	287.811	0.577	0.5	9.4±0.2	5.1±0.3	53.8*	1010	LMXB, B, A, T
SS 433	287.957	4.974	0.5	14.5±0.2	7.3±0.3	89.0*	1090	HMXB
IGR J19140+0951[35]	288.525	9.872	0.5	9.5±0.2	5.7±0.3	54.7*	981	HMXB?, NS?
GRS 1915+105	288.798	10.940	0.5	288.1±0.2	108.8±0.3	1591.0*	926	LMXB, T, BH
4U 1916-053	289.697	-5.243	0.5	9.3±0.2	3.9±0.3	42.1*	682	LMXB, B, D
IGR J19284+0107	292.098	1.119	1.3	1.2±0.2	<0.9	6.8*	857	?
IGR J19308+0530	292.692	5.502	1.4	0.8±0.2	1.5±0.3	6.6***	949	?
RX J1940.1-1025	295.066	-10.408	1.1	3.0±0.3	2.1±0.6	8.1*	267	CV
NGC 6814	295.644	-10.332	1.0	3.1±0.3	3.9±0.6	9.9**	248	AGN, Sy1.5
KS 1947+300	297.396	30.210	0.5	38.4±0.6	23.9±1.0	55.6*	93	HMXB, T, XP
Cyg X-1	299.592	35.194	0.5	812.9±0.6	944.3±1.0	1417.3**	100	HMXB, BH, U
Cyg A	299.878	40.755	1.1	5.4±0.6	6.0±1.0	8.8**	91	AGN, Sy1.9
EXO 2030+375	308.046	37.630	0.5	38.9±0.5	20.4±0.8	74.6*	147	HMXB, XP, Be, T
Cyg X-3	308.108	40.953	0.5	201.1±0.4	82.2±0.7	418.4*	151	HMXB
SAX J2103.5+4545	315.891	45.743	0.5	33.4±0.4	18.5±0.7	78.4*	166	HMXB, XP, Be, T
IGR J21247+5058	321.151	50.980	0.7	5.7±0.4	8.1±0.7	16.3**	143	AGN, Sy1?
IGR J21335+5105	323.375	51.092	1.2	2.9±0.4	<2.1	7.8**	143	CV
1H 2140+433	325.745	43.587	1.1	4.4±0.4	<2.2	8.8*	127	Dwarf nova, CV
Cyg X-2	326.168	38.318	0.5	26.7±0.5	<2.7	43.9*	96	LMXB, B, Z
4U 2206+543	331.974	54.514	0.6	12.8±0.5	9.2±0.8	24.6*	114	HMXB, NS, Be
Cas A	350.822	58.792	1.1	3.9±0.5	3.3±0.9	8.0**	95	SNR

[1]Names in bold face indicate new detections since first catalogue

[2]Position errors are expressed as radius of 1σ error circle

[3]Fluxes are expressed in units of mCrab; appropriate conversion factors are: (20-40 keV) 10 mCrab = 7.57×10^{-11} erg cm^{-2} s^{-1} = 1.71×10^{-3} ph cm^{-2} s^{-1}; (40-100 keV) 10 mCrab = 9.42×10^{-11} erg cm^{-2} s^{-1} = 9.67×10^{-4} ph cm^{-1} s^{-1}

[4]Maximimum significance is quoted in either (*) 20–40 keV band, (**) 20–100 keV band, (***) 30–60 keV band, (no mark) significance in one revolution

[5]Exposure is the corrected on-source exposure in ksec

[6]Source type classifications: A=Atoll source (neutron star); AGN=Active galactic nuclei; AXP=Anomalous X-ray pulsar; B=Burster (neutron star); Be=B-type emission-line star; BH=Black hole (confirmed mass evaluation); BHC=Black hole candidate; Cluster=Cluster of galaxies; CV=Cataclysmic variable; D=Dipping source; G=Globular Cluster X-ray source; HMXB=High-mass X-ray binary; LMXB=Low-mass X-ray binary; Mol Cloud=Molecular cloud; NS=Neutron Star; PSR=Radio pulsar; PWN=Pulsar wind nebula; QSO = Quasar; SGR=Soft gamma-ray repeater; SNR=Supernova remnant; Sy=Seyfert galaxy; Symb=Symbiotic star; T=Transient source; U=Ultrasoft source; XB=Galactic X-ray binary; XP=X-ray pulsar; Z=Z-type source (neutron star)

Table C.2: Footnotes accompanying Table C.1

Number	Footnote
7	4U0352+30 in 1st IBIS/ISGRI catalog (Cat1)
8	Values derived from staring observations during revolutions 50,154 and 203.
9	Detected during revolution 139
10	Cannot recover fluxes due to proximity to 4U0919-54
11	Detected during revolution 203
12	A1145.1-6141 in Cat1
13	Position taken from 1E catalog, due to blending with 2E1145.5-6155
14	Position taken from 1E catalog, due to blending with 2E1145.1-6141
15	4U1516-569 in Cat1
16	IGR J16195-4945 in Cat1
17	Triangulum Australis
18	IGR J16393-4643 in Cat 1
19	PSR J1649-4349 in Cat1
20	Equally well associated with NGC 6221, also Sy2
21	Detected during revolution 171
22	EXMS B1709-232 in Cat1
23	Tentative association with NGC6334
24	IGRJ17254-3616 in Cat1
25	Detected during revolution 120
26	1E1740.7-2943 in Cat1
27	M1741-293 in Cat1
28	Within 1.1′ of Sgr A*
29	Fluxes unreliable due to blending in final mosaic, see Section 3.6
30	Detected during revolution 175
31	IGR J18027-2016 in Cat1
32	HESS source (SNR/PWN?)
33	4U1849-31 in Cat1
34	Detected during revolution 189
35	IGR J19140+098 in Cat1

Appendix D

Images of the 2^{nd} IBIS/ISGRI Survey Catalogue

From the mosaics of the 2^{nd} IBIS/ISGRI survey it is possible to construct a false colour image of the γ-ray sky. Figures D.1–D.6 show 30° × 18° sections of the Galactic Plane. The image is construced from the 15–20 keV (red), 20–30 keV (green) and 30–40 keV (blue) energy bands. The exposure map of the 2^{nd} IBIS/ISGRI Survey Catalogue is shown in Fig. D.7.

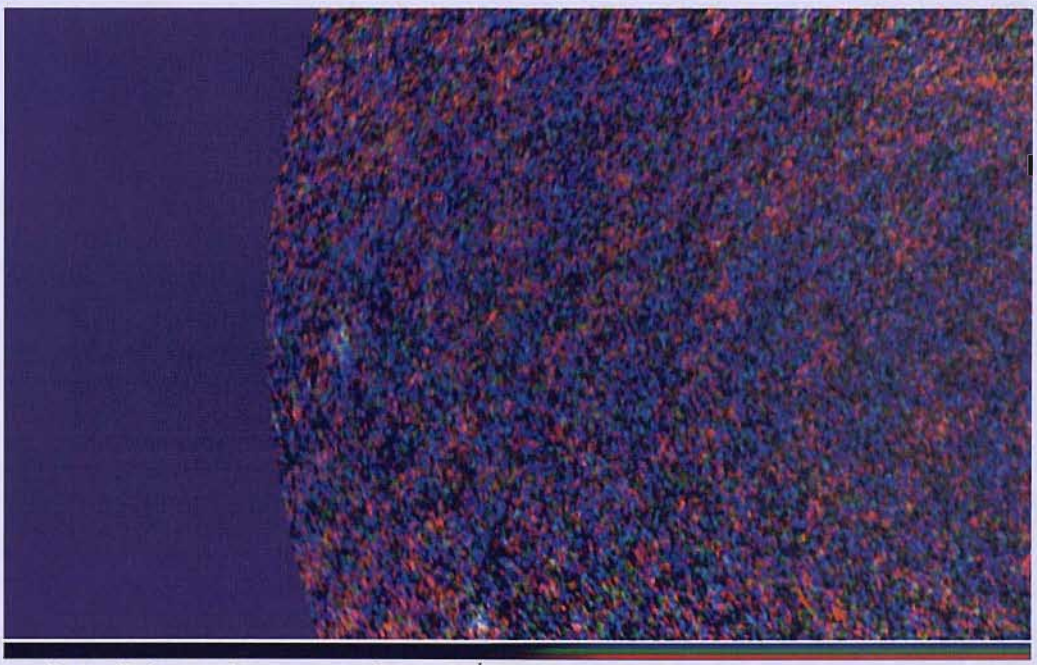

Figure D.1: False colour map of the 2^{nd} IBIS/ISGRI Survey Catalogue from 180°< l^{II} <150° and -9.0°< b^{II} <+9.0°

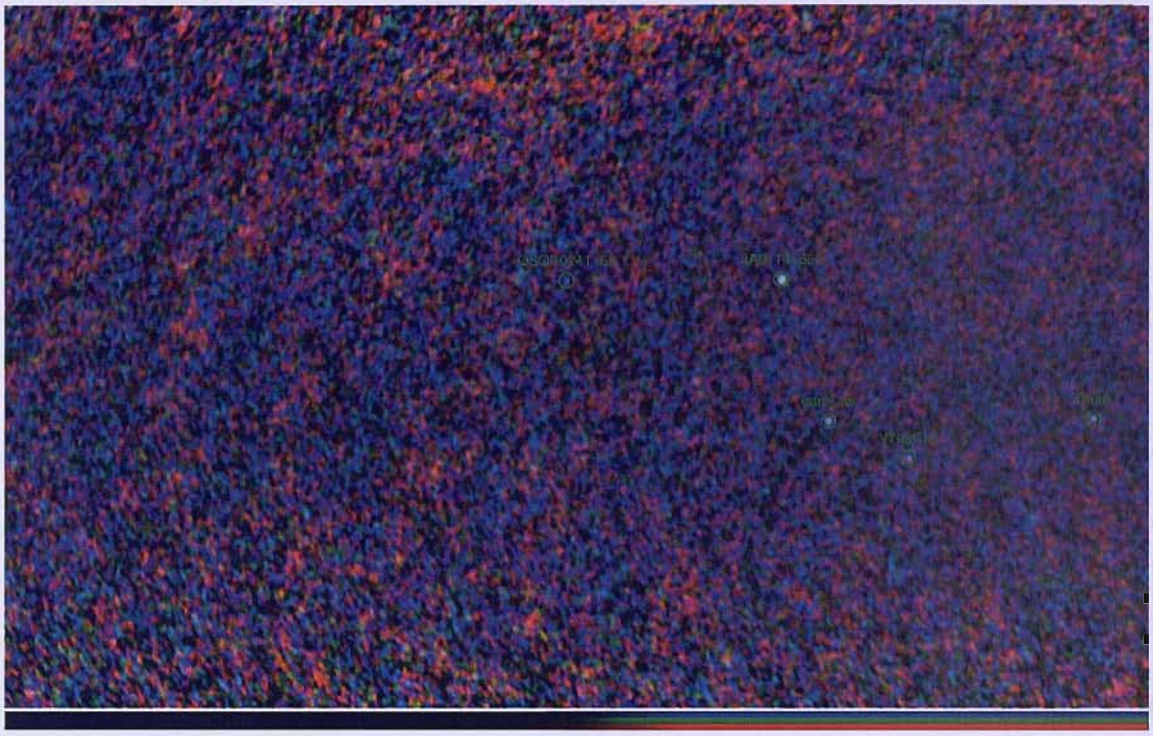

Figure D.2: False colour map of the 2nd IBIS/ISGRI Survey Catalogue from 150°< l^{II} <120° and -9.0°< b^{II} <+9.0°

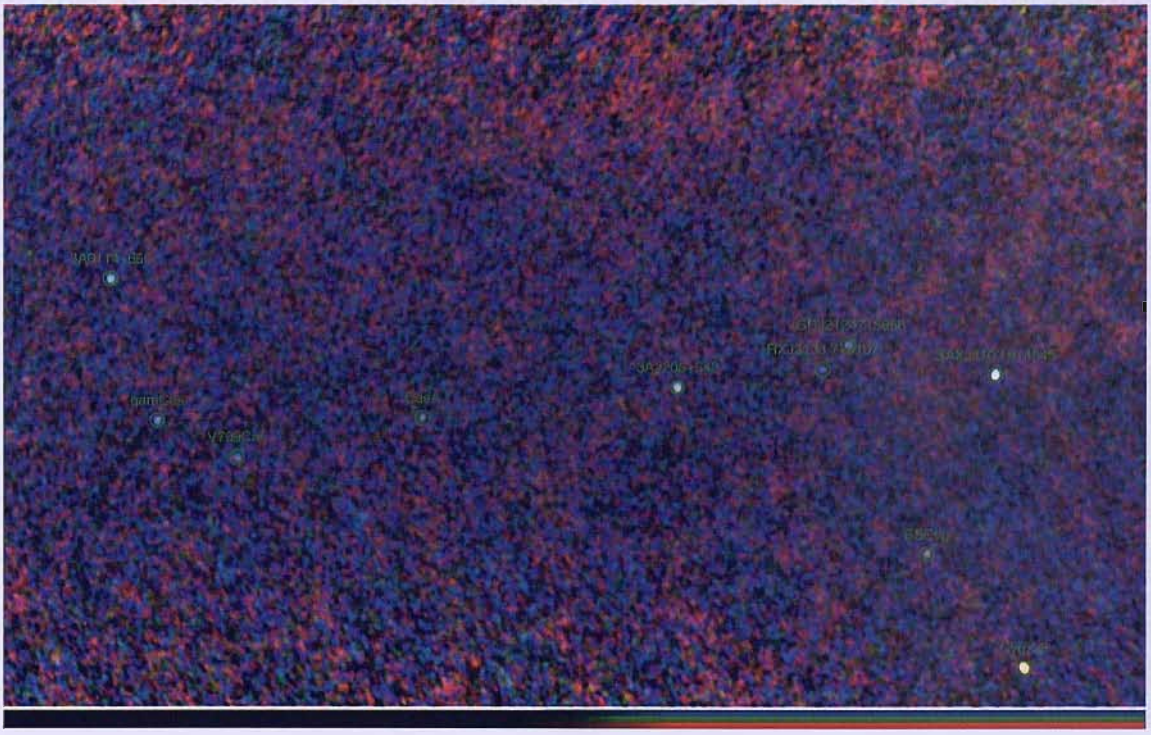

Figure D.3: False colour map of the 2nd IBIS/ISGRI Survey Catalogue from 120°< l^{II} <90° and -9.0°< b^{II} <+9.0°

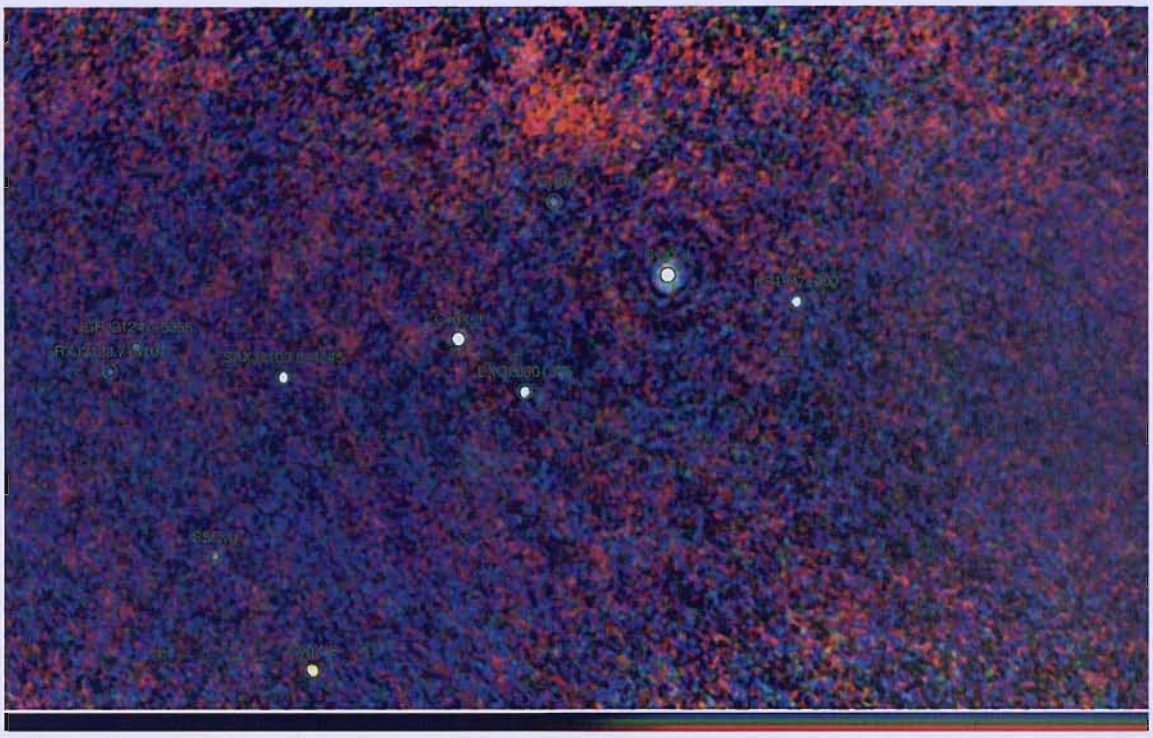

Figure D.4: False colour map of the 2nd IBIS/ISGRI Survey Catalogue from 90°< l^{II} <60° and -9.0°< b^{II} <+9.0°

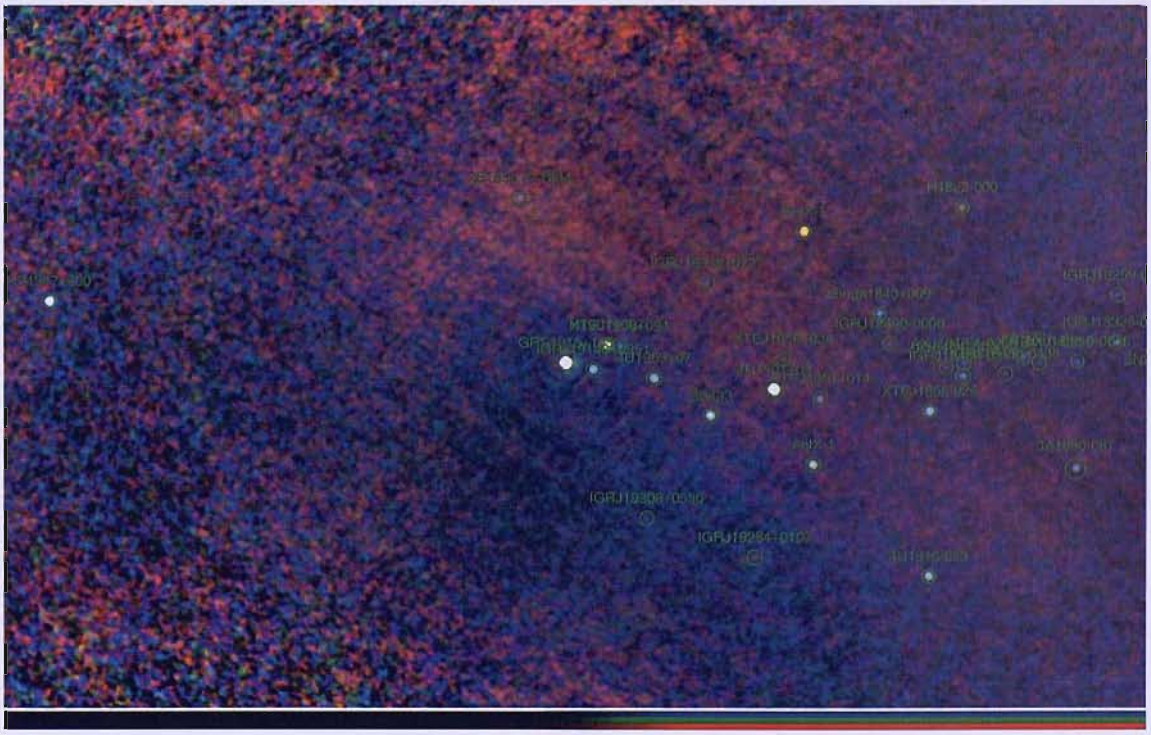

Figure D.5: False colour map of the 2nd IBIS/ISGRI Survey Catalogue from 60°< l^{II} <30° and -9.0°< b^{II} <+9.0°

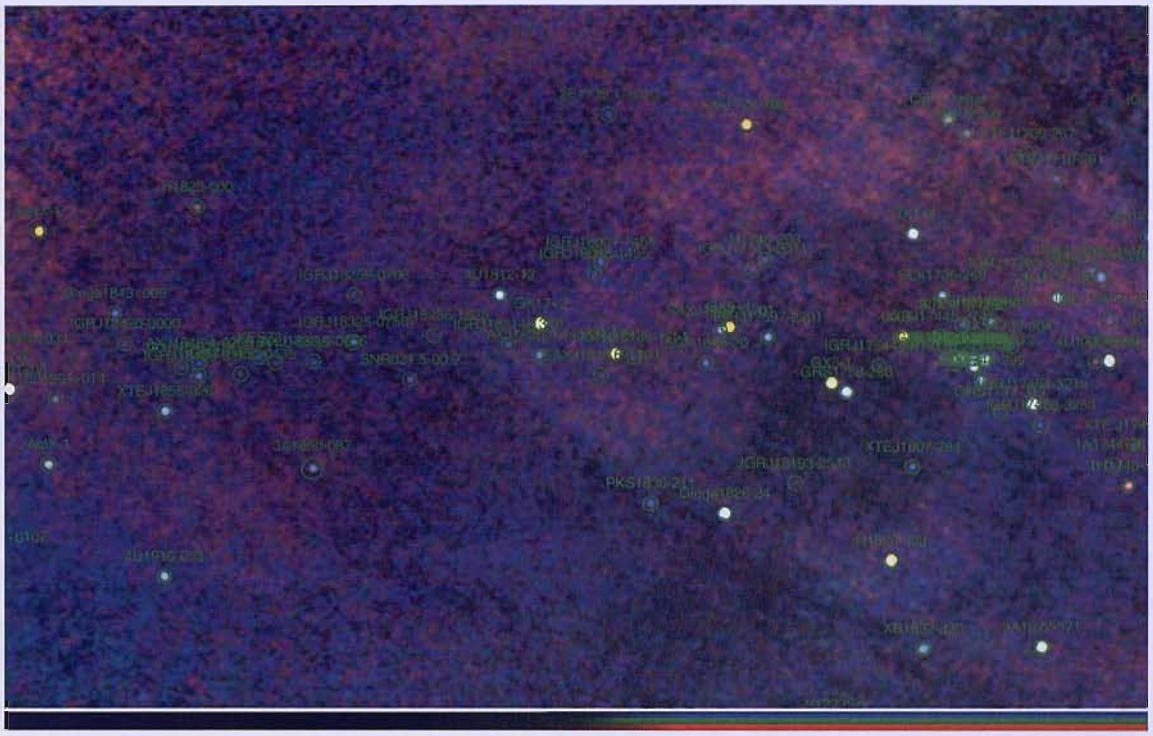

Figure D.6: False colour map of the 2nd IBIS/ISGRI Survey Catalogue from 30°< l^{II} <0° and -9.0°< b^{II} <+9.0°

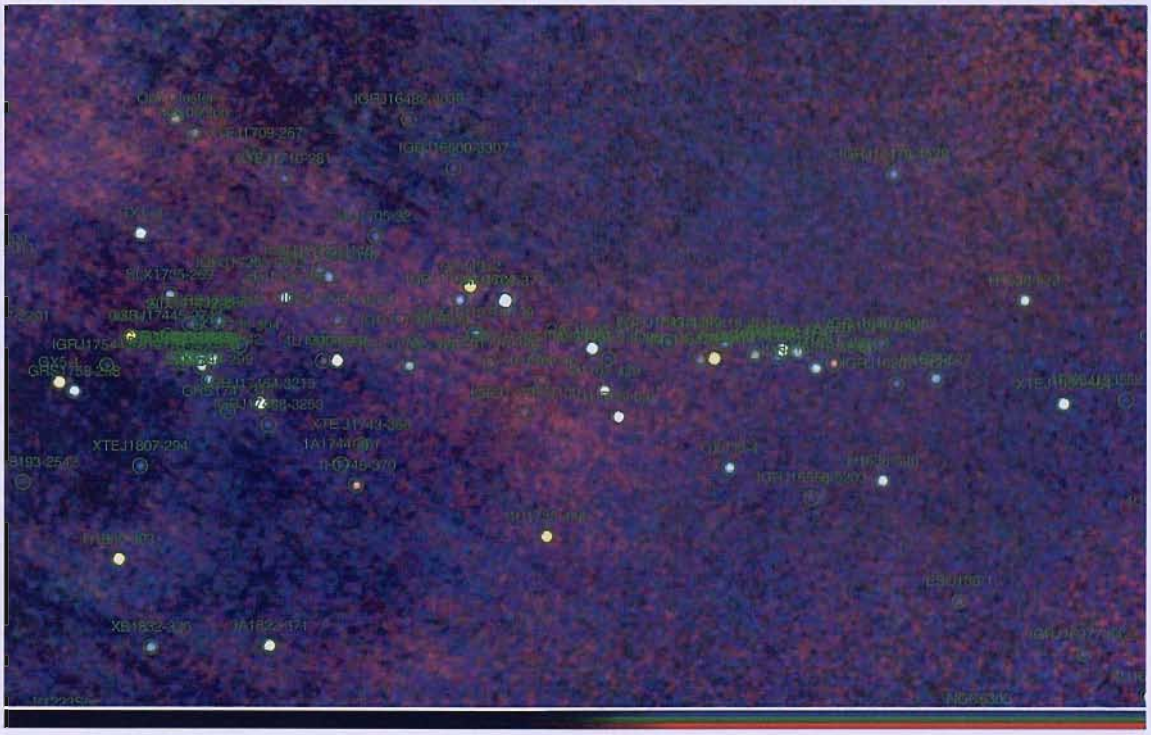

Figure D.7: False colour map of the 2nd IBIS/ISGRI Survey Catalogue from 0°< l^{II} <-30° and -9.0°< b^{II} <+9.0°

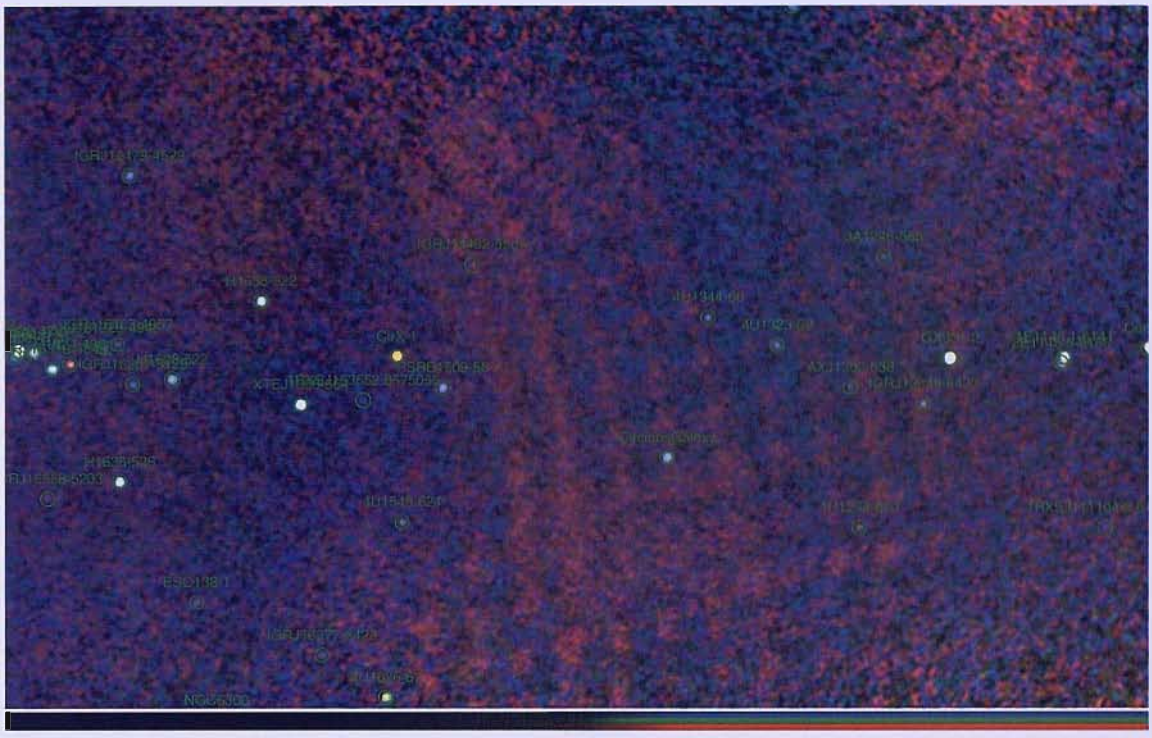

Figure D.8: False colour map of the 2nd IBIS/ISGRI Survey Catalogue from -30°< l^{II} <-60° and -9.0°< b^{II} <+9.0°

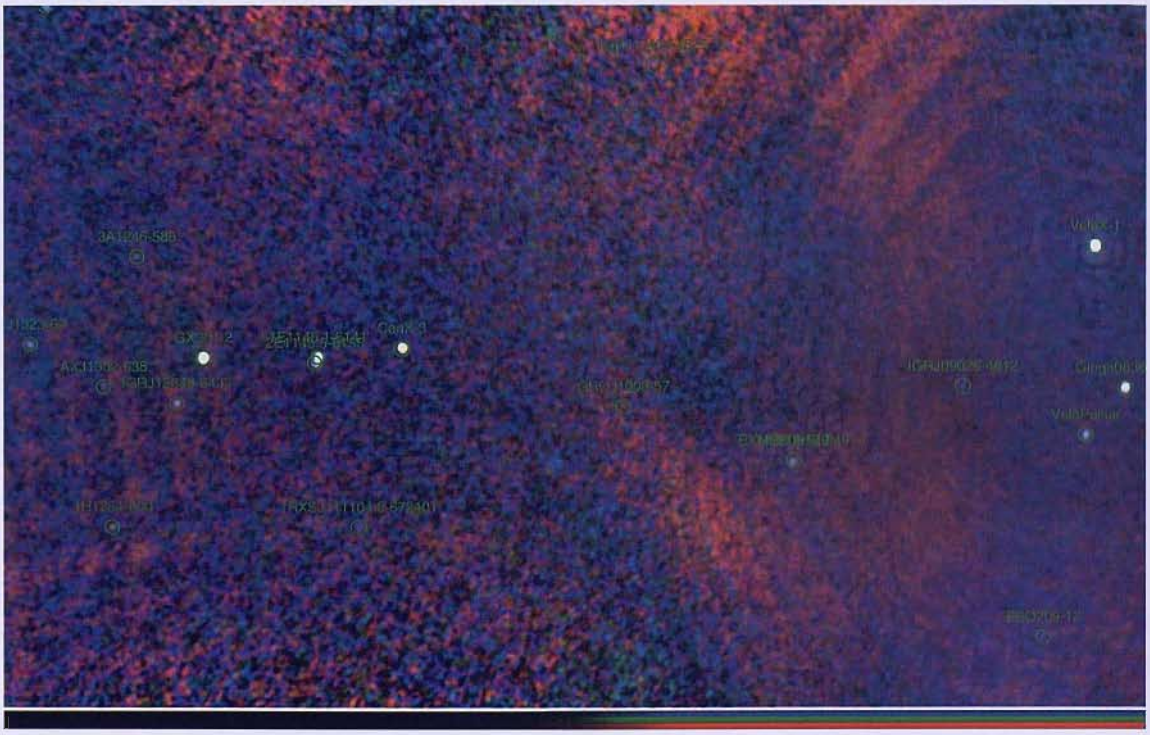

Figure D.9: False colour map of the 2nd IBIS/ISGRI Survey Catalogue from -60°< l^{II} <-90° and -9.0°< b^{II} <+9.0°

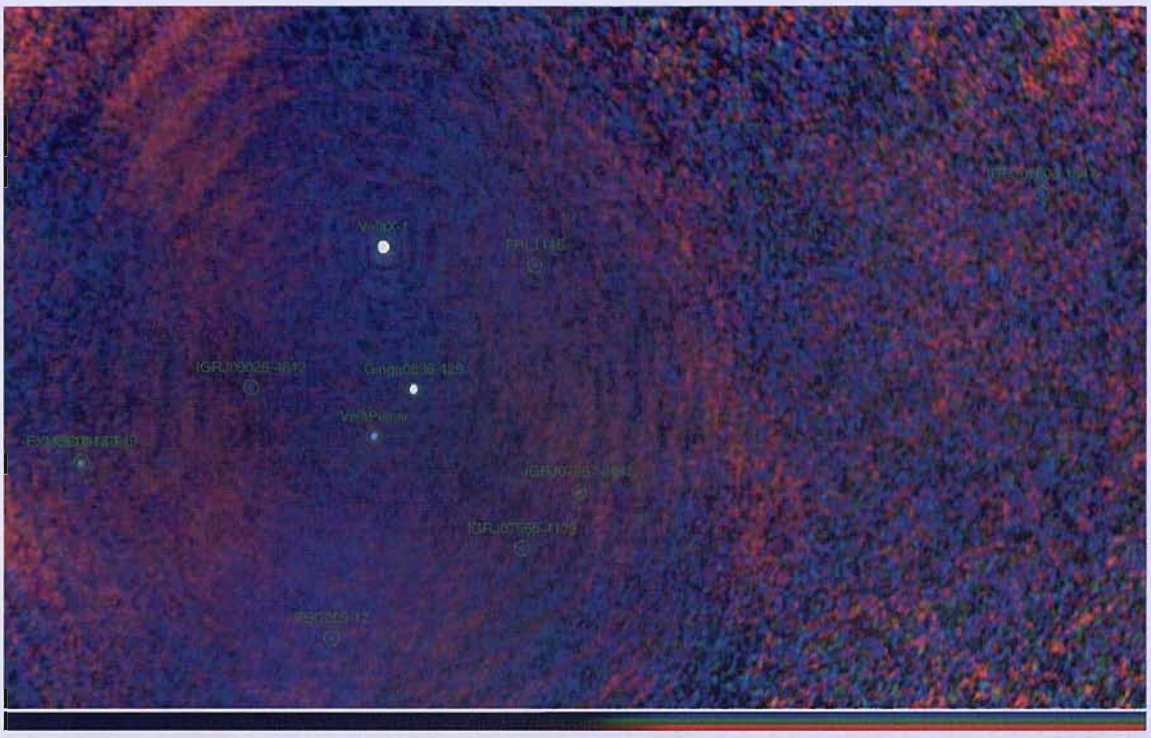

Figure D.10: False colour map of the 2nd IBIS/ISGRI Survey Catalogue from -90°< l^{II} <-120° and -9.0°< b^{II} <+9.0°

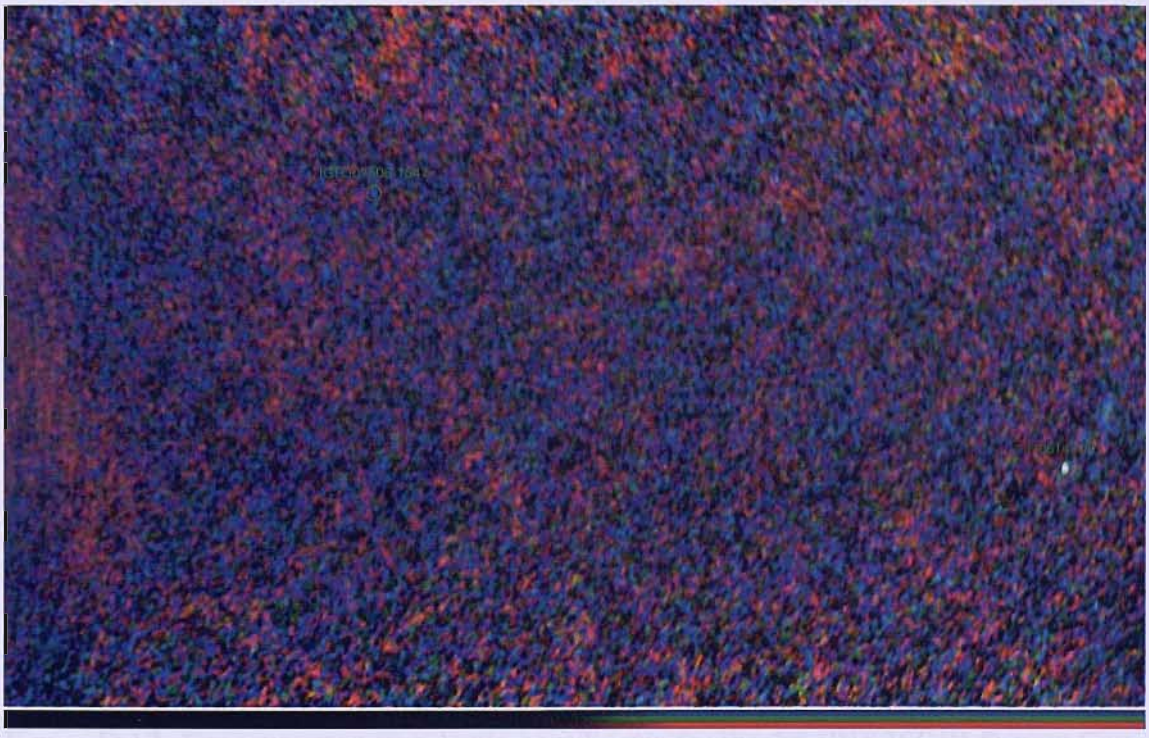

Figure D.11: False colour map of the 2nd IBIS/ISGRI Survey Catalogue from -120°< l^{II} <-150° and -9.0°< b^{II} <+9.0°

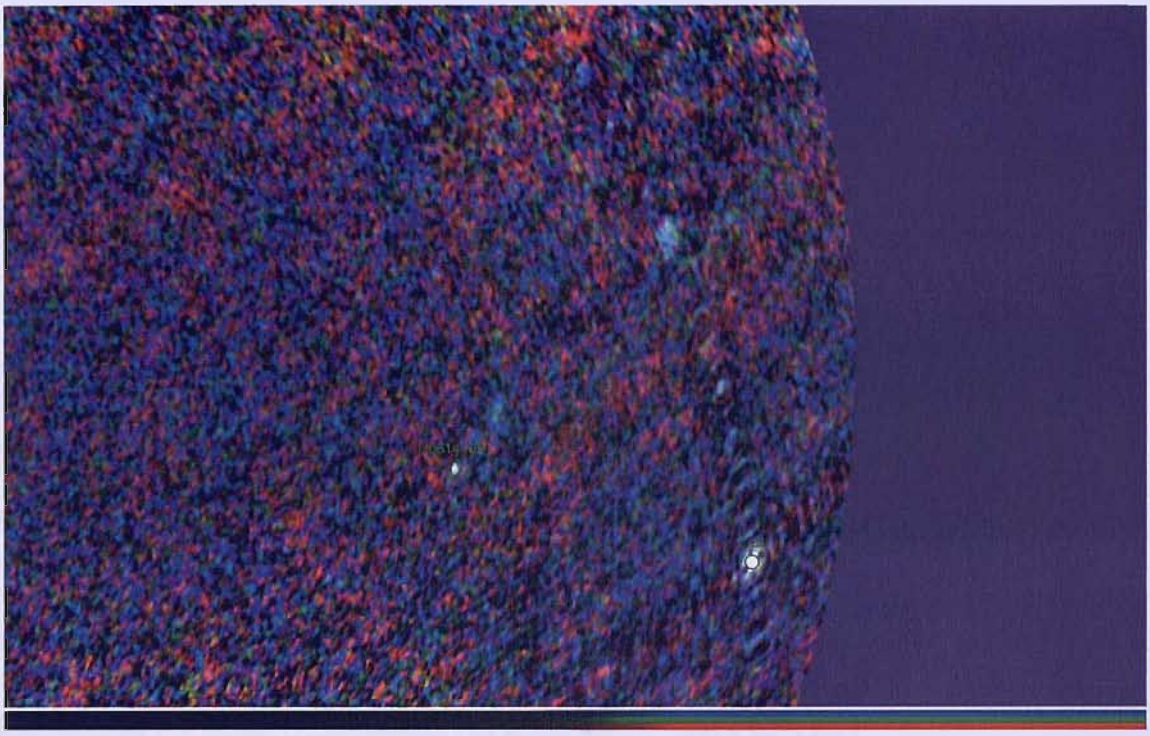

Figure D.12: False colour map of the 2nd IBIS/ISGRI Survey Catalogue from -150°< l^{II} <-180° and -9.0°< b^{II} <+9.0°

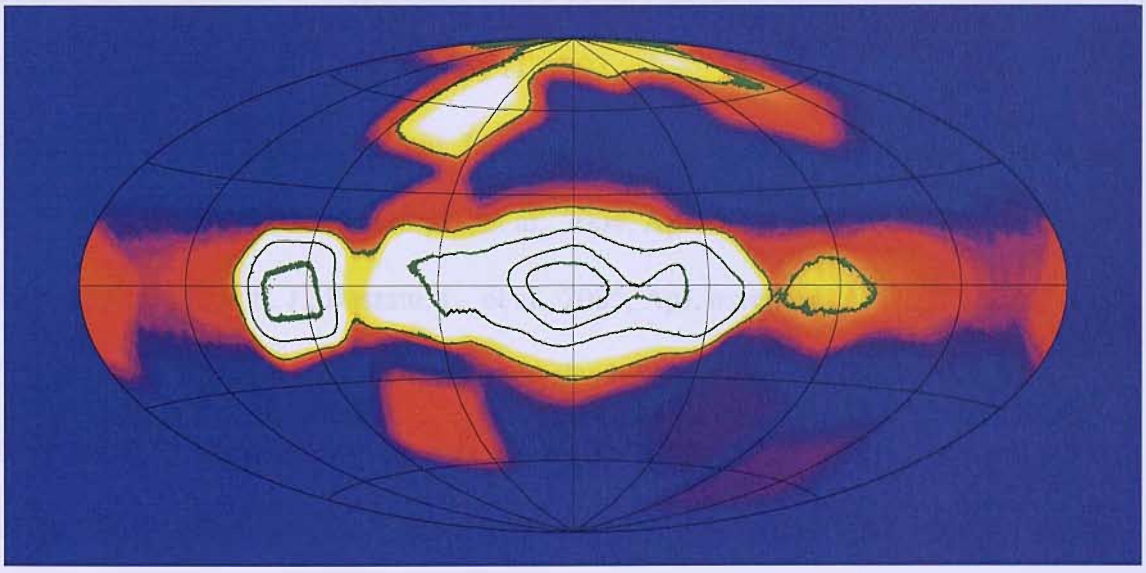

Figure D.13: Exposure map in galactic coordinates for the 2nd IBIS/ISGRI Survey Catalogue. The contours represent expsoures of: 200 ksec; 750 ksec; 1.5 Msec; 2.0 Msec.

Bibliography

Antonucci, R. R. J., 1993, ARA&A, 31, 473

Augello, G., Iaria, R., Robba, N.R., et al., 2003, ApJ, 596, L63

Barlow, E. J., 2006, Ph.D. thesis, School of Physics & Astronomy, University of Southampton, UK, Submitted February 2006

Barret, D., McClintock, J.E. & Grindlay, J.E., 1996, ApJ, 473, 963

Bassani, L., De Rosa, A., Bazzano, A., et al., 2005, ApJL, 634, L21

Bassani, L., Molina, M., et al., 2006, ApJL, 636, L65

Bélanger, G., Goldwurm, A., Goldoni, P., et al. 2004, ApJ 601, L163

Belian, R. D., Conner, J. P. & Evans, W. D., 1976, ApJ, 206, L135

Bertin, E. & Arnouts, S. 1996, A&AS, 117, 393

Bildsten, L., Chakrabarty, D., Chiu, J., et al., 1997, ApJS, 113, 367

Bird, A. J., Barlow, E. J., Bassani, L., et al., 2004, ApJ, 607L, 33B

Bird, A. J., Barlow, E. J., Bassani, L., et al., 2005, ApJ, accepted

Bowers, R. & Deeming, T., 1984, Astrophysics I: Stars, (Jones & Bartlett), 319

Bradt, H. V. D., Ohashi, T., & Pounds, K. A., 1992, ARA&A, 30, 391

Briggs, M. S., Pendleton, G. N., Kippen, R. M., et al. 1999, ApJS, 122, 503

Brown, G.E., Lee, C.H., & Bethe, H.A., 1999, New Astronomy, 4, 313

Charles, P. A. & Seward, F. D., 1995, in Exploring the X-ray Universe, (Cambridge University Press), p. 155–218

Chevalier, R.A., 1993, ApJ, 411, L33

Clark, G. W., Woo, J. W., & Nagase, F., 1994, ApJ, 442, 336

Coburn, W., Heindl, W. A., Rothschild, R. E., et al., 2002, ApJ, 580, 394

Cocchi, M., et al., 2001, ESA-SP-459: Proceeding of the 4th INTEGRAL Workshop, p279

Córdova, F. A. D., 1995, in X-Ray Binaries, eds W. H. G. Lewin, J. van Paradijs & E. P. J. Van den Heuvel (Cambridge University Press), p. 331–389

Courvoisier, T. J. -L., Walter, R., Beckman, V., et al., 2003, A&A, 411, L53

Corbet, R. H. D., 1986, MNRAS, 220, 1047

Crawford, D. F., Jauncey, D. L.& Murdoch, H. S., 1970, ApJ, 162, 405

Dean, A. J., Lei, F., Gurriaran, R., et al. 2000, Journal of the British Interplanetary Society, 53, 97

Dean, A. J., Bird, A. J., Diallo, N., et al. 2003, Space Science Reviews, 105, 285

Dean, A. J., Bazzano, A., Hill, A. B., Stephen, J. B., Bassani, L., Barlow, E. J., Bird, A. J., Lebrun, F., Sguera, V., Shaw, S. E., Ubertini, P., Walter, R., Willis, D. R., 2005, A&A, 443, 485

Dehnen, W. & Binney, J., 1998, MNRAS, 294, 429

Dias, W.S. & Lepine, J.R.D., 2005, ApJ, 629, 825

Dwek, E., Arendt, R., Hauser, M., et al. 1995, ApJ, 445, 716

Ebisawa, K., Bourban, G., Bodaghee, A., et al., 2003, A&A, 411, L59

Englmaier, P., & Gerhard, O., 1999, MNRAS, 304, 512

Feast, M. & Whitelock, P., 1997, MNRAS, 291, 683

Fender, R. P., Garrington, S. T., McKay, D. J., 1998, New Astron., 42, 593

Fishman, G. J., Meegan, C. A., Wilson, R. B., et al. 1989a, in Gamma Ray Observatory Science Workshop, Goddard, Greenbelt, ed. N. Johnson, Vol. 2, 39–50

Fishman, G. J., Meegan, C. A., Wilson, R. B., et al. 1989b, in Gamma Ray Observatory Science Workshop, Goddard, Greenbelt, ed. N. Johnson, Vol. 3, 47–62

Forman, W., Jones, C., Cominsky, L., et al., 1978, ApJS, 182, 489

Frank, J., King, A. R., & Raine, D. J., 1992, in Accretion Power in Astrophysics, (Cambridge University Press), p. 1 – 7 & 117 – 170

Giacconi, R., Gursky, H., Paolini, F., & Rossi, B., 1962, Phys. Rev. Letters, 9, 439

Gehrels, N., Chipman, E., Kniffen, D., 1994, ApJS, 92, 351

Gehrels, N., & on behalf of the Swift team, 2004, New Astronomy Rev., 48, 431

Goldwurm, A., David, P., Foschini, J., Gros, A., Laurent, P., Sauvageon, A., Bird, A. J., Lerusse, L., & Produit, N., 2003, A&A, 411, L223

Grimm, H.-J., Gilfanov, M., Sunyaev, R., 2002, A&A, 391, 923

Grindlay, J. E., Gursky, H., Schnopper, H., et al., 1976, ApJ, 205, L127

Grindlay, J. E., 2005, New Astronomy Rev., 49, 436

Gros, A., Goldwurm, A., Cadolle-Bel, M., Goldoni, P., Rodriguez, J., Foschini, L., Del Santo, M., & Blay, P., 2003, A&A, 411, L179

Harmon, B. A., Wilson, R. B., Finger, M. H., et al. 1992a, IAU Circ., 5510, 2

Harmon, B. A., Wilson, R. B., Fishman, G. J., et al. 1992b, IAU Circ., 5584, 2

Harmon, B. A., Fishman, G. J., Wilson, C. A., et al. 2002, ApJS, 138, 149

Harmon, B. A., Wilson, C. A., Fishman, G. J., et al. 2004, ApJS, 154, 585

Hartman, R. C., Bertsch, D. L., Bloom, S. D., et al. 1999, ApJS, 123, 79

Herrero, A., Kudritzki, R. P., Vilchez, J. M., et al., 1992, A&A, 261, 209

Hertz, P. & Grindlay, J., 1984, ApJ, 278, 137

Hill, A.B., Walter, R., Knigge, C., et al., 2005, A&A, 439, 255

Högbom, J. A. 1974, A&AS, 15, 417

Horne, J. H., & Baliunas, S. L., 1986, ApJ, 302, 757

Iben, Jr.I, & Livio, M. 1993, PASP, 105, 1373

in't Zand, J.M, Verbunt, F., Heise, J., 2004, NuPhS, 132, 486

Jonker, P.G. & Nelemans, G., 2004, MNRAS, 354, 355

Kanbach, G., Bertsch, D. L., Fichtel, C. E., 1988, Space Science Rev., 49, 69

Kawano, H., & Higuchi, T., 1995, GeoRL, 22, 307K

Kaper, L., Van der Meer, A., & Tijani, A. H., 2004, RMxAC, 21, 128K

Koyama, K., Kamada, M., Kunieda, H., et al., 1990, Nature, 343, 148

Knödlseder, J. 1999, BATSE All-sky Imaging using Earth Occultation, Tech. Rep. BATSE-RP-CESR-1: 2, Centre d'Etude Spatiale des Rayonnements, Toulouse

Kuulkers, E., den Hartog, P.R., in't Zand, J.J.M., et al., 2003, A&A, 399, 663

Kuulkers, E., Norton, A., Schwope A., Warner, B., 2004, in Compact Stellar X-ray Sources, eds. W.H.G. Lewin & M. van der Klis, Chapter 10, [arXiv:astro-ph/0302351]

Labanti, C., Di Cocco, G., Ferro, G., et al., 2003, A&A, 411, L149

Lamb, F. K., Fabian, A. C., Pringle, J. E., Lamb, D. Q., 1977, ApJ, 217, 197

Lebrun, F., Leray, J. P., Lavocat, P., et al., 2003, A&A, 411, L141

Levine, A. M., Lang, F. L., Lewin, W. H. G., et al. 1984, ApJS, 54, 581

Lewin, W.H.G. & Joss, P.C., 1983, in Accretion driven stellar X-ray sources, eds. W.H.G. Lewin & E.P.J. van den Heuvel, (Cambridge University), 41

Lewin, W.H.G., van Paradijs, J. & Taam R.E., 1993, Space Sci. Rev., 62, 223

Lewin, W.H.G., van Paradijs, J. & Taam R.E., 1995, in X-Ray Binaries, eds W. H. G. Lewin, J. van Paradijs & E. P. J. Van den Heuvel (Cambridge University Press), p. 175–232

Lin, C.C., & Shu, F.H., 1964, ApJ, 0140, 646

Lin, C.C., Yuan, C. & Shu, F.H., 1969, ApJ, 155, 721

Ling, J. C., Wheaton, W. A., Wallyn, P., et al. 2000, ApJS, 127, 79

Liu, Q.Z., van Paradijs, J., van den Heuvel, E.P.J., 2001, A&A, 368, 1021

Liu, Q.Z., van Paradijs, J., van den Heuvel, E.P.J., 2000, A&AS, 147, 25

Lund, N., Budtz-Jorgensen, C., Westergaard, N. J., et al., 2003, A&A, 411, L231

Lutovinov, A., Revnivtsev, M., Molkov, S. & Sunyaev, R., 2005, A&A, 430, 997

Macomb, D.J. & Gehrels, N., 1999, ApJS, 120, 335

Malizia, A., et al., 2000, ApJ, 589, L17

Malizia, A., Bassani, L., Stephen, J. B., et al., 2005, ApJ, 630, L157

Mas-Hesse, J. M., Giménez, A., Culhane, J. L., et al., 2003, A&A, 411, L261

Matt, G. & Guainazzi, M., 2003, MNRAS, 341, L13

Meegan, C. A., Fishman, G. J., Wilson, R. B., et al. 1992, Nat, 355, 143

Murdoch, H. S. & Crawford, D. F., 1973, ApJ, 183, 1

Nagase, F., 1989, PASJ, 41, 1

Negueruela, I. , 1998, A&A, 338, 505

Negueruela, I. & Coe, M. J., 2002, A&A, 385, 517

Negueruela, I., 2004, The Many Scales of the Universe - JENAM 2004 Astrophysics Reviews, (Kluwer Academic Publishers). [arXiv:astro-ph/0411759]

Nelemans, G. & van den Heuvel, E.P.J., 2001, A&A, 376, 950

Pendleton, G. N., Briggs, M. S., Kippen, R. M., et al. 1999, ApJ, 512, 362

Piccinotti, G., Mushotzky, R. F., Boldt, E. A., et al., 1982, ApJ, 253, 485

Piro, L., Scarsi, L., & Butler, R. C., 1995, Proc. SPIE 2517, 169

Psaltis, D., 2004, in Compact Stellar X-ray Sources, eds. W.H.G. Lewin & M. van der Klis, Chapter 1, [arXiv:astro-ph/0410536]

Press, W. H. & Rybicki, G. B., 1989, ApJ, 338, 277P

Revnivtsev, M.G., 2003, Astro. Lett., 29, 644

Revnivtsev, M., sunyaev, R. A., Varshalovich, D. A., et al., 2004, AstL, 30, 382R

Reynolds, A. P., Bell, S. A., & Hilditch, R. W., 1992, MNRAS, 256, 631

Robba, N. R., Burderi, L., Di Salvo, T., Iaria, R., & Cusumno, G., 2001, ApJ, 562, 950

Rodriguez, J., Tomsick, J.A., Foschini, L., et al., (2003), A&A, 407, L41

Scargle, J. D., 1982, ApJ, 263, 835

Shaw, S. E., Bird, A. J., Dean, A. J., et al. 2001, in Exploring the Gamma-Ray Universe: Proceedings of the 4th INTEGRAL Workshop, Alicante, 2000, ed. A. Gimenez, V. Reglero, & C. Winkler, Vol. ESA SP-459, 521–524

Shaw, S. E., Westmore, M. J., Bird, A. J., et al. 2003, A&A, 398, 391

Shaw, S. E., Westmore, M. J., Hill, A. B., Bird, A. J., Dean, A. J., Ferguson, C., Knödlseder, J., Lockley, J. J., Willis, D. R., 2004, A&A, 418, 1187

Schönfelder, V., et al., 1993, ApJS, 86, 657

Stephen, J.B., Bassani, L., Molina, M., et al., 2005a, A&A, 432, L49

Stephen, J.B., Bassani, L., Molina, M., et al., 2005b, A&A, accepted

Strüder, L., Briel, U., Dennerl, K., et al., 2001, A&A, 365, L18

Sugizaki, M., Mitsuda, K., Kaneda, H., et al., 2001, ApJS, 134, 77

Swank, J. H., Becker, R. H., Boldt, E. A., et al., 1977, ApJ, 212, 73

Taam, R.E. & Sandquist, E.L., 2000, ARA&A, 38, 113

Tauris, T.T., & van den Heuvel, E.J.P., 2004, astro-ph/0303456

Taylor, J., & Cordes, J. 1993, ApJ, 411, 674

Thompson, D. J., 2004, New Astronomy Rev., 48, 543

Turner, T.J., Perola, G.C., Fiore, F., et al., 2000, ApJ, 531, 245

Turner, M. J. L., Abbey, A., Arnaud, M., et al., 2001, A&A, 365, L27

Ubertini, P., et al., 1997, Proceedings of the 4th CGRO Symposium, Editors: Charles D. Dermer, Mark S. Strickman, & James D. Kurfess, AIP 410, 1527

Ubertini, P., Lebrun, F., Di Cocco, G., et al., 2003, A&A, 411, L427

Ubertini, P., Bassani, L., Malizia, A., et al., 2005, ApJ, 629, L109

Vallée, J. P., 2002, ApJ, 566, 261

van den Heuvel, E.J.P., & Heise, J., 1972, Nature, 239, 67

van den Heuval, E.P.J., 1975, ApJ, 198, L109

van Paradijs, J., & White, N. 1995, ApJ, 447, L33

Vargas, M., Goldwurm, A., Denis, et al., 1996, A&AS, 120, C291

Vargas, M., Paul, J., Goldwurm, A.,et al., 1997, ESA SP 382: Proceedings of the 2nd INTEGRAL workshop - The Transparent Universe, Editors: C. Winkler, Courvoisier, T. J. -L., & Ph. Durouchoux, p129

Vedrenne, G., Roques, J.-P., Schönfelder, V., et al., 2003, A&A, 411, L63

Warwick, R.S., Marshall, N., Fraser, G.W., et al., 1981, MNRAS, 197, 865

Walter, R., Rodriguez, J., Foschini, L., et al., 2003, A&A, 411, L427

Walter, R., Courvoisier, T. J. -L., Foschini, L., et al., 2004, ESA SP 552: Proceedings of the 5th INTEGRAL workshop - The INTEGRAL Universe, Editors: V. Schönfelder, G. Lichti & C. Winkler, p417

Westmore, M. J. 2002, PhD thesis, Dept. of Physics and Astronomy, University of Southampton, UK., Submitted October 2002

White, N.E., Becker, R. H., Boldt, E. A., 1981, ApJ, 247, 994

White, N. E., Nagase, F., & Parmar, A. N., 1995, in X-Ray Binaries, eds W. H. G. Lewin, J. van Paradijs & E. P. J. Van den Heuvel (Cambridge University Press), p. 1–57

White, N.E., & van Paradijs, J., 1996, ApJ, 473, L25

Wilson, I. R. G. & Dopita, M. A., 1985, A&A, 149, 295

Winkler, C., 2001, ESA SP 459: Proceedings of the 4th INTEGRAL workshop - Exploring the Gamma-ray Universe, Editors: A. Giménez, V. Reglero & C. Winkler, p471

Winkler, C., Courvoisier, T. J. -L., Di Cocco, G., et al., 2003, A&A, 411, L1

Zhang S. N., et al. 1994, IEEE Trans. Nucl. Sci, 41, 1313

Zombeck, M. V. 1990, Handbook of Space Astronomy and Astrophysics, 2nd edn. (Cambridge University Press)